THE PROCESSING OF AEROSOL PARTICLES AND SOLUBLE TRACE GASES BY CHEMICALLY HETEROGENEOUS RADIATION FOGS

Hui Chang

Jeffrey L. Collett, Jr., Adviser

Funding agencies:

San Joaquin Valleywide Air Pollution Study Agency
National Science Foundation (ATM-9980540, ATM-0222607)

Colorado State University

DEPARTMENT OF ATMOSPHERIC SCIENCE

PAPER NO. 751

THE PROCESSING OF AEROSOL PARTICLES AND SOLUBLE TRACE GASES BY CHEMICALLY HETEROGENEOUS RADIATION FOGS

by
Hui Chang

Department of Atmospheric Science
Colorado State University
Fort Collins, CO

San Joaquin Valleywide Air Pollution Study Agency

National Science Foundation

Under grants ATM-9980540 and ATM-0222607

July 2004

Atmospheric Science Paper No. 751

ABSTRACT

The processing of aerosol particles and soluble trace gases by chemically heterogeneous radiation fogs

Persistent radiation fogs often form in California's San Joaquin Valley (SJV) during periods of winter air stagnation. During winter 2000/2001 an extensive fog study was conducted in the San Joaquin Valley (SJV) in California, within the framework of the California Regional PM10/PM2.5 Air Quality Study (CRPAQS). The purpose of the study was to gain more information about the role of fogs in aerosol processing in the San Joaquin Valley. In addition to the CRPAQS fog study, samples from an additional radiation fog field campaign in January 2004 in Fresno, California were also analyzed as part of this project.

The dominant contributors to SJV fog composition include ammonium, nitrate, sulfate, nitrite, acetate, formate, formaldehyde, glyoxal, and methyl glyoxal. Significant differences were observed between the composition of small and large SJV fog drops. Small drops contain higher concentrations of ammonium, nitrate, sulfate, and organic carbon, but lower concentrations of nitrite. The pH values measured in large and small fog drops were similar in this study, in contrast to previous measurements in the SJV.

SJV fogs typically have high pH values, above 6, due to large atmospheric concentrations of water soluble ammonia. The high drop pH promotes rapid formation of aqueous aldehyde-S(IV) complexes and rapid oxidation of dissolved sulfur dioxide by ozone. Model simulations indicate that formation of the S(IV)-formaldehyde adduct hydroxymethanesulfonate is the dominant fate of dissolved sulfur dioxide in both large and small fog drops. S(IV) oxidation is limited due to finite rates of reactant mass transport into the drops and competition for available sulfite and bisulfite by formaldehyde.

Fogs play an important role as cleansers of the polluted winter SJV atmosphere. Scavenging of atmospheric fine particles and soluble trace gases by fog drops, followed by drop deposition to the ground, removes large amounts of nitrate, sulfate, ammonium, and organic carbon from the atmosphere. Deposition fluxes of fog water were observed to vary with fog liquid water content and drop effective diameter. Deposition velocities for nitrate, ammonium, sulfate, and organic carbon were observed to be of the order of 1 cm/s, much larger than expected in the absence of fog. Deposition velocities for nitrate, sulfate, ammonium, and organic carbon in fog were observed to be slightly lower than the deposition velocity of fog water itself. This pattern results from enrichment of these species in smaller fog drops that settle more slowly and the dominance of sedimentation as a drop deposition mechanism in environments with low wind speeds and low surface roughness. The deposition velocity of nitrite was typically higher than for fog water, due to its enrichment in larger, faster settling droplets. Overall, the observed deposition fluxes of these major inorganic aerosol species are significant and can offset or exceed aqueous phase production of new aerosol mass. Typical reductions in boundary layer concentrations of organic carbon, nitrate, sulfate, and ammonium due to fog deposition were estimated to be of the order of 1 $\mu g/m^3 \cdot hr$.

Numerous reports have appeared in the recent literature indicating the likelihood of fog/cloud processing of carbonaceous aerosol particles. Fog composition measurements also indicate the important role fogs play as processors of carbonaceous species. This study reveals the presence of numerous organic species in SJV fog, including formaldehyde, low molecular weight carboxylic acids such as acetate and formate, di-carboxylic acids, carbonyls and dicarbonyls including glyoxal and methyl glyoxal. Together these compounds make up the majority of low molecular weight (< 500 Daltons) carbon in the fog water. Significant amounts of higher molecular weight organic matter were also identified in the fogs using ultrafiltration. Identification of the nature and properties of this higher molecular weight material should be a focus in future fog studies. In order to provide some additional insight into the types of organic molecules present in the fog water, we followed an approach previously outlined by Decesari et al.

(2000) using anion exchange chromatography on a DEAE cellulose column. Chromatograms obtained using this approach have been claimed to indicate the composition of the sample as divided into neutral/basic, mono- and di-carboxylic acid, and polycarboxylic acid fractions. Results from this approach have been widely used in recent studies to derive new models for the organic composition of aerosols and fogs. Chromatograms obtained for the California fog samples are similar in appearance to those reported elsewhere in the literature. However, tests of this method using individual compound standards reveal a tendency for the method to misclassify important families of organic compounds (e.g., phenolic compounds and dicarbonyls) as carboxylic acids. Caution is certainly warranted, therefore, in interpretation of sample chromatograms obtained with this method.

ACKNOWLEDGEMENTS

I am grateful to Dr. Sonia M. Kreidenweis, Dr. William Cotton and Dr. Ken Carlson, for their innovative suggestions, comments and recommendations for this work.

I am also very grateful to Pierre Herckes and Taehyoung Lee for their great efforts in both field campaigns and in sample analysis. J. Reilly, G. Kang, D. Sherman, S. Youngster and S. Emert were also helpful during the field campaign.

At various times, many additional group members provided guidance for the completion of this work and leaded to the success of the project. Pierre Herckes was instrumental to organic analysis; Taehyoung Lee completed IC analysis; S(IV) and HCHO analysis were due in part to the help of Laurie Trenary. Katharine Moore gave useful suggestions on metal analysis.

This research was supported by the San Joaquin Valleywide Air Pollution Study Agency and the National Science Foundation (ATM-9980540 and ATM-0222607). The statements and conclusions presented are those of the contractor and not necessarily those of the California Air Resources Board, the San Joaquin Valleywide Air Pollution Study Agency, or its Policy Committee, their employees, or their members. The mention of commercial products, their sources, or their use in connection with material reported herein is not to be construed as actual or implied endorsement of such products.

TABLE OF CONTENTS

1. Fog Chemistry Review (Introduction) 1
1.1 What is fog and how is it formed and maintained? 1
1.2 Aerosol activation 2
1.3 Aerosol scavenging, removal and production in fogs 7
1.4 Fog scavenging of gases and secondary aerosol production 9
1.4.1 S(IV) oxidation by hydrogen peroxide (H_2O_2) 12
1.4.2 S(IV) oxidation by ozone (O_3) 13
1.4.3 S(IV) oxidation by oxygen (O_2) 15
1.4.4 Reaction of dissolved SO_2 with HCHO 15
1.4.5 The overall fate of S(IV) 16
1.5 Aqueous phase reactions of organics 17
1.6 Solute deposition in fogs 17
1.7 Issues of drop size-dependent fog composition 18
1.8 Net effects of fogs on pollutant concentrations 19
1.9 Investigating the chemistry of fog formation and dissipation in California's Central Valley 19
1.9.1 Terrain and weather conditions in the valley 20
1.9.2 Fog composition 21
1.9.3 Sulfur reactions 23
1.9.4 Size dependent composition 24
1.9.5 Fog deposition and net effects of Central Valley fogs on aerosol populations 24
1.9.6 Organics in Central Valley fogs 26
1.10 Open questions and major research goals 28
1.10.1 Major findings to date in Central Valley fogs 28
1.10.2 Remaining needs for improving our understanding of Central Valley fogs, their composition, and their influence on aerosol populations 29
1.10.3 The primary objectives of this study 29
2. Experimental description 31
2.1 Sampling sites and times 31
2.1.1 Angiola sampling site 31
2.1.2 Fresno sampling site 32
2.2 Sampling 33
2.2.1 Meteorological measurements 33
2.2.2 Bulk fog collection 34
2.2.3 Size-resolved fog composition 36
2.2.4 Size distribution of fog droplets 39
2.2.5 Fog deposition 41
2.2.6 Gas phase measurements 43

2.2.7 Size-resolved aerosol composition 43
2.3 Sample handling and chemical analysis 44
2.3.1 Sample weight 46
2.3.2 pH measurements 46
2.3.3 Ion concentrations 46
2.3.4 Metals 47
2.3.5 S(IV) 47
2.3.6 Formaldehyde 47
2.3.7 H_2O_2 (aq) 48
2.3.8 Organic Acids 48
2.3.9 TOC/DOC and GC/MS analysis 49
2.3.10 Ultrafiltration (molecular weight measurement) 50
2.3.11 Carbonyl and functional group analysis 50
2.4 Quality Control 51
2.4.1 Ion concentrations 53
2.4.2 Organic acids 54
2.4.3 S(IV), HCHO, H_2O_2, metal (Fe, Mn), TOC and DOC 54
2.4.4 MOUDI 55
2.5 Instrumental quality control 56
2.5.1 Meteorological measurements 56
2.5.2 Flow rate measurements 56
2.5.3 CSASP uncertainties 57
3.Overview of fog episodes and fog composition 58
3.1 Summary of fog sampling 58
3.2 Weather conditions 59
3.3 Drop size distribution and evolution 63
3.3.1 comparison between CSASP and PVM 63
3.4 Bulk composition 66
3.4.1 Components and concentrations 66
3.4.1.1 Major inorganic ions and pH 66
3.4.1.2 Organics 70
3.4.2 Average fog solute concentrations 72
3.5 Size dependent compositions 75
3.5.1 pH and inorganic species 76
3.5.2 Size distribution of CSU 5-stage collector 83
4. Aerosol processing and removal by fogs 85
4.1 Overview 85
4.2 Results and Discussion 88
4.2.1 Ion concentrations and flux calculation from deposition plates 88
4.2.2 Water fluxes derived from the balances 99
4.2.3 Comparison of water fluxes to plates and balances and flux variation with fog liquid water content and effective diameter 102
4.2.4 Deposition velocities 104
4.3 Sulfur dioxide oxidation in fog drops 110
4.3.1 Theoretical reaction rates 110
4.3.2 Predicted S(IV) oxidation rates 112

4.3.3 Experiment approach 115
4.3.4 Results and discussion 117
4.3.4.1 Model results 117
4.3.4.2 Theoretical S(IV) reaction rates 123
4.3.4.3 Comparison of theoretical and modeled rates 125
4.4 Overall effects of fog on atmospheric species concentration 127
5. Organic composition 131
5.1 Overview 131
5.1.1 TOC and DOC 131
5.1.2 MW analysis of DOC 132
5.1.3 DOC composition 133
5.2 Determination of carbonyl compounds by HPLC 134
5.2.1 Overview 134
5.2.2 Instruments and reagents 135
5.2.2.1 HPLC conditions 135
5.2.2.2 Reagents 136
5.2.3 Procedures 137
5.2.4 HPLC method results 138
5.2.4.1 Chemical structures of carbonyls and dicarbonyls 138
5.2.4.2 Example chromatograms 139
5.2.4.3 Carbonyl calibration results 141
5.2.4.4 Blank and Minimum Detection Limit (MDL) 142
5.2.4.5 DNPH Recrystallization 144
5.2.4.6 HPLC Uncertainty (RSD) 146
5.2.4.7 Standard Accuracy 146
5.2.4.8 Artificial fog water samples 147
5.2.4.9 Stability of samples 148
5.2.5 California SJV fog water samples analysis 151
5.2.6 Fresno fog water analysis 152
5.2.6.1 Fresno fog sample pH and pH size distribution 153
5.2.6.2 Fresno bulk fog samples' carbonyl and dicarbonyl concentrations 156
5.2.6.3 Fresno bulk fog sample composition 157
5.2.6.4 Comparison of HCHO measurement techniques 157
5.2.6.5 Species size distribution of Fresno fog samples 161
5.3 Functional group characterization of organic acids 166
5.3.1 Overview 166
5.3.2 Instruments and reagents 166
5.3.2.1 HPLC conditions 167
5.3.2.2 Reagent 167
5.3.3 Procedures 167
5.3.4 Results 168
5.3.4.1 Method Test 168
5.3.5 Sample results 178
5.3.5.1 Blanks 178
5.3.5.2 California fog samples (Angiola) 179
5.3.5.3 Fresno fog samples 183

6. Conclusions and future work 187
6.1 Conclusions 187
6.2 Recommendations for future work 189

References 190

Appendix A Collector flow measurements and size cut calculations 205
Appendix B Simulated air flow and particle tracks in sampling tube of CSASP 223
Appendix C CSASP data treatment procedures 233
Appendix D Discussion and correction of drop size distribution data at Angiola 241
Appendix E Timelines of temperature and wind speed for CRPAQS 245
Appendix F Aqueous chemistry model code 248
Appendix G The composition of DOC for individual Fresno fog samples. 263

LIST OF FIGURES

Figure 1-1. Köhler curves for NaCl and $(NH_4)_2SO_4$ particles for various dry particle diameters (Hanel, 1976). 3
Figure 1-2. a, Conventional Köhler curve for a 30 nm dry particle consisting of ammonium sulphate at 298 K. b, A similar particle containing an additional, insoluble 500 nm core (the amount of ammonium sulphate is the same as with a). 4
Figure 1-3. Typical size distribution of aerosol particles. 7
Figure 1-4. Simplified chemistry of a cloud/fog drop. 9
Figure 1-5.Rate of S(IV) oxidation by O_3 in the aquous phase under conditions typical of a Los Angelos atmosphere, with SO_2=20ppb and O_3=50ppb (adapter from Hoffmann, 1986). 14
Figure 1-6. Oxidation rates of the three S(IV) oxidation pathways, along with the rate of HMS formation for typical conditions in central California fogs. 16
Figure 1-7. Terrain map of California Central Valley area. Red dot on the map is the main Angiola sampling site. 20
Figure 1-8. Measured composition in a typical bulk fog sample collected at Fresno during IMS95. All concentrations are listed in μN. 22
Figure 2-1. Photo of the Angiola field laboratory, where collected fog samples were processed. 31
Figure 2-2. Angiola sampling site overview on a foggy day. 32
Figure 2-3. Overview of the Fresno sampling site on a foggy day. 32
Figure 2-4. Gerber Scientific Particulate Volume Monitor (model PVM-100). 34
Figure 2-5. Caltech Active Strand Cloud Collector (CASCC). 35
Figure 2-6. Fan revolution speed and air velocity measured for the CASCC as a function of applied fan voltage. "Corrected" means the flow rate has been corrected due to air pressure diference at different altitude. 35
Figure 2-7. Corrected air speed and revolution speed vs voltage on metal organic CASCC (ss-CASCC). "Corrected" means the flow rate has been corrected due to air pressure difference at different altitude. 36
Figure 2-8. An all-plastic size-fractionating CASCC (sf-CASCC) mounted on site. The first stage, second stage, sampling bottle and fan parts can clearly be seen. 37
Figure 2-9. Corrected air velocity and revolution speed vs voltage on sf-CASCC. "Corrected" means the flow rate has been corrected due to air pressure difference at different altitude. 37
Figure 2-10. Corrected air velocity and revolution speed vs voltage on ss-sf-CASCC. "Corrected" means the flow rate has been corrected due to air pressure difference at different altitude. 38

Figure 2-11. The CSU 5-stage collector shown deployed in an earlier cloud campaign at Whiteface Mtn, NY. Photo by K. Moore. 39
Figure 2-12. CSASP-100-HV optical probe. 39
Figure 2-13. Two deposition plates deployed during CRPAQS. The plastic sheeting beneath the plates was used to eliminate possible contamination from the ground. 42
Figure 2-14. Two balances set up to record deposition fluxes to a bare metal and an artificial grass surface. 42
Figure 2-15. Gas phase measurements of total soluble hydroperoxides by continuous monitor. 43
Figure 2-16. A Microorifice Uniform Deposit Impactor (MOUDI). 44
Figure 2-17. Schematic describing sample fractionation. 49
Figure 2-18. HP 1050 HPLC system. 51
Figure 3-1. Effective Diameter and LWC measured by PVM on 12/17 &12/18/00. 61
Figure 3-2. Effective diameter and LWC on 12/18 & 12/19/00. 61
Figure 3-3. Effective Diameter and LWC on 01/21/00. 62
Figure 3-4. Effective diameter and LWC on 01/25/00. 62
Figure 3-5. Effective diameter and LWC on 02/01/00. 62
Figure 3-6. Comparison between effective diameters obtained from PVM and CSASP on 12/17 & 12/18/00. 64
Figure 3-7. Comparison of effective diameter from PVM and CSASP of the fog event on 12/17 & 12/18/00. 64
Figure 3-8. Comparison of LWC obtained by PVM and CSASP of the fog event on 12/17 & 12/18/00. 65
Figure 3-9. Drop size distribution evolution with time on 12/17 & 12/18/00. 66
Figure 3-10 timelines of three ion concentrations and pH in CASCC samples. 67
Figure 3-11. Timelines of three major ions, nitrite and pH in CASCC samples on 12/17/00&12/18/00 fog event. 67
Figure 3-12. Timelines of three major ions, nitrite and pH in CASCC samples on 12/18/00&12/19/00 fog event. 68
Figure 3-13. Timelines of three major ions, nitrite and pH in CASCC samples on 01/17/01. 68
Figure 3-14. Timelines of three major ions, nitrite and pH in CASCC samples on 01/21/01. 68
Figure 3-15. Timelines of three major ions, nitrite and pH in CASCC samples on 01/25/01. 69
Figure 3-16. Timelines of three major ions, nitrite and pH in CASCC samples on 01/31/01. 69
Figure 3- 17. Ammonium concentrations vs. total concentration of nitrate, sulfate and nitrite for all fog events. 69
Figure 3-18. Timelines of formate, acetate, TOC and HCHO concentrations for all fog events. HCHO concentration was from CASCC collector, other were from organic ss-CASCC collector. HCHO concentration and collecting time corresponds main x, y-axises. 70
Figure 3-19 Timelines of three major ions and pH in CASCC samples in the

12/17&12/18/00 fog event 71
Figure 3-20. Timelines of three major ions and pH in CASCC samples on 01/17/01 71
Figure 3-21. Measured composition for fog episodes during winter 2000/2001. All concentrations are listed as μN. Other cations include sodium, potasium, calcium, magnesium and H^+. Other anions include chloride, propionate, pyruvate and oxalate. 74
Figure 3-22. Total cation concentrations vs. total anion concentrations. 75
Figure 3-23. Large vs. small pH for all fog events of CRPAQS. Error bars represent analytical RSD listed in chapter two. 77
Figure 3-24. Large vs. small Cl^- concentrations for all fog events of CRPAQS. Error bars represent analytical RSD listed in chapter two. 77
Figure 3-25. Large vs. small NO_3^- concentrations for all fog events of CRPAQS. Error bars represent analytical RSD listed in chapter two. 77
Figure 3-26. Large vs. small SO_4^{2-} concentrations for all fog events of CRPAQS. Error bars represent analytical RSD listed in chapter two. 78
Figure 3-27. Large vs. small Na^+ concentrations for all fog events of CRPAQS. Error bars represent analytical RSD listed in chapter two. 78
Figure 3-28. Large vs. small NH_4^+ concentrations for all fog events of CRPAQS. Error bars represent analytical RSD listed in chapter two. 78
Figure 3-29. Large vs. small K^+ concentrations for all fog events of CRPAQS. Error bars represent analytical RSD listed in chapter two. 79
Figure 3-30. Large vs. small Mg^{2+} concentrations for all fog events of CRPAQS. Error bars represent analytical RSD listed in chapter two. 79
Figure 3-31. Large vs. small Ca^{2+} concentrations for all fog events of CRPAQS. Error bars represent analytical RSD listed in chapter two. 79
Figure 3-32. Large vs. small total Fe concentrations for all fog events of CRPAQS. Error bars represent analytical RSD listed in chapter two 80
Figure 3-33. Large vs. small total Mn concentrations for all fog events of CRPAQS. Error bars represent analytical RSD listed in chapter two. 80
Figure 3-34. Large vs. small NO_2^- concentrations for all fog events of CRPAQS. Error bars represent analytical RSD listed in chapter two. 80
Figure 3-35. Large vs. small HCHO concentrations for all fog events of CRPAQS. Error bars represent analytical RSD listed in chapter two. 81
Figure 3-36. Large vs. small TOC concentrations for all fog events of CRPAQS. Error bars represent analytical RSD listed in chapter two. 81
Figure 3-37. Large vs. small formate concentrations for all fog events of CRPAQS. Error bars represent analytical RSD listed in chapter two. 81
Figure 3-38. Large vs. small acetate concentrations for all fog events of CRPAQS. Error bars represent analytical RSD listed in chapter two. 82
Figure 3-39. Large vs. small propionate concentrations for all fog events of CRPAQS. Error bars represent analytical RSD listed in chapter two. 82
Figure 3-40. Large vs. small oxalate concentrations for all fog events of CRPAQS. Error bars represent analytical RSD listed in chapter two. 82
Figure 3-41. pH value vs. theoretical Dp50 of 5-stage collector. 83
Figure 3-42. Major ion concentrations vs. theoretical Dp50 of 5-stage collector on day 01/17/01. 84

Figure 3- 43. Major ion concentrations vs. theoretical Dp50 of 5-stage collector on day 12/19/00 84
Figure 3-44. Major ion concentrations vs. Theoretical Dp50 of 5-stage collector on day 01/31/01 84
Figure 4-1. Comparison of fog water mass collected by two deposition plates. The solid line is data trendline; the dashed line is the 1:1 line. Error bars represent the pooled standard deviation of replicate samples from 2 collocated deposition plates. 89
Figure 4-2. Comparison of fog water flux collexted by two deposition plates. The Solid line is data trendline; The dashed line is the 1:1 line. Error bars represent the pooled standard deviation of replicate samples from two collocated deposition plates. 89
Figure 4-3. Comparison of Cl^- concentration collected by two deposition plates. The solid line is data trendline; the dashed line is the 1:1 line. Error bars represent the pooled standard deviation of replicate samples from 2 collocated deposition plates. 89
Figure 4-4. Comparison of Cl^- flux collected by two deposition plates. SolidThe Solid line is data trendline; The dashed line is the 1:1 line. Error bars represent the pooled standard deviation of replicate samples from 2 collocated deposition plates 90
Figure 4-5. Comparison of NO_3^- concentration collected by two deposition plates. The solid line is data trendline; the dashed line is the 1:1 line. Error bars represent the pooled standard deviation of replicate samples from 2 collocated deposition plates. 90
Figure 4-6. Comparison of NO_3^- flux collected by two deposition plates. The Solid line is data trendline; The dashed line is the 1:1 line. Error bars represent the pooled standard deviation of replicate samples from 2 collocated deposition plates 90
Figure 4-7. Comparison of SO_4^{2-} concentration collected by two deposition plates. solid line is data trendline; the dashed line is the 1:1 line. Error bars represent the pooled standard deviation of replicate samples from 2 collocated deposition plates. 91
Figure 4-8. Comparison of SO_4^{2-} flux collected by two deposition plates. The Solid line is data trendline; The dashed line is the 1:1 line. Error bars represent the pooled standard deviation of replicate samples from 2 collocated deposition plates 91
Figure 4-9. Comparison of Na^+ concentration colected by two deposition plates. The solid line is data trendline; the dashed line is the 1:1 line. Error bars represent the pooled standard deviation of replicate samples from 2 collocated deposition plates. 91
Figure 4-10. Comparison of Na+ flux collected by two deposition plates. The Solid line is data trendline; The dashed line is the 1:1 line. Error bars represent the pooled standard deviation of replicate samples from 2 collocated deposition plates 92
Figure 4-11. Comparison of NH_4^+ concentration collected by two deposition plates. Solid line is data trendline; the dashed line is the 1:1 line. Error bars

represent the pooled standard deviation of replicate samples from 2 collocated deposition plates. 92
Figure 4-12. Comparison of NH_4^+ flux collected by two deposition plates. The Solid line is data trendline; The dashed line is the 1:1 line. Error bars represent the pooled standard deviation of replicate samples from 2 collocated deposition plates....92
Figure 4-13. Comparison of K^+ concentration collected by two deposition plates. The solid line is data trendline; the dashed line is the 1:1 line. Error bars represent the pooled standard deviation of replicate samples from 2 collocated deposition plates. 93
Figure 4-14. Comparison of K^+ flux collected by two deposition plates. The Solid line is data trendline; The dashed line is the 1:1 line. Error bars represent the pooled standard deviation of replicate samples from 2 collocated deposition plates....93
Figure 4-15. Comparison of Mg^{2+} concentration collected by two deposition plates. solid line is data trendline; the dashed line is the 1:1 line. Error bars represent the pooled standard deviation of replicate samples from 2 collocated deposition plates. 93
Figure 4-16. Comparison of Mg^{2+} flux collected by two deposition plates. The Solid line is data trendline; The dashed line is the 1:1 line. Error bars represent the pooled standard deviation of replicate samples from 2 collocated deposition plates....94
Figure 4-17. Comparison of Ca^{2+} concentration collected by two deposition plates. solid line is data trendline; the dashed line is the 1:1 line. Error bars represent the pooled standard deviation of replicate samples from 2 collocated deposition plates. 94
Figure 4-18. Comparison of Ca^{2+} flux collected by two deposition plates. The Solid line is data trendline; The dashed line is the 1:1 line. Error bars represent the pooled standard deviation of replicate samples from 2 collocated deposition plates....94
Figure 4-19. Comparison of NO_2^- concentration collected by two deposition plates. solid line is data trendline; the dashed line is the 1:1 line. Error bars represent the pooled standard deviation of replicate samples from 2 collocated deposition plates. 95
Figure 4-20. Comparison of NO_2^- flux collected by two deposition plates. The Solid line is data trendline; The dashed line is the 1:1 line. Error bars represent the pooled standard deviation of replicate samples from 2 collocated deposition plates....95
Figure 4-21. Comparison of TOC concentration collected by two deposition plates. The solid line is data trendline;the dashed line is the 1:1 line. Error bars represent the pooled standard deviation of replicate samples from 2 collocated deposition plates. 95
Figure 4-22. Comparison of TOC flux collected by two deposition plates. The Solid line is data trendline; The dashed line is the 1:1 line. Error bars represent the pooled standard deviation of replicate samples from 2 collocated deposition plates....96

Figure 4-23. Area normalized balance reading on 12/18/00. Temperature and wind speed trendlines are also presented for reference. 98
Figure 4-24. Comparison of 10 minute average water flux on two balances in day 12/18/00. The dashed line is the 1:1 line. 100
Figure 4-25. Comparison of 10 minute average water flux on two balances in day 12/19/00. The dashed line is the 1:1 line. 100
Figure 4-26 Comparison of 10 minute average water flux on two balances on day 01/15/01. The dashed line is the 1:1 line. 100
Figure 4-27. Comparison of 10 minute average water flux on two balances in day 01/17/01. The dashed line is the 1:1 line. 101
Figure 4-28. Comparison of 10 min average water flux on two balances in day 01/21/01. The dashed line is the 1:1 line. 101
Figure 4-29. Comparison of 10 minute average water flux on two balances in day 01/25/0. The dashed line is the 1:1 line. 101
Figure 4-30. Comparison of 10 min average water flux on two balances in day 01/31/01. The dashed line is the 1:1 line. 102
Figure 4-31. Comparison of water fluxes of balances and deposition plates for all fog events. 104
Figure 4-32. Deposition velocities of fogwater, TOC , NH_4^+, SO_4^{2-}, NO_3^- and NO_2^- 107
Figure 4-33. Deposition velocities of fogwater, Cl^-, Na^+, K^+, Mg^{2+} and Ca^{2+} 107
Figure 4-34. Size distributions of NH_4^+, SO_4^{2-}, NO_3^-, TOC, NO_2^- and Ca^{2+}. Error bars represent relative standard deviation derived from replicate samples of ion chromatograph. 108
Figure 4-35. Deposition velocity vs. small/large ratio for samples in day 12/18/00, for each line, from the left to the right, it is NO_2^-, NH_4^+, SO_4^{2-} and NO_3^- respectively. 109
Figure 4-36. S(IV) sinks as calculated by the aquous phase chemistry model for both the large (upper panel) and small (lower panel) drop fractions from the sf-CASCC. 120
Figure 4-37. Sensitive test of rate of HMS formation to HCHO concentrations. 121
Figure 4-38. Sensitivity test of rate of the H_2O_2-S(IV) oxidation pathway to H_2O_2 concentrations.. 122
Figure 4-39. Sensitivity test of the rate of the O_3-S(IV) oxidation pathway to O_3 concentrations. 122
Figure 4-40. Theoretical rates of ozone and hydrogen peroxide oxidation and HMS formation for all the fog samples. 124
Figure 4-41. Comparison of HMS formation modeled rates and theoretical rates. 125
Figure 4-42. Comparison of ozone oxidation modeled rates and theoretical rates. 125
Figure 4-43. Theoretical and model rate comparison to large/small ratios for all fog sample periods.. 126
Figure 4-44. Timelines of deposition removal rates of four major ions CASCC samples on 12/17/00&12/18/00 fog event. 128
Figure 5-1. Average fraction of TOC and DOC for CRPAQS samples. 131
Figure 5-2. Molecular weight analysis of DOC for six fog water samples. 132
Figure 5-3. Mass fractions of CRPAQS fog DOC comprised by several key low MW species. 133

Figure 5-4. 2-D and 3-D views of an example chromatogram showing retention times and wavelength dependent absorption for several carbonyls in a standard. 140
Figure 5-5. Several example calibration curves. Formaldehyde, acetaldehyde, acrolein+acetone and calibration curves were based on standards analyzed on 01/25/04 with absorbance monitored at 360 nm. Glyoxal and methyl glyoxal calibration curves were constructed on the same date, but absorbance of these compounds was monitored at 430 nm. 141
Figure 5-6. Carbonyl stability test in real fog water base matrix 151
Figure 5-7. Comparison of pH between large and small fog drops. 153
Figure 5-8. Typical composition of carbonaceous material comprising the total dissolved organic carbon (DOC) content observed for several California Fresno radiation fog samples. 157
Figure 5-9. Concentrations of HCHO measured by the HPLC method and fluorescence in large and small drop samples collected with the ss-sf-CASCC in Fresno radiation fogs on the night started from Jan 10-Jan 11, 2004 161
Figure 5-10. Concentrations of acetaldehyde measured by the HPLC method in large and small drop samples collected with the ss-sf-CASCC in Fresno radiation fogs on the night started from Jan 10-Jan 11, 2004. 162
Figure 5-11. Concentrations of acrolein and acetone measured by the HPLC method in large and small drop samples collected with the ss-sf-CASCC in Fresno radiation fogs on the night started from Jan 10-Jan 11, 2004. 163
Figure 5-12. Concentrations of isovaleraldehyde measured by the HPLC method in large and small drop samples collected with the ss-sf-CASCC in Fresno radiation fogs on the night started from Jan 10-Jan 11, 2004. 163
Figure 5-13. Concentrations of glyoxal measured by the HPLC method in large and small drop samples collected with the ss-sf-CASCC in Fresno radiation fogs on the night started from Jan 10-Jan 11, 2004. 164
Figure 5-14. Concentrations of methylglyoxal measured by the HPLC method in large and small drop samples collected with the ss-sf-CASCC in Fresno radiation fogs on the night started from Jan 10-Jan 11, 2004. 164
Figure 5-15. Concentrations of m-Tolualdehyde measured by the HPLC method in large and small drop samples collected with the ss-sf-CASCC in Fresno radiation fogs on the night started from Jan 10-Jan 11, 2004. 165
Figure 5-16. Concentrations of p-Tolualdehyde measured by the HPLC method in large and small drop samples collected with the ss-sf-CASCC in Fresno radiation fogs on the night started from Jan 10-Jan 11, 2004. 165
Figure 5-17. Concentrations of hexaldehyde measured by the HPLC method in large and small drop samples collected with the ss-sf-CASCC in Fresno radiation fogs on the night started from Jan 10-Jan 11, 2004. 166
Figure 5-18. HPLC chromatograms of fog water. The three fractions defined in the test (FR1, FR2 FR3) are indicated by the horizontal bars above the chromatogram. The peak due to nitrate is also evidenced. (taken from Decesari et al., 2000). 168
Figure 5-19. HPLC chromatogram of sodium nitrate using DEAE method 171

Figure 5-20. HPLC chromatogram of sodium nitrite using DEAE method. 171
Figure 5-21. HPLC chromatogram of methyl glyoxal using DEAE method. 172
Figure 5-22. HPLC chromatogram of benzene using DAEA method. 172
Figure 5-23. HPLC chromatogram of phenol using DEAE method.....173
Figure 5-24. HPLC chromatogram of vanillin using DEAE method. 173
Figure 5-25. Normalized abundance in the aerosol water extract and fog sample of nonexchangeable protons in the four categories (Taken from Decesari et al. (2000)).....176
Figure 5-26. HPLC chromatogram of DI water using DEAE method. 179
Figure 5-27. HPLC chromatogram of real California sample using DEAE method. 179
Figure 5-28. HPLC chromatogram of California sample AGCC03101 using DEAE. method.....180
Figure 5-29. HPLC chromatogram of California sample AGPCL03101 using DEAE. method.....181
Figure 5-30. HPLC chromatogram of California sample AGPCL03102 using DEAE method.....181
Figure 5-31. HPLC chromatogram of California sample AGPCL03103 using DEAE method.....182
Figure 5-32. Peak areas vs. concentrations for nitrite and nitrate.....182
Figure 5-33. HPLC chromatogram of FSC01101 using DEAE method.....184
Figure 5-34. HPLC chromatogram of FSC01102 using DEAE method.....185
Figure 5-35. HPLC chromatogram of FSC01103 using DEAE method.....185
Figure 5-36. HPLC chromatograms of (1) 50% FSC01101 with 50% DI (2) 50% Nitrate plus 50% FSC01101 (3) 50% Methyl Glyoxal plus 50% FSC01101 (4) 50% Nitrite plus 50% FSC01101, using DEAE method.....186

LIST OF TABLES

Table 2-1. Calibration table of CSASP during CRPAQS study 40
Table 2-2. Aliquot preservation protocol. 45
Table 2-3. RSD, MDL and sample concentration summaries for CRPAQS fog ions. 53
Table 2-4. Statistical analysis for organic acids. 54
Table 2-5. Statistical analysis for S(IV), HCHO, H_2O_2, Fe^{2+}, Mn^{2+}, TOC and DOC. 55
Table 2-6. Statistical analysis for MOUDI. 55
Table 2-7. Summary of collectors' flow rate and size cut. 57
Table 3-1. Summary of collected fog samples in Angiola by collector type. 60
Table 3-2. Summary of weather conditions of all fog events. 60
Table 3-3. Volume-weighted average concentrations of solute species in all fog events. 72
Table 3-4 Summary of bulk fog sample composition 73
Table 4-1. Deposited fog water mass, ion and TOC concentrations observed on the two deposition plates. 86
Table 4-2. Fog water, ion and TOC fluxes derived from the two deposition plates. 87
Table 4-3. Summary of observed deposition fluxes for CRPAQS fogs. 96
Table 4-4. Relative standard deviation of concentrations and fluxes derived from two deposition plates. 97
Table 4-5 Regression results 103
Table 4-6. Average deposition velocities of all species on two deposition plates. 105
Table 4-7. Typical range of deposition velocities and relative standard deviations. 106
Table 4-8 Parameters and initial conditions in the model 115
Table 4-9. Concentrations used for fog events at Angiola main site. 116
Table 4-10. the partition function, Q, and rate for hydrogen peroxide, ozone oxidation, and HMS formation reaction rates respectively. 118,119
Table 4-11. Theoretical oxidation rate and HMS formation rate for all fog samples. 123
Table 4-12. Deposition removal rates of each species for all fog events. 127
Table 4-13. Total mass removal of species by fog episodes during CRPAQS 128
Table 4-14. Estimated reduction in ground level ambient concentrations by fog episodes during CRPAQS assuming a 100 m fog depth. 129
Table 5-1. Required reagents to carbonyl and di-carbonyl analysis. 136
Table 5-2. Chemical Structures of carbonyls and dicarbonyls 138
Table 5-3. Carbonyl and dicarbonyl concentrations in blanks (20 ml DI water) 142
Table 5-4. Minimum detection limits of aldehydes based on replicate low level (0.015 μg/ml) standard analyses 143
Table 5-5. DNPH recrystallization results. 145
Table 5-6. Precision of carbonyl analyses based on replicate standard (0.15μg/ml) analyses. 146

Table 5-7. Accuracy for carbonyls analysis. 147
Table 5-8. Concentrations of artificial fog water parallel samples. 148
Table 5-9. Comparison of concentrations of artificial fog water samples. 149
Table 5- 10. Stability test in a real fog water matrix. 150
Table 5-11. Carbonyl and dicarbonyl concentrations of California SJV fog samples. 154
Table 5-12. Sampling information and concentrations of detectable carbonyls and dicarbonlys in Fresno fog samples. 155
Table 5-13. Summary of Fresno bulk organic fog sample composition. 156
Table 5-14. Comparison of two HCHO measurements. 158
Table 5-15. Free HCHO and HMS measurement. 159
Table 5-16. Chemical compositions of cloudwater and fogwater collected by size-fractionating CASCC (Adapted from Rao et al., 1995). 161
Table 5-17A. Expected and observed separation regions of some organic compounds. 174
Table 5-17B. Organic compounds, tested with the HPLC DEAE separation but yielding no absorption 175
Table 5-18. Evaluation of effects of aromatic compounds on DEAE HPLC chromatogram 178

Chapter 1

Fog Chemistry Review

1.1 What is fog and how is it formed and maintained?

Fog is a layer-type cloud that makes contact with the ground. It is comprised of tiny water droplets, typically ranging in size from several micrometers to several tens of micrometers. These drops form by water vapor condensing onto aerosol nuclei. As atmospheric relative humidity surpasses one hundred percent, some aerosol particles (known as cloud condensation nuclei or CCN) are activated to form fog droplets through the process of heterogeneous nucleation. The first particles to activate tend to be larger in size and contain a high fraction of soluble material. As the supersaturation in the air mass continues to rise, additional particles can also activate to form drops. Activation of new drops will continue until the peak supersaturation is reached. At this point depletion of water vapor due to condensational drop growth prevents the superaturation from climbing higher. A fog droplet with a diameter of ~25μm settles under the influence of gravity at about 5cm per second. At this rate most droplets in a fog layer would reach the ground in a few hours. Maintaining a fog beyond several hours, therefore, requires a replenishment of droplets.

There are four main types of fog: radiation fog, frontal fog, advection fog and ice or snow fog corresponding to the primary three mechanisms for fog formation:

(1) cool the air to below its dew point temperature. Fog produced by strong radiative cooling of the earth's surface is called "radiation fog" since radiation and conduction are the primary means for cooling stable nighttime air near the ground. Formation of radiation fog requires calm winds and clear skies. Clear skies promote effective radiative cooling of the surface which, in turn, cools the air layer adjacent to the ground. The presence of modest to strong winds inhibits cooling of the surface air layer due to promotion of vertical mixing. As a radiation fog develops, the upper reaches of the fog layer itself cool by radiation to a clear sky, leading to cooling of overlying air parcels and entrainment. This process occurs throughout the night, if conditions are favorable, leading to a deepening fog layer. Cooling of an air parcel to form fog also occurs in advection fog. Advection fog occurs when warm, moist air moves over a colder surface that cools the overlying air parcel to its dew point resulting in fog formation.

(2) "Ice or snow fog" forms when a very cold air parcel reaches its saturation conditions with respect to ice as a result of adding a small amount of water vapor.

(3) "Frontal fog" typically forms on the colder side of a front. Steady stratiform precipitation transfers water in the form of precipitation to the subcloud layer where it evaporates, sometimes producing a saturated air parcel and forming frontal fog.

Once fog forms, it is maintained by newly formed water droplets. If the air cannot at least maintain its degree of saturation either by continual cooling or by evaporation and mixing of vapor into the air, the fog will begin to dissipate. There are three important mechanisms for fog dissipation: (1) the sizes of fog droplets increase so that they become heavy and settle to the ground (possibly as a light drizzle); (2) the air is heated and fog evaporates; and (3) cooler saturated air near the surface mixes with the warmer unsaturated air above.

1.2 Aerosol activation

Fog is more likely to form in an environment with large CCN concentrations characterized by a low activation critical supersaturation. Köhler theory is used to

compute the equilibrium vapor pressure over a solution droplet. It defines the critical diameter at which a droplet is activated and begins to grow spontaneously by water vapor uptake. It also describes the equilibrium growth of aerosol particles in terms of their size, chemical composition and corresponding concentrations in the droplets. The Köhler equation can be written as

$$s = 1 + \frac{2\sigma_s M_w}{RT\rho_w r} - \frac{3M_w \Phi_s}{4\pi\rho_s r^3} \tag{1-1}$$

where s is the equilibrium saturation ratio of water vapor above a drop surface, M_w is the molecular weight of the solute, ρ_w is the density of water, σ_s is the droplet surface tension, r is the droplet radius, Φ_s is the osmotic coefficient of the aqueous solution, R is the gas constant and T is absolute temperature.

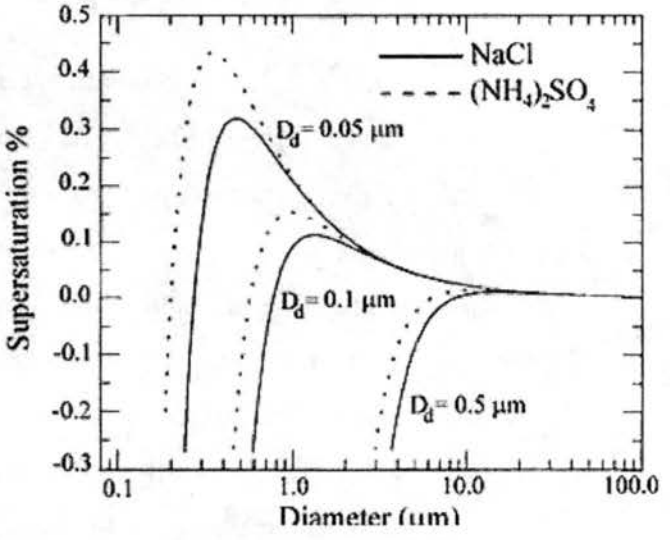

Figure 1-1. Köhler curves for NaCl and $(NH_4)_2SO_4$ particles for various dry particle diameters (Hanel, 1976).

Figure 1-1 shows Köhler curves for NaCl and $(NH_4)_2SO_4$ particles for various dry particle diameters (Hanel, 1976). As the environmental humidity increases, a solution drop "grows" up the left side of the curve. This portion of the curve describes a stable equilibrium: droplets which deviate slightly in size from the equilibrium value tend to be returned to that equilibrium size by evaporation of condensation. A particle in stable equilibrium is called a haze droplet. The peak values of s on a Köhler curve is known as

the critical supersaturation; the corresponding diameter or radius is termed the critical diameter or critical radius. Once a droplet has crossed this critical size, it is said to be activated and begins to grow unstably by spontaneous addition of water vapor. The larger the drop grows, the lower the equilibrium saturation value and, hence, the lower the ambient supersaturation needs to be to continue to promote droplet growth. The portion of the curve to the right of the critical size represents a situation of unstable equilibrium. An activated droplet in the unstable equilibrium regime is called a fog or cloud drop.

The shape of a Kohler curve is determined by a competition between multiple effects. The second term on the right hand side of the Köhler equation, the Kelvin term, includes the influence of surface tension within the Kelvin effect, that is, the increase of the water vapor pressure due to the curvature of the droplet surface. The third term, the Raoult term, defines the equilibrium vapor pressure reduction due to dissolved solute in the Raoult effect.

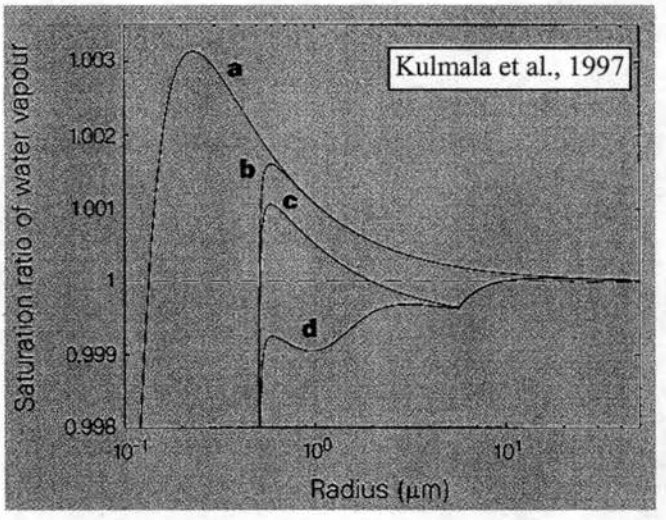

Figure 1-2. a, Conventional Köhler curve for a 30 nm dry particle consisting of ammonium sulphate at 298 K. b, A similar particle containing an additional, insoluble 500 nm core (the amount of ammonium sulphate is the same as with a). The effect of insoluble material has been studied in detail. c, Particle containing a slightly soluble 500 nm core. The solubility used (0.00209 g cm^{-3}) corresponds to that of $CaSO_4$. The sharp minimum of the curve shows the point at which all of the core is dissolved. $CaSO_4$ particles occur commonly in air, and dissolved $CaSO_4$ has been found in fog-water collected in the Po Valley, Italy. d, Effect of an added, highly soluble gas, nitric acid. Initial gas-phase concentration of HNO_3 was 1 p.p.b.v., and the Henry's law constant used (mole-fraction scale) was 853.1 atm^{-1}. Because nitric acid is allowed to deplete from

the gas as it is absorbed by the droplets, the term $b_a(r)$ in equation (1) depends on the aerosol number concentration, which in this case was assumed to be 100 cm^{-3}. Aerosol size distribution was taken to be monodisperse (a qualitatively similar curve would result if the aerosol population was 1,000 cm^{-3} and initial HNO_3 concentration 3 p.p.b.v.). The smooth minimum in the curve is caused by the depletion.

Although Köhler theory has long been applied to growth and activation of droplets formed on inorganic salt particles, many atmospheric particles contain both water soluble (inorganic ions and some organics) and insoluble substances (dust, elemental carbon, etc...). Köhler theory readily explains the behavior of water soluble particles in the atmosphere. Figure 1-2 illustrates some of the factors that complicate the typical interpretation of Kohler theory as applied to inorganic salt particles (Kulmala et al., 1997). Effects are illustrated for the inclusion of an insoluble or slightly soluble core and for uptake of highly soluble nitric acid. All of these cases suggest possible changes in the critical activation size and critical supersaturation.

In terms of organic compounds, which represent an important part of the aerosol water soluble fraction, some researchers have examined Köhler theory with hypothesized organic components and concentrations. Some surfactants can change the surface characteristics of droplets, which is important to the activation of aerosol particles to form cloud condensation nuclei (Decesari et al., 2000; Mircea et al., 2002). Shulman et al. (1996) measured solubilities and surface tensions for difunctional organic acids (malonic acid, glutaric acid, succinic acid, oxalic acid, adipic acid, phthalic acid, and cis-pinonic acid) in various concentrations of $(NH_4)_2SO_4$ and NH_4HSO_4 aqueous solutions. These experiments simulate the growth of cloud droplets nucleating on sulfate aerosols. Model results using these data indicate that the organic compounds affect cloud droplet growth by two mechanisms: (1) by gradual dissolution in the growing (diluting) droplet, which affects the shape of the Kohler growth curve, and (2) by reducing the droplet surface tension which decreases the critical supersaturation. Recently, several investigators (Laaksonen et al., 1998; Facchini et al., 1999a; Facchini et al., 1999b; Hitzenbergeret al., 2002; Mircea et al., 2002) used a modified Köhler equation and variable surface tension

values derived from field data to demonstrate that organic compounds with surface active properties will decrease the surface tension of droplets, and will highly increase CCN number concentrations. However, a similar method was used by Li et al. (1998) and they concluded that "Reduction in critical supersaturation caused by the reduction in □(Kelvin effect) associated with the surfactant is dominated by the increase in S_c with the decreasing number of moles of solute in the droplet (Raoult effect) as surfactant displaces NaCl solute mass". The different conclusions were questioned and discussed in the literature (Rodhe, 1999; Facchini et al., 2001; Rood et al., 2001). The major difference appears to result from the fact that they used different organic compounds in the models. The influence of organic compounds on aerosol hygroscopicity in general is also receiving increasing attention. Saxena et al. (1995) found that aggregate hygroscopic properties of inorganic particles are altered substantially when organics are also present, and alterations can be positive or negative. For non-urban location, organics appeared to enhance water absorption by inorganics; for urban locations, the net effect of organics was to diminish water absorption by the inorganics. Certainly, however, the effects in any individual case will require more knowledge than we presently have about the organic compounds present in atmospheric aerosols.

Understanding the influence of organics on fog drop activation requires improved information about the organic composition of particles that are actively scavenged by fogs via nucleation. Because there are hundreds, perhaps thousands, of individual organic compounds present in fog drops (not all of which extract in a single solvent or elute through a gas chromatograph), it may be more effective initially to focus on characterizing the types/families of compounds that are present and considering their ability to modify drop surface tension. Without such knowledge, it is very difficult to accurately predict the effects of organics on drop activation. Many current efforts to do so make unrealistic assumptions about the composition of organics involved. A frequent inaccurate assumption is that dicarboxylic acids dominate organic carbon in aerosol particles and fog drops.

Overall, Köhler theory can work to predict activation of soluble inorganic and organic species when composition is simple and well described (Raymond et al., 2002). An extension to treat more complex mixtures containing many low-solubility (higher molecular weight) organic species is necessary due to their abundance in fog water (Herckes et al., 2002b).

1.3 Aerosol scavenging, removal and production in fogs

Over the last 20 years, it has become increasingly evident that clouds and fogs play an important role as processors of aerosol particles and trace gases (Waldman et al., 1983; Jacob et al., 1984; Fuzzi, 1988; Dlugi, 1989; Collett et al., 1990; Cereceda et al., 1991; Fuzzi et al., 1994; Collett et al., 1999b;). Fogs comprise a complex multiphase system. Fogs act both as reactors for the production of new chemical species and as a pathway for particle and trace gas removal, mainly via wet deposition and direct deposition of fog drops to the ground or to vegetation.

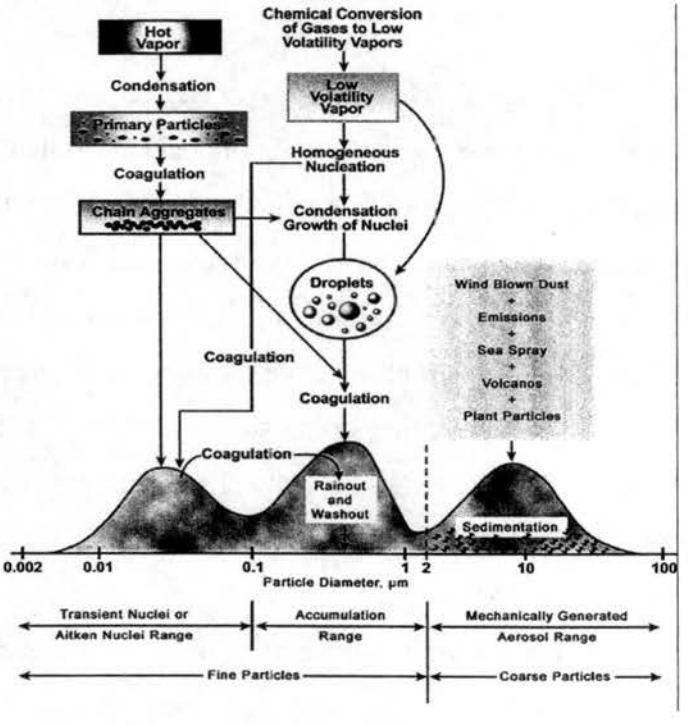

Figure 1-3. Typical size distribution of aerosol particles (Whitby, 1978).

There are mainly three mechanisms for aerosol scavenging by fog. The dominant mechanisms vary depending on the size of the particle (size distribution of aerosol

particles are shown in Figure 1-3 (Whitby, 1978)). For Aitken particles ($r < 0.1\mu m$), the primary scavenging process is Brownian diffusion. For accumulation mode particles ($0.1\ \mu m < r < 1.0\ \mu m$), the primary scavenging process is nucleation (as described above). For even larger particles, collision between aerosol particles and fog droplets (scavenging by impaction and interception, hydrodynamic capture) is typically more effective.

Particles with diameters bigger than 10 μm tend to settle on the ground near their emission source. Particles with diameters less than 0.1 μm also tend to have short lifetimes in the atmosphere and aids in their dry deposition, due to their rapid diffusion and coagulation, which leads to larger sizes. Accumulation mode particles, by contrast, have rather long lifetimes in the atmosphere (on the order of several days) and thus can be transported long distances. These long lifetimes can be shortened considerably by interactions with precipitating clouds or, in some environments, with radiation fogs. Removal of accumulation mode aerosol particles from the atmosphere is of keen interest because of the important roles they play in impacting radiative transfer (with implications for climate and visibility) and human respiratory health.

Munger et al. (1983a) proposed a cyclical relationship between the occurrence of smog and fog, which was termed a "smog-fog-smog" cycle. A polluted atmosphere with a high aerosol concentration assists the formation of late night and early morning fog, which appears to enhance smog production, visibility reduction, and aerosol concentration levels during the following day. Several investigators, however, have also recognized that long-lived fogs can actually help cleanse the atmosphere by nucleation scavenging of particles followed by fog drop settling to the surface. Jacob et al. (1984) were among the first to propose that enhanced aerosol deposition in fog layers efficiently limits pollutant buildup during air stagnation episodes.

Fogs can produce additional aerosol material by uptake of soluble gases that react in the droplets to form non-volatile products. When the fog evaporates, this new non-volatile solute is left behind as part of the residual aerosol. The classic example of fog production of aerosol mass is uptake of sulfur dioxide followed by its oxidation to

sulfate. Since the reaction time of sulfur oxidation in drops is several minutes to hours, the typical lifetime of fog is sufficient for the production of significant sulfate (Pandis et al., 1992). Although sulfate production has received the most attention, there are other aqueous phase reactions that can also lead to secondary aerosol production. These include reactions that produce low volatility organic compounds. The production of non-volatile material in fog drops leads to the release from dissipating fogs of aerosol particles that may be larger and more soluble than the CCN on which the drops originally formed. The new aerosol particles are likely to be more effective CCN than their precursors.

1.4 Fog scavenging of gases and secondary aerosol production

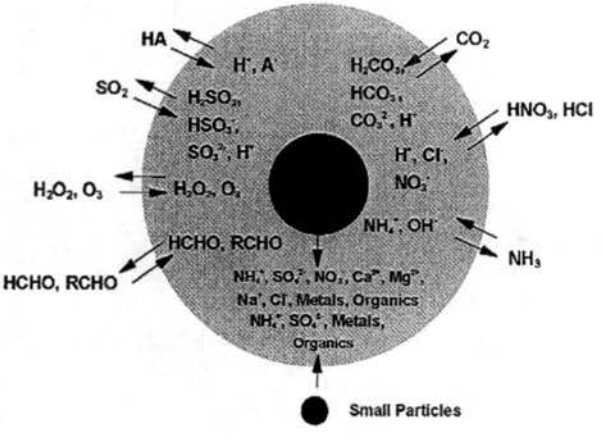

Figure 1-4. Simplified chemistry of a cloud/fog drop.

The fundamental scavenging role of water droplets is widely recognized and interactions for some species have been investigated (Chameides et al., 1983; Calvert et al., 1985; Jacob, 1986; Laj et al., 1997). As shown in Figure 1-4, chemical species of interest include SO_2, CO_2, nitrogen compounds (NO, NO_2, HNO_3, NH_3), oxidants (H_2O_2, organic peroxides, and O_3), and a large variety of organic compounds (formaldehyde and other low molecular weight aldehydes, small carboxylic acids, phenols, etc.). Many of these soluble gases play an important role in determining fog/cloud pH. In remote environments, for example, pH is determined largely by uptake of carbon dioxide along with formic and acetic acids. In more polluted environments uptake of gaseous acids (e.g., HNO_3) and bases (NH_3) exert significant control on drop composition and acidity.

Soluble gases dissolving into fog drops sometimes undergo significant reaction to form non-volatile products, a topic introduced above. Uptake of gas phase oxidants can be an important aspect of these reactions as well. O_3 and H_2O_2, for example, can act as important oxidants for dissolved sulfur dioxide. HCHO is of interest because it can react with sulfur dioxide to form hydroxymethanesulfonate (HMS) at high pH (Boyce et al., 1984; Munger et al., 1986).

Gas uptake by fog drops includes four major steps: transport through the gas phase to the drop surface, transport across the gas-liquid interface, transport within the aqueous phase, and chemical reaction (e.g., ionization) in the drop (Daum et al., 1984). The partitioning of a gas into fog droplets depends on its solubility. Henry's law describes the equilibrium solubility:

$$[A(aq)] = H_A p_A \tag{1-2}$$

where p_A is the partial pressure of species A in the gas phase (unit: atm); and [A(aq)] is the aqueous phase concentration of A in equilibrium with p_A (unit: mol L^{-1}). H_A is the Henry's law equilibrium constant (unit: mol L^{-1} atm^{-1}), which depends on temperature. Solubility typically increases as temperature declines.

Henry's law as written above only describes the physical solubility. For some gases such as SO_2, ionization in the aqueous phase is important and enhances the solubility:

$$SO_2(g) \leftrightarrow H_2SO_3(aq) \tag{1-3}$$

$$H_2SO_3(aq) \leftrightarrow HSO_3^- + H^+ \tag{1-4}$$

$$HSO_3^- \leftrightarrow SO_3^{2-} + H^+ \quad . \tag{1-5}$$

Using the equations above we can derive H_A^*, an "effective" Henry's Law constant, for SO_2 which includes the enhanced solubility due to ionization:

$$H^{*}_{SO_2} = H_{SO_2}\left(1+\frac{K_1}{[H^+]}+\frac{K_1K_2}{[H^+]^2}\right) \qquad (1\text{-}6)$$

where K_1 and K_2 are the acid dissociation constants corresponding to reactions (1-4) and (1-5) above, respectively. Note that H_{SO2}^{*} depends on the pH of the solution. The solubility increases as pH increases. Thus the effect of ionization in solution is to increase the effective solubility. Other important gases that have enhanced solubility due to ionization include carbon dioxide, nitric acid, ammonia, and carboxylic acids.

The solubility of HCHO in fog drops is also enhanced in solution by the formation of a gem diol:

$$HCHO(aq) + H_2O \leftrightarrow H_2C(OH)_2 \qquad . \qquad (1\text{-}7)$$

The effective Henry's law coefficient for the total dissolved formaldehyde H_{HCHO}^{*} is:

$$H^{*}_{HCHO} = H_{HCHO}(1+K_{HCHO}) \cong H_{HCHO}K_{HCHO} \qquad . \qquad (1\text{-}8)$$

K_{HCHO} is rather large at 298K, suggesting that hydration is essentially complete and that practically all dissolved formaldehyde will exist in its gem diol form.

Gas-to-particle conversion of chemical species in the atmosphere generates secondary aerosol matter. As mentioned above fog drops can serve as micro-reactors to convert primary pollutants, such as gas phase SO_2, to secondary aerosol species such as sulfates (Seinfeld et al., 1998). Aqueous phase production of secondary aerosol requires the following combination of processes: dissolution of soluble gases in fog drops and subsequent reaction in the droplets to form new non-volatile species.

Many chemical species incorporated in water droplets can react in the aqueous phase (Fuzzi, 1995). Considerable attention has been focused on the aqueous oxidation of

dissolved sulfur dioxide to sulfate because sulfate comprises a significant fraction of the atmospheric aerosol and contributes significantly to issues such as acid deposition, visibility degradation, and climate forcing. Aerosol sulfates comprise about 5 to 20 percent of the total suspended particulate matter in urban air (Wark et al., 1998). Outside urban areas this fraction can grow even higher.

Oxidation of sulfur in the atmosphere can occur both in the gas and in the aqueous phases. Aqueous phase oxidation is of special interest because it occurs much more rapidly than gas phase oxidation. Because dissolved SO_2 can have different forms in solution, the oxidation state (+4) is used to represent all the forms:

$$S(IV) = SO_2 \bullet H_2O + HSO_3 + SO_3^{2-} + HMS \tag{1-9}$$

and the final oxidized state (+6) of sulfate, bisulfate, or sulfuric acid is referred to as S(VI).

Several sulfur oxidation mechanisms occur in the aqueous phase, their importance depending on the drop pH and the availability of oxidants and catalysts. Three important pathways are oxidation by hydrogen peroxide, oxidation by ozone, and oxidation by oxygen (auto-oxidation) catalyzed by Fe(III) and Mn(II).

1.4.1 S(IV) oxidation by hydrogen peroxide (H_2O_2)

The oxidation of S(IV) by hydrogen peroxide is typically considered the major pathway in acidic environments. H_2O_2 in the gas phase can easily dissolve into cloud or fog droplets due to its high solubility. According to (McArdle et al., 1983), the reaction proceeds via a nucleophilic attack of hydrogen peroxide on bisulfite as the principal reactive S(IV) species:

$$HSO_3^- + H_2O_2 \leftrightarrow SO_2OOH^- + H_2O \tag{1-10}$$

The peroxymonosulfurous acid formed reacts with a proton to produce sulfuric acid:

$$SO_2OOH^- + H^+ \rightarrow H_2SO_4 \quad . \tag{1-11}$$

The latter reaction becomes faster if the aqueous phase gets more acidic. Hoffmann et al., (1985) suggest the following reaction rate expression:

$$\frac{d[SO_4^{2-}]}{dt} = \frac{k[H^+][H_2O_2][HSO_3^-]}{1+K[H^+]} \tag{1-12}$$

where k=7.5 x 10^7 $M^{-1}s^{-1}$ and K=13 M^{-1} at 298K. A lack of pH dependence for pH > 2 in the overall rate expression results from the fact that the concentration of HSO_3^- declines at lower pH, due to a decrease in H_{SO2}^* and a shift in speciation from HSO_3^- to H_2SO_3, offsetting the influence of H^+ on the rate of reaction (1-11).

Organic peroxides have also been proposed as potential aqueous S(IV) oxidants. For example, hydroxymethyl hydroperoxide ($HOCH_2OOH$) may be important in S(IV) oxidation, depending on the relative amount compared to H_2O_2 (Zhou et al., 1992). Generally, however, concentrations and solubilities of organic hydroperoxides are thought to be low enough that they are of only minor importance as S(IV) oxidants.

S(IV) oxidation by hydrogen peroxide is viewed as the most effective reaction at low pH values. This pathway can be detectable in the cloud or fog through a decrease of gas phase SO_2 and H_2O_2 or an increase of S(VI) in the aqueous phase (Husain, 1989).

1.4.2 S(IV) oxidation by ozone (O_3)

Ozone reacts very slowly with SO_2 in the gas phase where the OH radical is the dominant oxidant. However, the aqueous phase oxidation of S(IV) by ozone can be rapid and can even dominate aqueous phase sulfate production when drop pH is high or hydrogen peroxide is depleted. This reaction can simply be written as:

$$S(IV) + O_3 \rightarrow S(VI) + O_2 \quad . \tag{1-13}$$

This reaction can be considered as nucleophilic attack by S(IV) species on O_3, Hoffmann (1986) has found that this oxidation process can be treated in terms of individual reactions of the various forms of S(IV): $SO_2.H_2O$, HSO_3^- and SO_3^{2-} each can react with ozone separately with a unique mechanism and rate constant. The total oxidation rate can be written as:

$$-\frac{dS(IV)}{dt} = (k_0\alpha_0 + k_1\alpha_1 + k_2\alpha_2)[S(IV)][O_3] \tag{1-14}$$

where α_0, α_1 and α_2 are the fractions of free S(IV) present as $SO_2.H_2O$, HSO_3^- and SO_3^{2-}, respectively, and k_0, k_1 and k_2 are rate constants.

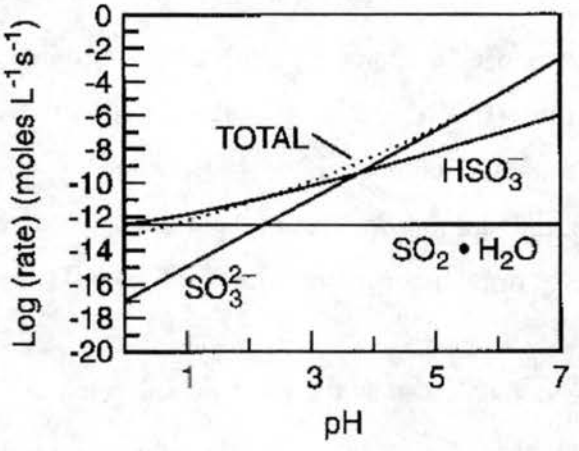

Figure 1-5. Rate of S(IV) oxidation by O_3 in the aquous phase under conditions typical of a Los Angelos atmosphere, with SO_2=20 ppb and O_3=50 ppb (adapter from Hoffmann, 1986).

Existing experimental kinetic and mechanistic data suggest that this reaction has a complex pH dependence (Maahs, 1983; Martin, 1984; Penkett et al., 1979). Figure 1-5 shows the pH dependence of the total reaction and individual reaction by the three sulfur species. Because the effective solubility of sulfur dioxide increase with pH and because sulfite is oxidized much more rapidly than bisulfite, which is oxidized more rapidly than sulfurous acid, the reaction rate of sulfate production by this pathway increase strongly with increasing pH. Therefore, S(IV) oxidation by ozone is most important at high pH.

1.4.3 S(IV) oxidation by oxygen (O_2)

S(IV) oxidation by oxygen is very slow except in the presence of catalysts such as Fe(III) and Mn(II). Synergistic effects were found for the catalysis when Fe(III) and Mn(II) co-exist in the aqueous phase (Martin, 1994). In fog water these two trace metal ions can be relatively abundant because they are common aerosol components often coming from earth crust erosion. The catalyzed auto-oxidation mechanism and its kinetics are very complex. Even though several researchers have reported rate expressions, no common form has been accepted. The reaction rate is sensitive to various factors such as pH, ionic strength and concentrations of all species. Generally, we know that the catalyzed reaction is most likely to be important when pH is about neutral, in the range of about 6-7. Although an accurate measurement of the iron and manganese oxidation states is difficult in the field, an upper bound to S(IV) oxidation by oxygen can be determined by using the total Fe and Mn concentrations. In general, since S(IV) oxidation by oxygen is only significant when pH value is near neutral, i.e., in the range of 6~7, and at this pH range, formation of HMS and S(IV) oxidation by ozone can be even faster, metal catalyzed S(IV) oxidation typically doesn't play a large role in overall sulfate production in fogs (Rao et al., 1998).

1.4.4 Reaction of dissolved SO_2 with HCHO

Field studies have found that total S(IV) concentrations in fog water are sometimes much higher than Henry's law predicts, because HSO_3^- and SO_3^{2-} in fog can react with dissolved aldehydes. The most important reaction is with formaldehyde, to produce hydroxymethanesulfonate, $HOCH_2SO_3H$ (HMS) (Boyceet al., 1984):

$$HCHO(aq) + HSO_3^- \rightarrow HOCH_2SO_3^- \quad (1\text{-}15)$$

$$HCHO(aq) + SO_3^{2-} \rightarrow {}^-OCH_2SO_3^- \quad . \quad (1\text{-}16)$$

The right side of the first reaction $HOCH_2SO_3^-$ is HMSA, anion of HMS since HMS is a strong acid and dissociates completely in fog water. HMSA can dissociate further to form $^-OCH_2SO_3^-$, though the second dissociation is weak.

Formation of HMS is favored at high pH. It is accordingly an important additional sink for sulfur dioxide in high pH drops. An interesting feature of HMS chemistry is that the high pH condition favored for its production is not good for its preservation. Munger et al. (1986) found that if the fog pH is initially high but decreases due to formation of S(VI) by oxidation processes, HMS will be produced and maintained in fog water.

Oxidation by OH radical is probably the major sink of HMS in daytime fog (Jacob, 1986; Pandis et al., 1989b). The lifetime of HMS is about 1 hour to 10 hours. Therefore, in high pH fogs with abundant HCHO, measured S(IV) will be mostly comprised of HMS, not HSO_3^- or SO_3^{2-} (Rao et al., 1998).

1.4.5 The overall fate of S(IV)

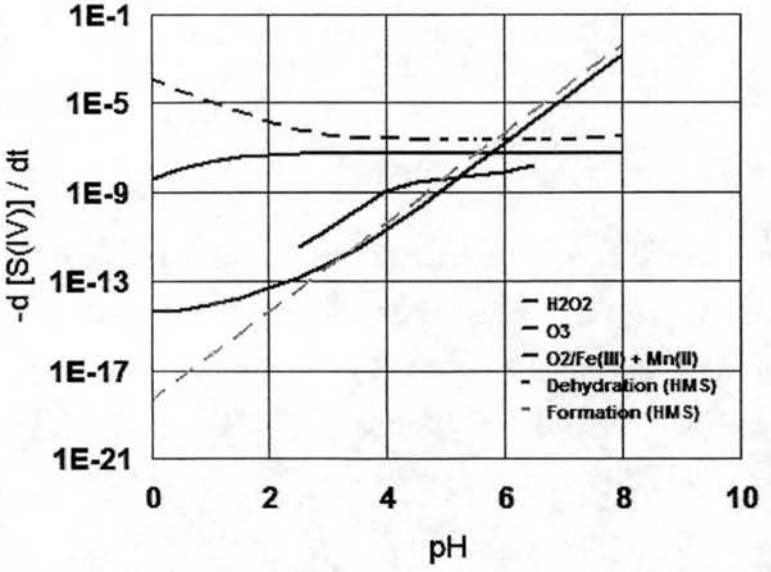

Figure 1-6. Oxidation rates of the three S(IV) oxidation pathways, along with the rate of HMS formation for typical conditions in central California fogs.

Figure 1-6 shows the oxidation rates of the three S(IV) oxidation pathways described above along with the rate of HMS formation for typical conditions in central California fogs. The oxidation of S(IV) by hydrogen peroxide is important and is typically considered the major pathway in most environments, where pH is below 5-6. Oxidation

by ozone is important at high pH where it competes with HMS formation for SO_2 taken up from the gas phase. S(IV) oxidation via oxygen is too slow to be an important contributor to the fate of dissolved SO_2.

1.5 Aqueous phase reactions of organics

A variety of aqueous phase reactions also exist that involve organic compounds. In fact, it is possible that a significant portion of secondary organic aerosol (SOA) formation takes place in cloud and fog droplets (Facchini et al., 1992; Blando et al., 2000). Aumont et al. (2000) proposed that high carboxylic acid concentrations in cloud water samples cannot be explained by a gas-phase source, which suggests that besides aerosol and gas scavenging, VOC oxidation in cloud and fog water are also important for carboxylic acid formation. Aqueous phase oxidation processes can enhance the solubility of organic aerosol by introducing polar functional groups into the molecular structure (e.g., mono- and dicarboxylic acids, aldehydes, alcohols, ketones and organic peroxides, which are fairly abundant in fog water (Facchini et al., 1999a; Blando et al., 2000). Blando et al. 2000) summarize evidence that cloud and fog processes produce fine organic particulate matter in the atmosphere and could be important contributors to SOA formation, although the contribution of this formation pathway should be further investigated. Specific compounds identified as potential precursors include aldehydes (e.g., formaldehyde, acetaldehyde and propionaldehyde), acetone, alcohols (e.g., methanol, ethanol, 2-propanol and phenol), monocarboxylic acids, and organic peroxides. Carboxylic acids (e.g. diacids), glyoxal, esters, organosulfur compounds, polyols, amines and amino acids are potential products of cloud and fog processing.

Most of the research to date on aqueous phase SOA formation has been theoretical in nature and rather speculative. The importance of aqueous phase oxidation remains unclear and cannot yet be fully assessed. Further research is certainly required.

1.6 Solute deposition in fogs

As mentioned earlier fog drop deposition can be an important mechanism for removing pollutants from the atmosphere. Deposition mechanisms for fog droplets include inertial impaction, interception and sedimentation (Burkhard et al., 2000; Eugster et al., 2001; Wrzesinsky et al., 2001). Sedimentation is the dominant mechanism for radiation fogs in locations with low wind speeds and low surface roughness. Impaction and interception are important for capture of drops by vegetation such as montane forest canopies. In some areas fog/cloud drop deposition can significantly enhance total wet deposition to terrestrial ecosystems. Collett et al. (2001) found that key solute (e.g., nitrate, sulfate and ammonium) deposition velocities in radiation fogs range from approximately 1 to 10 cm s^{-1}. These values are much higher than deposition velocities for accumulation mode aerosol particles, suggesting fogs are important contributors to cleansing of the atmosphere. Lillis et al. (1999) evaluated fog effects on the production and removal of particulate matter in a polluted fog layer and found that aerosol and gas scavenging and drop deposition can significantly reduce atmospheric nitrate and ammonium concentrations while removal of sulfate was roughly offset by aqueous phase sulfate production. Little attention has been paid to the effectiveness of fogs in removal of carbonaceous aerosols.

1.7 Issues of drop size-dependent fog composition

One topic receiving increased concern in recent years is the variation of solute concentrations across the fog drop size spectrum. A variety of factors can contribute to this variation, including the size-dependent composition of CCN, faster dilution of small droplets by condensational growth, and faster uptake of soluble gases by smaller fog drops. Initial differences in fog drop composition with drop size can be further enhanced by differing rates of aqueous phase reactions (due to the reaction rate dependence on reactant concentrations). A number of experimental studies revealed that fog drop composition can vary with drop size and point out several implications of these variations (Noone et al., 1988; Heintzenberg et al., 1989; Munger et al., 1989b; Ogren et al., 1989; Pandis et al., 1990; Collett et al., 1993; Collett et al., 1994a; Collett et al., 1995; Demoz et al., 1995; Bator et al., 1997; Collett et al., 1998; Rao et l., 1998; Hoag et al., 1999a; Xu

et al., 1999; Herckes et al., 2001; Reilly et al., 2001; Moore et al., 2002; Straub et al., 2002;). Studies in radiation fogs often reveal that small drops are more acidic than large drops and also contain higher concentrations of key solutes. The differences in drop composition are believed to give rise to drop size-dependent rates of sulfate production (e.g., Gurciullo et al., 1997; Rattigan et al., 2001; Reilly et al., 2001). Because drop sedimentation is a strong function of drop size, size-dependent fog drop composition can also give rise to enhanced deposition velocities for species enriched in large fog drops and reduced deposition velocities for species enriched in small drops. Hoag et al. (1999a) point out the importance of simulating drop size-dependent fog composition for accurately predicting effects of fogs on pollutant removal.

1.8 Net effects of fogs on pollutant concentrations

Fog constitutes a multiphase atmospheric system; gaseous species, particulate matter and liquid droplets coexist. The net effect of fogs on aerosol and gas concentrations can be described as follows:

- Fog formation occurs by condensation of water vapor onto atmospheric aerosol particles when the temperature reaches its dew point. Which aerosol particles activate depends on the peak supersaturation and aerosol characteristics.
- After fog forms fog drops scavenge gases and unactivated aerosol particles, and heterogeneous chemical reactions occur within fog drops to form new species.
- Some fog droplets are removed by deposition onto the ground or vegetation, acting as a vector for removal of scavenged material.
- Modified aerosol particles containing new secondary aerosol components are generated when drops evaporate during fog dissipation.

1.9 Investigating the chemistry of fog formation and dissipation in California's Central Valley

The two regions of the world where fog chemistry has been most extensively studied are the Po Valley of northern Italy and California's Central Valley. Because my research focuses on California fog chemistry, I review here some of the history of fog studies in this region and summarize key findings from this earlier work.

1.9.1 Terrain and weather conditions in the valley

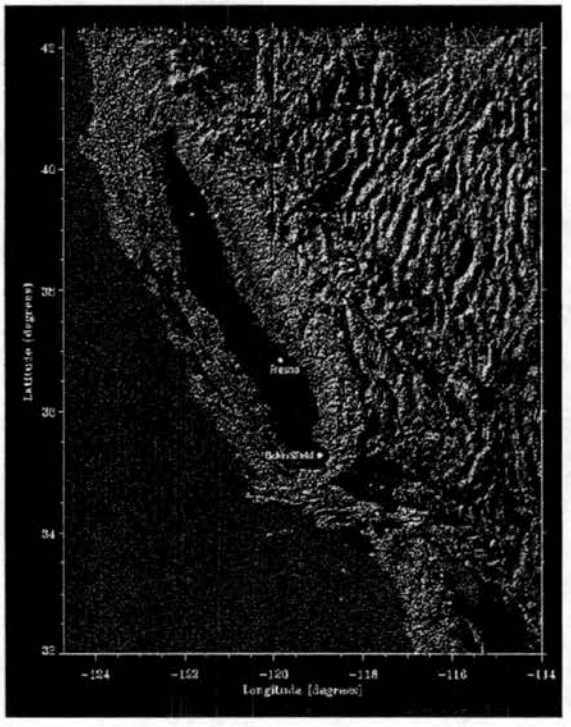

Figure 1-7. Terrain map of California Central Valley area. Red dot on the map is the main Angiola sampling site.

Figure 1-7 shows the California Central Valley, which lies between the Coastal Range and the Sierra Nevada range and is home to the San Joaquin and Sacramento rivers. Sometimes called the Great Valley, the Central Valley is about 450 miles long from points in the northwest to the southeast. The Central Valley is the most important farming area west of the Rocky Mountains and comprises about three-fifths of California's productive farmland (Carpenter et al., 1998).

As would be expected in such a large and diverse land area as California, the climate is varied. During the winter time, high pressure over the Great Basin, known as the Great Basin High, creates a strong subsidence inversion over the valley with a base typically a few hundred meters off the valley floor and below the surrounding mountain ridges (Holets et al., 1981). With the help of the mountains, this strong inversion forms a lid

over the air basin, trapping the cool, moist air within the valley. Tracer studies have documented a lack of ventilation in the valley during these prolonged episodes (Reible, 1982; Jacob et al., 1987). The subsiding air over the valley results in clear skies providing excellent conditions for strong radiative cooling at night and, if sufficient moisture is present, the formation of dense, widespread radiation fogs.

Holets et al. (1981) summarized the meteorological data in the Central Valley typical of fog episodes: surface temperature is about 2°C, the lapse rate inside the fog layer is between the dry and moist adiabatic lapse rates, wind speeds are less than 1 m s^{-1}, and the mean fog layer thickness is approximately 300m. Some different patterns of fog episodes have been observed in the valley (Jacob et al., 1986a; Welch et al., 1986; Lee, 1987;). Welch et al. (1986) concluded that fogs in the San Joaquin Valley (SJV), the southern section of the Central Valley, have relatively constant thickness throughout the valley. Lee (1987) found distinct fog layers existed in the valley by using satellite imagery from the Geostationary Orbiting Earth Satellite (GOES). Jacob et al. (1986a) observed two types of mixing height diurnal patterns.

Due to the persistence of the Great Basin High, the Central Valley often experiences extended periods of stagnation and associated degradation of air quality during the winter. As mentioned above, these stagnation episodes are frequently accompanied by nightly fog formation, with fogs forming anytime after 6PM and often lasting into the late morning (episodes can last up to 18 hours or more). These frequent, long lasting, dense fog events yield low visibilities and can result in major traffic accidents.

1.9.2 Fog composition

Studies of the chemical composition of Central Valley fogs began in the early 1980s. Munger et al. (1983b) measured the pH of fog water and the concentrations of major ions in Oildale (near Bakersfield) and three sites in the Los Angeles air basin. Several studies (Munger et al., 1983a; Waldman et al., 1983; Hoffmann, 1984) showed that fog chemistry is strongly related to the composition of the air mass in which it forms. Jacob et al. (1986a) found that fogwater acidity in the SJV is determined largely by the relative abundances of local acidic (SO_2, NO_x) and alkaline (NH_3) emissions, and that fogs

formed in areas of high alkalinity tend to be rather basic (pH greater than 5.6, the value expected from equilibrium with atmospheric carbon dioxide). Jacob et al. (1986a) and Jacob et al. (1986b) also found that sufficient ammonia was available everywhere in the valley, except near the western edge, to neutralize the acidity of fog water.

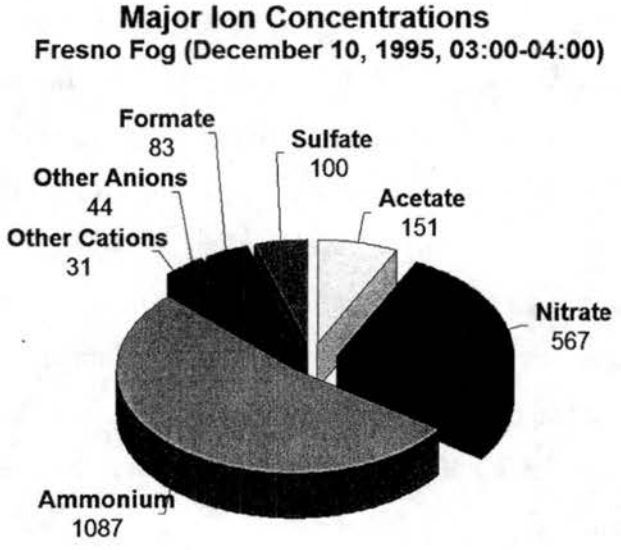

Figure 1-8. Measured composition in a typical bulk fog sample collected at Fresno during IMS95. All concentrations are listed in μN. (Collett et al., 1999b)

Jacob et al. (1984) pointed out that the major inorganic ions in fog water in the Central Valley are ammonium, nitrate and sulfate and that their aqueous-phase concentrations varied depending on the fog growth stage. Later studies (Collett et al., 1994a; Collett et al., 1994b; Rao et al., 1995; Rao et al., 1998) also found that the pH is relatively basic and ammonium and nitrate are major contributors to fog composition, with smaller inputs from sulfate, formaldehyde, and HMS. Figure 1-8 shows a typical fog sample composition measured in Fresno during the 1995 Integrated Monitoring Study (IMS95) (Collett et al., 1999b). These typical 1995 concentrations of most species are comparable to those measured more than a decade earlier (Jacob et al., 1984; Jacob et al., 1986a; Munger et al., 1989a). However, sulfate and S(IV) were present at much lower concentrations than in the period 1982-1984. These declines appear to reflect intervening decreases in valley SO_2 emissions. In addition the IMS95 measurements revealed that two carboxylic acids, formic and acetic acid, comprise a significant part of the fog ion content. Acetate concentrations were typically higher than formate concentrations and

also higher than sulfate concentrations (Collett et al., 1999b).

1.9.3 Sulfur reactions

One key focus of past Central Valley fog studies was to examine S(IV) oxidation processes. We now know that S(IV) can be oxidized by H_2O_2, ozone, and O_2 catalyzed by metals (Fe and Mn), or can react with HCHO to form HMS. Pandis et al. (1989b) proposed that the oxidation of S(IV) by H_2O_2, O_2 catalyzed by metals (Fe and Mn), OH and NO_2 were the main pathways for the aqueous-phase production of sulfate.

S(IV) oxidation by hydrogen peroxide (H_2O_2) is viewed as the most effective reaction at low pH. Pandis et al. (1989b) found that H_2O_2 was present in significant amounts above the fog layers in Bakersfield, and new H_2O_2 is entrained into the fog layer and is available for the S(IV) oxidation; after the depletion of H_2O_2, metal (Fe and Mn) catalyzed oxidation was predicted to be the major sulfate production pathway. The concentrations of metals (Fe and Mn) have been reported (Munger et al., 1983a; Jacob et al., 1984; Erel et al., 1993) to vary between valley sampling sites. Later studies (e.g., Hoag et al., 1999; Reilly et al., 2000) indicated that ozone and hydrogen peroxide were the dominant oxidants for S(IV) in Central Valley fogs but that these oxidation pathways compete with HMS formation for available dissolved sulfur dioxide.

Beginning in the 1980s, Munger et al. (1984) measured HCHO concentrations and discovered that the formation of S(IV)-aldehyde adducts represents an important sink for dissolved SO_2 in the high pH valley fogs. Munger et al. (1986) also measured HMS formation in valley fogs and found that HMS comprised the major fraction of S(IV). Because HMS formation is even faster than S(IV) oxidation at high pH, it competes with S(IV) oxidation for the fate of dissolved SO_2 (Collett et al., 1994a; Collett et al., 1994b; Rao et al., 1995; Rao et al., 1998). Reilly et al. (2000) showed that mass transport limitations, combined with the fast rate of HMS formation, strongly limited the amount of S(IV) oxidation, particularly in large fog drops. Subsequent work by the group of Kim Prather (Silva et al., 1999; Whiteaker et al., 2003), using a single particle aerosol mass

spectrometer, has demonstrated the importance of HMS formation in aerosol particles processed by high pH Central Valley fogs.

1.9.4 Size dependent composition

A number of studies have examined the drop size-dependent composition of Central Valley fogs (Collett et al., 1994a; Rao et al., 1995; Bator et al., 1997; Rao et al., 1998; Collett et al., 1999; Hoag et al., 1999; Reilly et al., 2000; Moore et al., 2004). These studies revealed significant differences between the composition of small and large fog drops. Smaller fog drops were observed to have lower pH than large drops and to contain higher concentrations of ammonium, nitrate and sulfate. Patterns of size-dependence were more variable for metals while nitrite has been observed to be enriched in higher pH, large drops. Moore et al. (2004) demonstrated that the composition variability observable with a 5-stage cloud impactor was even larger than observed with earlier 2- and 3-stage collectors.

Because of the pH and metals concentration differences with drop size, S(IV) oxidation reactions may proceed at different reaction rates in small and large drops. As pointed out above, however, competing reactions (especially HMS formation) and finite rates of mass transport of reactants into large fog drops also influence droplet size-dependent oxidation rates (Reilly et al., 2000). Studies have also shown that in alkaline environments, where ozone is an important aqueous S(IV) oxidant, variations in pH among a droplet population can result in faster rates of sulfate production than are expected based on average fog drop properties (Collett et al., 1999a; Hoag et al., 1999b), due to the non-linear dependence of the oxidation rate on the H^+ concentration. Rates of HMS formation have also been found to vary with drop size (Rao et al., 1995), given the dependence of the HMS formation rate on pH.

1.9.5 Fog deposition and net effects of Central Valley fogs on aerosol populations

Deposition processes in Central Valley fogs have been of increasing interest due to the

influence they may exert on pollution buildup during winter stagnation episodes. Jacob et al. (1984) suggested that enhanced aerosol deposition in fogs efficiently limits pollutant accumulation during stagnation episodes. Waldman et al. (1987) suggested that sulfate deposition in fog drops was fast enough to balance aqueous phase sulfate production, thus preventing sulfate levels from rising during extended fog episodes. Pandis et al. (1989a) modeled one radiation fog episode and found that a fog episode can reduce aerosol concentrations effectively. Lillis et al. (1999) used the Carnegie Mellon University bulk fog chemistry model to simulate the fog effect on ground based concentration of sulfate, nitrate and ammonium; they proposed that a typical SJV fog episode will remove thousands of nanograms per square meter of sulfate, nitrate and ammonium.

Recent studies have indicated that the drop size-dependence of Central Valley fog composition can also influence deposition rates of fog solutes. Preferential enrichment of species in small fog drops decreases deposition velocities (Collett et al., 1998; Hoag et al., 1999a; Collett et al., 2001). Deposition plates have been used to measure the deposition fluxes and velocities of fog borne ions (Collett et al., 2001), revealing that deposition velocities for species enriched in small fog drops are smaller than the fog water deposition velocity and that the ordering of deposition velocities (ammonium > sulfate > nitrate) appears to reflect how strongly they are enriched in small drops. Moore et al. (2003) took this a step further by showing that nitrite in Davis fogs, which is enriched in large fog drops, has a deposition velocity much higher than the other solutes and typically even higher than fog water. Hoag et al. (1999a) used a drop size-resolved version of the Carnegie Mellon University fog chemistry model to reproduce observations of fog composition and deposition in the IMS95 study and revealed more detail about changes in deposition velocities at different fog stages. The model predicted a low deposition velocity for nitrate, a result of its enrichment in smaller drops. Sulfate had a slightly higher deposition velocity. Ammonium had the highest event average deposition velocity; because of the high fog pH, ammonia is still available in the gas phase even after several hours of fog and can dissolve into larger fog droplets with higher settling velocities.

The aerosol scavenging efficiency of a fog determines which preexisting aerosol

particles can be processed by the fog. Munger et al. (1990) suggested that aerosol scavenging ratios in urban fogs range from 10% to 90%. Hoag et al. (1999a) suggested that particles smaller than 1.1 μm (at 95% RH) were not affected by the fog. Size-dependent aerosol scavenging efficiencies by fogs have the potential to differentially affect fog-processed aerosol size distributions. Illustrating this, Moore et al. (2004) examined aerosol size distributions before and after fog episodes in Davis, California and found evidence of large particle removal and build up of smaller particles.

Through this series of studies, the net effect of Central Valley fogs on aerosol concentrations has begun to clarify. Short fog episodes generally allow sufficient time for aqueous sulfate production but do not provide sufficient time for appreciable pollutant removal by fog drop deposition. As fog episodes lengthen, sulfate production, which is concentrated during the first hours of an event, becomes less important relative to pollutant deposition, which occurs at a significant rate throughout the entire fog episode. As mentioned earlier, Central Valley fog simulations by Lillis et al. (1999) suggest that the main effect of fogs on aerosol populations is removal for nitrate and ammonium while sulfate removal is approximately balanced by new sulfate production. Little is known, however, about the influence of fogs on carbonaceous aerosols.

1.9.6 Organics in Central Valley fogs

Fog/cloud processing of carbonaceous aerosol particles has been of increasing interest over the past several years (Capel et al., 1990; Erel et al., 1993; Luttke et al., 1997; Luttke et al., 1997; Facchini et al., 1999a; Facchini et al., 1999b; Decesari et al., 2000; Facchini et al., 2000; Limbeck et al., 2000; Fuzzi et al., 2001;). Studies in California Central Valley fogs have shown that organic carbon comprises a significant fraction of the total solute loading (Collett et al., 1999; Herckes et al., 2002). Major individual organic species in these fogs include formate, acetate and formaldehyde (Munger et al., 1989; Erel et al., 1993; Rao et al., 1995; Collett et al., 1999). Work by the group of Anastasio in Davis fogs (Anastasio et al., 2000; Anastasio et al., 2001; McGregor et al., 2001; Zhang et al., 2001) has also illustrated that organic nitrogen compounds are present

in significant concentrations and that photochemical reactions involving these species can be relatively fast. Measurements by Collett et al. (1990) in clouds intercepting the Sierra Nevada downwind of the Central Valley reveal significant concentrations of dicarbonyl compounds, including glyoxal and methyl glyoxal. The speciation of much of the organic carbon in Central Valley fogs (and in other clouds and fogs, too), however, remains unknown.

In addition to contributing significantly to fog solute loading, some of the low molecular weight organic compounds show interesting drop size-dependence or exert interesting effects on fog chemistry. Rao et al. (1995) found that formaldehyde concentrations were generally higher in small drops than in large drops. These observations contradicted expectations that mass transport of HCHO into the drops should be fast enough to maintain gas-liquid equilibrium in the presence of drop growth or formaldehyde hydration in solution and that equilibrium concentrations of HCHO should not vary with drop size. Martin et al. (1991) proposed that for urban areas formate could reduce the rate of the Fe(III) catalyzed oxidation by as much as a factor of 10 in the high pH regime. Collett et al. (1999b) found that bicarbonate, ammonium, formate and acetate can provide the droplet with acid-buffering capacity to slow the anticipated rapid pH drop due to oxidation of S(IV) by ozone in the high pH environment. Additional buffering from unidentified compounds (possibly including humic like substances) has a similar effect. Numerical simulation of this effect (Collett et al., 1999b) indicated a significant impact on aqueous phase sulfate production by the pH sensitive ozone pathway, with drop pH remaining 0.3 – 0.7 pH units higher and sulfate production increasing by 50%.

While spatial variability in inorganic fog solute concentrations in the Central Valley is generally modest, greater differences between urban and rural fog chemistry were observed for organic species, including acetic acid and formaldehyde. Collett et al. (1999b) found that acetate tends to be more concentrated at the urban sites, consistent with contributions from combustion and a shorter atmospheric lifetime. Measurements also show that fog concentrations of formaldehyde and total organic carbon (TOC) are

more concentrated in urban sites.

So far we know little about fog processing of organic aerosol particles and trace gases. Numerous organic compounds, including various alkanes, polycyclic aromatic hydrocarbons (PAH) and alkanoic acids were found in Davis (California) fog water samples (Herckes et al., 2002a) where ~30% of the total dissolved organic matter and about 2/3 of the low molecular weight fraction (MW<500 Da) has been identified. Numerous compounds were present in both the dissolved and insoluble phases, indicating a need to include both phases in studies of scavenging behavior. The presence in fog drops of organic markers for wood smoke, vehicle exhaust, and other carbonaceous aerosol sources suggest that fogs play an important role as processors of many types of carbonaceous particles.

1.10 Open questions and major research goals

1.10.1 Major findings to date in Central Valley fogs:

- A fair body of data is available concerning inorganic and low molecular weight organic species concentrations in Central Valley fogs. Nitrate, ammonium, nitrite, acetate, formate, and formaldehyde are major contributors to the fog composition.
- These fogs often have high ammonium concentrations yielding a high pH.
- Formaldehyde reacts with dissolved SO_2 in fogs stabilizing it as HMS and reducing the amount of sulfate formed. This reaction is favored under the basic conditions often observed.
- The fogs contain a large amount of organic carbon; however, the speciation of most of this carbon is unknown.
- Significant chemical composition differences have been found among droplets of different size. These differences impact fog processing of valley aerosols.
- Fog chemistry models (especially the Caltech/CMU model) have been used to predict Central Valley fog composition and to examine aerosol processing by these fogs. Model predictions, which compare reasonably well with observations, indicate

that considering drop size-dependent fog composition is important to accurately predicting solute deposition velocities and aqueous phase sulfate production.

1.10.2 Remaining needs for improving our understanding of Central Valley fogs, their composition, and their influence on aerosol populations:

- More observations are needed of the drop size distributions and liquid water contents of Central Valley fogs. These have seldom been measured well in previous studies, making it more difficult to understand fog evolution and drop deposition.
- More information is needed with regard to the drop size-dependence of solute concentrations. In particular, there is a need to look in more detail at organic species and nitrite, which have received little prior attention.
- More observations of fog solute deposition fluxes and deposition velocities are needed to evaluate the role of these fogs as atmospheric cleansers and to better constrain model simulations. Deposition observations are needed for all major solutes, but there is a particularly strong need to quantify organic carbon deposition in fogs.
- More information is needed about the large fraction of fog solute loadings comprised of organic species.

1.10.3 The primary objectives of this study

- Make real observations of fog composition and microphysics during the California Regional Particulate Air Quality Study (CRPAQS). This study will provide a data set suitable for evaluating numerical predictions of fog chemistry and physics.
- Better characterize the size-dependent composition of Central Valley fogs, including better resolution of the size-dependence and more observations of organic carbon.
- Characterize deposition fluxes of inorganic and organic fog solutes. Attempt to explain observed differences in solute deposition velocities using measured drop size-dependent solute concentrations. Examine how fog-related solute removal fluxes vary with fog episode duration.

- Examine the capacity of the atmosphere for new aerosol mass formation, via aqueous S(IV) oxidation and HMS formation, during fog episodes. Such information is a key component for understanding net effects of the fog episodes on boundary layer sulfate concentrations.
- Develop new methods for speciation of fog organics. Better characterize the organic composition and organic species' concentrations.

Chapter 2

Experimental description

2.1 Sampling sites and times

Fog sampling was conducted in California's Central Valley in winter 2000/2001 and again in January 2004. A typical fog sampling period is from 1 to 2 hours. At the end of each sampling period, fog samples were retrieved from collectors, weighed and measured for pH in a small field laboratory in a trailer (Figure 2-1). Some sample aliquots were made for further analysis of formaldehyde, S(IV), Fe and Mn using procedures described below from Standard Operating Procedures written for the 1995 Integrated Monitoring Study (IMS95). Samples were then refrigerated and sent to the laboratory for later analysis.

Figure 2-1. Photo of the Angiola field laboratory, where collected fog samples were processed.

2.1.1 Angiola sampling site

The main fieldwork for this study was carried out in winter 2000/2001 as part of the California Regional Particulate Air Quality Study (CRPAQS). Equipment set up at the Angiola core site is depicted in Figure 2-2.

Figure 2-2. Angiola sampling site overview on a foggy day.

Fog samples were collected during CRPAQS at one core site (Angiola) and three satellite sites. The Angiola core site is located in the center of the San Joaquin Valley (35°35'N, 119°32'W, 60m above sea level), surrounded by a large area of agricultural farmland. The site was enclosed by a wire fence, where cloud collectors and other instruments were set up. The fog collectors were spaced about 15 to 20m apart to avoid influencing each other.

2.1.2 Fresno sampling site

Some additional fog samples were collected during January 2004 in Fresno (36°43'N, 119°49'W), an urban area in the central San Joaquin Valley.

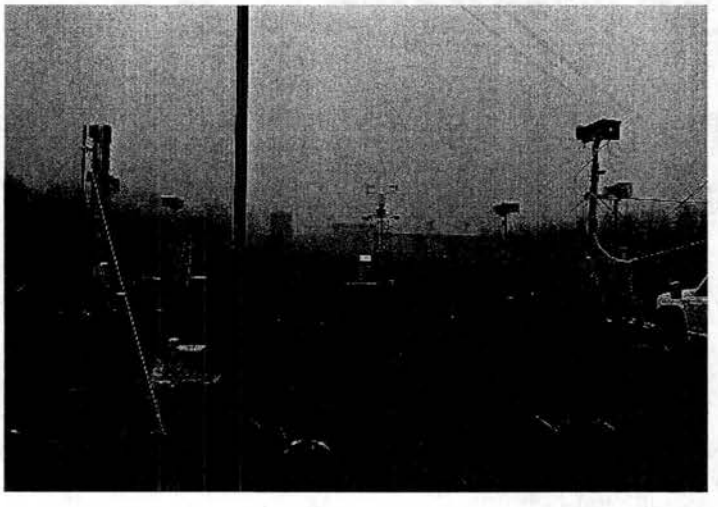

Figure 2-3. Overview of the Fresno sampling site on a foggy day.

Sampling was conducted on the campus of Fresno State University in north central Fresno. Figure 2-3 shows an overview of the sampling site. Fog samples were collected and treated on site then transferred to the lab to analyze. Here, we mainly discuss the results related to the organic components in the fog.

2.2 Sampling

This section outlines the sampling and analytical methods used in the field experiments and the laboratory. Some of the analysis methods are included in the Standard Operating Procedures written for the 1995 Integrated Monitoring Study (IMS95).

Field measurements included ground-based observations of bulk and size-resolved fog composition, vertical profiles of fog presence and composition (Angiola only), and fog deposition fluxes of water and major ions.

2.2.1 Meteorological measurements

At Angiola, meteorological measurements included temperature, relative humidity, ambient pressure, wind speed and wind direction, and fog liquid water content.

A Gerber Scientific Particulate Volume Monitor (model PVM-100) (Figure 2-4) was used to provide continuous measurements of liquid water content (LWC). LWC was used to monitor the start time of a fog event. When the LWC reaches a certain value (usually taken as 75mg/m^3) for a period of 15 minutes, the data acquisition system will page a site operator. PVM calibrations (both of LWC and particle surface area (PSA)) were regularly performed using a manufacturer supplied disk.

A newly designed CSU optical fog detector (OFD) was also used (Emert, 2001; Carrillo et al., 2004) on the ground and on a tower at Angiola. The ground-based OFD was co-located with the PVM-100 to provide a basis of assessing whether the optical sensor data can be used to determine fog presence and thickness. OFDs were also deployed at three levels of a 100 m tower to activate tower-based fog collectors.

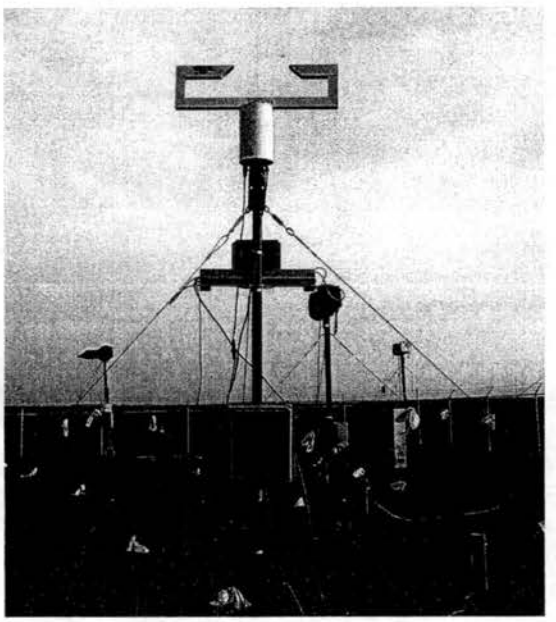

Figure 2-4. Gerber Scientific Particulate Volume Monitor (model PVM-100).

2.2.2 Bulk fog collection

On the ground we set up a Caltech Active Strand Cloud Collector (CASCC) (Figure 2-5) (Demoz, et al., 1996), which was used to collect bulk fog samples. It employs a fan to draw air across six rows of 508 μm Teflon strands. The fog drops are collected based on their inertia. Drops with too much inertia to follow the fluid streamline around the strands impact. The collected droplets run down the strands and are collected into a polyethylene collection bottle.

The collector flow rate and cut size are influenced by fan revolution speed, which determines the air velocity through the collector. Under different applied DC voltages, the fan will rotate at different speeds and draw air through the collector at different velocities. Because fog drops are collected based on their inertia, altering the sampling velocity will change the collector efficiency curves. Corrections for flow rate are needed to determine modified flow rates and cut sizes as a function of applied fan voltage.

Figure 2-6 shows the CASCC average velocity measurement results made at CSU following the field experiment. These values were determined using a hot wire anemometer, corrected for standard conditions, in a cross section of the CASCC. The data indicate that the fan revolution speed and average velocity through the collector

are linear functions of applied fan voltage. Theoretically, the 50% cut size of the CASCC is 3.5μm at a flow rate of 8.5 m/s (Demoz, et al., 1996). Based on the voltage we used in CRPAQS study (10.6V for CASCC), we observe an average velocity of approximately 9.9m/s, producing a 50% cut size still at about 3.5 μm (size cut doesn't change much with velocity for this system). Details are provided in Appendix-A.

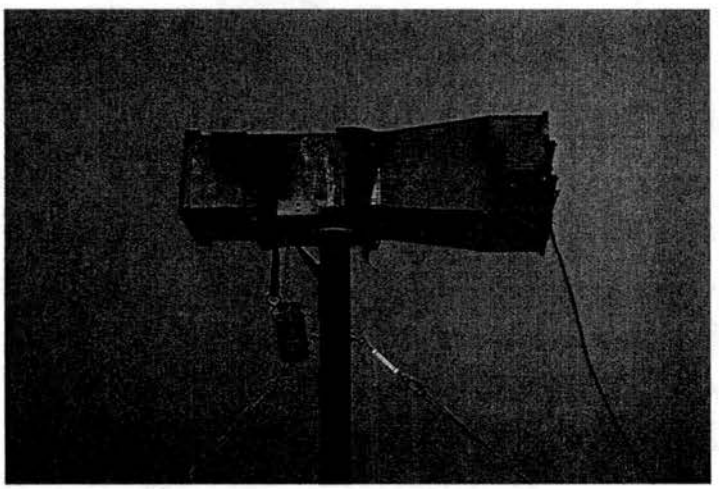

Figure 2-5. Caltech Active Strand Cloud Collector (CASCC).

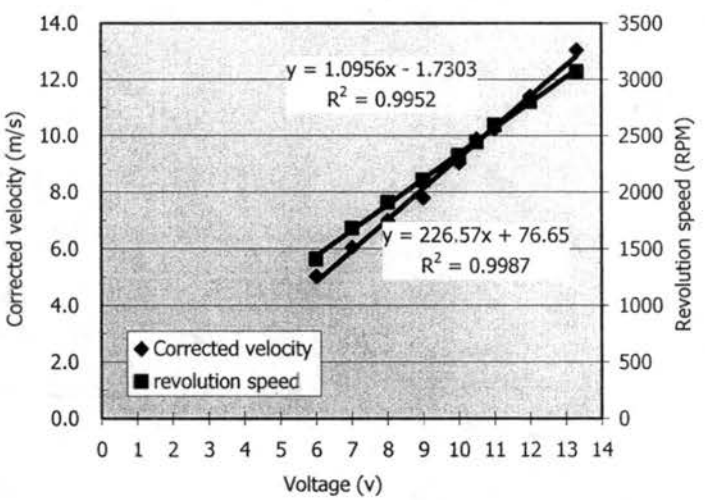

Figure 2-6. Fan revolution speed and air velocity measured for the CASCC as a function of applied fan voltage. "Corrected" means the flow rate has been corrected due to air pressure diference at different altitude.

A Caltech Heated Rod Cloud Collector (CHRCC) (Demoz, et al., 1996) was also used in some fog events when air temperatures fell below freezing. The collection mechanism of the CHRCC is the same as the CASCC, except that CHRCC use hollow stainless steel rods as impaction surfaces. Each rod contains nichrome wire encased in a Teflon sleeve. This permits internal heating of the rods by passage of a current through the nichrome wire. During CRPAQS when supercooled drops froze

on CHRCC collection surfaces, the CHRCC was turned off at about 15 minute sampling intervals, then heating was turned on for an appropriate time (usually about 15 seconds) to let the frozen rime melt and flow into the sampling bottle. Frequent heating can prevent significant ice from accumulating on the rods, changing the diameter of the rods and changing their cut size. Turning off the fan while heating and heating for a very short period both minimize potential sample evaporation from the rods.

A bulk stainless steel CASCC (ss-CASCC) (Herckes et al., 2000) was used to collect fog for analysis of total organic carbon (TOC) and individual organic species by Gas Chromatography / Mass Spectrometry (GC/MS). The structure of the ss-CASCC is similar to the CASCC, except the ss-CASCC uses stainless steel walls, stainless steel strands, a stainless steel trough and sampling tube, and glass sample bottles. Figure 2-7 shows the ss-CASCC sampling velocity as a function of applied fan voltage. The data are similar to the CASCC results shown above, consistent with their design similarities. Based on CRPAQS fan voltages, the sampling velocity and size cut for the ss-CASCC are approximately 9.9m/s and 3.5μm, respectively. Details are stated in the Appendix-A.

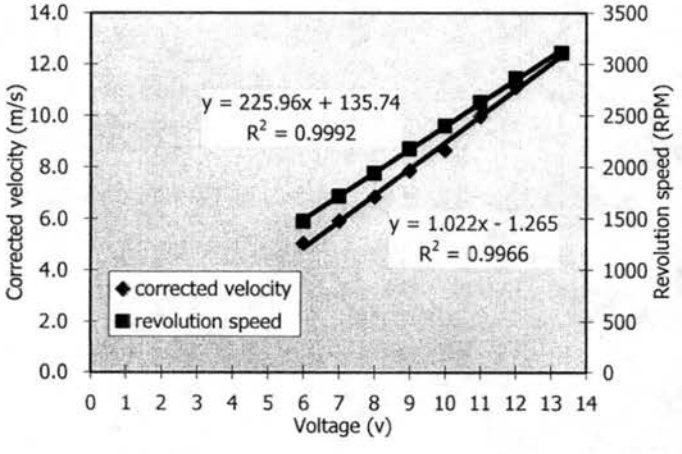

Figure 2-7. Corrected air speed and revolution speed vs voltage on metal organic CASCC (ss-CASCC). "Corrected" means the flow rate has been corrected due to air pressure difference at different altitude.

The CASCC, CHRCC and ss-CASCC collectors were used to collect sequential fog samples at time intervals between 1 and 2 hours throughout each fog event.

2.2.3 Size-resolved fog composition

An all-plastic size-fractionating CASCC (sf-CASCC) (Figure 2-8) (Demoz, et al.,

1996), was used to collect and analyze drop size-resolved fog samples. The sf-CASCC is similar to the CASCC but has an extra inlet stage (4 rows of eight 12.7 mm diameter Teflon rods) before the 6 rows of 508 μm strands. Theoretically, it draws the droplets through the sampler at a velocity of 6.7 m/s and has a total flow rate of 19 m^3/min; and theoretical 50% cut sizes for the two stages of the sf-CASCC have been estimated as 4μm and 23μm. Similar to bulk fog samples, sample weight and pH were measured on site, and preserved aliquots were made for some species.

As with the CASCC some fan voltage corrections needed to be applied to calculate the real flow rate and cut size. Figure 2-9 shows the velocity-voltage relationship measured for the sf-CASCC. The fan voltage used in CRPAQS was 11.1v, corresponding to a 7.5 m/s average sample velocity. The size cut for the second stage doesn't change much due to this velocity decrease, remaining about 3.5 μm, but the size cut for the first stage changes to about 21 μm. These results are described in more details in Appendix-A.

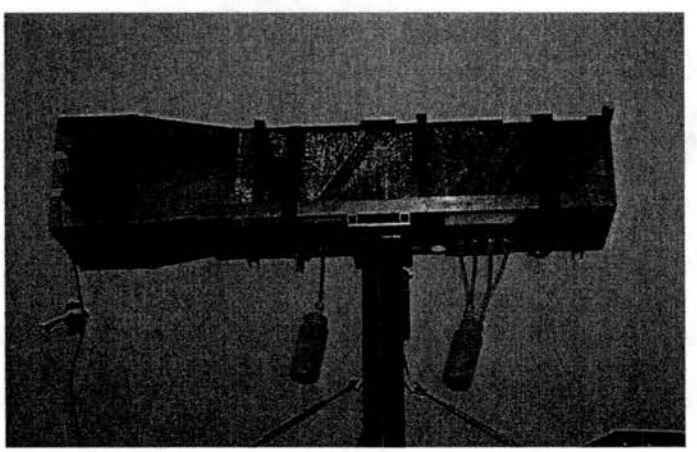

Figure 2-8. An all-plastic size-fractionating CASCC (sf-CASCC) mounted on site. The first stage, second stage, sampling bottle and fan parts can clearly be seen.

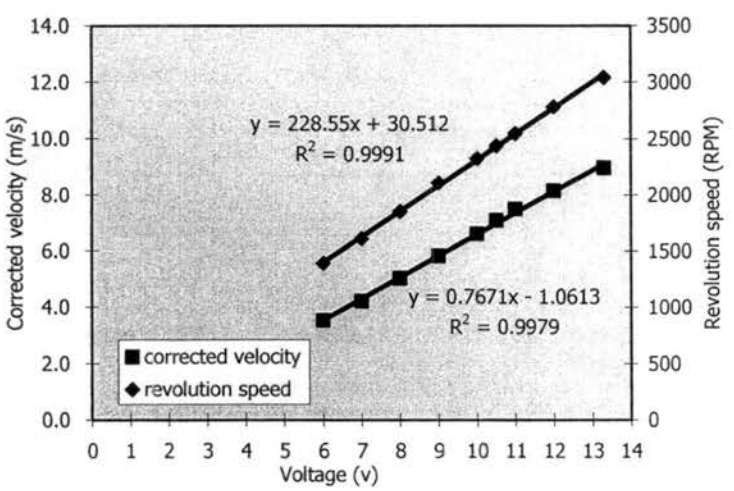

Figure 2-9. Corrected air velocity and revolution speed vs voltage on sf-CASCC. "Corrected" means the flow rate has been corrected due to air pressure difference at different altitude.

A two-stage stainless steel size-fractioning CASCC (ss-sf-CASCC) was used to collect samples for organic analysis. The principle of this collector is the same as the sf-CASCC, but it is twice as large in width and uses two fans side to permit greater sample collection. The data from this collector were used to examine how TOC concentrations vary between large and small fog drops. Figure 2-10 shows the relationship between fan voltage and average sample velocity for the ss-sf-CASCC. The operational sample velocity in the field was 8.2m/s with 50% size cuts of 19 μm for the first stage and 3.5 μm for the second stage (see Appendix-A for detail).

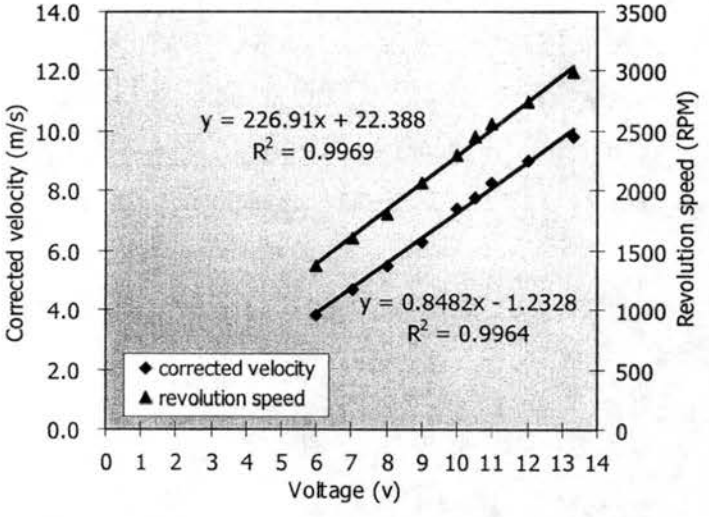

Figure 2-10. Corrected air velocity and revolution speed vs voltage on ss-sf-CASCC. "Corrected" means the flow rate has been corrected due to air pressure difference at different altitude.

Samples from the CSU 5-stage collector (Figure 2-11) (Moore et al., 2002; Straub et al., 2002) provided detailed information on how major ions concentrations and fog pH vary across the drop size spectrum. The 5-stage collector is a cascade impactor that consists of five stages, with stage size cuts ranging from 5 to 30μm theoretically (30, 25, 15, 10 and 4 μm for stage-1 to stage-5). Lab and model evaluations of the collector performance (Straub et al., 2002) show that the collector works approximately as designed, although there is some overlap between drop sizes collected in the first two stages.

As seen from Figure 2-11, the collector is mounted at 45°to the horizontal to help collected water drain toward polyethylene sample vials mounted on one end of each stage. At the end of sampling period, a set of clean rubber spatulas is used to remove the remaining water from each stage.

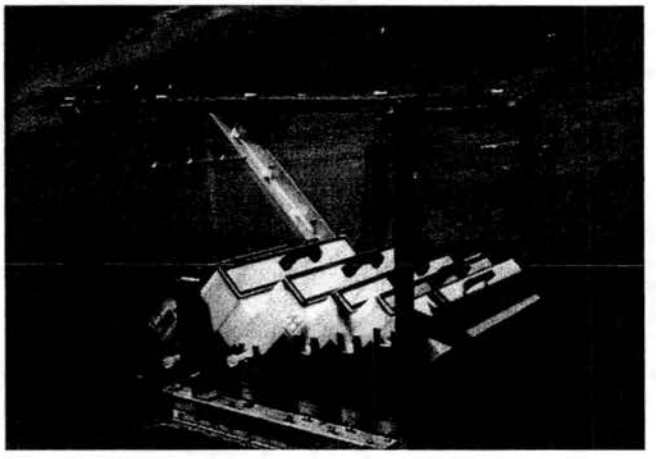

Figure 2-11. The CSU 5-stage collector shown deployed in an earlier cloud campaign at Whiteface Mtn, NY. Photo by K. Moore.

2.2.4 Size distribution of fog droplets

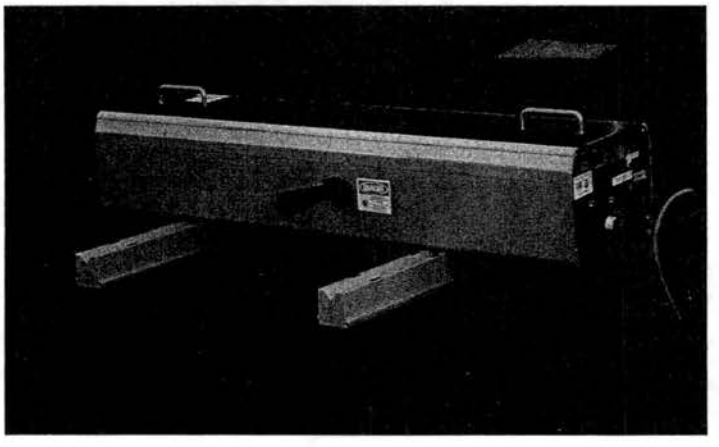

Figure 2-12. CSASP-100-HV optical probe.

Size distributions of fog drops were measured by a Particle Measurement Systems Classical Scattering Active Spectrometer (CSASP) CSASP-100-HV optical probe (Figure 2-12). We set the CSASP to use 20 bins to measure fog drops from 5μm to 47μm diameter. The CSASP can provide information on how fog drop size distribution changes with time, with sampling intervals as short as one second.

Just one month before the CRPAQS study, some critical updates were made to the CSASP to improve its performance. First, a Droplet Measurement Technologies (DMT) Signal Processing Package (SPP), including a new laser and new signal processing electronics, replaced the original PMS electronics package. The SPP not only duplicates all the critical functions of the original PMS electronics package, but

also provides some new features (e.g., it makes the data treatment much easier by eliminating dead time losses, and now it offers the flexibility with respect to selecting the number of size channels to use when classifying particle sizes. The user has complete flexibility to select how many channels and the size threshold to use for each channel). Also, a new signal processing software is used. Details of CSASP data treatment are included in Appendix-C.

Table 2-1. Calibration table of CSASP during CRPAQS study

Date	Bead Diameter (μm)	Reading (Ave Drop Dia) (μm)	Dia from conversion table (μm)
23 Dec 2000	10 ± 1.0	8.33	9.5-10
	20 ± 1.4	15.83	19-19.5
	30 ± 2.0	23.97	29.5-30
	Zero Reading	7.26 (average for 78 seconds)	
19 Jan 2001	10 ± 1.0	13.81	16-16.5
	20 ± 1.4	19.49	24-24.5
	30 ± 2.0	23.65	29-29.5
	Zero Reading	5.45 (average for 67 seconds)	

The CSASP calibration was checked by DMT during the probe's upgrade. It was subsequently checked, using monodisperse glass beads, twice during the CRPAQS study (detailed operation procedures of CSASP are described by Pinnick et al. (1979) and Pinnick et al. (1981)). Table 2-1 shows the CSASP calibration table for CRPAQS. Comparing the expected diameters from the conversion table with true bead diameters, the calibration was good on Dec 23rd 2000, but somewhat further off on Jan 19th 2001.

Another frequently used drop size distribution measurement instrument is the Forward Scattering Spectrometer Probe (FSSP), which use the same principles as CSASP but is non-aspirated. Both PVM-100 and FSSP were used in some experiments (Fuzzi et al., 1992, Wobrock et al. 1994, Choularton et al. 1997; Fuzzi et al., 1998, Bower et al., 1999), and measurements of LWC from the PVM-100 were compared to LWC measurements from a FSSP-100. CSASP measurements were only found in limited experiments (e.g., Pinnick et al., 1979). Therefore, most of the discussions about problems with drop size distribution measurement here are based on

the literature discussion of the FSSP, but also include CSASP characteristics in CRPAQS studies, and many of the issues are common to both instruments.

During CRPAQS we found that the effective diameters (D_{eff}) measured by the CSASP agreed well with PVM measurements of the same parameter; however, the CSASP tended to substantially overestimate the LWC relative to the PVM. Two factors possibly contributing to this difference are:

- A possible bias in PVM LWC for large drop sizes: the response of the PVM is known to drop off for drop sizes larger than about 40 μm diameter (Gerber et al., 1991), although Wendisch et al. (1998) report individual PVM units may show a negative LWC bias at a lower threshhold. Therefore, the PVM in CRPAQS may underestimate LWC when there is high LWC comprised by fog with large fog drops.
- A possible bias in CSASP LWC: Gerber et al. (1999) demonstrate that flow focusing and concentration of droplets in the sensing volume of an FSSP can lead to a significant overestimate of LWC. We conducted a simple computational fluid dynamics simulation of droplet focusing in the CSASP by using the commercial Fluent model. Results are presented in Appendix-B. Our results suggest that the inlet of the CSASP also acts as a droplet concentrator, artificially enhancing the concentrations of large droplets sensed by the probe and producing an overestimation of LWC. It's also possible that the sensing volume in our CSASP is not accurately defined.

Due to the difficulty of finding comparable and reproducible conditions in ground-based field measurements, no general agreed explanations of the discrepancy between the measurements of these two instruments exists. Since the average diameter of fog droplets in CRPAQS was of the order of 25 μm, PVM measured LWC should be accurate enough. Based on the analysis above, the CSASP drop size distributions were normalized to PVM LWC.

2.2.5 Fog deposition

Fog deposition measurements were carried out by using two deposition plates

(Figure 2-13) and two recording balance systems (Figure 2-14). The deposition plates are made of Teflon and have been tested in Davis California radiation fogs (Collett et al., 2001; Moore et al., 2004b). Two square Teflon deposition plates ($0.30m^2$) were used to assess possible sample contamination because the plates are ground-based. Samples were typically collected at 2 hr intervals to match other cloud composition measurement periods or to provide sufficient sample (>10 ml) for composition analysis.

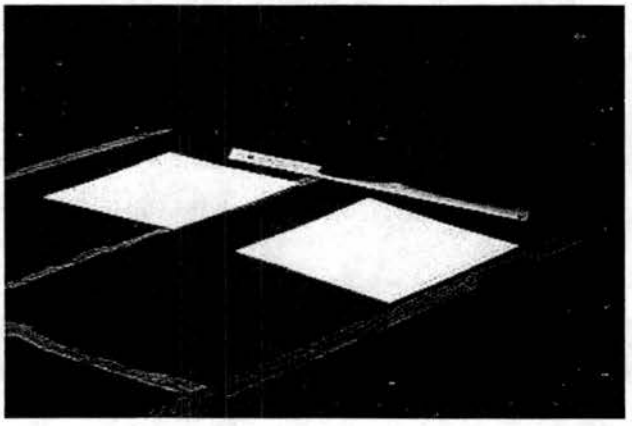

Figure 2-13. Two deposition plates deployed during CRPAQS. The plastic sheeting beneath the plates was used to eliminate possible contamination from the ground.

Collected fog water was scraped from the interior of the plate and transferred to a polyethylene sample bottle. Right after collection, samples were weighed and aliquots were taken for measurements of ion concentrations and Total Organic Carbon (TOC).

Figure 2-14. Two balances set up to record deposition fluxes to a bare metal and an artificial grass surface.

In addition to the Teflon deposition plates, we operated an automated deposition flux monitoring system previously tested at Davis (Collett et al., 2001). This system consists of two recording balances (PB3002-S, Mettler Toledo, Switzerland) that record the mass flux of water with a time resolution of 1Hz. The difference between these two balances was that a rectangular ($0.029m^2$) artificial grass surface was put on one of the two balances to examine surface roughness effects on deposition, while the

other balance used its own round bare metal weighing pan ($0.024m^2$) as the sampling surface. The data were averaged to 10 minute intervals to evaluate the possible difference between these two surfaces, and then averaged to 20 minute interval as the input of regression analysis in Chapter 4.

2.2.6 Gas phase measurements

Gas phase measurements of total soluble hydroperoxides at Angiola were measured using a continuous monitor based on the method of Lazrus et al. (1986) at 10 minute intervals (Figure 2-15). Soluble hydroperoxides (including hydrogen peroxide and soluble organic peroxides) were captured from the air into solution where they are reacted to produce a fluorescent dimer, the concentration of which is measured by an on-line fluorimeter. Although the instrument responds to both hydrogen peroxide and soluble organic hydroperoxides, this mixture is strongly dominated by hydrogen peroxide in most cases, including IMS95 measurements in the SJV.

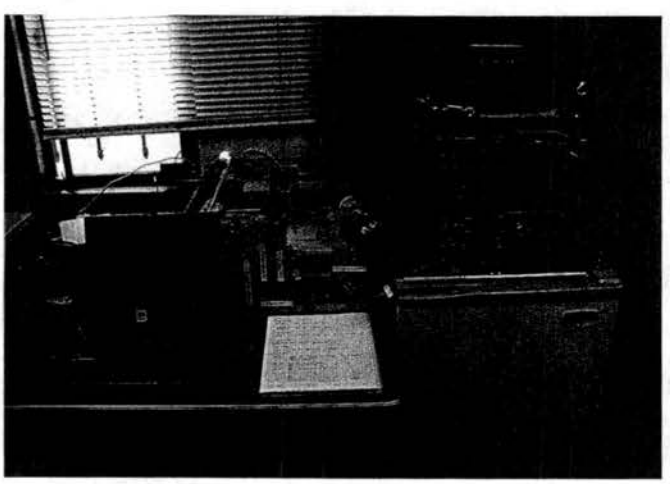

Figure 2-15. Gas phase measurements of total soluble hydroperoxides by continuous monitor.

2.2.7 Size-resolved aerosol composition

A Microorifice Uniform Deposit Impactor (MOUDI) was used to sample pre- and post-fog size-resolved aerosol (Figure 2-16). The MOUDI has 8 impaction stages and one afterfilter. The working flow rate was 30 lpm, set by monitoring the calibrated pressure drop through the instrument and verified by use of a dry gas meter. The MOUDI was operated over a time period of eight to fourteen hours depending on the

status of pre-/post-fog measurements.

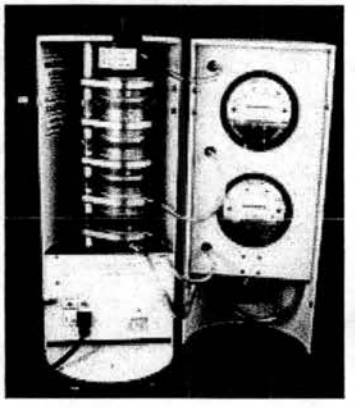

Figure 2-16. A Microorifice Uniform Deposit Impactor (MOUDI).

2.3 Sample handling and chemical analysis

During each fog event collected fog samples were immediately brought to a small field lab (Figure 2-1). Samples were first weighed together with the bottle to get net sample weight (sample bottle had been weighed before putting onto the collectors). Then samples were aliqotted for chemical analysis later in our lab at CSU. Table 2-2 lists the species aliquots prepared in the field and the amount of added preservation solutions for each species. pH measurement had the highest priority for all the samples, then ion chromatography (IC) analysis. For other species, the priority depends on the sample type and collector used. For example, metal analysis had higher priority for the 5-stage collector, while TOC/ DOC aliquots usually had higher priority for stainless steel collector samples. Table 2-2 also lists the sample amount needed/desired for each species. Large and small refer to the sample volume required. Available sample volumes determine how much sample can be used to make aliquots, and what analysis can be done for each sample. In cases where sample volume was limited, small volume aliquot procedures were available for some aliquots. These generally use only 100 μl sample (amount of preservation solutions are also changed proportionately to sample volume).

Table 2-2. Aliquot preservation protocol.

Aliquot*		Sample amount	Preferred vial	9.7% HNO_3 Solution	S(IV) Preservative Solution	Catalase Solution	H_2O_2 Conditioning Reagent	H_2O_2 Flurescent Reagent	HCHO preservative solution	Chloroform
pII		40 µl	0.5 ml micro centrifuge tube							
IC		500 µl	Plastic IC vial (lid w/septum)							
Metals:										
	Large	1 ml	1.2 ml cryovial	100 µl						
	Small	100 µl	plastic IC vial	10 µl						
H2O2:										
	Large	1 ml	1.5 ml glass vial				200 µl	200 µl		
	Small	100 µl	glass insert vial				20 µl	20 µl		
S(IV):										
	Large	1 ml	1.5 ml glass vial		100 µl	100 µl				
	Small	100 µl	glass insert vial		10 µl	10 µl				
HCHO:										
	Large	1 ml	1.5 ml glass vial						100 µl	
	Small	100 µl	glass insert vial						10 µl	
TOC/DOC		5~15 ml	Glass vial							
Organic acid		500 µl	Glass vial							20 µl

*large (small) means how much the sample amount would be if the amount of water of a sample is sufficient (unsufficient).

2.3.1 Sample weight

A sample bottle was replaced at defined intervals, usually 1 or 2 hours depending on LWC. The sample weight was obtained by subtracting empty bottle weight from the weight of the bottle with sample.

2.3.2 pH measurements

The pH of samples was measured on site with an Orion Model 290A or 250A pH meter and a Microelectrodes, Inc. Model MI-710 pH combination electrode, calibrated with pH 4 and 7 standards. A periodic calibration check was made to assure the calibration accuracy.

2.3.3 Ion concentrations

Sample aliquots were prepared for major ion analysis by pipetting 500 μl of sample into a polypropylene auto-sampler vial. The vial was sealed with a Teflon-lined septum and lid.

Inorganic anion (NO_3^-, NO_2^-, SO_4^{2-}, and Cl^-) concentrations were determined by using a Dionex DX-500 ion chromatograph equipped with an AS3500 auto-sampler, an AG4A-SC guard column, AS4A-SC separation column, suppressed by Dionex Anion Self-Regenerating Suppressor (ASRS), and detected by conductivity detection. Separation was achieved using a 1.8 mM Na_2CO_3/1.7 mM $NaHCO_3$ eluent at a flow rate of 2.0 ml/min.

Inorganic cation (Na^+, $NH4^+$, K^+, Mg^{2+} and Ca^{2+}) concentrations were determined using a second DX-500 ion chromatograph equipped with an AS3500 auto-sampler, CG-12 and CS-12 guard and separation columns, suppressed by a Dionex Cation Self Regenerating Suppressor (CSRS) and detected by conductivity detection. Separation was achieved by using a 20 mM methanesulfonic acid eluent at a flow rate of 1.0 ml/min.

Both IC systems were calibrated daily using a series of lab-prepared ion standards. Calibration accuracy was monitored by injection of independent, NIST traceable standards. Calibration stability during each day's analysis was monitored by periodic injection of a standard solution.

2.3.4 Metals

Samples were analyzed for Fe and Mn using a Varian Model 640Z Graphite Furnace Atomic Absorption Spectrometer (GFAAS) with Zeeman background correction. If the sample concentration is too high, either a manual or an automatic dilution was used. Modified (optimized by Katharine Moore) varian-recommended analytical procedures (in GFAAS operation manuals) were used to determine Fe and Mn in the fog water. Aliquots were prepared in the field for trace metal analysis by acidification to near pH 1with trace metal grade nitric acid. Adding nitric acid stabilizes the samples by mimimizing precitation and wall adsorption.

2.3.5 S(IV)

Since S(IV) in fogwater can be oxidized by H_2O_2, O_3 and O_2 in the presence of transition metals, samples were stabilized by adding buffered HCHO to complex S(IV) in the solution to form hydroxymethanesulfonate (HMS) (Dasgupta et al., 1980), and by adding of catalase to destroy any hydrogen peroxide in the sample. Treated samples were analyzed on a Hach DR/4000 visible spectrophotometer by the pararosaniline method (Dasgupta, 1981). This technique provides a measurement of total S(IV), namely dissolved sulfur dioxide, bisulfite, and sulfite (together comprising "free" S(IV)) plus any HMS present before preservation of the sample.

2.3.6 Formaldehyde

Formaldehyde can form stable HMS in the presence of bisulfite. Formaldehyde was preserved by adding HCHO preservation solution containing bisulfite on site (20 mM

NaOH, 10 mM CDTA, 3 mM $NaHSO_3$). Samples were then analyzed by fluorescence spectrophotometer (Dong et al., 1987). This method measured the free formaldehyde and any HMS in the solution before preservation.

2.3.7 H_2O_2 (aq)

Aqueous phase H_2O_2 in the fog samples was stabilized by adding p-hydroxyphenylacetic acid (POHPA) solution in the field to form a dimer, then measured using a Shimadzu RF-1501 spectrophotometer (Lazrus et al., 1985; Rao et al., 1997). Generally, this method measures not only the free/inorganic H_2O_2 in the solution, but also organic peroxide. Because organic peroxide is typically not important and generally represents less than 1% of the aqueous peroxide concentration (Seinfeld et al., 1998), this measurement closely approximates the hydrogen peroxide concentration in the solution.

2.3.8 Organic Acids

Aliquots for later analysis of organic acids were prepared by addition of a small volume of chloroform, which acts as a biocide. C1-C3 carboxylic acids were analyzed using the anion Dionex IC. The organic acid column in this analysis was a Dionex AS-11 separation column with an AG-11 guard column. Separation was achieved using a 0.5 mM NaOH eluent at a flow rate of 2.0 ml/min. The IC was calibrated daily using a series of lab-prepared standards. Calibration stability during each day's analysis was monitored by periodic injection of a standard solution.

Figure 2-17 described sample fractionation methods. Immediately after sampling, aliquots were prepared for measurement of pH and TOC. Remaining sample was later filtered through baked quartz filters (Pall Gellman Pallflex Tissuquartz) in order to make a distinction between the dissolved phase (dissolved organic carbon, DOC) and the insoluble phase of the fog water. Then Ultrafiltration was used to separate organic matter as an approximate function of molecular weight and TOC content of each fraction was measured. Detail sample preparation and measurement were described below.

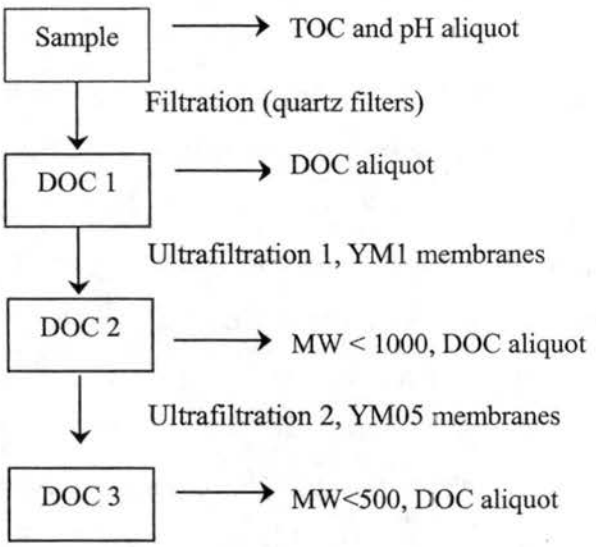

Figure 2-17. Schematic describing sample fractionation.

2.3.9 TOC/DOC and GC/MS analysis

Sample aliquots for total organic carbon (TOC) analysis were prepared by pipetting 5-20 ml of sample, depending on available sample, into a pre-baked glass vial and sealing with a Teflon-lined cap. TOC was measured using a Shimadzu TOC-5000A analyzer. The instrument vaporizes and oxidizes the sample on a platinum catalyst in a 680°C furnace, followed by infrared measurement of the evolved carbon dioxide. This yields a measurement of total carbon (TC) (elemental carbon theoretically is not included). A second measurement determining sample carbonate (inorganic carbon, IC) measures evolved carbon dioxide following sample acidification. TOC is determined as TC minus IC.

Additional sample was filtered through baked quartz filters (Pall Gellman Pallflex Tissuquartz) to make a distinction between the dissolved phase (dissolved organic carbon, DOC) and the insoluble phase of the fog water ("dissolved" refers to the filtrate and "insoluble" to the material retained on the filter).

The filter and filtrate were spiked with deuterated compounds used as internal standards for trace organic compound quantification. The filter samples were extracted three times with 25 ml of dichloromethane (DCM). Samples of 100–200 ml of filtrate, depending on available sample, were extracted three times with 25 ml of DCM after adjusting the sample pH to 1 and sample salinity to 50 g/l by adding NaCl. The DCM from the liquid/liquid extraction was dried over Na_2SO_4. DCM extracts were concentrated to 0.25 ml using a vacuum centrifuge and/or nitrogen blowdown prior to analysis. A first fraction of the concentrated extract was injected directly into an HP 6890/5973 Gas Chromatography coupled to Mass Spectrometry (GC-MS) for analysis. A second fraction was derivatized with diazomethane to transform organic acids to their methylester analogs prior to analysis. Greater detail about this methodology is provided by Herckes et al. (2002).

2.3.10 Ultrafiltration (molecular weight measurement)

Ultrafiltration was used to separate organic matter as an approximate function of molecular weight and the TOC content of each fraction was measured. The experimental set up for the ultrafiltration procedure was adapted from Likens et al. (1983). Physical separation of DOC into molecular size ranges was completed in a pressurized and stirred ultrafiltration cell (Amicon model 8050), using the following MILLIPORE ultrafiltration membranes: YM1 (nominal size cut of 1000 Daltons) and YC05 (nominal size cut of 500 Daltons).

2.3.11 Carbonyl and functional group analysis

An HPLC method was used for determining concentrations of carbonyl and dicarbonyl compounds in the fog samples. A second HPLC method was used to characterize the split of fog DOC among different functional group classes. Details of the sampling and preservation methods and analysis are described in Chapter 5. For the carbonyl analysis, Angiola fog samples were derivatized in our lab in Fort Collins more than a year after collection, while Fresno fog samples were derivatized on-site to prevent the fog samples

from degrading. Figure 2-18 shows the HPLC system we used, including solvent module, helium degasser / sparger, thermostatted column compartment, binary pump, diode array detector, and autosampler.

Figure 2-18. HP 1050 HPLC system.

2.4 Quality Control

Several procedures were used to ensure the integrity of each fog measurement, including calibrating instruments, cleaning collectors before each event, taking blanks, and analyzing replicate samples.

Individual instrument calibration was carried out at a certain time based on the instrument's maintenance requirement. Calibration of the PVM and CSASP was discussed above. Before the setup in the field, the collectors were first taken apart to thoroughly clean them with Triton-X100, and then rinse with deionized (DI) water. After mounting the collectors (except 5-stage collector), all the fog collectors were cleaned before each event. Some DI water was sprayed directly into the collectors using clean spray bottles and collected water served as a collector blank. This is to simulate the real process of fog droplet collection, since the sprayed water droplets follow approximately the same paths as the samples collected. A separate DI blank was taken from the DI water

bottle used for spraying.

Uncertainties and minimum detection limits (MDL) were calculated for each species measured through all the fog episodes. For CRPAQS samples, although the field campaign lasted for about two months, all the samples from different fog episodes were stored in the refrigerator and the laboratory measurements for most species were done at the same time. Therefore, only one precision estimate (relative standard deviation, RSD) and one MDL are calculated for each species.

During each fog event, for every 3~4 samples, a sample was chosen to make two identical sets of aliquots known as duplicates. Duplicates were used to test the consistency of making and analyzing sample aliquots. Sample replicates, replicate analyses of one sample aliquot in the lab, capture analytical measurement precision only.

Precision uncertainties were calculated and reported as RSD in percent. The RSD was calculated using duplicate sample pairs, or using analytical standard replicates if it was impossible to use sample replicates. The formula to calculate RSD is as follows:

$$RSD = \frac{\left[\left(\frac{1}{M}\right)\times\sum_{j=1}^{M}\left(\sigma_j\right)^2\right]^{\frac{1}{2}}}{\bar{x}}\times 100\% \qquad (2\text{-}1)$$

and the value for σ_j is calculated as in Equation (2-2)

$$\sigma_j = \frac{|x_1 - x_2|}{\sqrt{2}} \qquad (2\text{-}2)$$

where M represents the number of pairs of replicates used, σ_j is the standard deviation of each analysis pair and $\bar{x}$ is the average of all replicates.

To determine the minimum detection limit, blank samples analyzed for each species were used. The minimum detection limit $\Delta x_{\min}$ is:

$$x_{\min} - x_b = \Delta x_{\min} \geq t s_b \sqrt{\frac{N_1 + N_b}{N_1 N_b}} \tag{2-3}$$

where t is the value given at the 95% confidence level for the appropriate number of degrees of freedom, s_b is the blank standard deviation, N_1 is the number of sample measurements (for single analysis, N_1 =1), and N_b is the number of analyzed blanks. The subscript b refers to the blank determination.

2.4.1 Ion concentrations

Table 2-3. RSD, MDL and sample concentration summaries for CRPAQS fog ions.

		Cl^-	NO_3^-	NO_2^-	SO_4^{2-}	Na^+	NH_4^+	K^+	Mg^{2+}	Ca^{2+}
MDL (95% CL) (μN)		8.0	18.2	4.3	6.5	12.1	27.9	1.3	1.8	4.1
RSD (%)		4.7	3.6	4.6	7.6	7.3	5.5	21.2	9.0	7.4
# of sample pair		66	66	66	66	55	55	55	55	55
Sample concentration (μN)	Minimum	8.7	36.6	3.2	8.7	0.1	0.0	0.8	4.3	4.3
	Maximum	168.1	3547.0	321.2	1463.4	243.6	4492.1	80.1	78.1	116.3
	Mean	31.9	626.2	44.5	146.5	30.9	1104.4	12.4	9.8	28.2

Table 2-3 lists the statistical analysis for ions, including Cl^-, NO_3^-, NO_2^-, SO_4^{2-}, Na^+, NH_4^+, K^+, Mg^{2+} and Ca^{2+}. The MDL were calculated from blank measurements for all the samples from all the collectors except the 5-stage collector. The RSD were calculated from sample replicates. K^+ has a relatively higher RSD because its peak in the chromatogram is near the peak of NH_4^+, leading to greater interference when the concentration of NH_4^+ is high. The RSD of the remaining ions are all well below 10%.

These results are consistent with or better than past studies at Whiteface Mountain and Davis (Reilly, 2000). The MDL results are higher than at Whiteface Mountain and Davis, but still in a reasonable range because the MDL are all far below the sample means, except for sodium.

2.4.2 Organic acids

Table 2-4 shows the statistical analyses for organic acids. The RSD were calculated from sample replicates, and the MDL were calculated from standard measurement because the blanks of some species did not exhibit any detectable peaks. We can see that the RSD are all less than 10%, quite reasonable for organic acid analysis. MDL of acetate, formate and oxalate are smaller than sample means respectively, while for propionate, glutarate, succinate and malonate, their MDL are larger than measured sample means.

Table 2-4. Statistical analysis for organic acids.

		Acetate	Propionate	Formate	Oxalate	Glutarate	Succinic	Malonate
MDL (95% CL) (μN)		4.1	3.7	4.2	3.2	5.6	5.8	5.0
RSD (%)		3.8	3.8	2.4	2.8	4.6	4.8	5.4
# of sample pair		10	10	10	10	10	10	10
Sample concentration (μN)	Minimum	1.4	0.0	6.7	5.5	0.0	0.0	0.0
	Maximum	197.2	11.5	121.6	44.0	6.9	10.8	26.5
	Mean	44.7	3.2	40.1	12.3	1.0	2.3	2.1

* MDL was calculated by replicate standard analyses

2.4.3 S(IV), HCHO, H_2O_2, metal (Fe, Mn), TOC and DOC

Table 2-5 lists the statistical analysis results for S(IV), HCHO, H_2O_2, metals (Fe, Mn), TOC and DOC. MDL and RSD were obtained from blanks and sample replicates, except S(IV), which were calculated from standard analyses. Comparing the RSD and MDL of

S(IV), HCHO, H_2O_2 and metals with earlier results at Whiteface Mountain and Davis (Reilly, 2000), there is little difference between them. The RSD of iron is smaller here, only 4.1% compared with 11.1% in Whiteface Mountain and Davis.

Table 2-5. Statistical analysis for S(IV), HCHO, H_2O_2, Fe^{2+}, Mn^{2+}, TOC and DOC.

		S(IV) (μM)	HCHO (μM)	H_2O_2 (μM)	Fe^{2+} (μg/l)	Mn^{2+} (μg/l)	TOC (ppmC)	DOC (ppmC)
MDL (95% CL) (μN)		1.5	3.3	0.07	6.9	0.3	0.5	0.2
RSD (%)		6.7	7.1	6.6	4.1	2.7	2.1	5.7
# of sample pair		10	14	7	60	60	17	7
Sample concentration	Minimum	3.9*	5.4	0.8	12.4	0.8	0.3	3.9
	Maximum	5.9*	50.8	18.8	478.6	29.9	17.4	7.7
	Mean	5.1*	21.9	4.6	121.2	6.9	9.3	6.4

* min, max and mean are for standard.

2.4.4 MOUDI

Table 2-6. Statistical analysis for MOUDI.

	Na^+	NH_4^+	K^+	Mg^{2+}	Ca^{2+}	Cl^-	NO_3^-	SO_4^{2-}
MDL (95% CL) * (ng/m^3)	8.0	1.4	1.2	5.1	12.3	8.2	6.6	4.0
RSD (%)	5.3	2.6	4.5	2.2	3.8	9.6	13	6.0
# of sample pair	6	6	6	6	6	5	5	4
Mean ($\mu g/m^3$)	1.42	19.1	0.99	4.45	4.33	0.55	28.0	3.87

* MDLs were calculated from BRAVO data.

Table 2-6 shows the statistical data for MOUDI samples. Compared with BRAVO data

(Lee, 2002), the RSD of NO_3^- is a little higher, 13% vs. 5.9%, but still in a reasonable range. No reliable MDL values were obtained for the MOUDI due to the limited numbers of sample blanks in this study. MOUDI MDL values from the BRAVO study are included in Table 2-6 for information.

2.5 Instrumental quality control

This section summarizes the instrumental quality control and some uncertainties with the instruments. The instrumental quality control includes correct calibration of instruments, collector efficiency measurements, and corresponding cut size measurement.

2.5.1 Meteorological measurements

Meteorological measurements are subject to the precision of the instruments, generally stated in manufacturer's operation manual. Although our weather station has not been officially calibrated since its purchase, it was verified in some field campaigns. Further, meteorological measurements were used in this study only to provide qualitative information. Wind direction was verified in Davis and Whiteface, consistent with a compass and the field notes (Moore, 2001). The other parameter measurements provided are assumed to be good, but it is unknown how accurate they are in absolute terms. Ambient temperature measurements are assumed to be good to ± 1°C (Moore, 2001). Pressure and wind speed measurements were assumed to have negligible uncertainties and impact upon the results.

2.5.2 Flow rate measurements

As stated before the most important factor for the fog collectors impacting accuracy of sampling velocity and cut size is the fan voltage. The fan law (Wu et al., 2000) determines that the revolution speed of a DC-powered fan has a linear relation to the air flow velocity, and also has a linear relation to the voltage exerted on the fan. Therefore, the voltage is critical in determining the operation characteristics of collectors. Demoz et

al. (1996) proposed that the flow rates in the Caltech collectors are assumed to be accurate to within ± 5% of design values if the correct voltage is applied to the fans. Appendix-A shows how to apply the fan law to the fans of collector and collector's flow rate measure results. A summary of flow rate and size cut info for collectors is shown in Table 2-7.

Table 2-7. Summary of collectors' flow rate and size cut.

	Voltage (V)		Air Velocity (m/s)		Size Cut (μm)	
	Design	CRPAQS	Design	CRPAQS	Design	CRPAQS
CASCC	13.3	10.6	8.5	9.9	3.5	3.5
ss-CASCC	13.3	10.6	8.5	9.6	3.5	3.5
sf-CASCC	13.3	11.1	6.7	7.5	23(1^{st} stage) 4(2^{nd} stage)	21(1^{st} stage) 3.5 (2^{nd} stage)
ss-sf-CASCC	13.3	11.0	6.7	8.2	23(1^{st} stage) 4(2^{nd} stage)	19(1^{st} stage) 3.5 (2^{nd} stage)

As seen from Appendix-A, variation in voltage on the fan will change the flow rate dramatically, but modest variation in flow rate do not change the droplet collection efficiency and size cut very much.

2.5.3 CSASP uncertainties

As stated before a new laser and signal processing package and new software had been added to the CSASP just before the CRPAQS study. The new software and new probe are powerful and worked well, and some of the uncertainties caused by long dead time from the old probe were eliminated. The calibration procedure was carried out two times before the fog campaign as described earlier. Appendix-D shows a detailed uncertainty analysis of the CSASP data treatment.

Chapter 3

Overview of fog episodes and fog composition

3.1 Summary of fog sampling

During the study (winter 2000/2001), we met over ten warm fog events and successfully collected over two hundred fog samples. The measurements and analysis include weather conditions, physical size distributions, and chemical analysis of over ten species in gas and aqueous phases. In this chapter, these data will be presented and discussed. There were some short fog events and they were insufficient for fog collection since the duration was not long enough to collect enough sample. There were also some freezing fog events during which the temperatures were under zero Celsius degree, which would made fog water freeze on the sampling strands and rods, making it impossible to collect and causing some serious deflection of size distributions.

Table 3-1 summarizes collected fog samples in Angiola by collector type. Overall, the good sampling events are as follows:

- Dec 17/18 (day 352)

  A very good fog event with typical weather conditions of radiation fog, it started at 22:15pm and finished at 12:00 noon the next day. This event yielded a total of 66 samples, from different collectors and time periods.
- Dec 18/19 (day 353)

This fog event started at 23:00pm, then lifted but came back again at 1:20am until 7:30am in the morning. 25 samples were collected.

- Jan 6th

  We collected one fog sample from 6:00am to 8:00am by using CHRCC since its temperatures were below freezing.

- Jan 10th

  A total of 6 samples were collected from 6:15am to 7:55am.

- Jan 15th

  19 samples were collected from 23:30pm to 3:00am.

- Jan 17th

  A freezing fog event lasted from 12:00pm to 7:00am, 20 samples were collected.

- Jan 21st

  Total of 25 samples were collected form 6:00am to 9:00am.

- Jan 25th

  A patchy fog event. The fog event lasted from 3:30am until 8:00am, with interruptions of low LWC. 16 samples were collected.

- Jan 31st

  A short fog event from 4:00am until 9:30am. 25 samples were collected.

- Feb 1st

  A patchy fog event lasted from 1:00am to 5:20am. 16 samples were collected.

3.2 Weather conditions

Table 3-2 shows the summary of three basic weather parameters of all fog events: average wind speed, average temperature and average relative humidity. As we can see, the average temperatures of these fog events were above zero degree, except Jan 06 and Jan 17, whose average temperatures were below or close to zero degree. The wind speeds

were all less than 2m/s, consistent with the calm wind required for radiation fogs. These were the typical weather conditions for radiation fogs.

Table 3-1. Summary of collected fog samples in Angiola by collector type.

Date	CASCC	Sf CASCC	Heated CASCC	Dep Plates	ss CASCC	Sf ss CASCC	5-state collector	Tower Level 0	Tower Level 1	Tower Level 2	Tower Level 3	Total
Dec 17, 2000	13	11		6	8	12		12	4			**66**
Dec 18, 2000	4	3		1	2	3	1	3	8			**25**
Jan 06, 2001			1									**1**
Jan 10, 2001	2		2			2						**6**
Jan 15, 2001	1	1	1	1	1	1						**6**
Jan 17, 2001	3	3	4	4	4	1	1					**20**
Jan 21, 2001	3	3	3	2	1	1		4	3	5	5	**25**
Jan 25, 2001	3	2	3	2	2	2		2				**16**
Jan 31, 2001	4	3		2	2	2	1	5	6			**25**
Feb 01, 2001	2	2		1	2	2		3	4			**16**
Total	**35**	**28**	**14**	**19**	**22**	**24**	**3**	**29**	**25**	**5**	**5**	**206**

Multiple fraction from the same fractionating collector have been counted as one sample

Table 3-2. Summary of weather conditions of all fog events.

Date	Wind Speed (m/s)	Temperature (°C)	Relative Humidity (%)
Dec 17, 2000	0.4	5.1	97
Dec 18, 2000	0.7	2.7	97
Jan 06, 2001	0.8	-1.7	85
Jan 10, 2001	1.5	1.7	95
Jan 15, 2001	1.0	2.6	89
Jan 17, 2001	0.7	0.2	92
Jan 21, 2001	1.9	3.0	94
Jan 25, 2001	0.5	2.9	94
Jan 31, 2001	0.8	4.9	94
Feb 01, 2001	1.1	2.0	92

For each fog event, the PVM recorded LWC (mg/m^3) and the total surface area of all drops (S, unit: cm^2/m^3). We can calculate the effective diameter (D_{eff}, unit: μm) from these data. The equation is as follows:

$$D_{eff} = 60 \times \frac{LWC}{S} \tag{3-1}$$

Figure 3-1 to Figure 3-5 shows effective diameter (D_{eff}), LWC profile of the fog events. Appendix-E also shows the other parameters including temperature and wind speed.

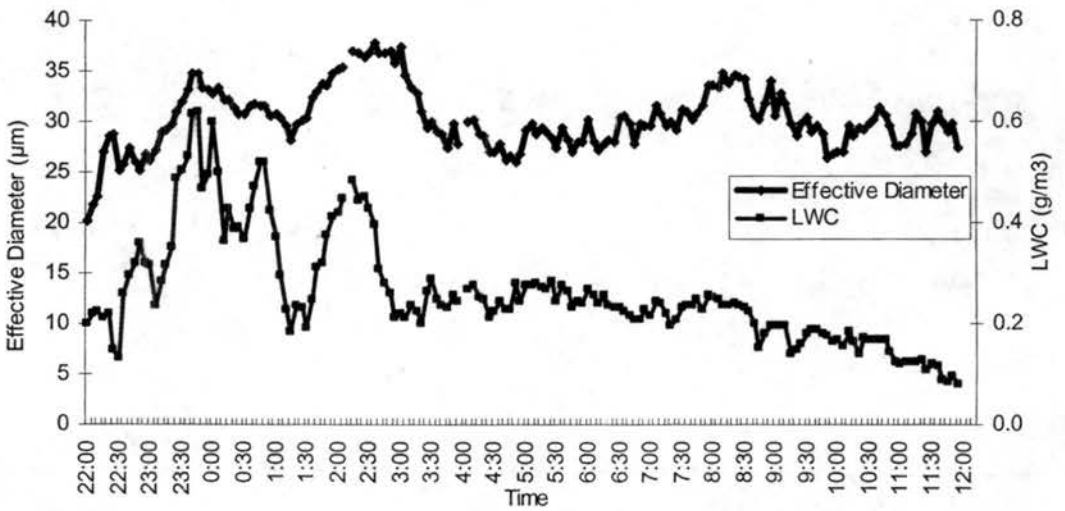

Figure 3-1. Effective Diameter and LWC measured by PVM on 12/17 &12/18/00.

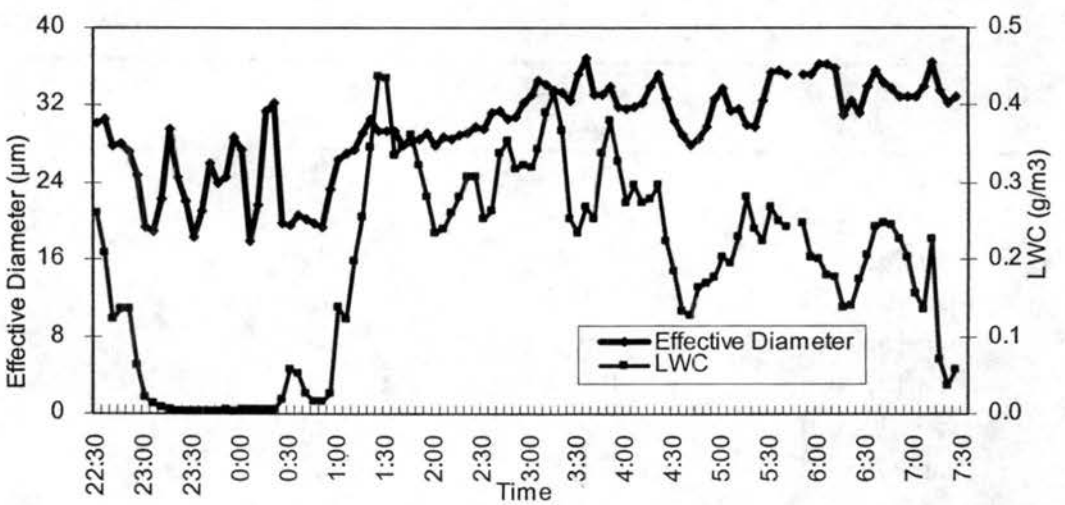

Figure 3-2. Effective diameter and LWC on 12/18 & 12/19/00.

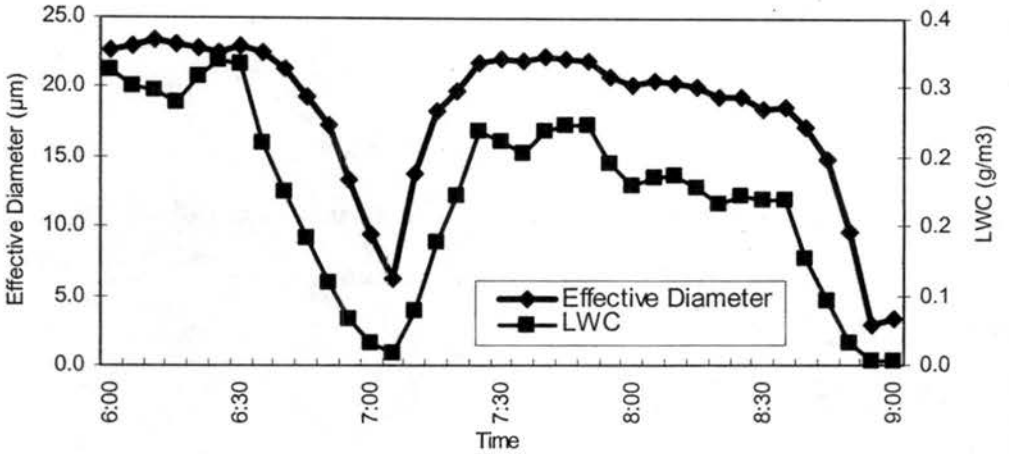

Figure 3-3. Effective Diameter and LWC on 01/21/00.

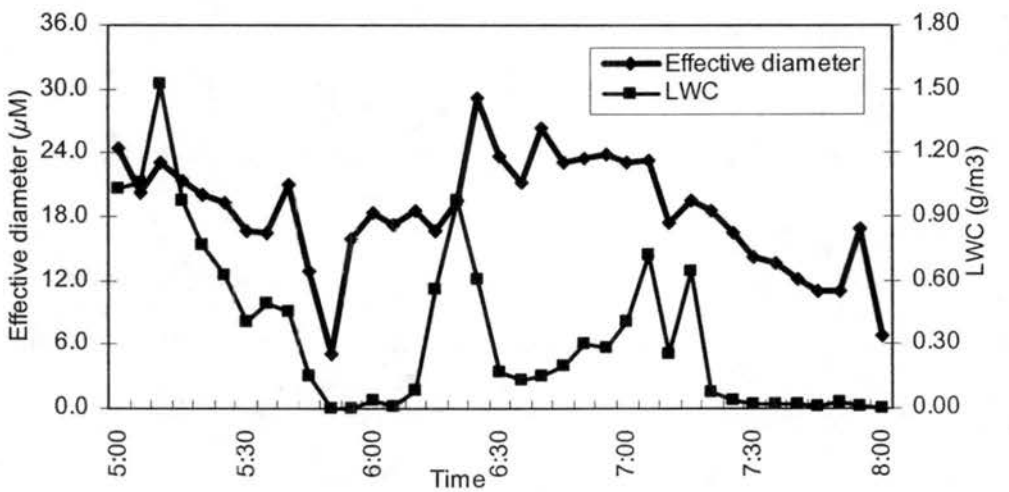

Figure 3-4. Effective diameter and LWC on 01/25/00.

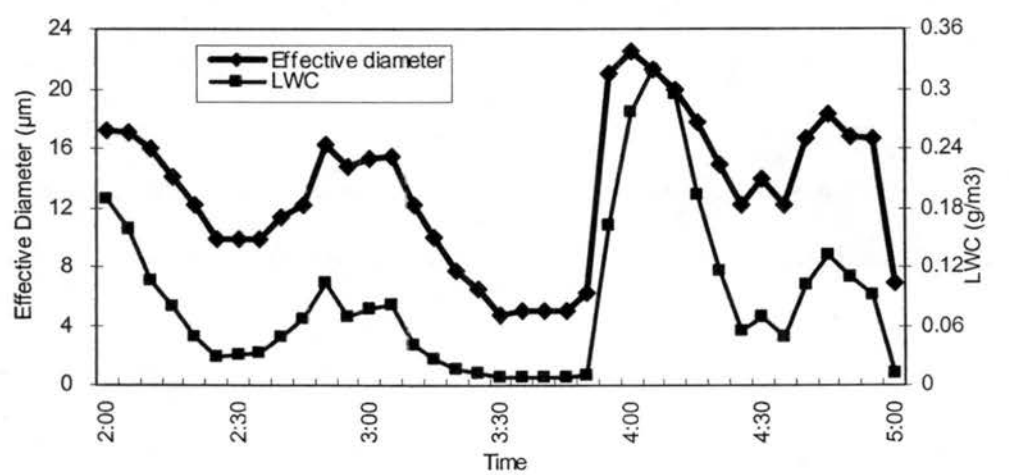

Figure 3-5. Effective diameter and LWC on 02/01/00.

3.3 Drop size distribution and evolution

The CSASP was used to measure the fog drop size distribution and its evolution in 20 bins, ranging from 5 μm to 47 μm. CSASP measures the distribution at one second interval and data are saved in files for further treatment.

3.3.1 Comparison between CSASP and PVM

Both PVM and CSASP can report LWC and effective diameter. As stated in chapter two, the intercomparisons are often very good, but large differences in ground-based LWC measurements made with the CSASP and PVM have also been observed (Wendisch 1998; Gerber et al., 1999). Therefore, an intercomparison of the data is necessary.

PVM can report LWC and particle surface area in two channels. CSASP reports absolute numbers of drops of each diameter and total sampling volume of air, then number concentrations of fog droplets in each diameter range can be calculated by dividing absolute numbers of drops by total sampling volume of air.

Figure 3-6 shows a timeline comparison of effective diameters of a fog event obtained from PVM and CSASP on 12/17 &12/18/00. The trend of these two timelines of effective diameter was similar, while we can see that PVM got larger effective diameters than CSASP. Figure 3-7 provides detailed view of comparison between these two effective diameters. The points are close to the 1:1 line, but a little bit close to PVM.

Figure 3-8 shows the LWC obtained from PVM and CSASP. We can see that LWC measurements showed a large difference. CSASP reported much higher LWC than PVM. In order to understand why CSASP tends to report higher LWC than PVM while size

distribution measurements are consistent with PVM, Appendix-B uses a 2-D model to simulate this process. CSASP is an active mode instruments. It uses a fan to make the air go through a horn-like tube, which acts like a flow regulator, then it uses a laser to measure the droplet size distribution, which is located at the center of the tube. Gerber et al. (1999) found that the inlet of CSASP can act as a "flow accelerator", thus can get large air flow rate than theory. This will over-calculate the flow rate and get larger sampling volume. Also, if the bigger droplets were to be accumulated to the center of sampling tube, it would cause CSASP to overestimate the LWC.

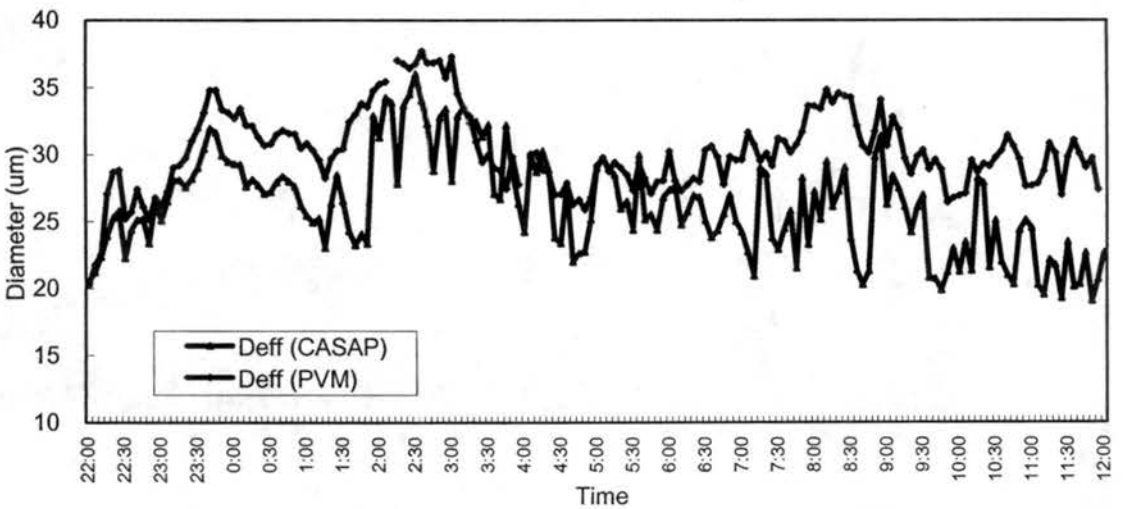

Figure 3-6. Comparison between effective diameters obtained from PVM and CSASP on 12/17 & 12/18/00.

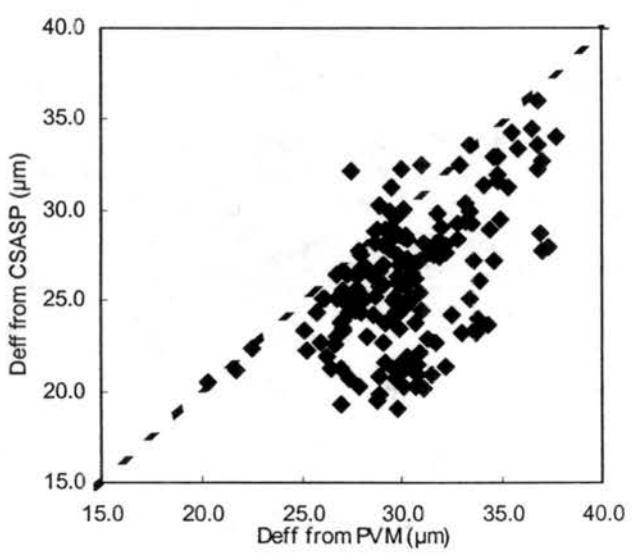

Figure 3-7. Comparison of effective diameter from PVM and CSASP of the fog event on 12/17 & 12/18/00.

Overall, For CRPAQS study the CSASP data cannot be used to calculate LWC, but its size distribution is good because (1) from the effective diameter data, we know that the fog droplets were not very big, within the measurement range of CSASP. (2) over-prediction of air flow rate/sampling volume would not affect size distribution. Therefore, we used PVM data to normalize CSASP data: first to get a correction factor using PVM LWC to divide by CSASP LWC, second to apply this correction factor to the number and mass concentrations obtained from CSASP.

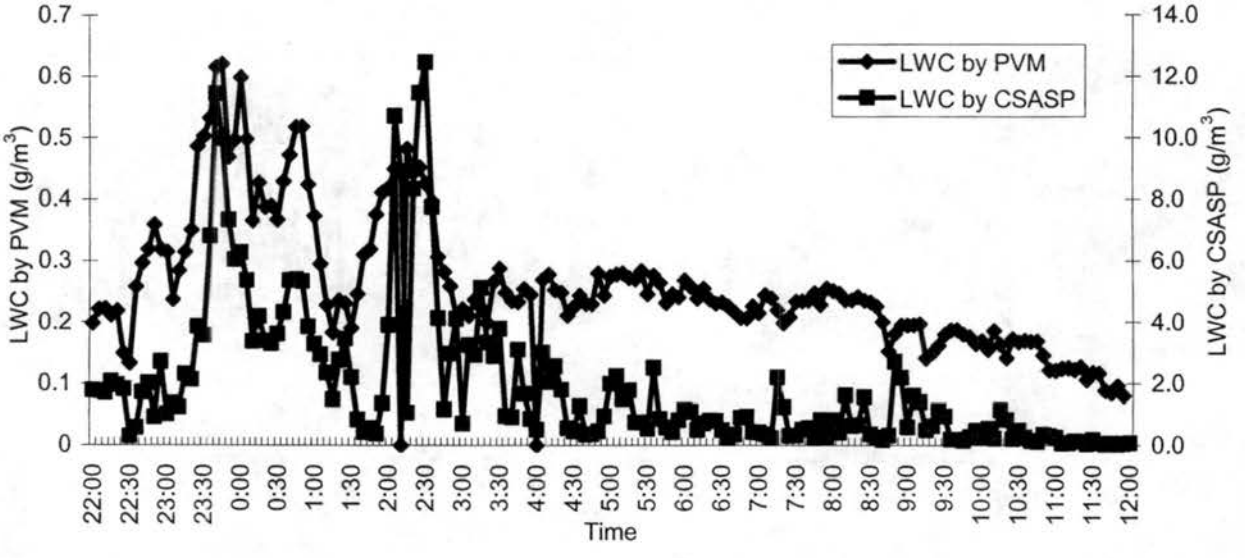

Figure 3-8. Comparison of LWC obtained by PVM and CSASP of the fog event on 12/17 & 12/18/00.

Figure 3-9 shows the fog drop size distribution evolution ($dN/dlogD_p$) with time on 12/18/00. The x axis is the time, averaged to one hour interval to have a simple but better view of the evolution of the size distribution. The y axis is the diameter ranges of the bins, from 5 μm to 47 μm. z axis is the number concentration.

This fog event started at 22:15pm, but we started CSASP at around 12:00am. After about two hours from the beginning of the fog event, fog droplets have a high number concentration with a monodisperse distribution, and the center of the peak was larger than

25 μm. With time passing by, the center of the peak shifted to the left with larger number concentration in smaller diameter range, also with the decrease of number concentration. This is because the radiation cooling effect on the top of the fog layer make the larger fog droplets grow faster by condensation, and thus leads to fast deposition of large fog droplets (Roach, 1976). Note that the absolute number concentration is less than the original distribution, implying that fog drops were depositing to the ground by wet deposition. After the first several hours, which was the fog developing stage, smaller aerosol particles then began to activate to form fog drops, thus having larger number concentrations of smaller drops than larger drops(a tail on the plots).

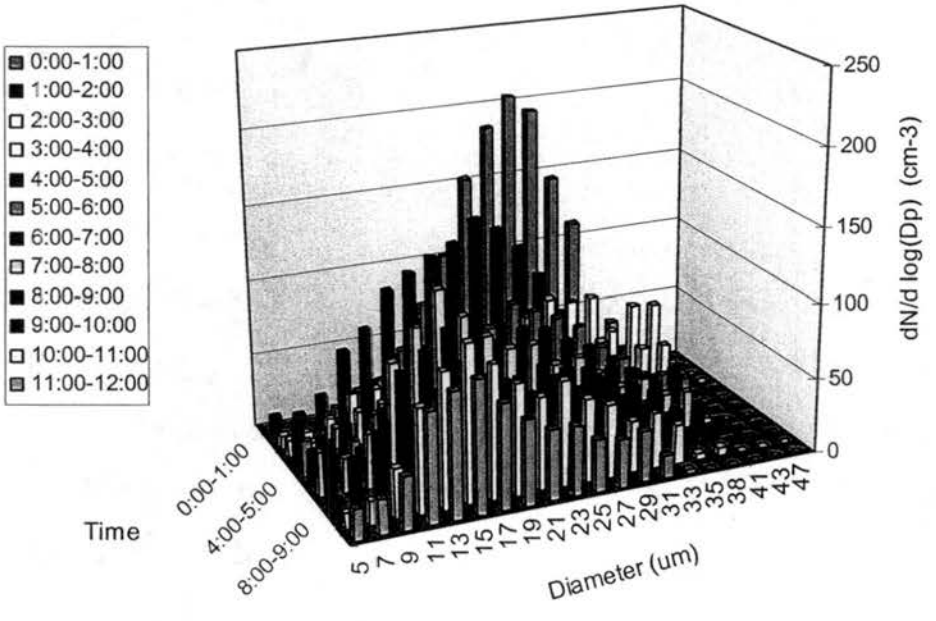

Figure 3-9. Drop size distribution evolution with time on 12/17 & 12/18/00.

3.4 Bulk composition

3.4.1 Components and concentrations

3.4.1.1 Major inorganic ions and pH

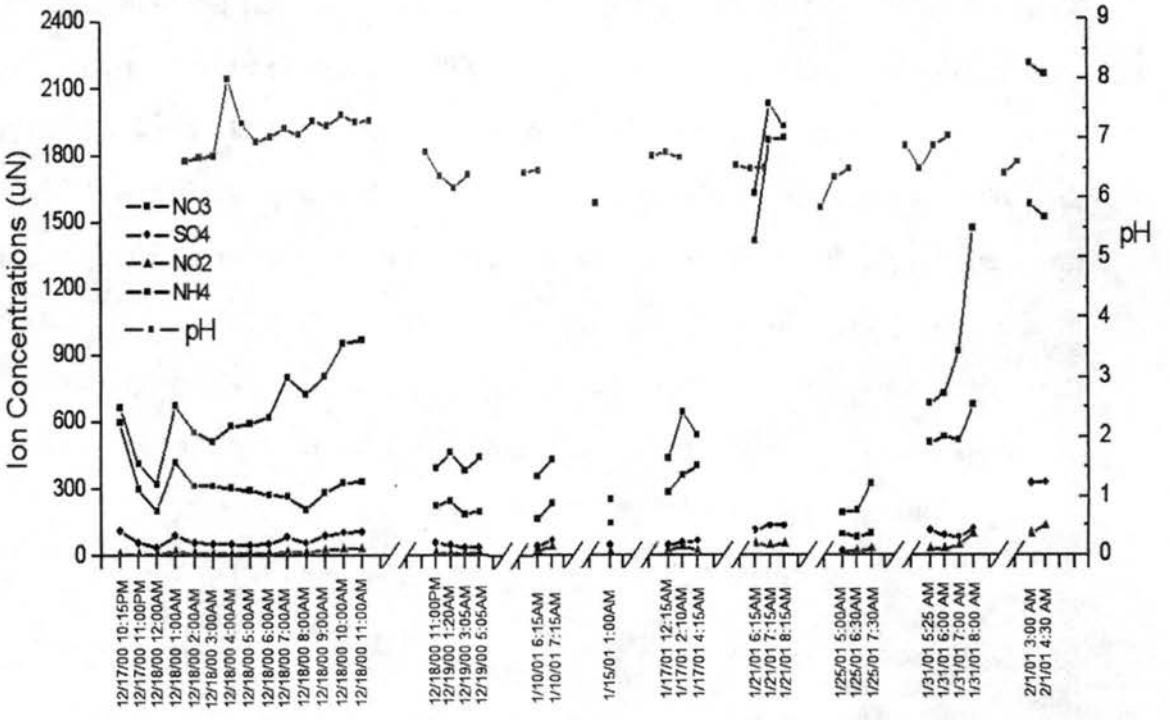

Figure 3-10. Timelines of three ion concentrations and pH in CASCC samples.

From past studies, we know that major inorganic ions in SJV fogs include ammonium, sulfate and nitrate. Figure 3-10 shows the timelines of pH value, these three major inorganic ions and nitrite concentrations for all the fog events in CASCC samples. Samples were plotted based on their sampling time. Figure 3-11 to Figure 3-16 shows the detail timelines of species in the sampling periods whose samples are more than two.

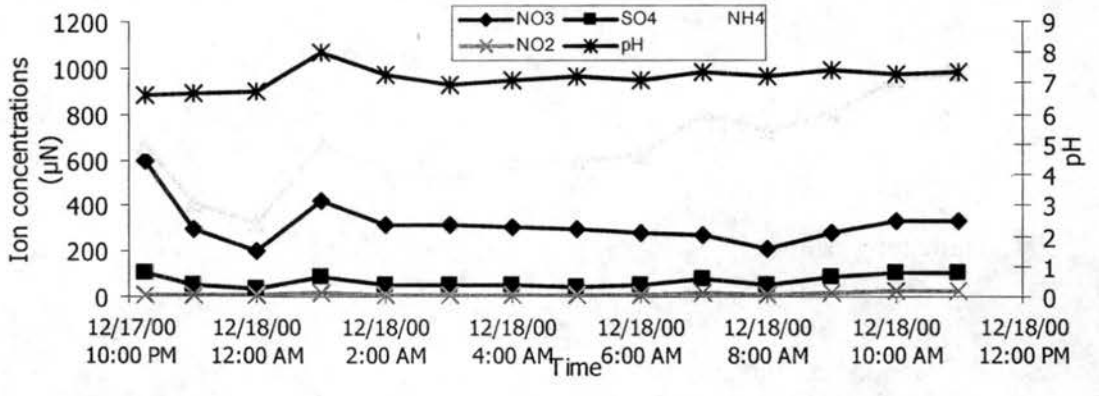

Figure 3-11. Timelines of three major ions, nitrite and pH in CASCC samples on 12/17/00&12/18/00 fog event.

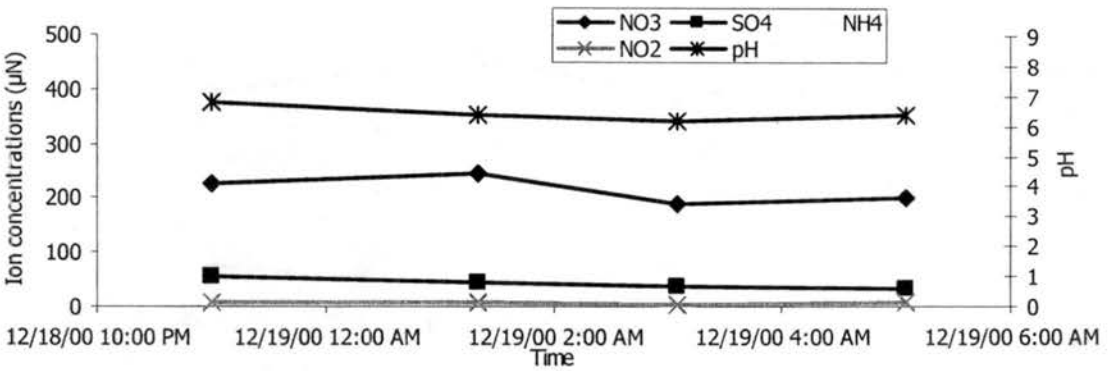

Figure 3-12. Timelines of three major ions, nitrite and pH in CASCC samples on 12/18/00&12/19/00 fog event.

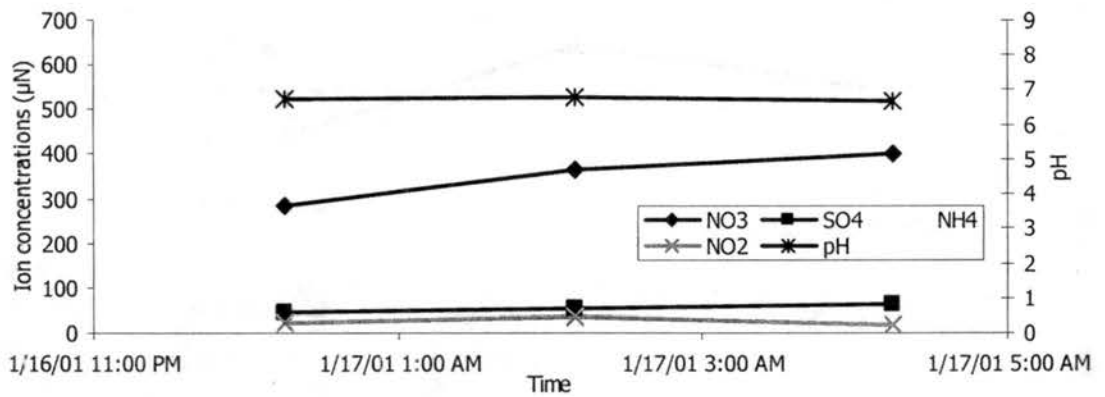

Figure 3-13. Timelines of three major ions, nitrite and pH in CASCC samples on 01/17/01.

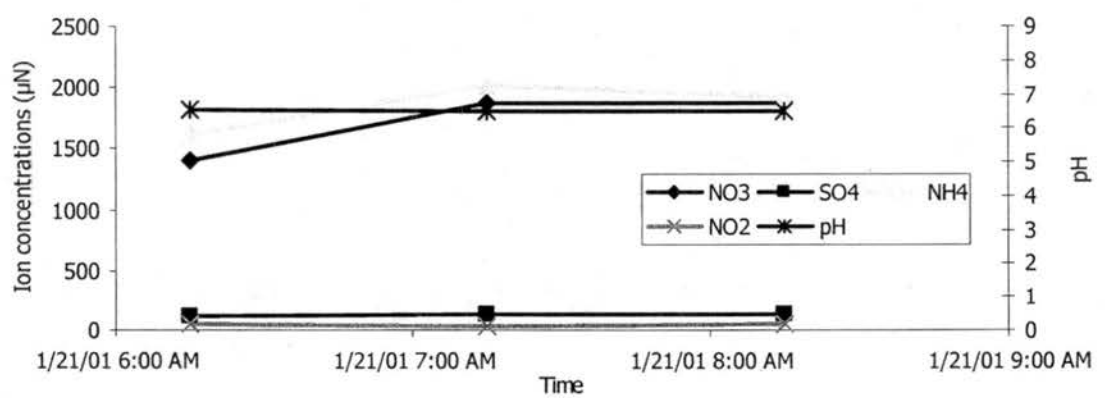

Figure 3-14. Timelines of three major ions, nitrite and pH in CASCC samples on 01/21/01.

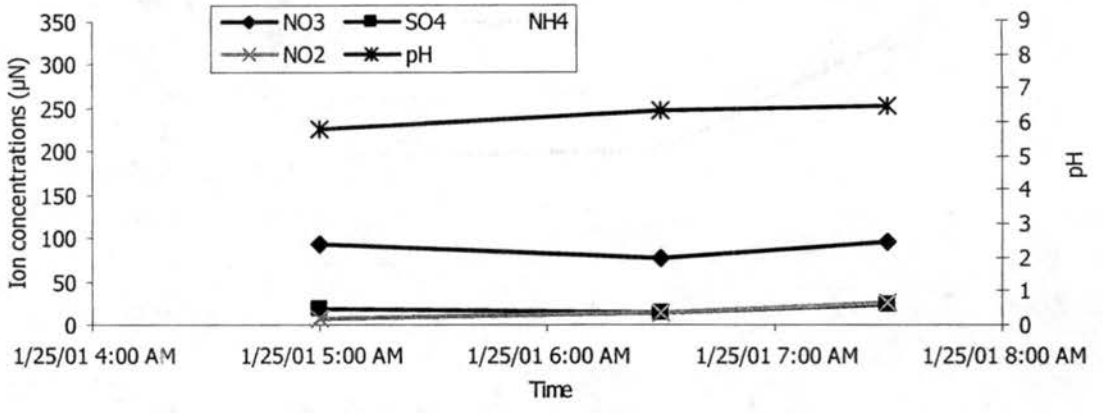

Figure 3-15. Timelines of three major ions, nitrite and pH in CASCC samples on 01/25/01.

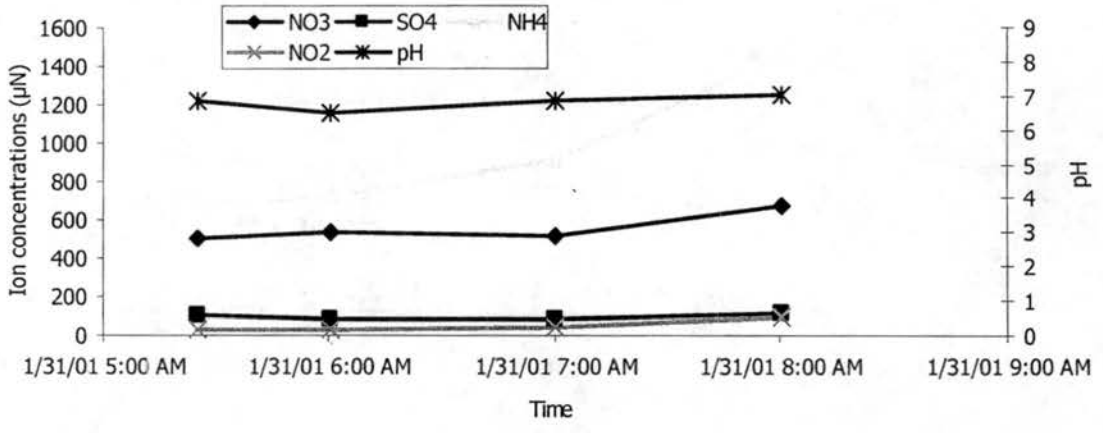

Figure 3-16. Timelines of three major ions, nitrite and pH in CASCC samples on 01/31/01.

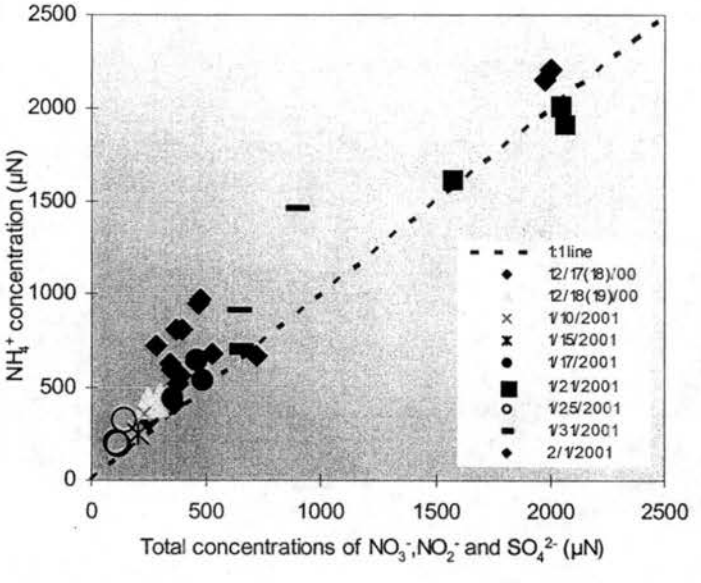

Figure 3- 17. Ammonium concentrations vs. total concentration of nitrate, sulfate and nitrite for all fog events.

The fog collected during CRPAQS was relatively alkaline, with the range of pH in the samples from 6.0 to 8.02, averaging 6.78. To understand this trend, we can take a look at the timelines of ammonium, nitrate and sulfate plotted in Figure 3-10, and also in Figure 3-17, which shows the ammonium concentration against total concentrations of nitrate, sulfate and nitrite. We can see that there were large amounts of ammonium in the fog drops, which can neutralize the acid species and make fog samples alkaline.

3.4.1.2 Organics

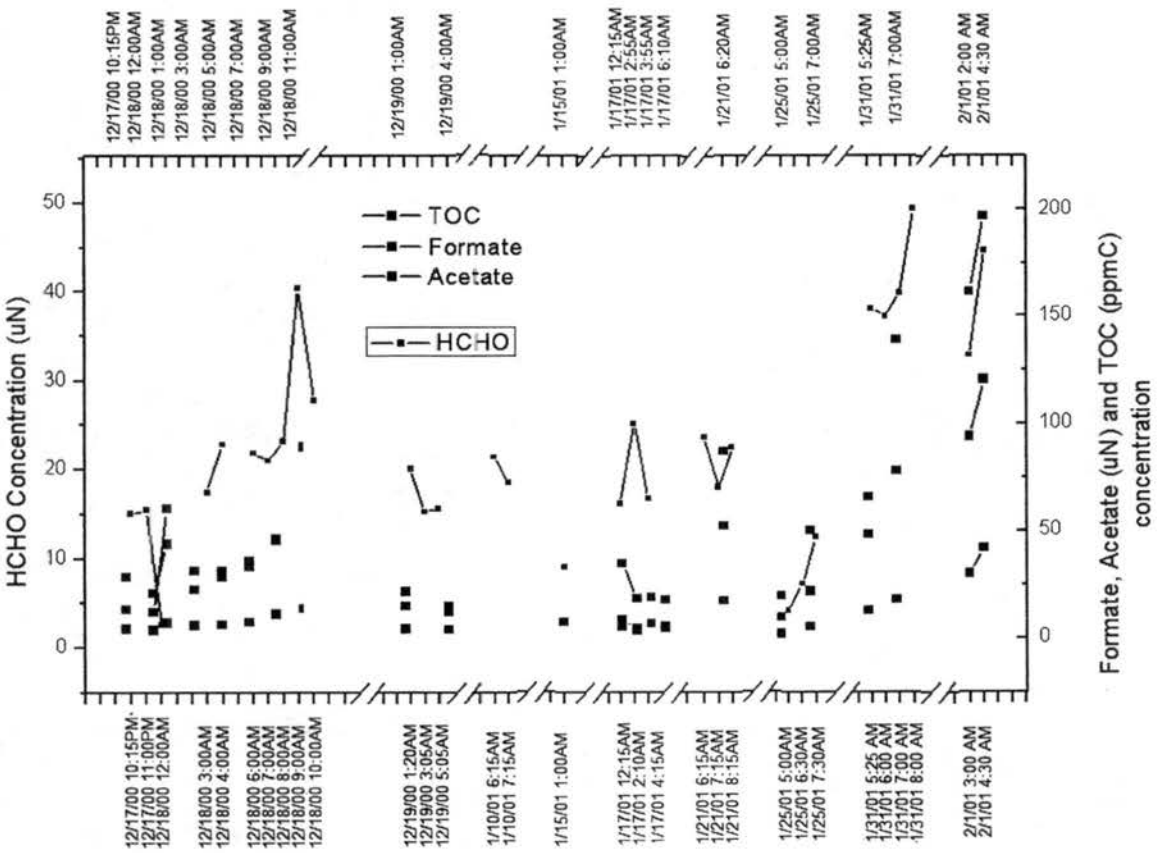

Figure 3-18. Timelines of formate, acetate, TOC and HCHO concentrations for all fog events. HCHO concentration was from CASCC collector, others are from the organic ss-CASCC collector.

Previous studies showed that formate and acetate are two dominant organic acid anions in fog drops. Formaldehyde is one of the dominant species in fog water as well. Figure 3-18 shows the timelines of formaldehyde, formate, acetate and total organic carbon (TOC) concentrations in fog samples. Figures 3-19 and 3-20 show the detail timelines on 12/17&18/00 and 01/17/01 fog events.

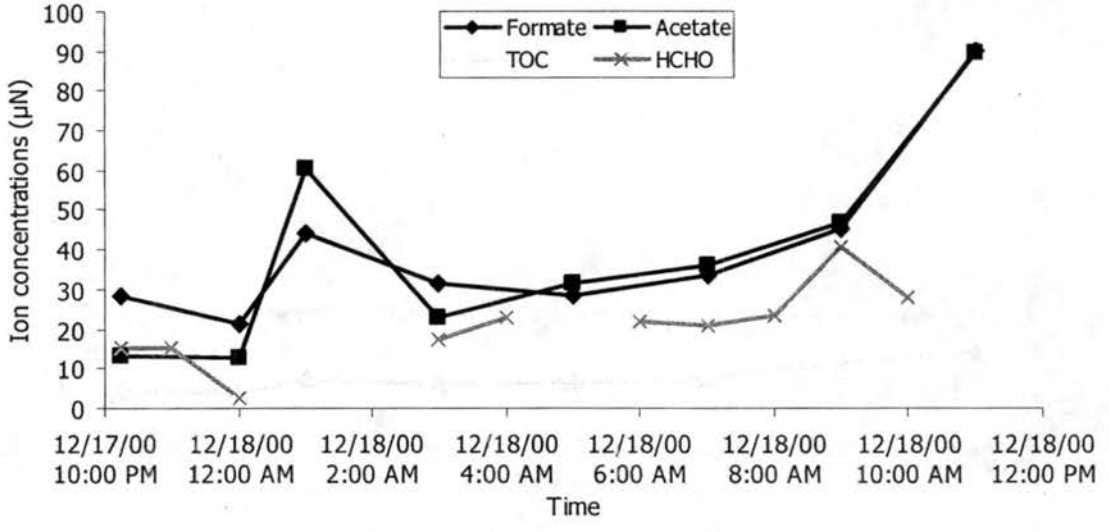

Figure 3-19 Timelines of formate, acetate, TOC and HCHO in CASCC samples in the 12/17&12/18/00 fog event

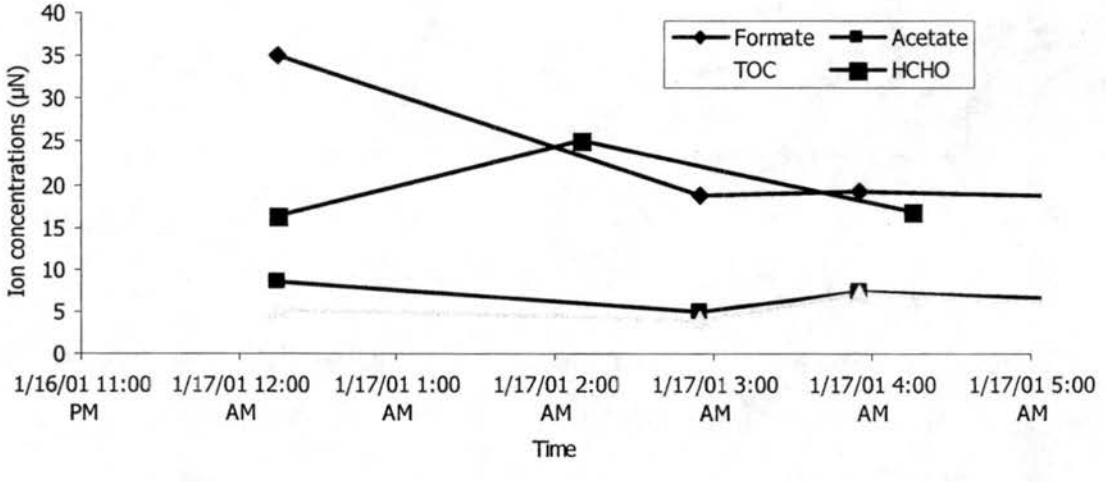

Figure 3-20. Timelines of formate, acetate, TOC and HCHO in CASCC samples on 01/17/01.

Formaldehyde concentrations range from 2.6 μN to 49.3 μN, averaging 22.4 μN; formate concentrations range from 14.9 μN to 120.7 μN, averaging 42.2 μN; acetate concentrations range from 5.0 μN to 197.8 μN, averaging 51.4 μN. TOC concentrations range from 2.3 ppmC to 41.9 ppmC, averaging 10.4 ppmC.

3.4.2 Average fog solute concentrations

Table 3-3. Volume-weighted average concentrations of solute species in all fog events.

Date	$[NO_3^-]$ (μN)	$[SO_4^{2-}]$ (μN)	$[NO_2^-]$ (μN)	$[NH_4^+]$ (μN)	[Formate] (μN)	[Acetate] (μN)	[Pyruvate] (μN)	[Oxalate] (μN)	TOC (ppmC)
12/18/00	308.0	62.5	9.9	597.5	33.7	32.6	0.0	7.0	6.6
12/19/00	210.6	38.2	6.3	426.2	19.0	14.3	0.0	6.6	4.4
1/10/01	181.3	43.4	--	374.7	--	--	--	--	--
1/15/01	145.9	44.5	--	250.7	--	--	--	--	--
1/17/01	348.1	54.6	6.6	499.1	23.0	6.7	0.0	7.3	5.1
1/21/01	1731.3	126.2	46.7	1879.8	52.6	87.2	0.0	11.4	17.7
1/25/01	85.7	15.9	15.6	214.3	20.7	24.3	0.0	1.2	3.3
1/31/01	555.7	97.6	53.8	922.3	64.6	106.2	0.0	8.4	15.9
2/1/01	1537.4	329.4	111.6	2173.0	103.6	174.4	0.2	21.5	34.4
Total Average	567.1	90.3	35.8	815.3	45.3	63.7	0.0	9.1	12.5

Date	$[Na^+]$ (μN)	$[Cl^-]$ (μN)	$[K^+]$ (μN)	$[Mg^{2+}]$ (μN)	$[Ca^{2+}]$ (μN)	Total [Fe] (μg/l)	Total [Mn] (μg/l)	H_2O_2 (ppbV)	S(IV) (μM)	HCHO (μN)
12/18/00	3.6	15.4	3.9	6.9	21.0	215.0	5.3	0.2	1.3	12.9
12/19/00	4.5	11.3	3.4	5.7	10.2	153.8	9.4	0.02	1.5	16.8
1/10/01	9.1	12.1	5.8	4.6	10.4	105.5	4.7	0.1	5.9	20.8
1/15/01	10.6	17.7	3.2	4.4	5.8	16.9	0.9	0.01	--	9.1
1/17/01	3.1	15.7	5.3	4.8	12.3	50.7	2.5	0.2	3.2	16.8
1/21/01	4.8	19.0	11.8	5.9	15.2	168.1	7.2	0.0	5.2	20.8
1/25/01	14.9	20.0	2.3	5.6	7.2	50.1	2.9	0.1	0.4	6.7
1/31/01	9.3	21.5	5.8	5.3	7.1	64.2	3.2	0.1	3.0	40.7
2/1/01	16.8	39.5	17.2	8.1	32.5	325.6	16.0	N/A	4.9	40.4
Total Average	8.5	19.1	6.5	5.7	13.5	127.8	5.8	0.1	3.2	20.6

-- means the concentrations were below detection limits or not detected

Table 3-3 lists the volume-weighted average concentrations of major ions and species for all the CRPAQS Angiola fog events. The concentrations of species for each fog episode were normalized by the sample weight of all samples (CASCC fog samples were used to calculate the concentrations of inorganic species, while ss-CASCC samples were used to calculate the concentrations of organic species), then a total average

concentrations of species were obtained by averaging the mass weighted concentration over all the fog events.

Table 3-4 Summary of bulk fog sample composition

Species	Number of samples	Concentration Range	Median
pH (pH units)	36	5.85-8.04	6.73
Cl- (μN)	36	10.5-39.8	16.3
NO_3^- (μN)	36	78.1-1872.1	303.5
NO_2^- (μN)	36	4.7-131.9	17.7
SO_4^{2-} (μN)	36	12.9-329.5	56.5
Formate (μN)	22	14.9-120.7	31.6
Acetate (μN)	22	5.0-197.2	31.4
Propionate (μN)	22	ND[a]-10.4	1.7
Pyruvate (μN)	22	ND-0.7	0.7
Oxalate (μN)	22	3.2-24.9	7.2
Na^+ (μN)	36	0.13-22.5	5.8
K^+ (μN)	36	1.9-18.6	4.3
NH_4^+ (μN)	36	193.2-2203.7	608.3
Mg^{2+} (μN)	36	4.2-24.8	5.3
Ca^{2+} (μN)	36	5.6-101.5	10.7
HCHO (μM)	36	2.6-49.3	21
Fe ($\mu g\ l^{-1}$)	24	16.9-341.9	77.5
Mn ($\mu g\ l^{-1}$)	24	0.9-16.5	4.1
TOC (ppmC)	22	2.3-41.9	6.9

ND[a] Not detected- the response was below the detection limit for this species.

Similar to Table 3-3, Table 3-4 shows the concentration ranges of all measured species in bulk fog samples collected at Angiola. It shows that species with the highest concentrations include ammonium, nitrate, sulfate, nitrite, formate, acetate and formaldehyde.

Based on Table 3-3, Figure 3-21 shows the pie diagram of average sample

composition for the SJV fogs. The dominant species measured were ammonium, nitrate, nitrite, sulfate, formate, acetate, consistent with former studies in the SJV. The ammonium concentration is comparable with the average measured in fog samples collected in the 1995 Integrated Monitoring Study (IMS95), 815 μN vs. 1087 μN. Average nitrate concentration is about six times higher than the sulfate concentration, also consistent with IMS95 observations.

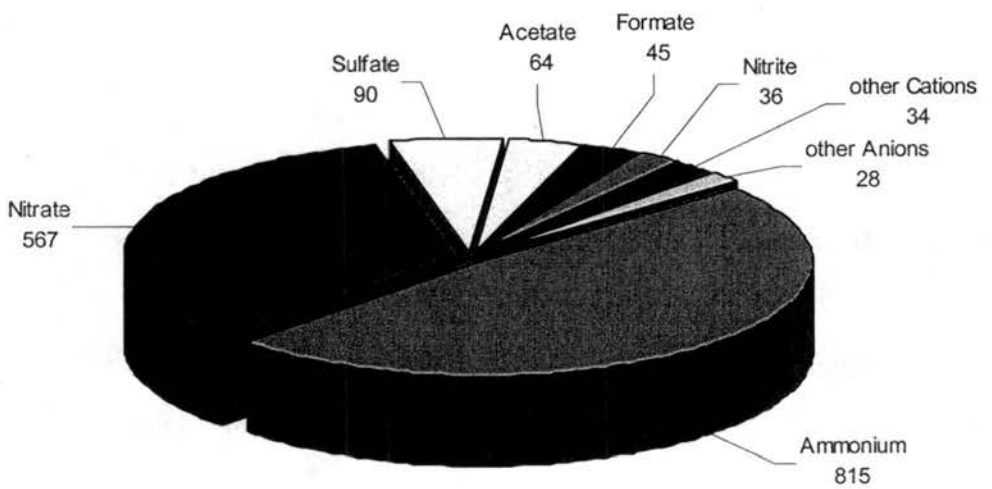

Figure 3-21. Measured composition for fog episodes during winter 2000/2001. All concentrations are listed as μN. Other cations include sodium, potasium, calcium, magnesium and H^+. Other anions include chloride, propionate, pyruvate and oxalate.

From Table 3-3 and Figure 3-21, we can roughly calculate the charge balance for each episode and the total balance for all fog events in SJV. A liquid solution should be electrically neutral, with the positive and negative charged ions balanced. For our fog samples, the electrical balance equation is roughly as follows (concentration unit: μN):

$$[H^+]+[NH_4^+]=[OH^-]+[NO_3^-]+[SO_4^{2-}]+[NO_2^-]+[Formate]+[Acetate] \quad . \quad (3\text{-}2)$$

Here, we assume the fog water solutions were carbon dioxide balanced but ignore this

term in the equation. Also, because formate and acetate are weak organic acids (formic acid pKa=3.75; acetic acid pKa = 4.75), they will not be fully ionized at a lower pH environment. For our samples since the pH value ranges from 6.0 to 8.02, averaging 6.78, the portion of unionized form of formate and acetate is very small thus can be ignored in the charge balance equation.

Taking account of the major anions (nitrate, sulfate, nitrite, formate, acetate and other anions) and major cations (ammonium and hydrogen concentrations), Figure 3-22 shows the comparison of total cation concentrations vs. total anion concentrations in the fog water. Total cation concentrations were slightly higher than total anion concentrations, possibly because there are other anions such as organic acids that were not counted in the equation. Overall, cation concentrations were only about 8% higher than anion concentrations, while the preferred range of anions/cations is 80~120%, suggesting that all charged species were reasonably measured given the uncertainty.

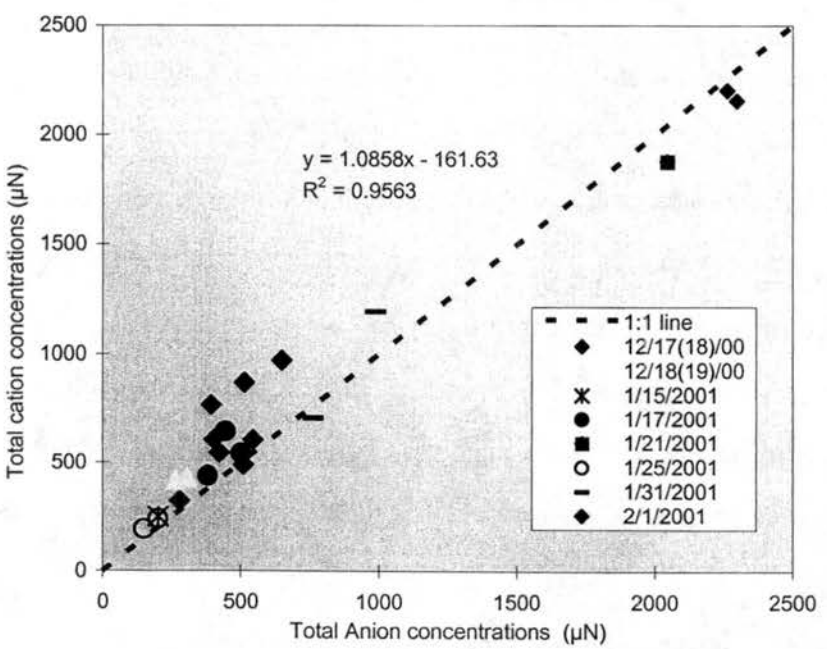

Figure 3-22. Total cation concentrations vs. total anion concentrations.

3.5 Size dependent compositions

3.5.1 pH and inorganic species

Figure 3-23 to Figure 3-34 plot the large vs. small pH and drop concentrations of inorganic species including Cl^- , NO_3^-, SO_4^{2-}, NH_4^+, Na^+, K^+, Mg^{2+}, Ca^{2+}, Fe, Mn and NO_2^- for all fog events. Samples were collected with 2-stage sf-CASCC. Figure 3-35 to Figure 3-40 show the large vs. small drop concentrations of organic species including HCHO, TOC, formate, acetate, propionate and oxalate for all fog events. Samples for organic analysis were collected by ss-sf-CASCC. Different fog events were shown as different colors. An error bar is plotted based on the analytical RSD of each species reported in chapter two.

From Figure 3-10, the timeline of pH values in the fog events, we know that pH values were a little bit alkaline (relative to equilibrium of CO_2, which is about 5.6), and unlike previous studies (Moore et al., 2000), which is in an urban area, our pH values of large and small droplets didn't show significant difference.

For inorganic species, significant chemical concentration differences were seen between large and small drop fractions. Chloride, ammonium, sulfate, nitrate, potassium, manganese, calcium and TOC were all enriched in smaller drops; total Fe and Mn showed no preference of enrichment; nitrite was enriched in larger drops. This size dependence is consistent with patterns observed previously in SJV fogs (Collett et al., 1999).

For organic species, formic acid showed a weak trend of enrichment in small drops. Formic acid enriched in small drops in most samples, but enrich in large drops in some samples as well. Acetic acid shows the same trend as formic acid. Propionate didn't show any preferred size distribution. It is almost evenly distributed along the 1:1 line with no

significant enrichment in large and small drops. Oxalate is the only di-acid that we measured, and shows very strong enrichment in small drops.

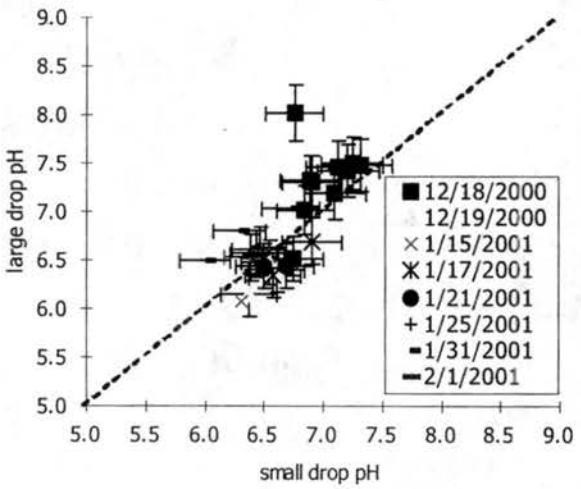

Figure 3-23. Large vs. small pH for all fog events of CRPAQS. Error bars represent analytical RSD listed in chapter two.

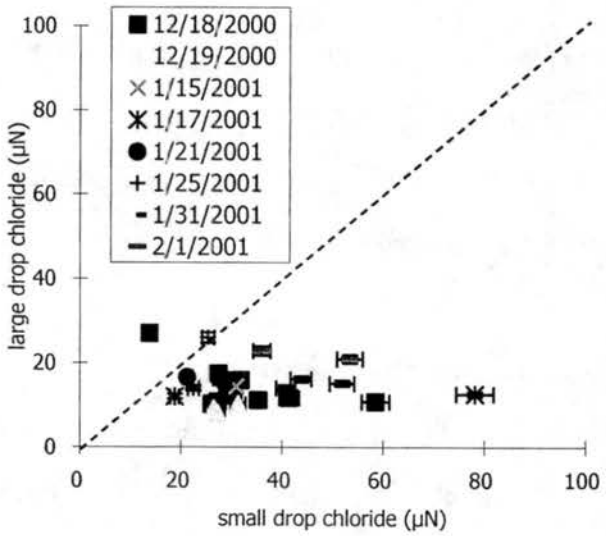

Figure 3-24. Large vs. small Cl^- concentrations for all fog events of CRPAQS. Error bars represent analytical RSD listed in chapter two.

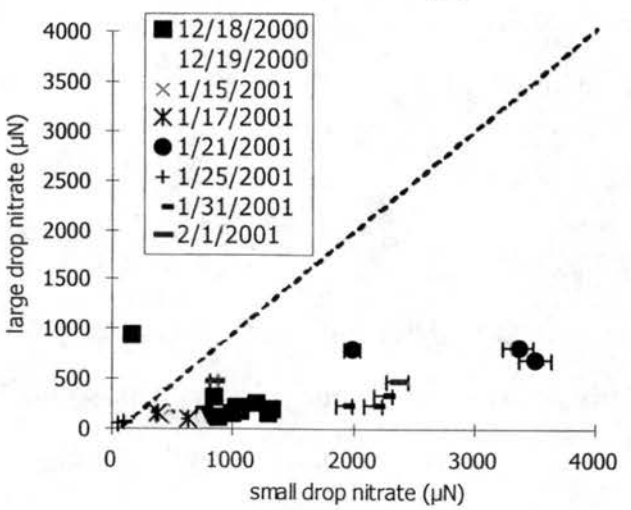

Figure 3-25. Large vs. small NO_3^- concentrations for all fog events of CRPAQS. Error bars represent analytical RSD listed in chapter two.

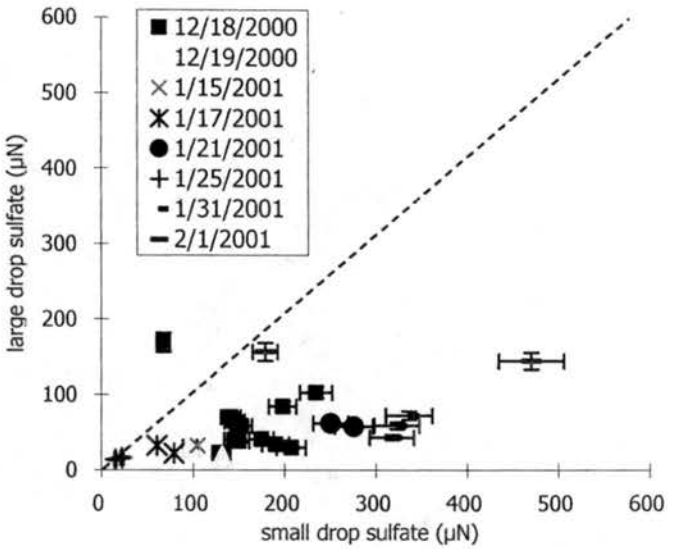

Figure 3-26. Large vs. small SO_4^{2-} concentrations for all fog events of CRPAQS. Error bars represent analytical RSD listed in chapter two.

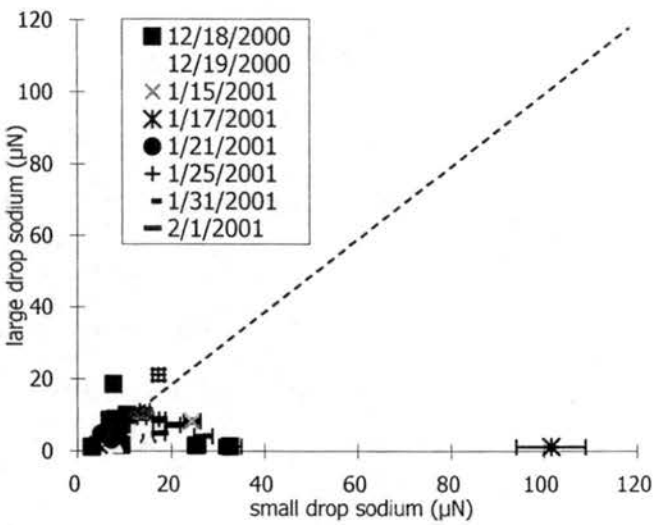

Figure 3-27. Large vs. small Na^+ concentrations for all fog events of CRPAQS. Error bars represent analytical RSD listed in chapter two.

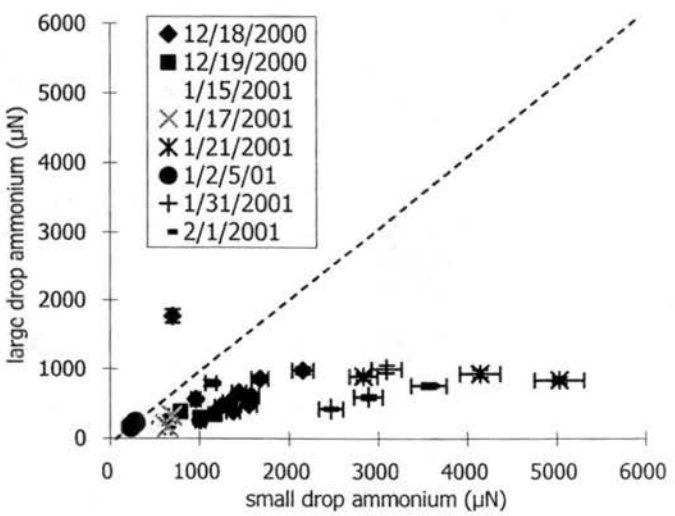

Figure 3-28. Large vs. small NH_4^+ concentrations for all fog events of CRPAQS. Error bars represent analytical RSD listed in chapter two.

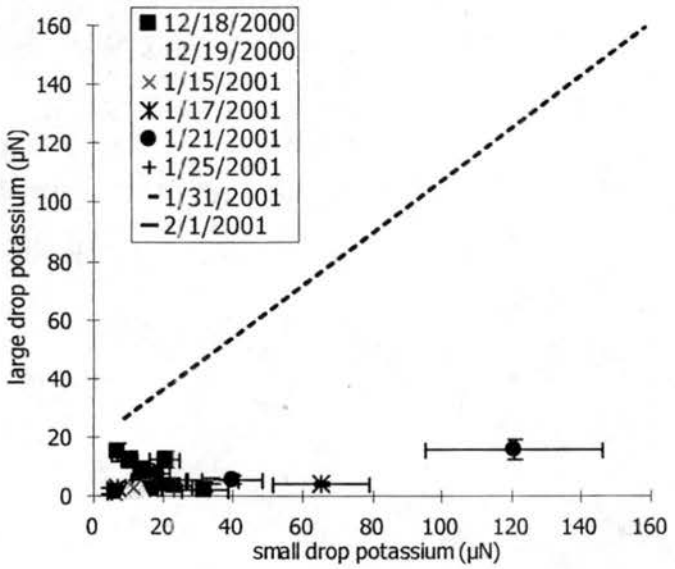

Figure 3-29. Large vs. small K^+ concentrations for all fog events of CRPAQS. Error bars represent analytical RSD listed in chapter two.

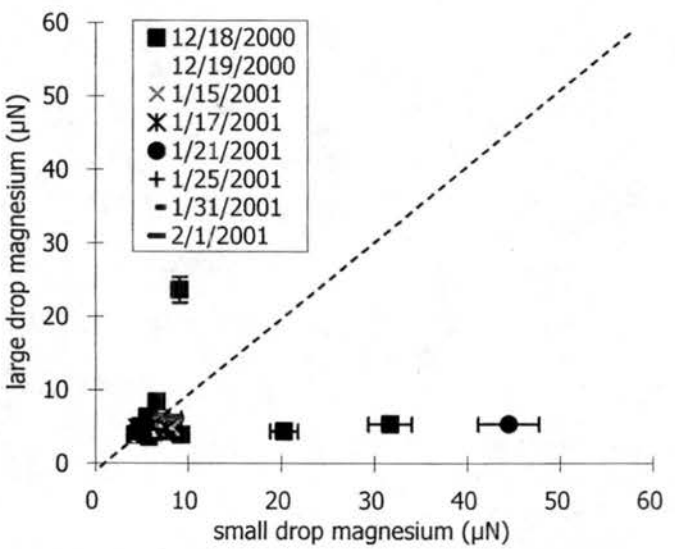

Figure 3-30. Large vs. small Mg^{2+} concentrations for all fog events of CRPAQS. Error bars represent analytical RSD listed in chapter two.

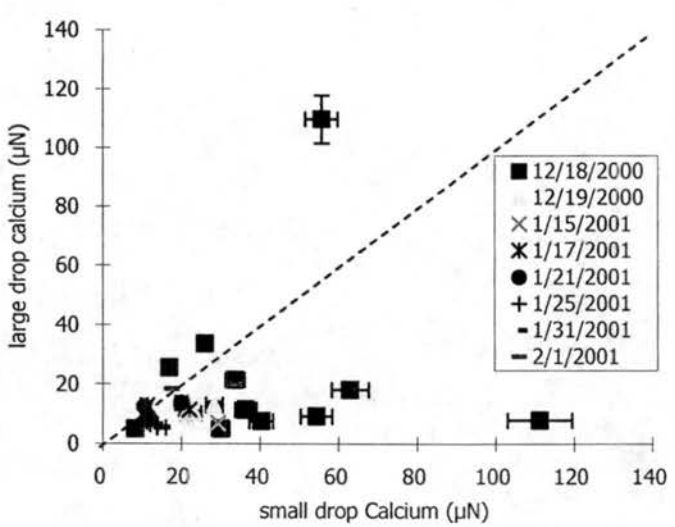

Figure 3-31. Large vs. small Ca^{2+} concentrations for all fog events of CRPAQS. Error bars represent analytical RSD listed in chapter two.

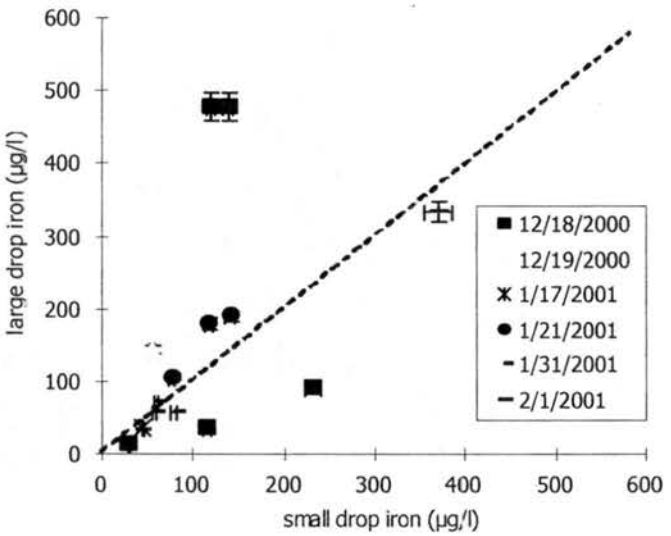

Figure 3-32. Large vs. small total Fe concentrations for all fog events of CRPAQS. Error bars represent analytical RSD listed in chapter two.

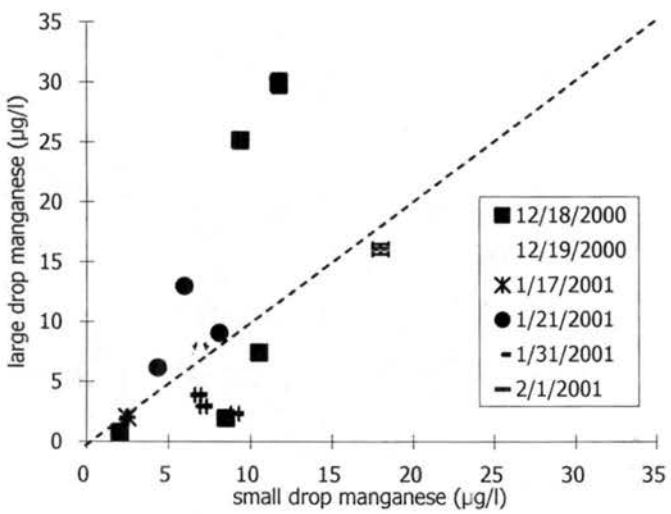

Figure 3-33. Large vs. small total Mn concentrations for all fog events of CRPAQS. Error bars represent analytical RSD listed in chapter two.

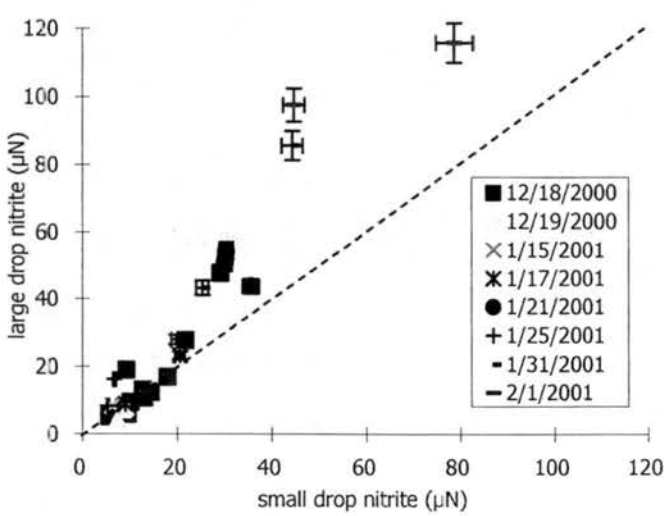

Figure 3-34. Large vs. small NO_2^- concentrations for all fog events of CRPAQS. Error bars represent analytical RSD listed in chapter two.

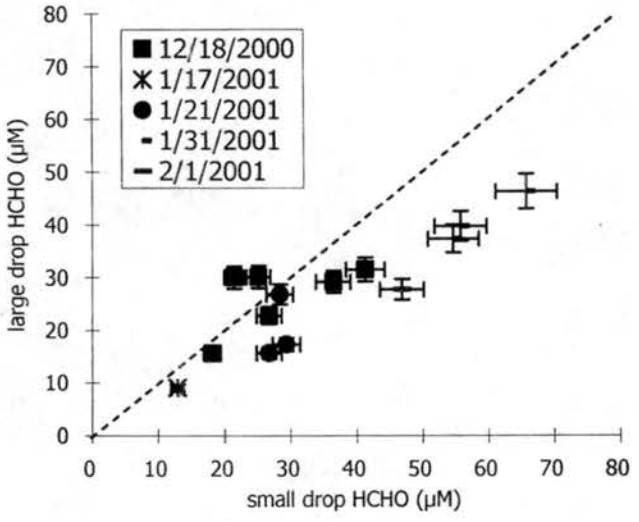

Figure 3-35. Large vs. small HCHO concentrations for all fog events of CRPAQS. Error bars represent analytical RSD listed in chapter two.

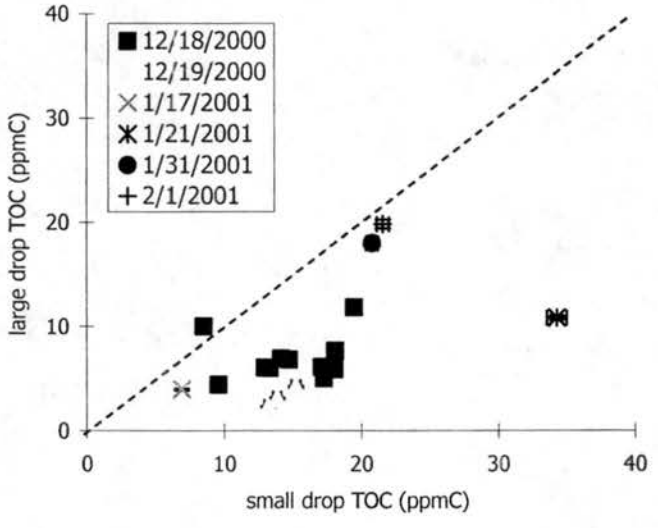

Figure 3-36. Large vs. small TOC concentrations for all fog events of CRPAQS. Error bars represent analytical RSD listed in chapter two.

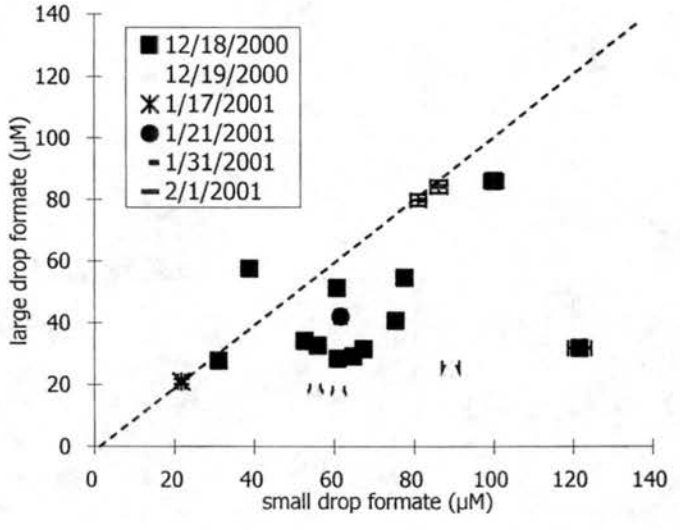

Figure 3-37. Large vs. small formate concentrations for all fog events of CRPAQS. Error bars represent analytical RSD listed in chapter two.

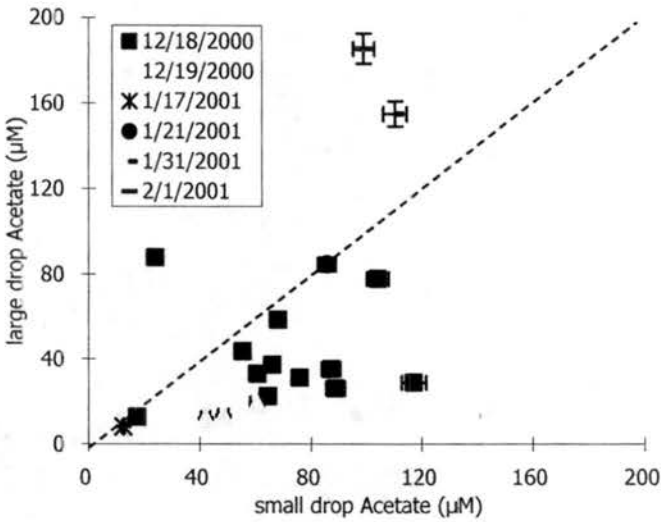

Figure 3-38. Large vs. small acetate concentrations for all fog events of CRPAQS. Error bars represent analytical RSD listed in chapter two.

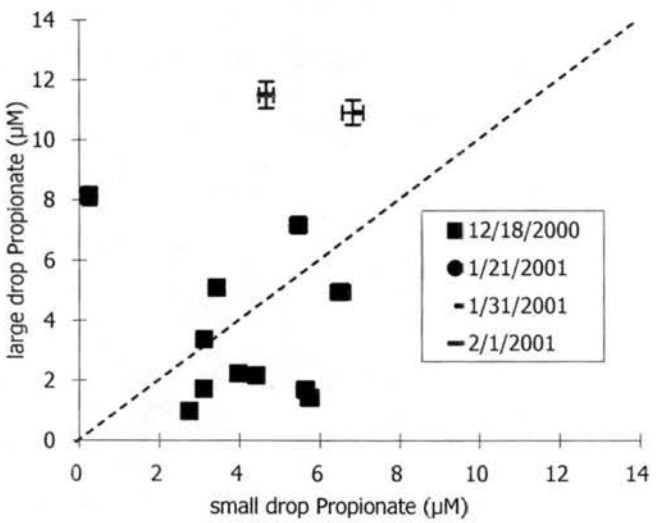

Figure 3-39. Large vs. small propionate concentrations for all fog events of CRPAQS. Error bars represent analytical RSD listed in chapter two.

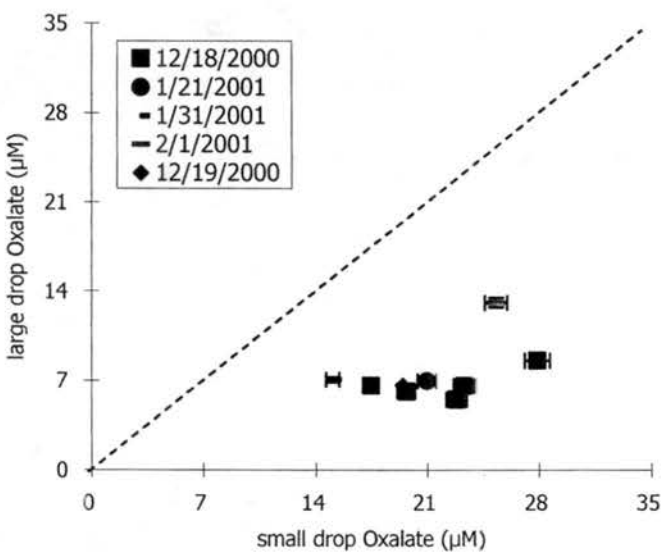

Figure 3-40. Large vs. small oxalate concentrations for all fog events of CRPAQS. Error bars represent analytical RSD listed in chapter two.

3.5.2 Size distribution of CSU 5-stage collector

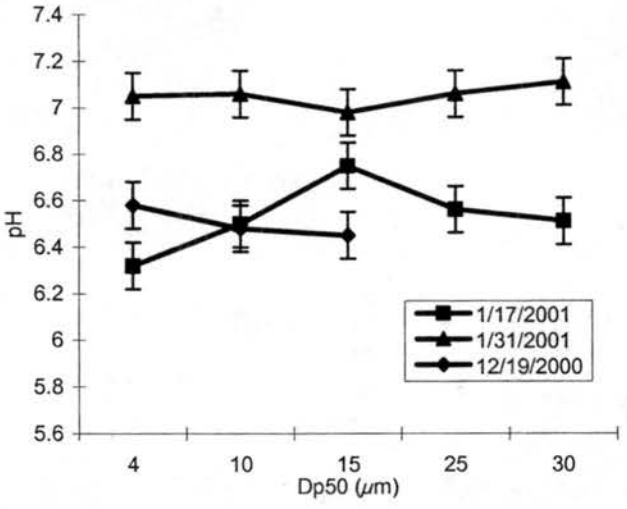

Figure 3-41. pH value vs. theoretical Dp50 of 5-stage collector.

The CSU 5-stage collector was used to get more detail size distribution information of fog droplets. Figure 3-41 shows pH value size distribution from the 5 stage collector for samples collected in the events of 12/18&12/19/00, 01/17/01 and 01/31/01 respectively. The pH values ranges from 6.32 to 7.11, averaging 6.7 for these three events, which is consistent with bulk fog samples pH values. For fog events 12/19/00 and 1/31/01, we don't see significant difference which is over the pH measurement uncertainties (±0.1). but for event on 1/17/2001, the pH value of Dp = 15 μm is slightly higher than others drop sizes. Figure 3-42 to 3-44 shows ammonium nitrate, nitrite and sulfate concentrations for the same three fog events. Ammonium and nitrate concentrations showed very strong size dependence, sulfate also had size difference between large and small drops. Nitrite showed less tendency of size dependence than the other three ions, which is consistent with the results of 2 stage sf-CASCC collectors.

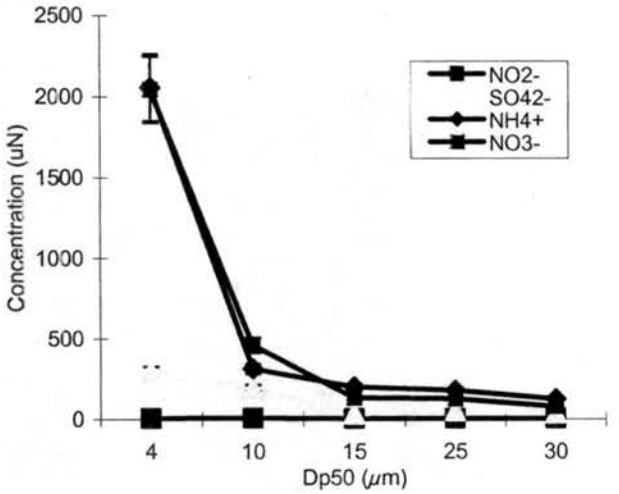

Figure 3-42. Major ion concentrations vs. theoretical Dp50 of 5-stage collector on day 01/17/01.

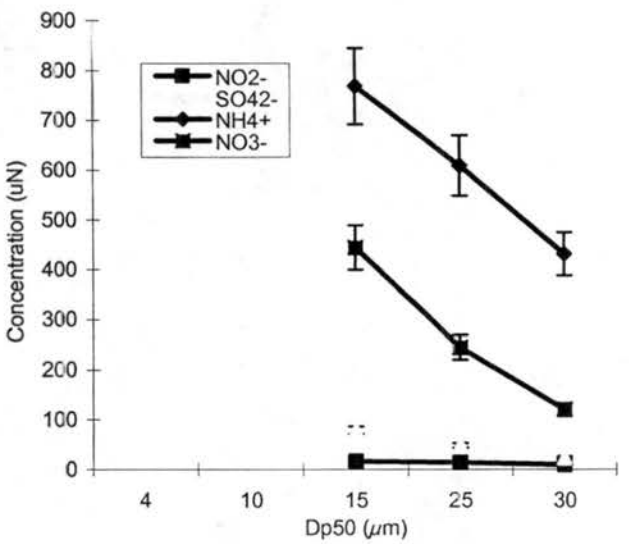

Figure 3- 43. Major ion concentrations vs. theoretical Dp50 of 5-stage collector on day 12/19/00.

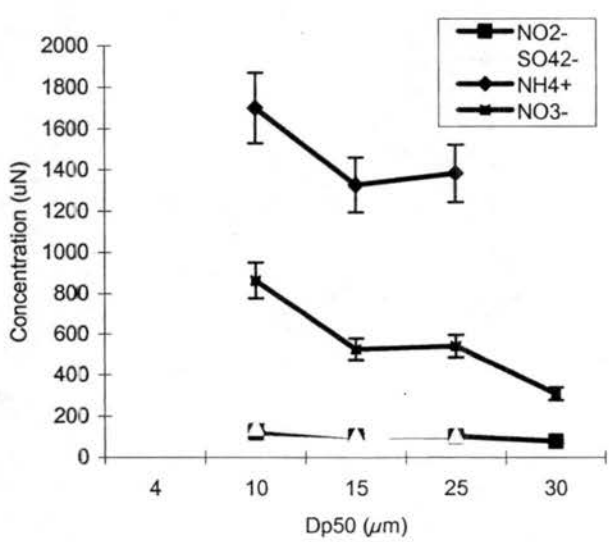

Figure 3-44. Major ion concentrations vs. theoretical Dp50 of 5-stage collector on day 01/31/01.

Chapter 4

Aerosol processing and removal by fogs

4.1 Overview

Fog scavenging of both particles and soluble gases followed by deposition of fog droplets can be an important wet removal process of air pollutants and other atmospheric species (Collett et al., 2001). Sedimentation dominates drop removal in low wind speed radiation fogs over smooth surfaces (Dollard et al., 1983; Fitzjarrald et al., 1986; Eugster et al., 2001), while impaction and interception can be quite important for capture of fog drops by forest canopies and grasslands (Eugster et al., 2001; Wrzesinsky et al., 2001). Formal studies shows that enhanced aerosol deposition in fogs efficiently limits pollutant accumulation during stagnation episodes; this limitation and even reductions have been attributed, at least in part, to removal of scavenged aerosols by deposition of fog drops (Jacob et al., 1984; Jacob et al., 1986; Waldman et al., 1987; Forkel et al., 1990; Pandis et al., 1992; Lillis et al., 1999).

In order to evaluate the role SJV radiation fogs played in pollutant removal during the CRPAQS study, several deposition measurements were made. The purposes of this study were to (1) evaluate the suitability and compare the consistency of several fog deposition measurement methods. (2) observe and evaluate the impacts of different underlaying surfaces. (3) characterize individual species deposition fluxes and velocities, and (4) examine the relationship between deposition velocity of an individual chemical species and its distribution across the fog drop size spectrum. We discuss the findings of these measurements here. The measurement methods were previously described in Chapter 2.

Table 4-1. Deposited fog water mass, ion and TOC concentrations observed on the two deposition plates

Sample Start Date	Sample Start Time	Sample End Time	Fog water (g)		Cl^- (μN)		NO_3^- (μN)		NO_2^- (μN)		SO_4^{2-} (μN)		Na^+ (μN)		NH_4^+ (μN)		K^+ (μN)		Mg^{2+} (μN)		Ca^{2+} (μN)		TOC (ppmC)	
			Dplate 1	Dplate 2	Dplate 1	Dplate 2	Dplate 1	Dplate 2	Dplate 1	Dplate 2	Dplate 1	Dplate 2	Dplate 1	Dplate 2	Dplate 1	Dplate 2	Dplate 1	Dplate 2	Dplate 1	Dplate 2	Dplate 1	Dplate 2	Dplate 1	Dplate 2
12/17/2000	11:00 PM	1:00 AM	9.28	8.39	--	17.2	--	167	--	8.81	--	35.1	--	8.52	--	452	--	5.68	--	6.51	--	35.7	4.31	--
12/18/2000	1:00 AM	3:10 AM	17.4	16.8	18.4	17.3	176	169	11.5	11.8	40.8	38.9	10.0	10.0	485	502	8.24	8.04	8.83	9.64	48.9	60.2	4.79	4.25
12/18/2000	3:10 AM	6:10 AM	33.1	--	15.5	13.7	158	160	8.55	9.20	31.4	32.6	4.96	3.82	520	526	6.12	4.71	5.98	6.38	18.8	29.1	3.18	--
12/18/2000	6:10 AM	8:15 AM	19.5	19.2	20.1	20.5	129	138	11.3	13.0	63.1	66.6	23.4	22.7	759	768	5.18	5.11	6.20	5.55	20.7	23.9	3.65	3.84
12/18/2000	8:15 AM	10:00 AM	8.90	8.10	39.5	33.3	154	160	17.9	18.3	84.3	89.4	45.2	30.6	891	902	21.8	9.44	8.34	8.06	36.6	44.5	5.85	5.79
12/18/2000	10:00 AM	12:00 PM	1.00	1.80	77.3	68.6	520	470	90.6	82.8	351	340	175	155	1859	1701	62.6	51.5	42.0	60.8	38.6	36.0	27.3	--
12/19/2000*	5:15 AM	7:35 AM	7.70	4.60	15.8	14.2	80.1	81.0	11.3	11.9	20.4	19.8	13.8	12.2	439	422	7.41	6.49	5.59	6.19	24.1	17.6	2.81	--
1/15/2001	1:00 AM	3:00 AM	5.10	5.30	18.7	23.3	45.8	49.7	11.1	9.65	12.4	13.7	13.7	14.2	231	223	9.01	8.69	5.43	4.85	13.2	18.7	3.67	4.91
1/17/2001	12:15 AM	2:00 AM	3.80	4.90	22.3	28.4	100	114	44.3	45.6	21.8	30.5	14.0	19.7	380	534	12.3	20.6	5.86	8.14	31.8	46.4	7.81	--
1/17/2001	2:00 AM	3:55 AM	8.00	7.70	14.4	19.5	80.3	83.8	33.9	35.5	19.4	21.0	4.20	11.0	335	374	5.68	10.2	4.97	5.27	14.8	20.2	5.15	6.59
1/17/2001	4:00 AM	6:00 AM	5.70	5.50	15.4	16.7	54.7	59.0	51.4	54.0	18.8	21.6	7.11	8.57	295	313	6.32	7.05	5.63	5.42	19.6	21.3	5.16	6.21
1/17/2001	6:00 AM	8:00 AM	7.40	6.90	18.8	19.4	63.0	69.1	55.9	61.2	20.6	23.2	9.99	10.2	316	313	8.08	6.19	5.65	5.54	16.7	16.6	--	--
1/21/2001	6:15 AM	7:15 AM	2.70	2.70	22.0	25.3	463	423	51.4	46.1	50.3	40.9	27.7	20.5	889	731	22.9	19.3	8.68	6.04	25.8	26.3	9.12	--
1/21/2001	7:15 AM	9:15 AM	7.00	7.20	24.6	16.8	365	352	61.8	56.6	61.2	56.5	30.1	16.8	786	703	17.0	8.88	10.1	7.65	42.9	40.7	11.9	11.0
1/25/2001	5:00 AM	6:00 AM	2.80	1.90	56.4	67.0	26.6	36.1	8.69	13.2	11.5	22.1	46.4	69.1	152	262	15.6	27.4	6.74	10.6	62.1	66.2	7.22	--
1/25/2001	6:00 AM	7:30 AM	2.90	2.70	54.5	63.6	37.1	40.4	18.3	19.6	13.9	18.3	41.6	50.5	250	259	6.55	10.8	6.87	7.58	14.0	25.7	6.67	--
1/31/2001	5:15 AM	7:00 AM	12.6	14.1	27.0	24.0	220	210	37.2	37.5	55.5	61.6	24.0	23.2	575	581	9.19	6.61	5.01	7.91	40.5	42.6	9.33	10.9
1/31/2001	7:00 AM	9:05 AM	3.30	2.90	28.8	30.0	450	459	129	135	108	115	38.9	37.0	1370	1301	16.8	16.4	7.64	6.88	27.8	31.0	23.5	20.9
2/1/2001	2:15 AM	3:55 AM	5.00	--	28.4	--	92.5	--	51.4	--	44.4	--	23.8	--	335	--	12.1	--	6.24	--	30.0	--	6.77	--

TOC, total organic carbon; Dplate , Deposition plate; μN, micronormal; ppmC, parts per million carbon by mass

* There was a problem on the second deposition plate, so only the data from the first plate is used

Table 4-2. Fog water, ion and TOC fluxes derived from the two deposition plates.

Sample Start Date	Sample Start Time	Sample End Time	Fog water (g/m2/min)		Cl - (neq/m2/min)		NO3- (neq/m2/min)		NO2- (neq/m2/min)		SO42- (neq/m2/min		Na+ (neq/m2/min)		NH4+ (neq/m2/min		K+ (neq/m2/min		Mg2+ (neq/m2/min)		Ca2+ (neq/m2/min)		TOC (μgC/m2/min)	
			Dplate 1	Dplate 2	Dplate 1	Dplate 2	Dplate 1	Dplate 2	Dplate 1	Dplate 2	Dplate 1	Dplate 2	Dplate 1	Dplate 2	Dplate 1	Dplate 2	Dplate 1	Dplate 2	Dplate 1	Dplate 2	Dplate 1	Dplate 2	Dplate 1	Dplate 2
12/17/2000	11:00 PM	1:00 AM	0.26	0.23	--	4.02	--	38.9	--	2.05	--	8.18	--	1.99	--	105	--	1.32	--	1.52	--	8.32	1.11	--
12/18/2000	1:00 AM	3:10 AM	0.45	0.43	8.19	7.45	78.7	72.9	5.14	5.08	18.2	16.8	4.48	4.31	216	216	3.68	3.46	3.94	4.15	21.8	25.9	2.14	1.83
12/18/2000	3:10 AM	6:10 AM	0.61	--	9.49	--	97.0	--	5.24	--	19.2	--	3.04	--	319	--	3.75	--	3.67	--	11.5	--	1.95	--
12/18/2000	6:10 AM	8:15 AM	0.52	0.51	10.5	10.5	67.1	70.4	5.89	6.65	32.8	34.1	12.2	11.6	395	393	2.69	2.62	3.22	2.84	10.8	12.2	1.90	1.97
12/18/2000	8:15 AM	10:00 AM	0.28	0.26	11.2	8.57	43.6	41.2	5.05	4.71	23.8	23.0	12.8	7.88	252	232	6.16	2.43	2.36	2.07	10.3	11.4	1.65	1.49
12/18/2000	10:00 AM	12:00 PM	0.03	0.05	2.15	3.43	14.4	23.5	2.52	4.14	9.76	17.0	4.85	7.76	51.6	85.1	1.74	2.57	1.17	3.04	1.07	1.80	0.76	--
12/19/2000	5:15 AM	7:35 AM	0.12	--	2.89	--	14.7	--	2.07	--	3.74	--	2.54	--	80.5	--	1.36	--	1.02	--	4.42	--	0.52	--
1/15/2001	1:00 AM	3:00 AM	0.14	0.15	2.65	3.43	6.49	7.32	1.57	1.42	1.76	2.02	1.94	2.09	32.8	32.9	1.28	1.28	0.77	0.71	1.87	2.75	0.52	0.72
1/17/2001	12:15 AM	2:00 AM	0.12	0.16	2.69	4.42	12.1	17.7	5.35	7.09	2.63	4.75	1.69	3.06	45.8	83.1	1.49	3.20	0.71	1.27	3.77	7.21	0.94	--
1/17/2001	2:00 AM	3:55 AM	0.25	0.24	3.65	4.78	20.4	20.5	8.60	8.68	4.92	5.12	1.07	2.70	85.2	91.3	1.44	2.49	1.26	1.29	3.76	4.94	1.31	1.61
1/17/2001	4:00 AM	6:00 AM	0.16	0.15	2.44	2.55	8.66	9.01	8.14	8.25	2.98	3.30	1.13	1.31	46.7	47.8	1.00	1.08	0.89	0.83	3.06	3.26	0.82	0.95
1/17/2001	6:00 AM	8:00 AM	0.21	0.19	3.86	3.72	12.9	13.2	11.5	11.7	4.23	4.44	2.05	1.95	65.0	59.9	1.66	1.19	1.16	1.06	3.43	3.19	--	--
1/21/2001	6:15 AM	7:15 AM	0.15	0.15	3.30	3.80	69.5	63.5	7.71	6.91	7.55	6.14	4.16	3.08	133	110	3.43	2.89	1.30	0.91	3.86	3.95	1.37	--
1/21/2001	7:15 AM	9:15 AM	0.19	0.20	4.78	3.35	71.0	70.5	12.0	11.3	11.9	11.3	5.85	3.37	153	141	3.30	1.78	1.96	1.53	8.35	8.14	2.32	2.20
1/25/2001	5:00 AM	6:00 AM	0.16	0.11	8.78	7.07	4.14	3.81	1.35	1.39	1.79	2.33	7.22	7.30	23.6	27.6	2.43	2.89	1.05	1.11	9.66	6.99	1.12	--
1/25/2001	6:00 AM	7:30 AM	0.11	0.10	5.85	6.36	3.98	4.04	1.96	1.96	1.49	1.83	4.47	5.05	26.9	25.9	0.70	1.08	0.74	0.76	1.47	2.57	0.72	--
1/31/2001	5:15 AM	7:00 AM	0.40	0.45	10.8	10.7	88.1	94.0	14.9	16.8	22.2	27.6	9.60	10.4	230	260	3.68	2.96	2.00	3.54	16.2	19.1	3.73	4.87
1/31/2001	7:00 AM	9:05 AM	0.09	0.08	2.53	2.32	39.6	35.5	11.3	10.4	9.48	8.91	3.42	2.86	121	101	1.47	1.27	0.67	0.53	2.45	2.40	2.07	1.61
2/1/2001	2:15 AM	3:55 AM	0.17	--	4.73	--	15.4	--	8.56	--	7.40	--	3.96	--	55.9	--	2.02	--	1.04	--	5.00	--	1.13	--

TOC, total organic carbon; Dplate, deposition plate;
neq/m2/min, nanoequivalents per square meter per minute; μgC/m2/min, microgram carbon per square meter per minute
* There was a problem on the second deposition plate, so only the flux from the first plate is used

Besides this removal mechanism, fog scavenges preexisting gases and aerosol particles and can increase the amount of particulate matter through chemical reactions in the aqueous phase. One of the most important reactions is the oxidation of aqueous free S(IV) into sulfuric acid. In order to study the new particle production in fogs via S(IV) oxidation, an aqueous chemical model was used to obtain the sulfate production rates with drop size and compare the rates with theoretical values in environments where aqueous phase S(IV) oxidation takes place predominantly via the H_2O_2, O_3 and catalyzed O_2 oxidation pathways. This model also includes S(IV) reaction to form HMS.

4.2 Results and Discussion

4.2.1 Ion concentrations and flux calculation from deposition plates

Teflon deposition plates were used to measure deposition fluxes of fog water and fog solutes in several CRPAQS fog episodes. Table 4-1 lists the sampling date and time of each fog event and concentrations of major ions and total organic carbon (TOC) measured in deposited fog water collected by two deposition plates operated side-by-side. Table 4-2 lists the fluxes of water, TOC and ions, including Cl^-, NO_3^-, SO_4^{2-}, Na^+, NH_4^+, Mg^{2+}, K^+, Ca^{2+} and NO_2^-. Figures 4-1 to 4-22 provide a comparison of water mass, solute concentrations and species fluxes observed on the replicate deposition plates. The results reveal that the two deposition plates agree well. Correlation coefficients (R^2) between the two plates for fluxes of water, NO_3^-, SO_4^{2-}, NH_4^+, Ca^{2+}, NO_2^- and TOC are higher than 0.9 (not shown in figures); while correlation coefficients for fluxes of Cl^-, Na^+, Mg^{2+} and K^+ are less than 0.9, probably because the concentrations of these four ions were relatively low, and they could more easily be affected by contamination from nearby dust or during sample handling.

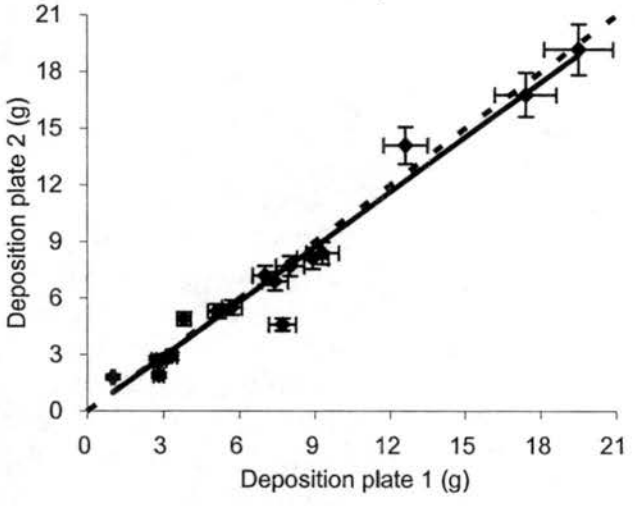

Figure 4-1. Comparison of fog water masses collected by two deposition plates. The solid line is a data trendline; the dashed line is the 1:1 line. Error bars represent the pooled standard deviation of replicate samples from 2 collocated deposition plates.

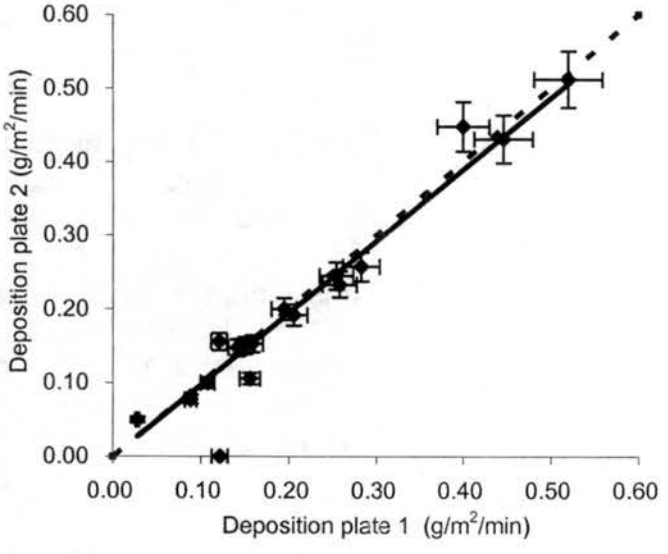

Figure 4-2. Comparison of fog water fluxes collected by two deposition plates. The solid line is a data trendline; The dashed line is the 1:1 line. Error bars represent the pooled standard deviation of replicate samples from two collocated deposition plates.

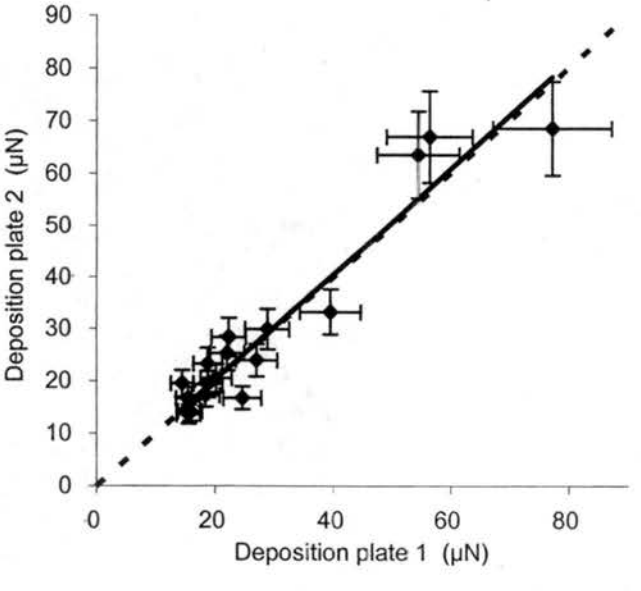

Figure 4-3. Comparison of Cl^- concentrations in fog water collected by two deposition plates. The solid line is a data trendline; the dashed line is the 1:1 line. Error bars represent the pooled standard deviation of replicate samples from 2 collocated deposition plates.

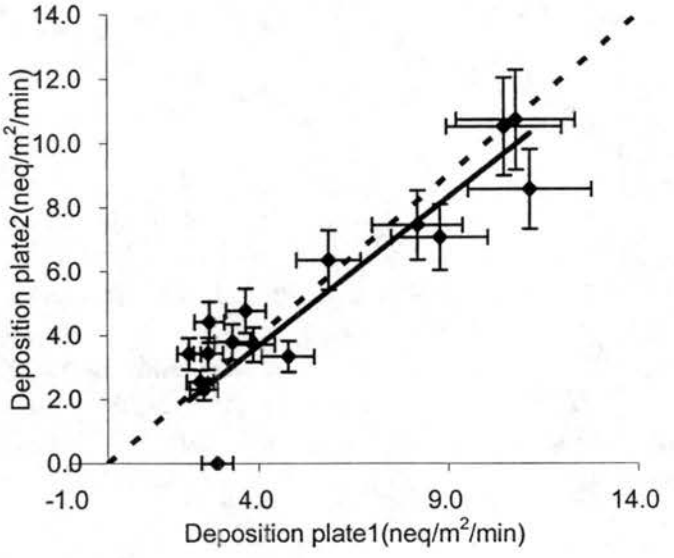

Figure 4-4. Comparison of Cl^- fluxes collected by two deposition plates. The solid line is a data trendline; the dashed line is the 1:1 line. Error bars represent the pooled standard deviation of replicate samples from 2 collocated deposition plates.

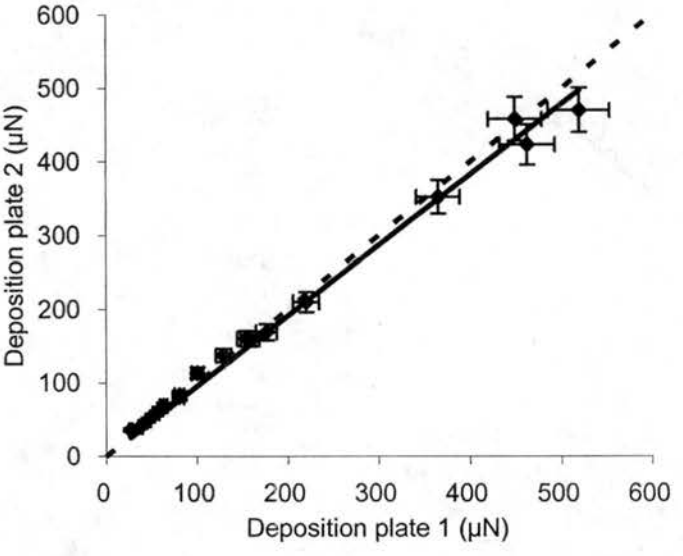

Figure 4-5. Comparison of NO_3^- concentrations in fog water collected by two deposition plates. The solid line is a data trendline; the dashed line is the 1:1 line. Error bars represent the pooled standard deviation of replicate samples from 2 collocated deposition plates.

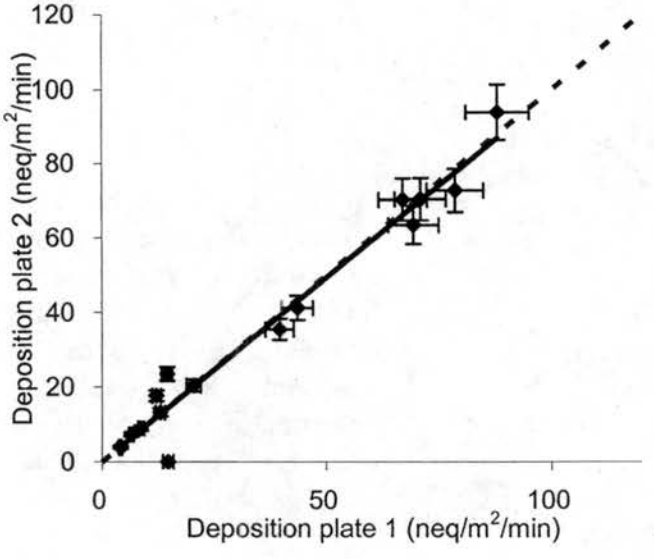

Figure 4-6. Comparison of NO_3^- fluxes collected by two deposition plates. The solid line is a data trendline; the dashed line is the 1:1 line. Error bars represent the pooled standard deviation of replicate samples from 2 collocated deposition plates.

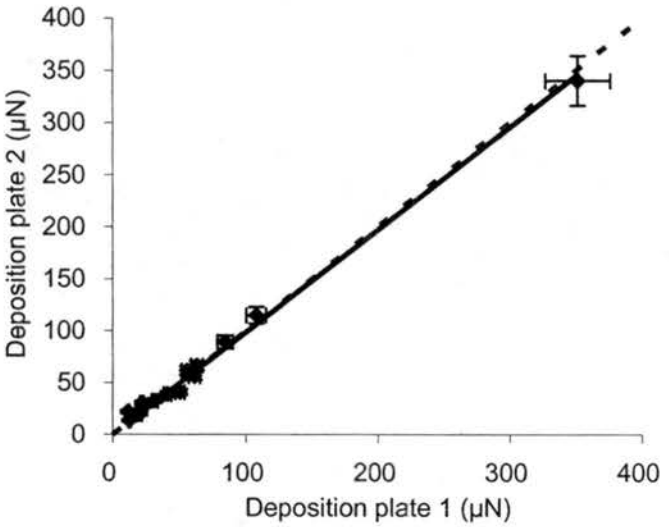

Figure 4-7. Comparison of SO_4^{2-} concentrations in fog water collected by two deposition plates. The solid line is a data trendline; the dashed line is the 1:1 line. Error bars represent the pooled standard deviation of replicate samples from 2 collocated deposition plates.

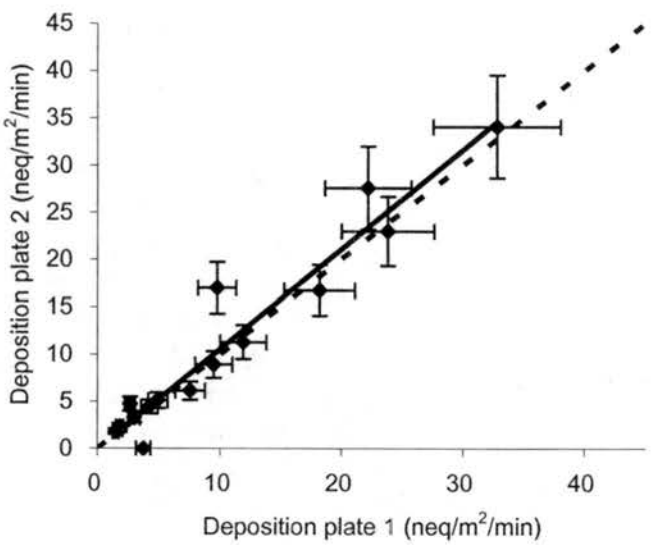

Figure 4-8. Comparison of SO_4^{2-} fluxes collected by two deposition plates. The solid line is a data trendline; the dashed line is the 1:1 line. Error bars represent the pooled standard deviation of replicate samples from 2 collocated deposition plates.

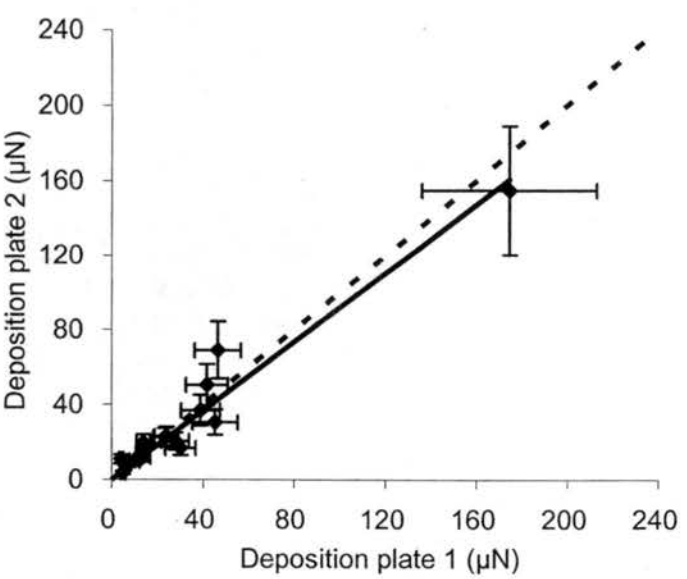

Figure 4-9. Comparison of Na^+ concentrations in fog water collected by two deposition plates. The solid line is a data trendline; the dashed line is the 1:1 line. Error bars represent the pooled standard deviation of replicate samples from 2 collocated deposition plates.

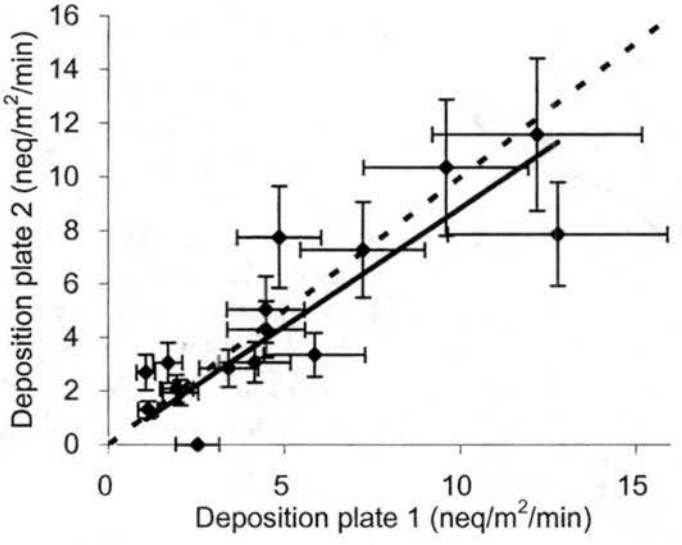

Figure 4-10. Comparison of Na+ fluxes collected by two deposition plates. The solid line is a data trendline; the dashed line is the 1:1 line. Error bars represent the pooled standard deviation of replicate samples from 2 collocated deposition plates.

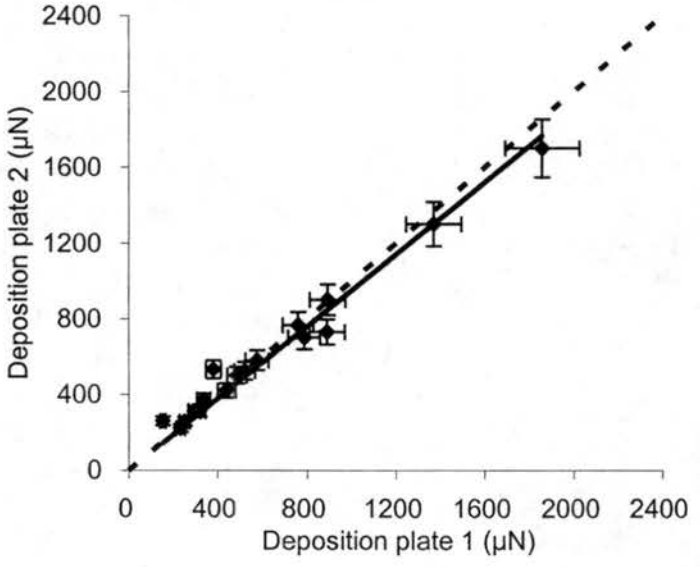

Figure 4-11. Comparison of NH_4^+ concentrations in fog water collected by two deposition plates. The solid line is a data trendline; the dashed line is the 1:1 line. Error bars represent the pooled standard deviation of replicate samples from 2 collocated deposition plates.

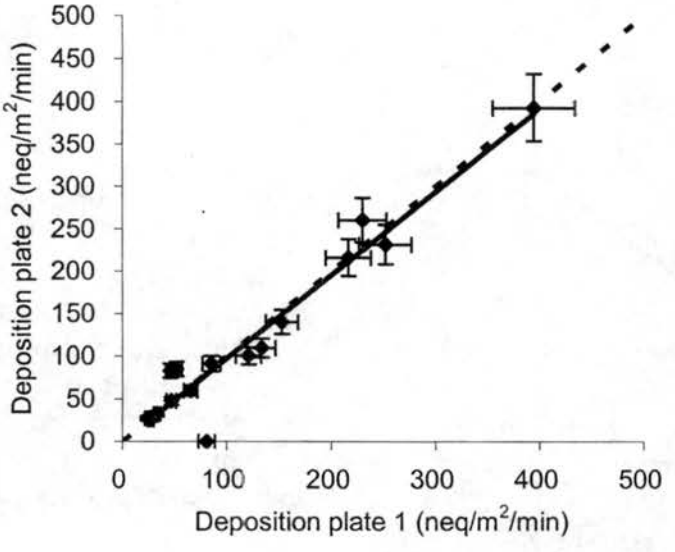

Figure 4-12. Comparison of NH_4^+ fluxes collected by two deposition plates. The solid line is a data trendline; The dashed line is the 1:1 line. Error bars represent the pooled standard deviation of replicate samples from 2 collocated deposition plates.

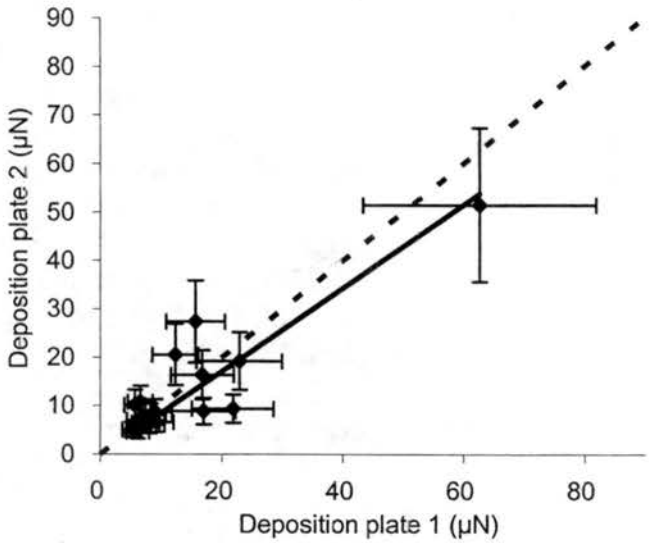

Figure 4-13. Comparison of K^+ concentrations in fog water collected by two deposition plates. The solid line is a data trendline; the dashed line is the 1:1 line. Error bars represent the pooled standard deviation of replicate samples from 2 collocated deposition plates.

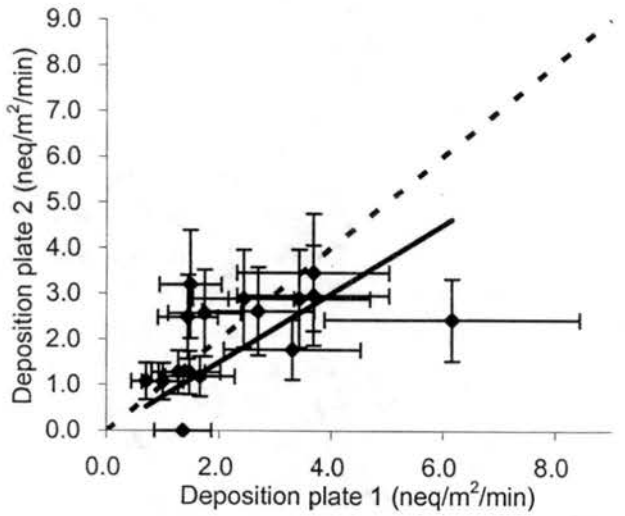

Figure 4-14. Comparison of K^+ fluxes collected by two deposition plates. The solid line is a data trendline; The dashed line is the 1:1 line. Error bars represent the pooled standard deviation of replicate samples from 2 collocated deposition plates.

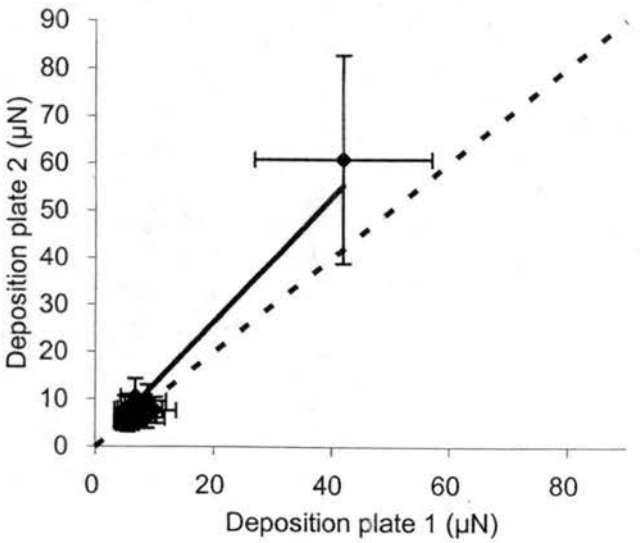

Figure 4-15. Comparison of Mg^{2+} concentrations in fog water collected by two deposition plates. The solid line is a data trendline; the dashed line is the 1:1 line. Error bars represent the pooled standard deviation of replicate samples from 2 collocated deposition plates.

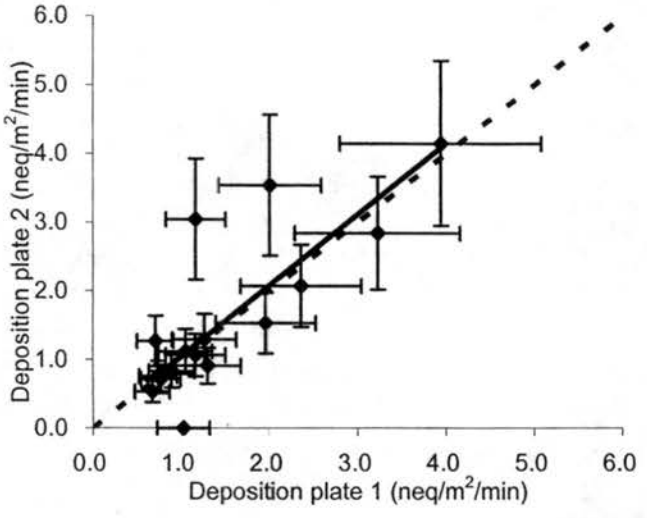

Figure 4-16. Comparison of Mg^{2+} fluxes collected by two deposition plates. The solid line is a data trendline; the dashed line is the 1:1 line. Error bars represent the pooled standard deviation of replicate samples from 2 collocated deposition plates.

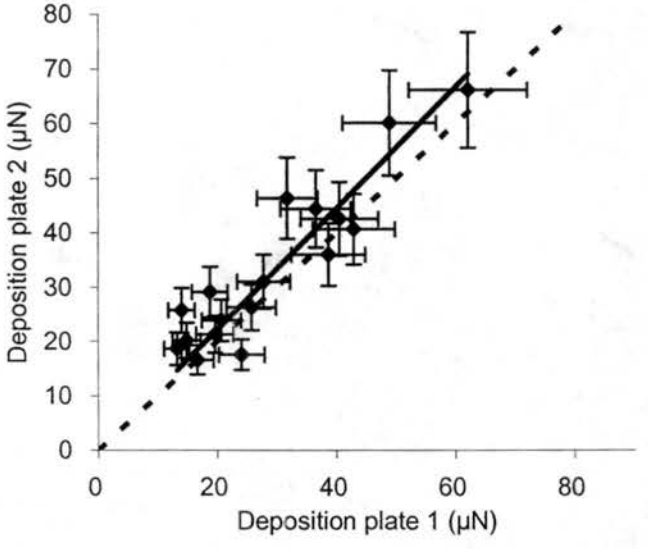

Figure 4-17. Comparison of Ca^{2+} concentrations in fog water collected by two deposition plates. The solid line is a data trendline; the dashed line is the 1:1 line. Error bars represent the pooled standard deviation of replicate samples from 2 collocated deposition plates.

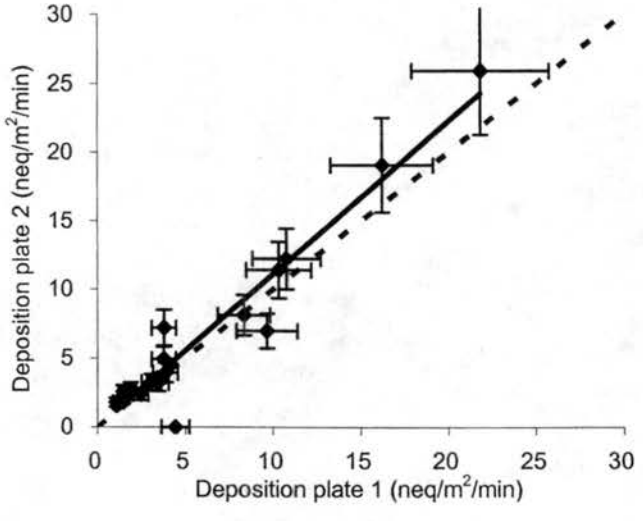

Figure 4-18. Comparison of Ca^{2+} fluxes collected by two deposition plates. The solid line is a data trendline; the dashed line is the 1:1 line. Error bars represent the pooled standard deviation of replicate samples from 2 collocated deposition plates.

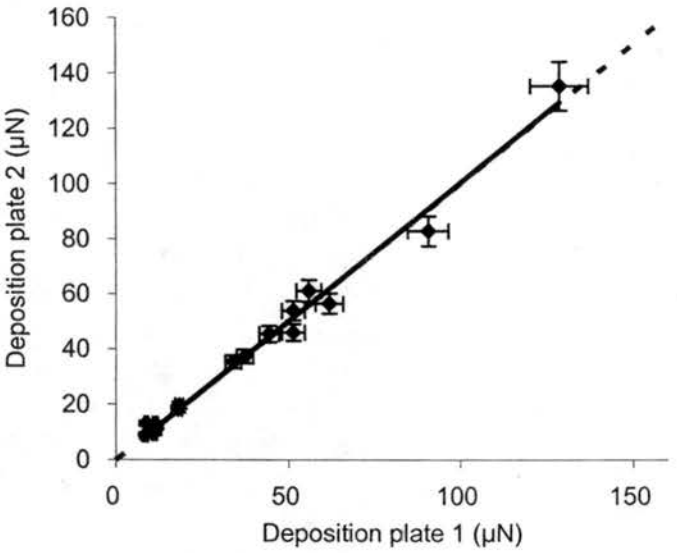

Figure 4-19. Comparison of NO_2^- concentrations in fog water collected by two deposition plates. The solid line is a data trendline; the dashed line is the 1:1 line. Error bars represent the pooled standard deviation of replicate samples from 2 collocated deposition plates.

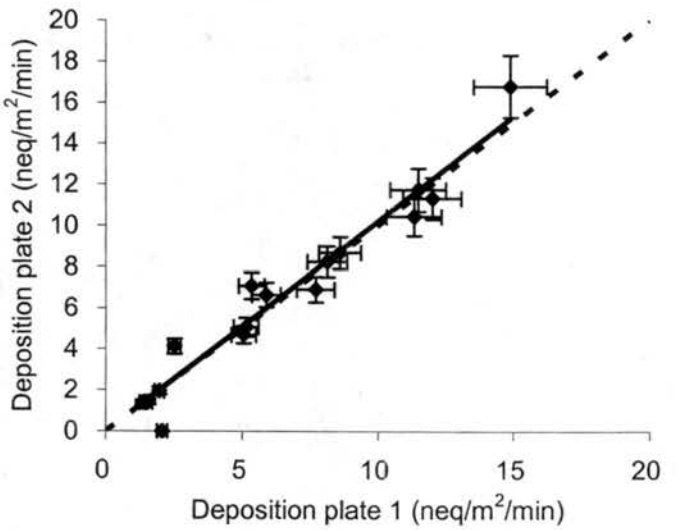

Figure 4-20. Comparison of NO_2^- fluxes collected by two deposition plates. The solid line is a data trendline; the dashed line is the 1:1 line. Error bars represent the pooled standard deviation of replicate samples from 2 collocated deposition plates.

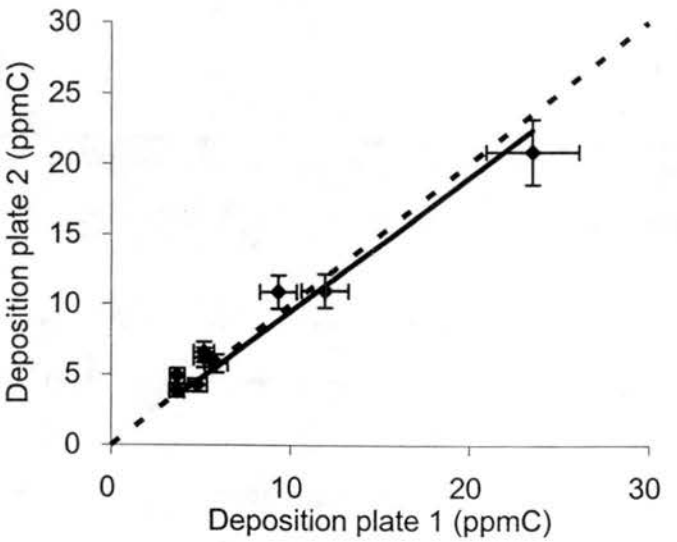

Figure 4-21. Comparison of TOC concentrations in fog water collected by two deposition plates. The solid line is a data trendline; the dashed line is the 1:1 line. Error bars represent the pooled standard deviation of replicate samples from 2 collocated deposition plates.

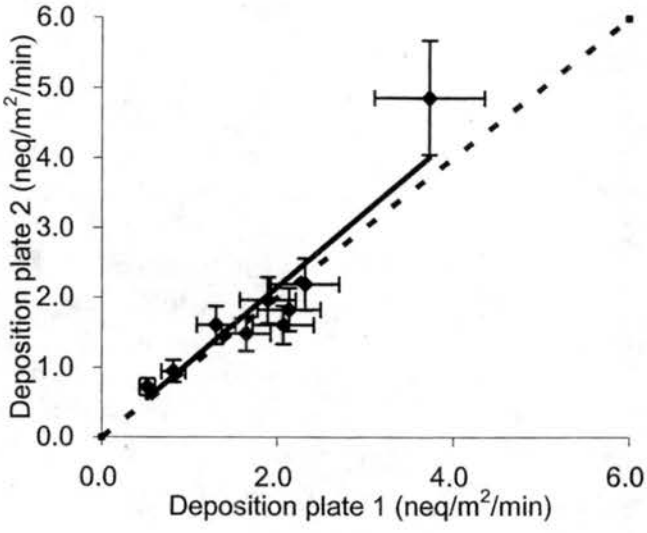

Figure 4-22. Comparison of TOC flux escollected by two deposition plates. The solid line is a data trendline; The dashed line is the 1:1 line. Error bars represent the pooled standard deviation of replicate samples from 2 collocated deposition plates.

Table 4-3. Summary of observed deposition fluxes in CRPAQS fogs.

(Solute)		*Minimum*	*Maximum*	*Average*
H_2O	($g/m^2/min$)	0.03	0.61	0.22
Cl^-	($neq/m^2/min$)	2.15	11.2	5.50
NO_3^-	($neq/m^2/min$)	3.81	97.0	36.9
NO_2^-	($neq/m^2/min$)	1.35	16.8	6.69
SO_4^{2-}	($neq/m^2/min$)	1.49	34.1	10.7
Na^+	($neq/m^2/min$)	1.07	12.8	4.80
NH_4^+	($neq/m^2/min$)	23.6	395	128
K^+	($neq/m^2/min$)	0.70	6.16	2.29
Mg^{2+}	($neq/m^2/min$)	0.53	4.15	1.65
Ca^{2+}	($neq/m^2/min$)	1.07	25.9	7.26
TOC	($\mu gC/m^2/min$)	0.52	4.87	1.60

$g/m^2/min$, gram per square meter per minute; $neq/m^2/min$, nanoequivalents per square meter per minute; $\mu gC/m^2/min$, microgram carbon per square meter per minute.

A summary of the range of water and ion fluxes is shown in Table 4-3. Fog water flux rates averaged 0.22 $g/m^2/min$ during the seven fog episodes. Flux rates for nitrate and ammonium were the highest among the chemical species, averaging 36.9 $neq/m^2/min$ and 128 $neq/m^2/min$, respectively. Sulfate flux rates averaged only 10.7 $neq/m^2/min$. Compared with results from an earlier study in Davis, California (Collett et al., 2001), in

which the mean fluxes of nitrate, ammonium and sulfate were 71.4 neq/m^2/min, 140.1 neq/m^2/min and 9.5 neq/m^2/min, the average fluxes of sulfate and ammonium are similar, but the Angiola CRPAQS nitrate flux is only about one half the Davis value. These results could reflect spatial variability in the large valley (Collett et al., 2001).

Table 4-4 lists the precision estimates of concentration and flux measurements, by species, as determined from the replicate deposition plate measurements. The results indicate that the deposition plates provided relatively precise measurements for major fog solute species, with relative standard deviation of 6.5-11.3% for water mass, sulfate, nitrate, nitrite, ammonium and TOC concentrations and 7.5-16.9% for measurements of water, sulfate, nitrate, nitrite, ammonium and TOC fluxes. Precision decreases somewhat for trace species.

Table 4-4. Relative standard deviations of deposited fog concentrations and fluxes derived from two deposition plates.

Solute	RSD of Concentration (%)	RSD of Flux (%)
Water	6.6	7.5
Cl^-	13.0	14.5
NO_3^-	6.6	8.0
NO_2^-	6.5	9.0
SO_4^{2-}	7.2	16.4
Na^+	21.4	24.5
NH_4^+	9.2	10.2
K^+	13.4	37.4
Mg^{2+}	35.9	29.3
Ca^{2+}	15.6	18.1
TOC	11.3	16.9

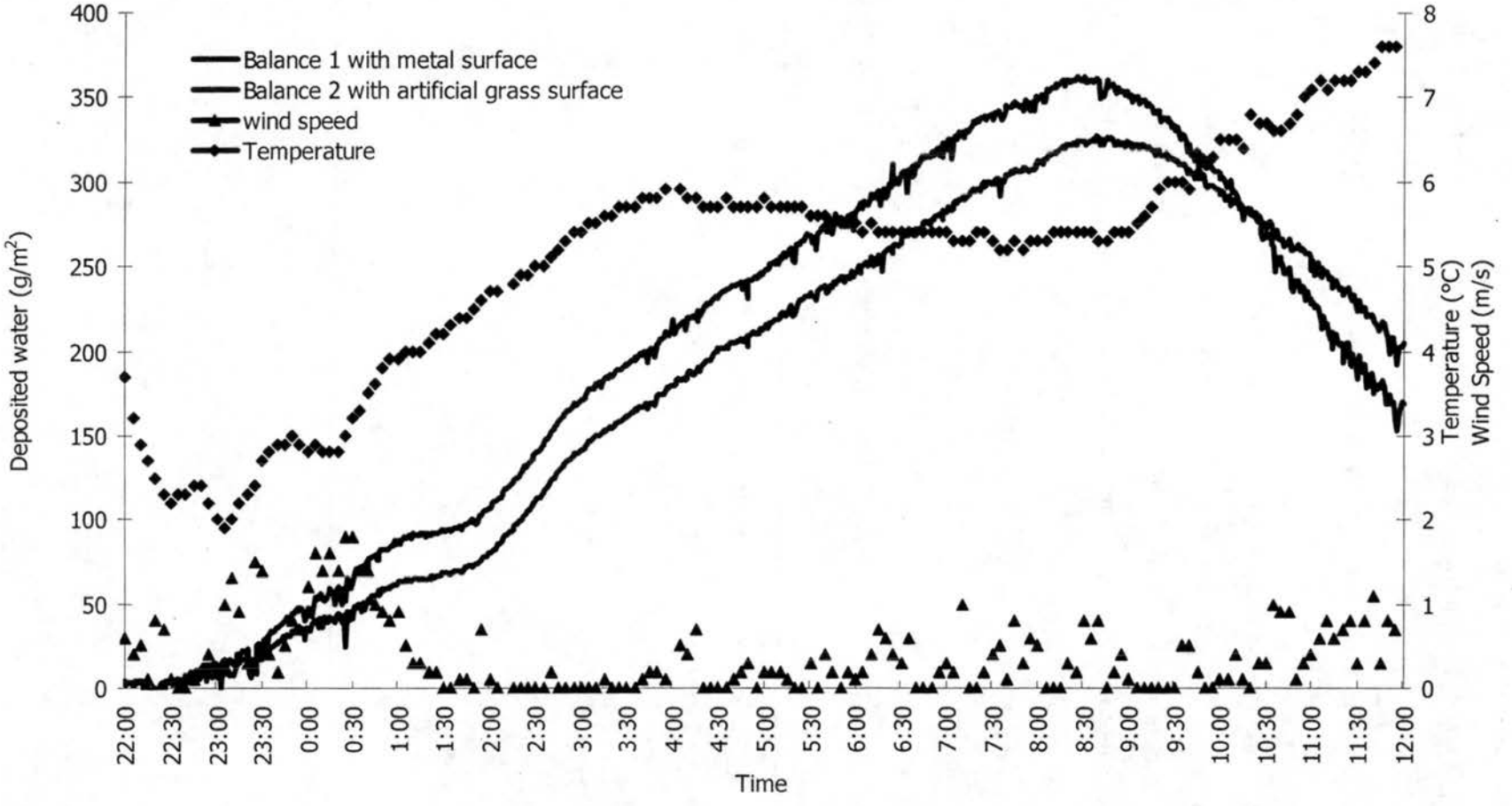

Figure 4-23. Area normalized balance reading on 12/18/00. Temperature and wind speed trendlines are also presented for reference.

4.2.2 Water fluxes derived from the balances

Figure 4-23 shows the temperature and wind speed profile and the accumulating water mass on two balances during one fog event (day 352, 12/17/00 22:00 to 12/18/00 12:00). The data were normalized by balance collection area so that we are able to compare them directly. The peaks on the water mass curves possibly represent turbulence effects on balance readings. The results show that the accumulation of water was higher on a balance with an artificial grass deposition surface than on one with a bare metal surface. The results also show that after sunrise, evaporation from the balances becomes significant. Evaporation eventually dominates the change in accumulated mass as the two balances show a net mass loss after about 8:00. Note the rate of loss is higher from the artificial grass surface than from the bare metal surface. A similar post-sunrise loss of water was reported by Collett et al. (2001).

Figure 4-24 to Figure 4-30 compare 10-minute average water fluxes on the two balances in the rest of the fog episodes. Data are included only for periods prior to 07:30 am, in order to avoid the post-sunrise evaporation effect. Data points above the 1:1 line indicate that the water flux on the grass surface is higher than on the metal surface, and vice versa. The results again indicate that the water fluxes tend to be somewhat higher on the grass surface. If we combine data from all the fog events together and regress deposition flux to the grass surface against deposition flux to the metal surface, we find that the enhancement in grass surface deposition averages approximately 5%. Enhanced deposition to the grass surface likely results from an increase in turbulent deposition to this rougher surface.

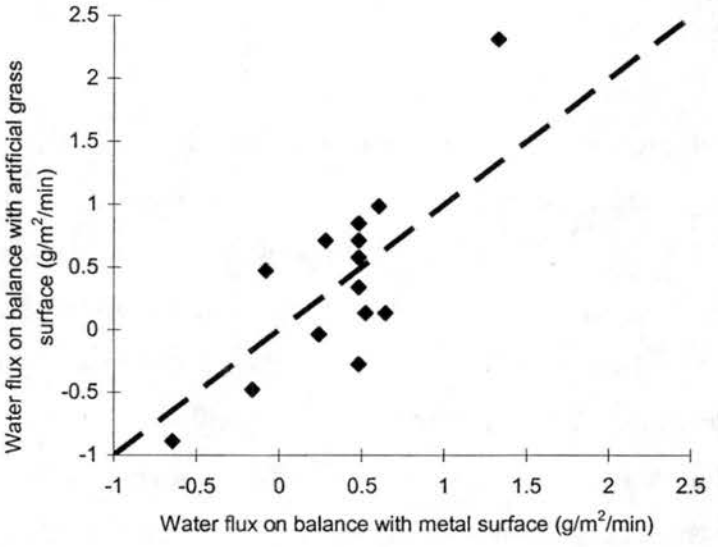

Figure 4-24. Comparison of 10 minute average water fluxes on two balances on 12/18/00. The dashed line is the 1:1 line.

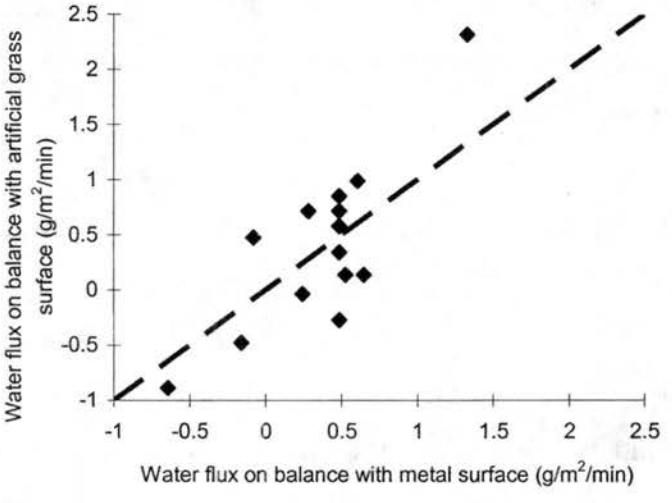

Figure 4-25. Comparison of 10 minute average water fluxes on two balances on 12/19/00. The dashed line is the 1:1 line.

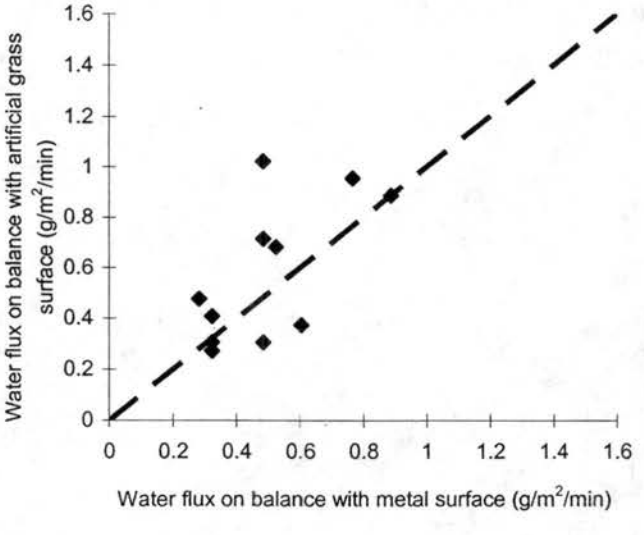

Figure 4-26 Comparison of 10 minute average water fluxes on two balances on 01/15/01. The dashed line is the 1:1 line.

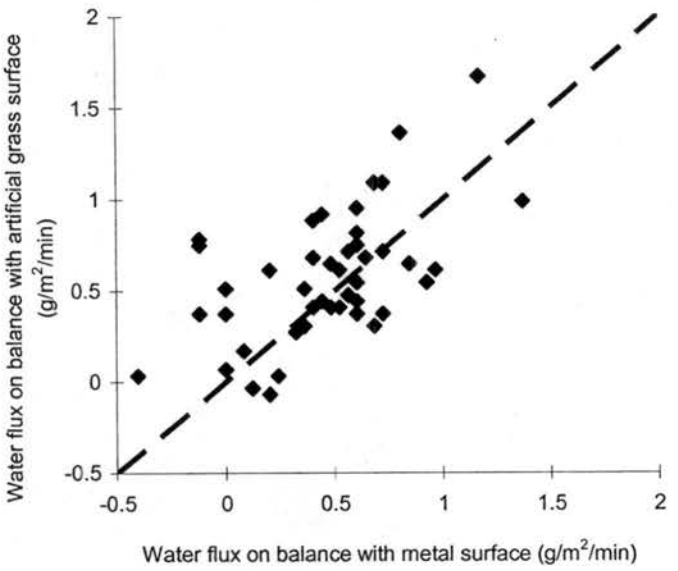

Figure 4-27. Comparison of 10 minute average water fluxes on two balances on 01/17/01. The dashed line is the 1:1 line.

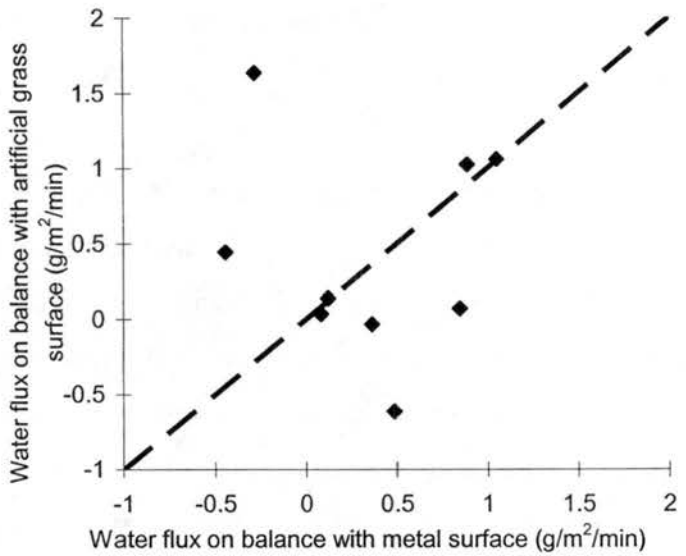

Figure 4-28. Comparison of 10 min average water fluxes on two balances on 01/21/01. The dashed line is the 1:1 line.

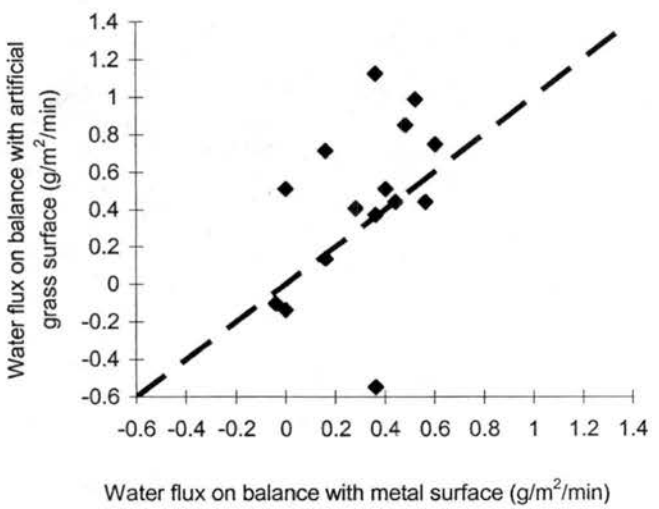

Figure 4-29. Comparison of 10 minute average water fluxes on two balances on 01/25/01. The dashed line is the 1:1 line.

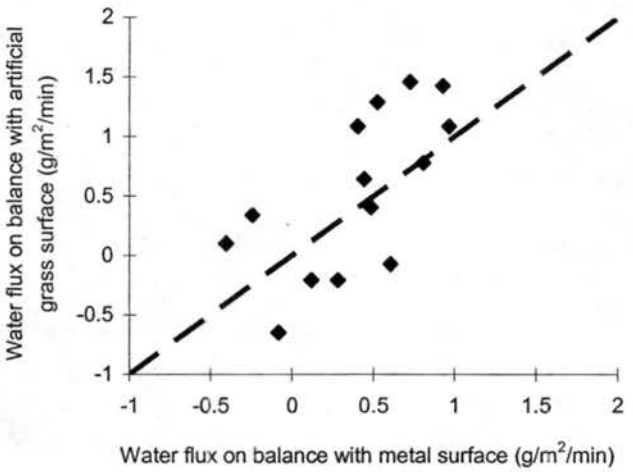

Figure 4-30. Comparison of 10 min average water fluxes on two balances on 01/31/01. The dashed line is the 1:1 line.

4.2.3 Comparison of water fluxes to plates and balances and flux variation with fog liquid water content and effective diameter

Fog liquid water content (LWC, with unit mg/m^3) was measured using a Gerber Scientific Particulate Volume Monitor (Model PVM-100) that was calibrated using a manufacturer supplied disk. The PVM also measures particle surface area (cm^3/m^3) and reports drop effective diameter (μm). PVM data were recorded at 1-minute intervals. Figure 4-31 shows 20-minute average water fluxes derived from the two balances along with fog LWC and effective diameter (D_{eff}), obtained from the PVM. Data from the two balances agree with each other reasonably well. Before sunrise, when PVM-LWC or effective diameter rose, so did the water fluxes measured by the two balances. When the temperature went higher, the fog started to evaporate; water fluxes to the two balances started to go down and showed negative values indicating net water evaporation from the deposition collection surface. Meanwhile, effective diameter and LWC didn't change dramatically, but slowly, consistent with the fog being maintained by evaporating deposited fog water on the ground.

It is apparent that fog LWC can affect fog water deposition fluxes as it is a measure of the airborne concentration of fog water. Since droplet settling velocities increase strongly as a function of drop diameter, we also expect to see some dependence of fog deposition

velocities in this low wind speed environment on effective diameter. In order to look at whether variations in fog LWC and effective diameter can explain the temporal variability in fog water flux rates, we performed a linear regression utilizing the simple, linear model:

$$Y = \alpha LWC + \beta D_{eff} + \gamma \quad (4\text{-}1)$$

where □and □are regression coefficients and □is a constant. The units of LWC, D_{eff} are gram per cubic meter and micrometer, respectively.

Table 4-5. Linear regression analysis of water flux to fog LWC and effective diameter for CRPAQS.

Model Summary	R	R^2	Adjusted R^2	Std. Error of the estimate
	0.629*	0.395	0.364	0.506

Coefficients		Unstandardized Coefficients		Standardized Coefficients		
		B	Std. Error	Beta	t	Sig.
	Constant	-1.377	0.893		-1.542	0.131
	LWC	3.462	0.849	0.575	4.077	0.000
	D_{eff}	2.294×10^{-2}	0.032	0.101	0.716	0.478

*Preditors: Constant, D_{eff} and LWC

Equation (4-1) was solved by linear regression analysis using averaged 20-minute average water fluxes to two balances in the 12/17/00 fog event. 42 data points were used in the regression. Table 4-5 shows the linear regression results. The unstandardized coefficients and constant are 3.462, 0.023 and -1.377 respectively, so the equation is

$$Y = 3.462\ LWC + 0.023\ D_{eff} - 1.377\ .$$

The correlation coefficient (R^2) of the regression analysis is 0.4, indicating that only ~ 40% of the observed flux variability is explained by the linear model. The absence of greater explanatory power for this model could be the result of several factors. First, the assumption that drop deposition occurs solely by sedimentation is not completely accurate, as some turbulent deposition certainly occurs. Second, LWC and effective diameter are measured at ~ 3 m above the surface while deposition is measured at the ground. Third, the model is flawed in that LWC and effective diameter are not truly independent variables and the dependence of deposition velocity on effective diameter is not truly a linear function. Nevertheless, the fact that this simple, linear model shows some dependence of deposition flux on LWC and D_{eff} is reassuring.

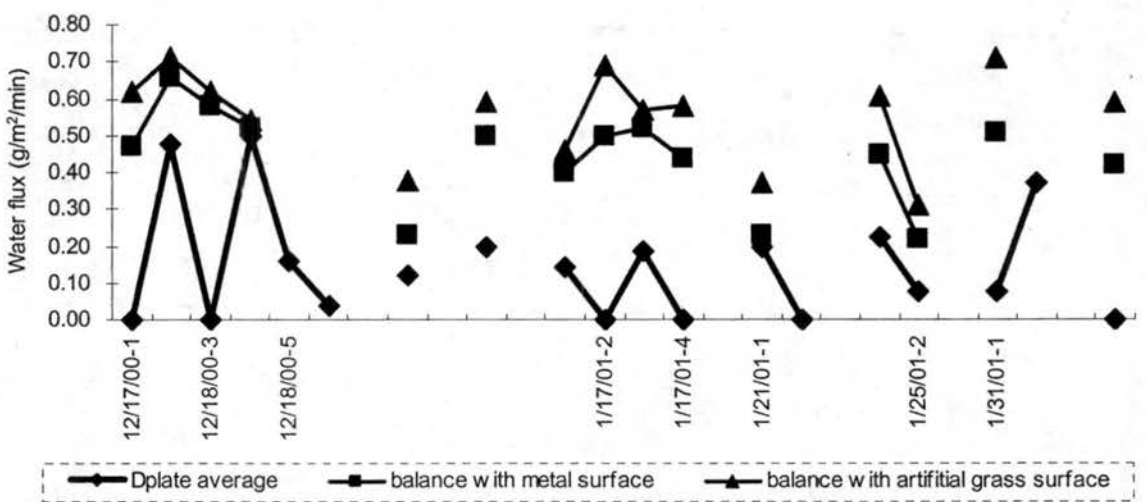

Figure 4-31. Comparison of water fluxes of balances and deposition plates for all events.

Figure 4-31 shows a water flux comparison between the balances and the deposition plates. Water fluxes to the balances were averaged to match the deposition plate measurement intervals. Surprisingly, a significantly higher deposition flux is observed to the balances than to the plates. In a past field campaign (Collett et al., 2001), the water fluxes measured to two deposition plates and to a balance (bare metal surface) agreed well. The reason for the discrepancy in CRPAQS has been investigated in some detail, but the lack of agreement remains puzzling.

4.2.4 Deposition velocities

Table 4-6. Average deposition velocities of all species on two deposition plates.

Samples	Water (cm/s)	Cl^- (cm/s)	NO_3^- (cm/s)	NO_2^- (cm/s)	SO_4^{2-} (cm/s)	Na^+ (cm/s)	NH_4^+ (cm/s)	K^+ (cm/s)	Mg^{2+} (cm/s)	Ca^{2+} (cm/s)	TOC (cm/s)
12/17/00-01	0.9	1.1	0.6	1.4	0.7	9.1	1.1	2.4	1.3	5.2	1.0
12/18/00-02	2.3	2.5	1.1	2.1	1.3	3.3	1.9	2.9	1.5	2.0	1.4
12/18/00-03	4.1	4.5	2.1	4.8	2.6	--*	3.7	8.6	4.7	6.8	2.0
12/18/00-04	3.7	4.7	1.8	3.9	3.6	10.1	4.0	5.2	4.5	6.6	1.9
12/18/00-05	2.4	6.0	1.5	2.7	2.9	--	2.8	9.4	3.9	7.7	1.5
12/18/00-06	0.5	2.2	0.7	1.5	1.6	13.2	0.9	3.8	3.6	0.6	0.8
12/19/00-01	1.0	2.2	0.6	4.2	2.0	0.9	3.9	1.5	3.0	1.4	1.0
1/15/01-01	3.4	4.0	1.1	3.8	1.0	4.5	3.1	9.3	3.9	9.4	1.9
1/17/01-01	0.9	1.7	0.4	1.9	0.6	10.2	1.0	3.8	1.4	3.2	1.2
1/17/01-02	1.7	2.0	0.4	1.7	0.6	10.2	0.9	2.6	1.8	2.6	2.4
1/17/01-03	3.1	2.8	0.4	--	1.0	5.2	1.7	3.2	3.6	4.8	2.5
1/17/01-04	1.7	2.6	0.7	--	1.2	6.9	2.5	3.9	1.8	2.1	--
1/21/01-01	1.4	2.1	0.4	1.7	0.6	13.2	0.7	3.1	2.4	3.5	0.7
1/21/01-02	2.0	2.1	0.4	2.7	0.9	8.7	0.8	2.4	2.4	4.9	1.3
1/25/01-01	3.0	--	1.0	4.7	2.6	16.6	3.0	--	4.5	--	--
1/25/01-02	1.6	4.2	0.8	2.2	2.0	4.4	2.0	6.8	2.1	5.2	2.1
1/31/01-01	2.5	2.8	1.0	3.5	1.5	5.9	2.1	4.8	3.2	--	2.0
1/31/01-02	1.0	1.4	0.8	2.4	1.1	4.6	1.1	2.1	1.4	3.9	1.2
2/1/01-01	6.0	4.3	0.4	3.3	0.8	11.1	0.9	5.0	5.3	5.9	1.4

--* : not detected or sample not available

Deposition velocities were determined for fog water, fog ions and TOC. The deposition velocity was calculated according to the following equation:

$$v_i = \frac{Flux_i}{LWC \times Concentration_i} \tag{4-2}$$

where v_i is the deposition velocity of species i, $Flux_i$ is the measured flux of species i to the deposition plates, LWC is the fog liquid water content measured by the PVM and $Concentration_i$ is the aqueous concentration of species i in the simultaneously collected

fog samples, which were collected by the Caltech Active Strand Cloudwater Collector (CASCC) for ion analysis and by the stainless steel CASCC (ss-CASCC) for TOC analysis.

Table 4-6 shows the overall computed deposition velocities of fog water and solute species in the study fog events. Table 4-7 presents the typical ranges of deposition velocities and the measurement precision (RSD) for each species determined from the replicate plate measurements. Fog water deposition velocities ranged from 0.5-6.0 cm/s, averaging 2.3 cm/s, comparable to previous observations in central California radiation fogs (Collett et al., 2001), which range from 1 cm/s to more than 10 cm/s. The TOC deposition velocity ranged from 0.7-2.5 cm/s, averaging 1.5 cm/s, which is similar to or smaller than the fog water deposition velocity. We can see that average deposition velocity trend is NO_2^- > water > NH_4^+ > TOC ~ SO_4^{2-} > NO_3^-. Figure 4-32 and 4-33 show the deposition velocities of these species for each fog events. The species dependent trend in average deposition velocities for each fog events is also NO_2^- > water > NH_4^+ > TOC ~ SO_4^{2-} > NO_3^-.

Table 4-7. Typical ranges of deposition velocities and relative standard deviations.

Solute	*Deposition velocity (cm/s)*				*RSD (%)*
	Minimum	*Maximum*	*Median*	*Average*	
NO_3^-	0.4	2.1	0.7	0.9	8.1
SO_4^{2-}	0.6	3.6	1.1	1.5	11.1
TOC	0.7	2.5	1.4	1.5	16.9
NH_4^+	0.7	4.0	1.7	1.9	10.4
Water	0.5	6.0	2.0	2.3	7.6
NO_2^-	1.4	4.8	2.4	2.7	9.2
Mg^{2+}	1.3	5.3	2.4	2.9	29.7
Cl^-	1.1	6.0	2.5	3.0	14.8
K^+	2.1	9.4	3.8	4.6	37.9
Ca^{2+}	0.6	9.4	4.8	4.6	18.3
Na^+	3.3	16.6	8.7	8.3	24.9

RSD, relative standard deviation, which is calculated from replicate samples of two collocated deposition plates.

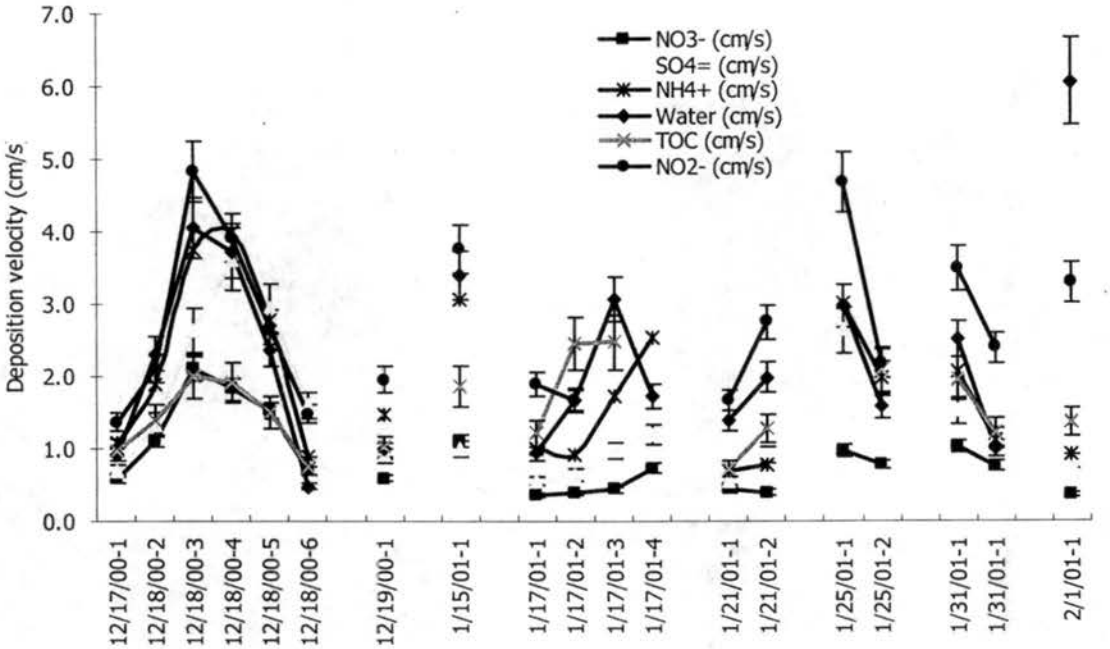

Figure 4-32. Deposition velocities of fogwater, TOC , NH_4^+, SO_4^{2-}, NO_3^- and NO_2^-.

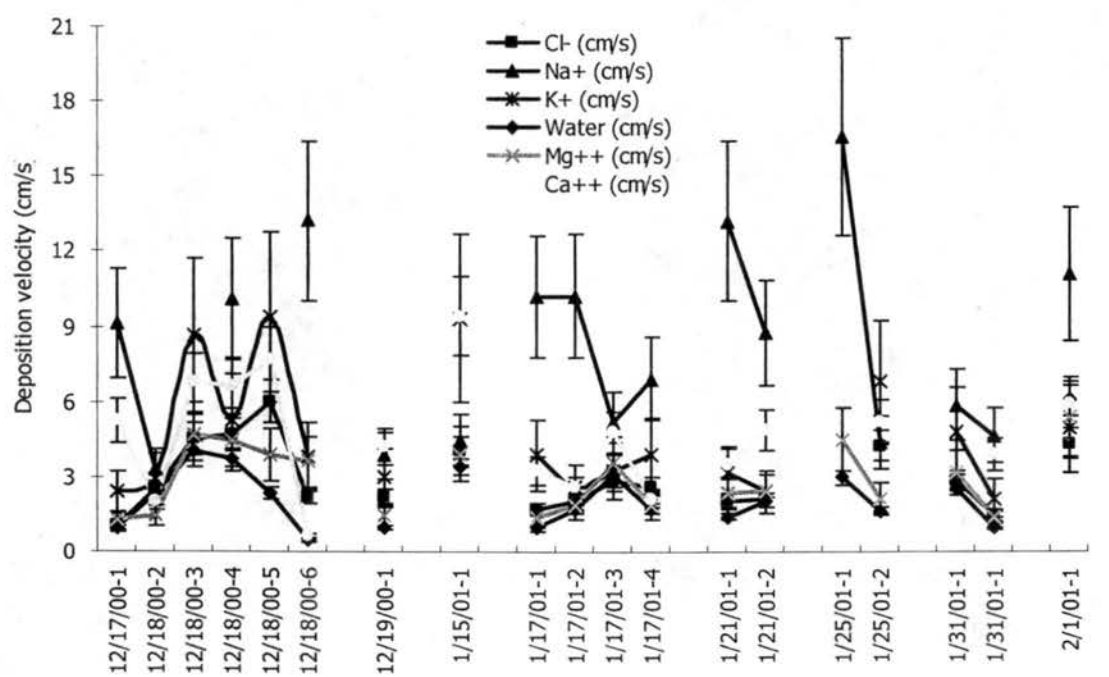

Figure 4-33. Deposition velocities of fogwater, Cl^-, Na^+, K^+, Mg^{2+} and Ca^{2+}.

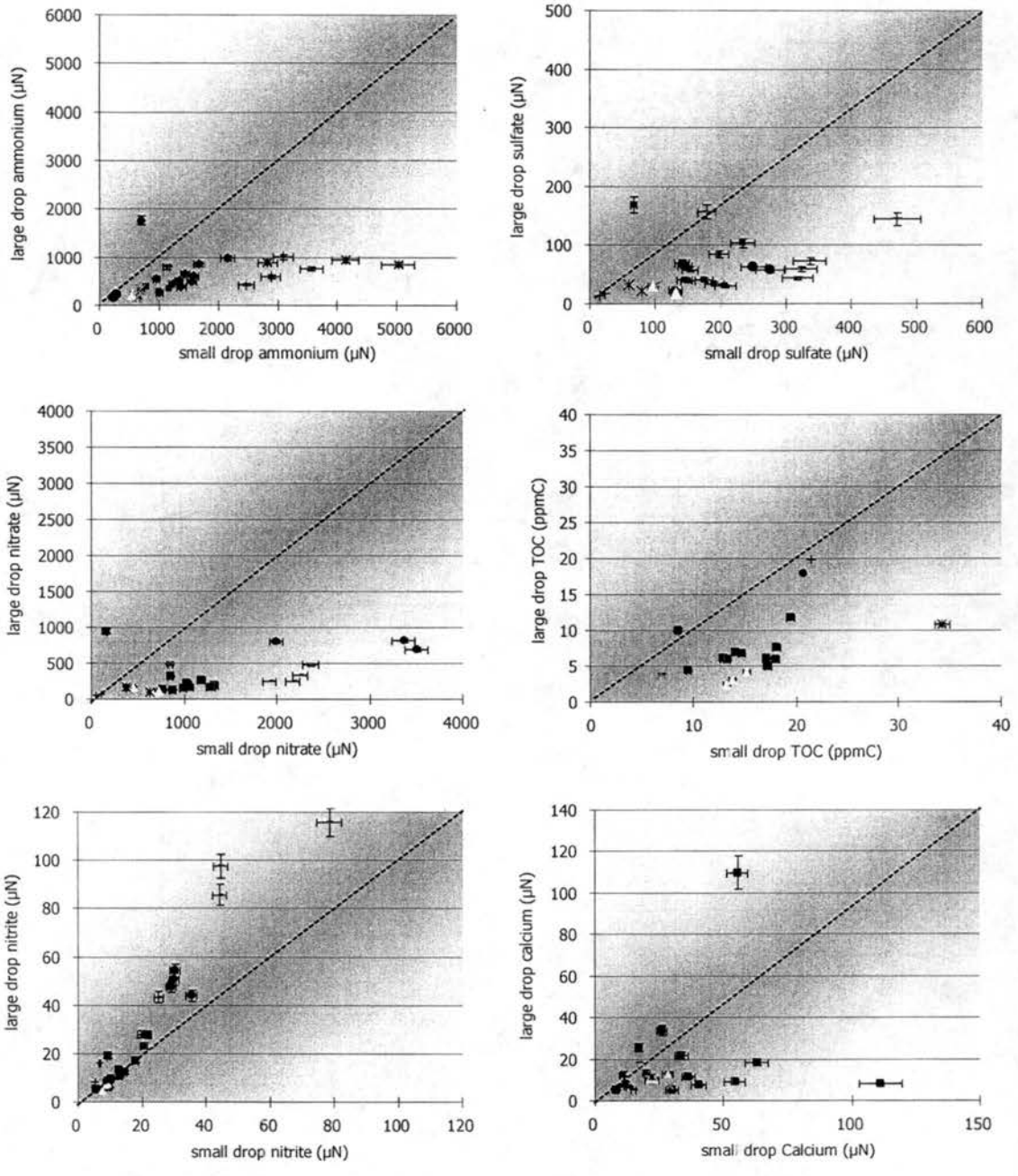

Figure 4-34. Size distributions of NH_4^+, SO_4^{2-}, NO_3^-, TOC, NO_2^- and Ca^{2+}. Error bars represent relative standard deviation derived from replicate samples of ion chromatograph.

To explain these results, Figure 4-34 shows scatter plots of individual species' concentrations in large vs. small drops. Any point below the diagonal 1:1 line indicates that the concentration in smaller drops is higher than that in larger drops. It is clear that ammonium, sulfate, nitrate and TOC are enriched in smaller drops, while nitrite is enriched in larger drops. Figure 4-35 shows the trend of deposition velocities of NH_4^+, SO_4^{2-}, NO_3^- and NO_2^- to their concentration ratios of small / large for fog events on 12/18/00. They were plotted for every sampling period; the lines are trendlines. For each sampling period, the higher the species' small/large drop concentration ratio, the lower deposition velocity is. This is consistent with former study by Moore et al. (2004), who found that fog solute deposition velocities depend on the species distribution across the drop size spectrum. Enrichment of species in small fog drops leads to lower deposition velocities, due to the dependence of settling velocity on drop size. Likewise, species enriched in large drops tend to exhibit higher deposition velocities.

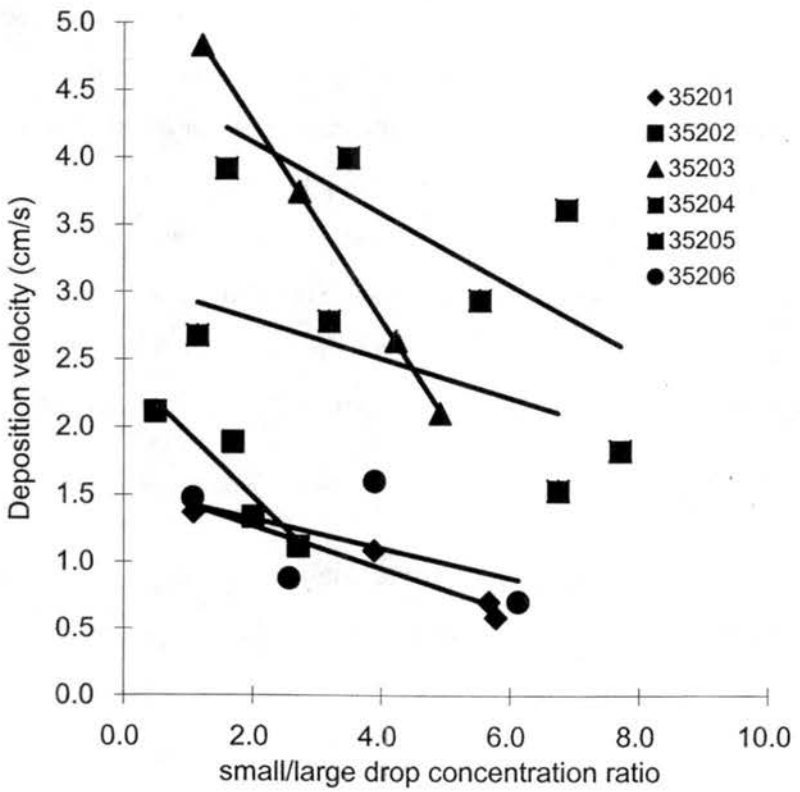

Figure 4-35. Deposition velocity vs. small/large drop concentration ratio for fog samples collected in the 12/18/00 fog event. Each point represents one species (from left to right NO_2^-, NH_4^+, SO_4^{2-} and NO_3^-).

Therefore, the tendency for the fog water deposition velocity to exceed the TOC deposition velocity is expected given the enrichment of TOC in smaller fog drops that settle from the atmosphere more slowly. Similarly, the average deposition velocities of sulfate, nitrate, and ammonium were all lower than that of water, since they were enriched in smaller fog drops. Nitrite is, by contrast, enriched in larger drops. Its deposition velocity ranged from 1.4-4.8 cm/s, averaging 2.7 cm/s, higher than the average deposition velocity of fog water. This is also consistent with the dependence of drop settling velocity on drop size.

4.3 Sulfur dioxide oxidation in fog drops

4.3.1 Theoretical reaction rates

As stated earlier dissolved sulfur dioxide has three potentially important oxidation reactions (oxidation by ozone, by hydrogen peroxide and by oxygen in the presence of trace metal catalysts) and can also react with HCHO to form HMS. Previous studies mentioned above have indicated that sulfate production rates can vary with drop size and that various of the S(IV) reaction pathways can be dominant, depending on environmental conditions (e.g., drop pH and concentrations of reactants and catalysts). In order to determine the dominant reaction pathways for S(IV) in various fog drop sizes during CRPAQS, literature expressions of the reaction rates of each relevant pathway were evaluated using the best available measurements or estimates of reactant concentrations and other relevant parameters.

The equations used for S(IV) oxidation rates calculations are as follows, with rate constants computed for a typical fog drop temperature of 283 K.

- For H_2O_2:

$$-\frac{d[S(IV)]}{dt} = \frac{k[H^+][H_2O_2][HSO_3^-]}{(1+13[H^+])} \qquad (4\text{-}3)$$

where k=3.2×10^7 M^{-1}S^{-1} (Seinfeld, 1986).

- For O_3:

$$-\frac{d[S(IV)]}{dt} = [O_3]\left(k_1[H_2SO_3] + k_2[HSO_3^-] + k_3[SO_3^{2-}]\right) \quad (4\text{-}4)$$

where k_1=2.4×10^4 M^{-1}S^{-1}, k_2=1.4×10^5 M^{-1}S^{-1}, and k_3=5.9×10^8 M^{-1}S^{-1} (Hoffmann, 1986).

- For O_2:

$$-\frac{d[S(IV)]}{dt} = k_2[Fe(III)][Mn(II)][S(IV)][H^+]^{-0.74} \quad \text{(when pH<4.2)} \quad (4\text{-}5)$$

$$-\frac{d[S(IV)]}{dt} = k_1[Fe(III)][Mn(II)][S(IV)][H^+]^{0.67} \quad \text{(when 4.2<pH<6.5)} \quad (4\text{-}6)$$

where k_1=6.3×10^{12} M^{-1}S^{-1}, k_2=9.31×10^6 M^{-1}S^{-1} (Ibusuki et al., 1987).

(Note: Only the second rate expression was used in this case since the pH was never low enough for the expression valid at pH < 4.2 to be relevant. The higher pH expression was used for all computations here, even when pH exceeded 6.5, due to lack of a more suitable published expression).

- For HCHO

$$-\frac{d[S(IV)]}{dt} = k_1\left[SO_3^{2-}\right]\left(\frac{k_2}{1+k_2}\right)[HCHO] \quad (4\text{-}7)$$

where k_1=5.4×10^6 M^{-1}S^{-1}, k_2=5.5×10^{-4} M^{-1}S^{-1} (Seinfeld, 1986).

4.3.2 Predicted S(IV) oxidation rates

An aqueous chemistry model (Reilly et al., 2002) was used to predict S(IV) oxidation rates for particular drop sizes during various fog event periods. The model couples gas phase and aqueous phase interactions, based on equations described by Seinfeld et al. (1998).

In the model we assume that temperature is fixed. During drop condensation/evaporation, latent heat will be released/absorbed, and the particle surface temperature will change until the rate of heat transfer balances the rate of heat generation/consumption. The criterion for neglecting these temperature effect can be described as (Seinfeld et al., 1998):

$$\frac{D_g}{\alpha}\left(\frac{M_A}{M_{air}}\right)In\left(\frac{1-x_{As}}{1-x_{A\infty}}\right)<<1 \qquad (4\text{-}8)$$

where D_g is the diffusivity of species A in air; □=k/□c_p is the thermal diffusivity of air; M_A and M_{air} are the molecular weights of species A and air; x_{As} and $x_{A□}$ are the mole fractions of A at the particle surface and far away from it. In most applications involving mass and heat transfer to atmospheric particles, this evaporation/condensation effect on temperature can be neglected (Davis, 1983).

Another assumption is that continuum transport properties are valid. If the mean free path of the diffusing vapor molecules becomes comparable to the particle diameter, continuum transport is not valid, and we need to use □, the accomodation coefficient to correct for free molecular effects. This coefficient can be approximated by (Fuchs et al., 1971):

$$\eta=\left\{1+\left[\frac{1.33+0.71K_n^{-1}}{1+K_n^{-1}}+\frac{4(1-a_w)}{3a_w}\right]K_n\right\}^{-1} \qquad (4\text{-}9)$$

where Kn is the Knudsen number (ratio of the mean free path of air to droplet radius) and a_w is a sticking coefficient that describes the probability that a gas molecule reaching the particle surface will adhere to it. This accomodation coefficient was calculated for each species in the model.

Finally, the effective Henry's law coefficient (accounting for ionization reactions in solution) was utilized for species such as dissolved SO_2, which can deprotonate in solution.

The basic equations we used in the model are (Seinfeld et al., 1998):

$$\frac{dP}{dt} = -k_{mt} w_L p + \frac{1}{H_A} k_{mt} C_{aq} w_L \tag{4-10}$$

$$\frac{dC_{aq}}{dt} = \frac{k_{mt}}{RT} p - \frac{k_{mt}}{H_A RT} C_{aq} - QR_{aq} \tag{4-11}$$

$$k_{mt} = \left[\frac{R_p^2 RT}{3D_g} + \frac{R_p \left(2\pi M_A RT\right)^{1/2}}{3\alpha} \right]^{-1} \tag{4-12}$$

where w_L is the cloud liquid water volume fraction, p is the bulk partial pressure of species A in the fog, C_{aq} is the corresponding aqueous-phase concentration at the surface of the drop, H_A is the effective Henry's law coefficient, k_{mt} is the mass transfer coefficient for gas-phase plus interfacial mass transport, R_{aq} is the overall rate of aqueous-phase reaction, and Q is a correction factor for any aqueous-phase mass transport limitations present, defined as:

$$Q = 3\left(\frac{\coth q}{q} - \frac{1}{q^2} \right), \qquad q = R_p \sqrt{\frac{k}{D_{aq}}} \tag{4-13}$$

where q is a dimensionless parameter, D_{aq} is the aquesous phase diffusivity and k is the corresponding rate constant if no mass transport limitations are considered (only consider $A(aq) \rightarrow B(aq)$ and $R_{aq}=k[A(aq)]=kH_AP_A$).

As stated above potentially important pathways of aqueous phase S(IV) oxidation include oxidation by hydrogen peroxide, by ozone and autooxidation catalyzed by Fe(III) and Mn(II). Previous SJV fog studies (Reilly et al., 2001) found that even if we assume that all Fe and Mn measured in the fog droplets is in a catalytically active form, the autooxidation pathway is still too slow to be an important contributor. So in our modeling, we did not include simulation of the autooxidation pathway; only oxidation of S(IV) by ozone and by hydrogen peroxide and complexation of S(IV) by formaldehyde were included.

One modification is to the aqueous phase mass transport limitation correction factor, Q. We used the formulation for Q for a first order reaction given in Seinfeld et al., (1998), but modified it to account for higher-order reactions. We calculated initial estimates of Q for S(IV), ozone and hydrogen peroxide, then iterated until convergence was reached for each of these species. The Q values for each species were examined as part of the simulation output. A large q (corresponding to a small Q) value indicates significant concentration gradients develop inside the drop.

One parameter which is also in the output file is the partition function of each species, defined as

$$PF = \frac{Real \quad aqueous \quad phase \quad concentration}{Theoretical \quad aqueous \quad phase \quad concentration} \tag{4-14}$$

This parameter related the aqueous phase concentration to the Henry's law predicted aqueous phase concentration. Because theoretical aqueous phase concentration is the equilibrium concentration with gas phase, this parameter indicates whether the species has reached equilibrium with the gas phase or not.

4.3.3 Experiment approach

The aqueous chemistry model was used to simulate the chemical evolution of large and small drop fog water fractions. Table 4-8 shows the Parameters and initial conditions used in the model. Appendix F shows the code in detail.

Table 4-8 Parameters and initial conditions in the model

Parameters	Species	Value
Sticking coefficient a_w	Default	0.05
	SO_2 (g)	0.035
	O_3 (g)	5.4×10^{-4}
	H_2O_2 (g)	0.18
	NH_3 (g)	0.06
	HNO_3 (g)	0.2
	HCHO (g)	0.05
Diffusivity D_g (cm^2/s)	S(IV), O_3 and H_2O_2	1×10^{-5}
Initial Q	S(IV), O_3 and H_2O_2	1.0
Initial PF	S(IV), O_3 and H_2O_2	1.0
Gas constant (L atm/mol K)		0.082058
Mean free path (cm)		6.5×10^{-6}

Table 4-9 shows the input parameters used for simulating fog events at the Angiola main site. Inputs were selected as follows. Temperature and pressure were measured by weather station, averaged to the appropriate sampling time. LWC was measured by the PVM. The pH values of fog water samples (large and small drop fractions) were measured on site. Aqueous concentrations of O_3 and H_2O_2 were calculated according to Henry's law equilibrium from measured gas concentrations averaged over appropriate sampling times. Concentrations of SO_2, unfortunately, were not measured in CRPAQS and had to be estimated based on results from previous measurements in the region (Reilly et al., 2000). Aqueous concentrations of dissolved SO_2 were then calculated using measured drop pH and assuming equilibrium phase partitioning. HCHO concentrations

Table 4-9. Model input parameters used for fog events at the Angiola main site.

Sample Name	pH	Radius (cm)	Temp (K)	Pressure (p)	SO_2 (ppb)	SO_2 (mol/L)	O_3 (ppb)	O_3 (mol/L)	H_2O_2 (ppb)	H_2O_2 (mol/L)	[HCHO] (M)	LWC (L/L)
AGPCL01501	6.08	0.0023	275.80	1015.96	0.94	4.16E-11	5.90	2.61E-10	0.01119	4.96E-13	1.08E-05	1.16E-07
AGPCL01701	6.70	0.0023	273.61	1019.35	0.94	4.21E-11	2.67	1.20E-10	0.19570	8.77E-12	1.79E-05	1.17E-07
AGPCL01702	6.52	0.0023	273.25	1020.09	0.94	4.22E-11	3.22	1.45E-10	0.12810	5.75E-12	1.18E-05	6.70E-08
AGPCL01703	6.35	0.0023	273.46	1020.95	0.94	4.22E-11	1.99	8.94E-11	0.17660	7.93E-12	9.09E-06	7.60E-08
AGPCL02101	6.45	0.0019	275.81	1016.15	0.94	4.17E-11	2.13	9.44E-11	0.00340	1.51E-13	2.35E-05	1.79E-07
AGPCL02102	6.44	0.0019	275.85	1017.33	0.94	4.17E-11	3.50	1.55E-10	0.00260	1.15E-13	1.54E-05	2.32E-07
AGPCL02103	6.58	0.0021	276.05	1017.33	0.94	4.17E-11	5.03	2.23E-10	0.02087	9.25E-13	1.57E-05	1.20E-07
AGPCL02501	6.43	0.0024	276.18	1019.69	0.94	4.17E-11	4.57	2.03E-10	0.05666	2.52E-12	5.22E-06	7.34E-08
AGPCL02502	6.58	0.0023	275.82	1020.68	0.94	4.18E-11	3.10	1.38E-10	0.08144	3.62E-12	7.43E-06	9.28E-08
AGPCL03101	6.50	0.0023	278.16	1019.00	0.94	4.14E-11	4.50	1.98E-10	0.03055	1.35E-12	3.97E-05	2.78E-07
AGPCL03102	6.81	0.0023	277.73	1019.77	0.94	4.15E-11	3.95	1.74E-10	0.04249	1.88E-12	3.74E-05	1.55E-07
AGPCL03103	7.04	0.0023	278.24	1020.77	0.94	4.15E-11	5.87	2.59E-10	0.13870	6.12E-12	4.63E-05	6.70E-08
AGPCL03201	6.61	0.0016	275.45	1021.00	0.94	4.19E-11	2.25	1.00E-10	0.11620	5.18E-12	2.61E-05	3.07E-08
AGPCL03202	6.53	0.0018	274.52	1021.00	0.94	4.20E-11	2.03	9.08E-11	0.11620	5.20E-12	2.78E-05	8.10E-08
AGPCL35201	6.52	0.0027	276.40	1022.54	0.94	4.18E-11	7.44	3.31E-10	0.97890	4.36E-11	1.56E-05	4.50E-07
AGPCL35202	8.02	0.0023	277.43	1022.00	0.94	4.16E-11	6.84	3.03E-10	0.01603	7.10E-13	1.81E-05	2.87E-07
AGPCL35203	7.19	0.0029	278.21	1022.00	0.94	4.15E-11	6.41	2.83E-10	0.05602	2.48E-12	2.05E-05	3.57E-07
AGPCL35204	7.02	0.0027	278.82	1021.50	0.94	4.14E-11	6.31	2.78E-10	0.04186	1.84E-12	2.29E-05	2.40E-07
AGPCL35205	7.31	0.0023	278.84	1021.50	0.94	4.14E-11	8.25	3.63E-10	0.11440	5.04E-12	2.53E-05	2.56E-07
AGPCL35206	7.32	0.0023	278.57	1022.00	0.94	4.15E-11	4.07	1.80E-10	0.16590	7.32E-12	2.77E-05	2.29E-07
AGPCL35207	7.50	0.0021	278.30	1022.42	0.94	4.15E-11	4.32	1.91E-10	0.15960	7.05E-12	3.02E-05	2.31E-07
AGPCL35208	7.42	0.0023	278.52	1022.92	0.94	4.15E-11	6.37	2.81E-10	0.20640	9.12E-12	2.28E-05	2.17E-07
AGPCL35209	7.48	0.0021	279.03	1023.08	0.94	4.15E-11	7.96	3.51E-10	0.03483	1.54E-12	3.00E-05	1.74E-07
AGPCL35210	7.49	0.0021	279.80	1022.83	0.94	4.13E-11	8.55	3.76E-10	0.24030	1.06E-11	2.92E-05	1.57E-07
AGPCL35211	7.47	0.0019	280.47	1022.08	0.94	4.12E-11	9.73	4.26E-10	0.05062	2.22E-12	3.15E-05	1.08E-07
AGPCL35301	6.48	0.0026	276.35	1019.86	0.94	4.17E-11	3.06	1.36E-10	0.02123	9.42E-13	2.27E-05	3.18E-07
AGPCL35302	6.15	0.0029	276.35	1019.12	0.94	4.17E-11	1.95	8.65E-11	0.01234	5.47E-13	2.27E-05	2.63E-07
AGPCL35303	6.41	0.0026	275.85	1020.22	0.94	4.18E-11	1.98	8.81E-11	0.03423	1.52E-12	2.27E-05	1.84E-07
AGPCS01501	6.30	0.0015	275.80	1015.96	0.94	4.16E-11	5.90	2.61E-10	0.01119	4.96E-13	1.08E-05	1.16E-07
AGPCS01701	6.91	0.0015	273.61	1019.35	0.94	4.21E-11	2.67	1.20E-10	0.19570	8.77E-12	1.28E-05	1.17E-07
AGPCS01702	6.91	0.0015	273.25	1020.09	0.94	4.22E-11	3.22	1.45E-10	0.12810	5.75E-12	1.28E-05	6.70E-08
AGPCS01703	6.58	0.0015	273.46	1020.95	0.94	4.22E-11	1.99	8.94E-11	0.17660	7.93E-12	1.28E-05	7.60E-08
AGPCS02101	6.50	0.0014	275.81	1016.15	0.94	4.17E-11	2.13	9.44E-11	0.00340	1.51E-13	2.83E-05	1.79E-07
AGPCS02102	6.68	0.0014	275.85	1017.33	0.94	4.17E-11	3.50	1.55E-10	0.00260	1.15E-13	3.11E-05	2.32E-07
AGPCS02103	6.44	0.0012	276.05	1017.33	0.94	4.17E-11	5.03	2.23E-10	0.02087	9.25E-13	2.94E-05	1.20E-07
AGPCS02501	6.56	0.0016	276.18	1019.69	0.94	4.17E-11	4.57	2.03E-10	0.05666	2.52E-12	1.31E-05	7.34E-08
AGPCS02502	6.60	0.0017	275.82	1020.68	0.94	4.18E-11	3.10	1.38E-10	0.08144	3.62E-12	1.31E-05	9.28E-08
AGPCS03101	6.00	0.0015	278.16	1019.00	0.94	4.14E-11	4.50	1.98E-10	0.03055	1.35E-12	5.58E-05	2.78E-07
AGPCS03102	6.29	0.0015	277.73	1019.77	0.94	4.15E-11	3.95	1.74E-10	0.04249	1.88E-12	5.47E-05	1.55E-07
AGPCS03103	6.73	0.0015	278.24	1020.77	0.94	4.15E-11	5.87	2.59E-10	0.13870	6.12E-12	6.58E-05	6.70E-08
AGPCS03201	6.46	0.0009	275.45	1021.00	0.94	4.19E-11	2.25	1.00E-10	0.11620	5.18E-12	4.69E-05	3.07E-08
AGPCS03202	6.39	0.0013	274.52	1021.00	0.94	4.20E-11	2.03	9.08E-11	0.11620	5.20E-12	4.69E-05	8.10E-08
AGPCS35201	6.75	0.0023	276.40	1022.54	0.94	4.18E-11	7.44	3.31E-10	0.97890	4.36E-11	1.81E-05	4.50E-07
AGPCS35202	6.76	0.0015	277.43	1022.00	0.94	4.16E-11	6.84	3.03E-10	0.01603	7.10E-13	1.93E-05	2.87E-07
AGPCS35203	7.10	0.0015	278.21	1022.00	0.94	4.15E-11	6.41	2.83E-10	0.05602	2.48E-12	2.05E-05	3.57E-07
AGPCS35204	6.85	0.0015	278.82	1021.50	0.94	4.14E-11	6.31	2.78E-10	0.04186	1.84E-12	2.16E-05	2.40E-07
AGPCS35205	6.91	0.0015	278.84	1021.50	0.94	4.14E-11	8.25	3.63E-10	0.11440	5.04E-12	2.28E-05	2.56E-07
AGPCS35206	6.89	0.0015	278.57	1022.00	0.94	4.15E-11	4.07	1.80E-10	0.16590	7.32E-12	2.40E-05	2.29E-07
AGPCS35207	7.25	0.0013	278.30	1022.42	0.94	4.15E-11	4.32	1.91E-10	0.15960	7.05E-12	2.51E-05	2.31E-07
AGPCS35208	7.21	0.0013	278.52	1022.92	0.94	4.15E-11	6.37	2.81E-10	0.20640	9.12E-12	2.68E-05	2.17E-07
AGPCS35209	7.32	0.0013	279.03	1023.08	0.94	4.15E-11	7.96	3.51E-10	0.03483	1.54E-12	2.15E-05	1.74E-07
AGPCS35210	7.25	0.0013	279.80	1022.83	0.94	4.13E-11	8.55	3.76E-10	0.24030	1.06E-11	3.65E-05	1.57E-07
AGPCS35211	7.12	0.0011	280.47	1022.08	0.94	4.12E-11	9.73	4.26E-10	0.05062	2.22E-12	4.13E-05	1.08E-07
AGPCS35301	6.54	0.0022	276.35	1019.86	0.94	4.17E-11	3.06	1.36E-10	0.02123	9.42E-13	3.38E-05	3.18E-07
AGPCS35302	6.37	0.0021	276.35	1019.12	0.94	4.17E-11	1.95	8.65E-11	0.01234	5.47E-13	3.38E-05	2.63E-07
AGPCS35303	6.60	0.0019	275.85	1020.22	0.94	4.18E-11	1.98	8.81E-11	0.03423	1.52E-12	3.38E-05	1.84E-07

were taken from measured aqueous concentrations. The average radius of large and small fog drop fractions were computed by combining information about the drop size distribution (from the CSASP) with sf-CASCC drop size dependent collection efficiencies. This approach yields the expected size distributions of drops collected during each sample period in the two sf-CASCC collection stages. The average volume weighted drop size was then computed for each "collected" distribution. When data were unavailable, concentrations from preceding or subsequent time periods were used.

4.3.4 Results and discussion

4.3.4.1 Model results

Table 4-10 shows key output parameters from the model simulations. Included are the partition function and correction factor, Q, for each species and the reaction rates for oxidation by hydrogen peroxide and by ozone and the HMS formation rate. Sample names with an "L" indicate they represent the large drop fraction from the sf-CASCC; those with an "S" represent the small drop fraction. From the partition functions of each species, we can see that partition function of ozone is nearly equal to one for all the fog samples. This is expected since ozone has low solubility in water and can quickly reach phase equilibrium. For S(IV) and H_2O_2, there are very small partition functions for some fog samples, implying the gas-aqueous phase has not had adequate time to reach equilibrium. Correction factors, Q of O_3 are not very large for all the fog samples indicating significant concentration gradients inside the drops. For most samples, the correction factors for H_2O_2 and S(IV) are close to one, implying concentration gradients inside the drops exist, but are not serious.

Table 4-10. Partition function, Q, and rate for hydrogen peroxide, ozone oxidation, and HMS formation reaction rates respectively.

Samples	S(IV) (mol/L)	HCHO (mol/L)	S(VI) (mol/L)	Partition function_S (IV)	Partition function_O_3	Partition function_H_2O_2	Q_O3	Q_H2O2	Q_SIV	r_O3ox (mol s^{-1})	r_H2O2ox (mol s-1)	r_HMS (mol s-1)	r_totS(IV) (mol s-1)
AGPCL0150	6.18E-05	1.08E-05	3.16E-05	7.84E-01	9.84E-01	8.53E-01	8.44E-02	1.00E+00	1.00E+00	2.32E-08	4.03E-09	4.11E-07	4.38E-07
AGPCL0170	5.33E-05	1.79E-05	3.37E-05	1.04E-01	9.74E-01	9.69E-01	5.52E-02	1.00E+00	9.99E-01	1.75E-08	1.31E-08	1.81E-06	1.84E-06
AGPCL0170	8.65E-05	1.18E-05	4.99E-05	2.80E-01	9.71E-01	9.25E-01	5.08E-02	1.00E+00	9.99E-01	2.32E-08	2.28E-08	1.43E-06	1.48E-06
AGPCL0170	9.82E-05	9.09E-06	6.96E-05	5.18E-01	9.74E-01	8.75E-01	5.52E-02	1.00E+00	1.00E+00	1.31E-08	5.41E-08	9.23E-07	9.90E-07
AGPCL0210	6.60E-05	2.35E-05	1.84E-05	3.13E-01	9.77E-01	9.55E-01	6.93E-02	1.00E+00	9.99E-01	1.51E-08	5.51E-10	1.97E-06	1.98E-06
AGPCL0210	8.58E-05	1.54E-05	3.36E-05	4.20E-01	9.74E-01	9.41E-01	6.14E-02	1.00E+00	1.00E+00	2.79E-08	5.52E-10	1.65E-06	1.68E-06
AGPCL0210	7.13E-05	1.57E-05	4.70E-05	2.38E-01	9.73E-01	9.59E-01	5.37E-02	1.00E+00	9.99E-01	3.76E-08	2.52E-09	1.79E-06	1.83E-06
AGPCL0250	1.14E-04	5.22E-06	5.41E-05	5.86E-01	9.69E-01	8.80E-01	4.25E-02	1.00E+00	1.00E+00	3.31E-08	1.53E-08	7.30E-07	7.78E-07
AGPCL0250	1.08E-04	7.43E-06	4.51E-05	3.53E-01	9.66E-01	9.27E-01	4.04E-02	1.00E+00	1.00E+00	2.60E-08	1.44E-08	1.28E-06	1.32E-06
AGPCL0310	3.02E-05	3.97E-05	2.41E-05	1.47E-01	9.83E-01	9.74E-01	7.57E-02	1.00E+00	9.98E-01	1.86E-08	1.92E-09	1.70E-06	1.72E-06
AGPCL0310	2.20E-05	3.74E-05	2.22E-05	4.12E-02	9.82E-01	9.92E-01	6.99E-02	1.00E+00	9.97E-01	1.79E-08	7.94E-10	1.93E-06	1.94E-06
AGPCL0310	1.35E-05	4.63E-05	2.98E-05	1.22E-02	9.83E-01	9.98E-01	7.56E-02	1.00E+00	9.95E-01	2.43E-08	7.40E-10	1.98E-06	2.00E-06
AGPCL0320	7.12E-05	2.61E-05	4.15E-05	2.08E-01	9.73E-01	9.77E-01	6.96E-02	1.00E+00	9.99E-01	2.25E-08	1.33E-08	3.11E-06	3.15E-06
AGPCL0320	6.20E-05	2.78E-05	3.47E-05	2.14E-01	9.76E-01	9.68E-01	7.27E-02	1.00E+00	9.99E-01	1.59E-08	1.47E-08	2.50E-06	2.53E-06
AGPCL3520	4.82E-05	1.56E-05	1.32E-04	1.95E-01	9.78E-01	9.42E-01	5.30E-02	1.00E+00	9.99E-01	3.40E-08	9.32E-08	1.09E-06	1.22E-06
AGPCL3520	1.93E-05	1.81E-05	5.44E-05	3.28E-04	9.73E-01	9.99E-01	4.86E-02	1.00E+00	9.96E-01	4.55E-08	2.47E-12	1.99E-06	2.03E-06
AGPCL3520	1.67E-05	2.05E-05	3.06E-05	8.91E-03	9.79E-01	9.91E-01	5.02E-02	1.00E+00	9.96E-01	2.55E-08	2.18E-10	1.28E-06	1.30E-06
AGPCL3520	2.01E-05	2.29E-05	3.25E-05	2.04E-02	9.79E-01	9.93E-01	5.29E-02	1.00E+00	9.97E-01	2.70E-08	3.52E-10	1.44E-06	1.47E-06
AGPCL3520	1.85E-05	2.53E-05	5.50E-05	6.64E-03	9.77E-01	9.99E-01	5.58E-02	1.00E+00	9.96E-01	4.58E-08	3.14E-10	1.97E-06	2.00E-06
AGPCL3520	1.71E-05	2.77E-05	2.66E-05	5.78E-03	9.78E-01	9.99E-01	5.82E-02	1.00E+00	9.96E-01	2.19E-08	4.07E-10	2.00E-06	2.01E-06
AGPCL3520	1.65E-05	3.02E-05	3.19E-05	2.71E-03	9.77E-01	1.00E+00	6.14E-02	1.00E+00	9.96E-01	2.65E-08	1.88E-10	2.37E-06	2.39E-06
AGPCL3520	1.92E-05	2.28E-05	4.52E-05	4.39E-03	9.76E-01	9.99E-01	5.32E-02	1.00E+00	9.96E-01	3.75E-08	3.87E-10	1.98E-06	2.01E-06
AGPCL3520	1.65E-05	3.00E-05	5.81E-05	3.08E-03	9.78E-01	1.00E+00	6.05E-02	1.00E+00	9.96E-01	4.85E-08	4.40E-11	2.35E-06	2.39E-06
AGPCL3521	1.65E-05	2.92E-05	6.30E-05	3.16E-03	9.77E-01	1.00E+00	5.89E-02	1.00E+00	9.96E-01	5.24E-08	2.90E-10	2.33E-06	2.38E-06
AGPCL3521	1.83E-05	3.15E-05	8.24E-05	3.99E-03	9.77E-01	1.00E+00	6.09E-02	1.00E+00	9.96E-01	6.88E-08	7.26E-11	2.79E-06	2.85E-06
AGPCL3530	4.23E-05	2.27E-05	1.75E-05	1.91E-01	9.80E-01	9.48E-01	6.09E-02	1.00E+00	9.99E-01	1.31E-08	1.99E-09	1.29E-06	1.31E-06
AGPCL3530	4.27E-05	2.27E-05	8.94E-06	4.68E-01	9.85E-01	8.60E-01	7.42E-02	1.00E+00	9.99E-01	5.48E-09	2.56E-09	6.92E-07	7.00E-07
AGPCL3530	4.54E-05	2.27E-05	1.39E-05	2.41E-01	9.81E-01	9.33E-01	6.34E-02	1.00E+00	9.99E-01	8.26E-09	4.16E-09	1.22E-06	1.23E-06

Table 4-10 (Continue). Partition function, Q, and rate for hydrogen peroxide, ozone oxidation, and HMS formation reaction rates respectively.

Samples	S(IV) (mol/L)	HCHO (mol/L)	S(VI) (mol/L)	Partition function_S (IV)	Partition function_O_3	Partition function_H_2O_2	Q_O3	Q_H2O2	Q_SIV	r_O3ox (mol s^{-1})	r_H2O2ox (mol s-1)	r_HMS (mol s-1)	r_totS(IV) (mol s-1)
AGPCS0150	1.04E-04	1.08E-05	7.24E-05	7.44E-01	9.75E-01	9.34E-01	8.03E-02	1.00E+00	1.00E+00	5.71E-08	4.19E-09	1.08E-06	1.14E-06
AGPCS0170	1.19E-04	1.28E-05	7.11E-05	1.19E-01	9.56E-01	9.87E-01	4.89E-02	1.00E+00	1.00E+00	4.59E-08	1.52E-08	3.89E-06	3.95E-06
AGPCS0170	1.20E-04	1.28E-05	7.69E-05	1.17E-01	9.56E-01	9.86E-01	4.92E-02	1.00E+00	1.00E+00	5.56E-08	1.01E-08	3.90E-06	3.97E-06
AGPCS0170	1.37E-04	1.28E-05	8.14E-05	3.77E-01	9.63E-01	9.58E-01	5.84E-02	1.00E+00	1.00E+00	2.88E-08	4.31E-08	2.73E-06	2.80E-06
AGPCS0210	8.33E-05	2.83E-05	2.90E-05	3.44E-01	9.73E-01	9.72E-01	7.97E-02	1.00E+00	1.00E+00	2.38E-08	6.15E-10	3.28E-06	3.30E-06
AGPCS0210	7.04E-05	3.11E-05	5.01E-05	1.72E-01	9.72E-01	9.86E-01	7.46E-02	1.00E+00	9.99E-01	4.18E-08	2.37E-10	4.12E-06	4.16E-06
AGPCS0210	9.40E-05	2.94E-05	8.42E-05	4.67E-01	9.74E-01	9.73E-01	9.14E-02	1.00E+00	1.00E+00	6.58E-08	5.01E-09	3.46E-06	3.52E-06
AGPCS0250	1.13E-04	1.31E-05	7.80E-05	4.03E-01	9.67E-01	9.60E-01	5.67E-02	1.00E+00	1.00E+00	5.52E-08	1.15E-08	2.29E-06	2.36E-06
AGPCS0250	1.07E-04	1.31E-05	5.75E-05	3.32E-01	9.67E-01	9.61E-01	5.35E-02	1.00E+00	1.00E+00	3.56E-08	1.41E-08	2.32E-06	2.37E-06
AGPCS0310	4.00E-05	5.58E-05	3.38E-05	7.26E-01	9.89E-01	9.47E-01	1.60E-01	1.00E+00	1.00E+00	1.95E-08	9.22E-09	1.18E-06	1.21E-06
AGPCS0310	4.92E-05	5.47E-05	3.97E-05	4.12E-01	9.83E-01	9.68E-01	1.11E-01	1.00E+00	9.99E-01	2.59E-08	7.74E-09	2.57E-06	2.60E-06
AGPCS0310	2.95E-05	6.58E-05	5.79E-05	7.34E-02	9.81E-01	9.94E-01	9.59E-02	1.00E+00	9.98E-01	4.42E-08	4.43E-09	4.06E-06	4.10E-06
AGPCS0320	9.91E-05	4.69E-05	8.21E-05	4.45E-01	9.73E-01	9.84E-01	1.17E-01	1.00E+00	1.00E+00	4.07E-08	2.86E-08	6.00E-06	6.06E-06
AGPCS0320	6.97E-05	4.69E-05	5.21E-05	3.56E-01	9.78E-01	9.72E-01	1.06E-01	1.00E+00	9.99E-01	2.03E-08	2.46E-08	3.68E-06	3.72E-06
AGPCS3520	4.59E-05	1.81E-05	1.04E-04	9.40E-02	9.74E-01	9.80E-01	5.29E-02	1.00E+00	9.99E-01	4.69E-08	4.66E-08	1.75E-06	1.85E-06
AGPCS3520	8.46E-05	1.93E-05	1.08E-04	1.81E-01	9.67E-01	9.85E-01	5.74E-02	1.00E+00	9.99E-01	8.94E-08	1.35E-09	3.54E-06	3.63E-06
AGPCS3520	5.94E-05	2.05E-05	1.05E-04	4.37E-02	9.65E-01	9.97E-01	5.38E-02	1.00E+00	9.99E-01	8.74E-08	1.07E-09	4.15E-06	4.23E-06
AGPCS3520	6.97E-05	2.16E-05	9.75E-05	1.24E-01	9.68E-01	9.91E-01	5.70E-02	1.00E+00	9.99E-01	7.98E-08	2.14E-09	3.79E-06	3.86E-06
AGPCS3520	6.27E-05	2.28E-05	1.28E-04	9.23E-02	9.68E-01	9.93E-01	5.76E-02	1.00E+00	9.99E-01	1.03E-07	4.34E-09	3.90E-06	4.01E-06
AGPCS3520	6.21E-05	2.40E-05	6.73E-05	9.55E-02	9.69E-01	9.93E-01	5.91E-02	1.00E+00	9.99E-01	5.01E-08	6.69E-09	3.95E-06	4.00E-06
AGPCS3520	5.56E-05	2.51E-05	8.63E-05	2.39E-02	9.64E-01	9.99E-01	5.94E-02	1.00E+00	9.99E-01	7.07E-08	1.66E-09	5.51E-06	5.58E-06
AGPCS3520	5.33E-05	2.68E-05	1.22E-04	2.70E-02	9.65E-01	9.99E-01	6.13E-02	1.00E+00	9.99E-01	1.00E-07	2.38E-09	5.46E-06	5.56E-06
AGPCS3520	5.99E-05	2.15E-05	1.66E-04	2.09E-02	9.62E-01	9.99E-01	5.44E-02	1.00E+00	9.99E-01	1.39E-07	2.98E-10	5.46E-06	5.59E-06
AGPCS3521	3.71E-05	3.65E-05	1.39E-04	1.79E-02	9.70E-01	9.99E-01	6.92E-02	1.00E+00	9.98E-01	1.15E-07	1.64E-09	5.48E-06	5.59E-06
AGPCS3521	4.82E-05	4.13E-05	1.97E-04	3.92E-02	9.69E-01	9.99E-01	7.48E-02	1.00E+00	9.99E-01	1.64E-07	7.11E-10	7.16E-06	7.32E-06
AGPCS3530	3.71E-05	3.38E-05	1.97E-05	1.42E-01	9.81E-01	9.73E-01	7.25E-02	1.00E+00	9.98E-01	1.53E-08	1.51E-09	1.88E-06	1.89E-06
AGPCS3530	4.61E-05	3.38E-05	1.33E-05	2.83E-01	9.82E-01	9.53E-01	7.93E-02	1.00E+00	9.99E-01	9.70E-09	1.72E-09	1.71E-06	1.72E-06
AGPCS3530	4.45E-05	3.38E-05	1.83E-05	1.38E-01	9.78E-01	9.80E-01	7.38E-02	1.00E+00	9.99E-01	1.32E-08	2.50E-09	2.49E-06	2.50E-06

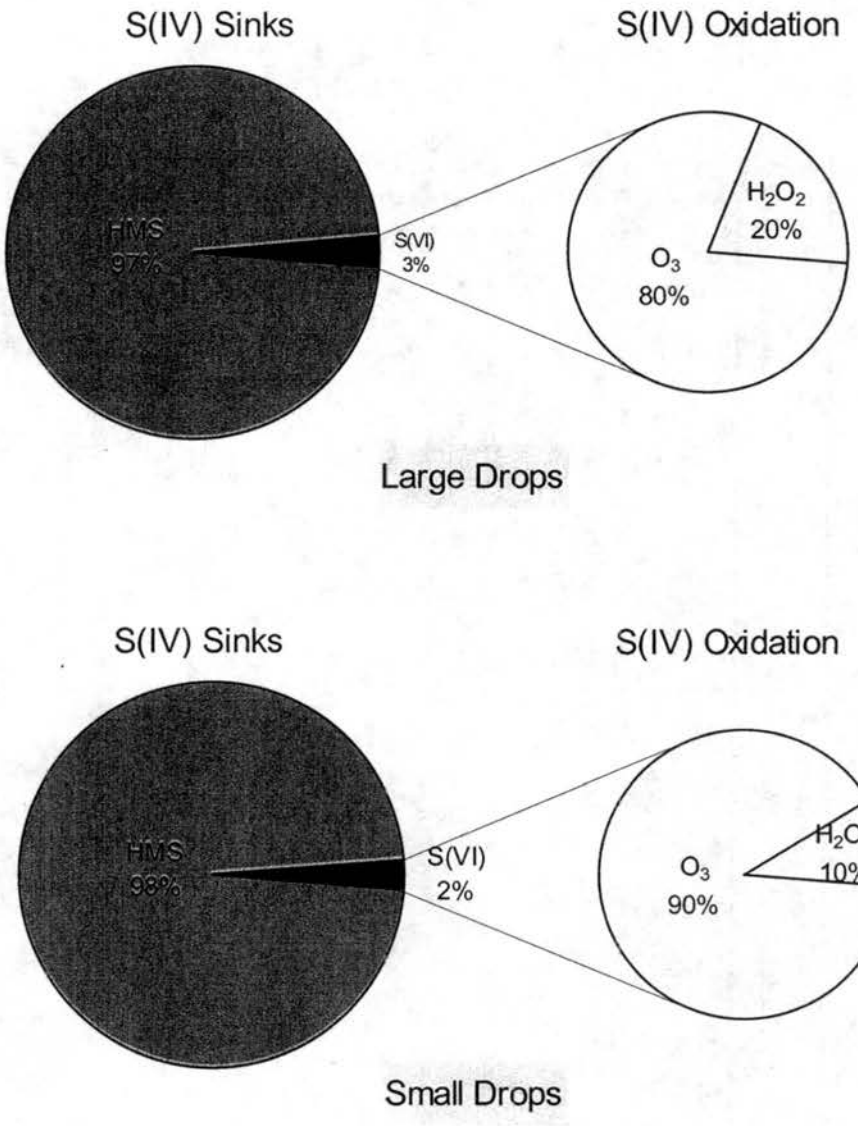

Figure 4-36. S(IV) sinks as calculated by the aqueous phase chemistry model for both the large (upper panel) and small (lower panel) drop fractions from the sf-CASCC.

Figure 4-36 summarizes model predicted average fates of S(IV) during the fog episodes for the large and small drop classes collected with the sf-CASCC. The largest sink of S(IV), based on the model prediction, is complexation with formaldehyde to form HMS. For the large drops, the HMS formation accounts for about 97% of the total S(IV) sink, while in the small drops, HMS formation accounts for 98%. Since the HCHO we

inputted into the model was the total HCHO we measured, including both "free" HCHO as well as HMS itself, the importance of this pathway may be slightly overestimated.

Figure 4-37 shows a sensitivity test of the dependence of the HMS formation rates on the HCHO concentration. Doubling the HCHO concentration has only a modest effect on the overall HMS formation rate because the rate is controlled primarily by the availability of S(IV) species brought into the drop. The average increase due to doubling HCHO concentration is only about 15%.

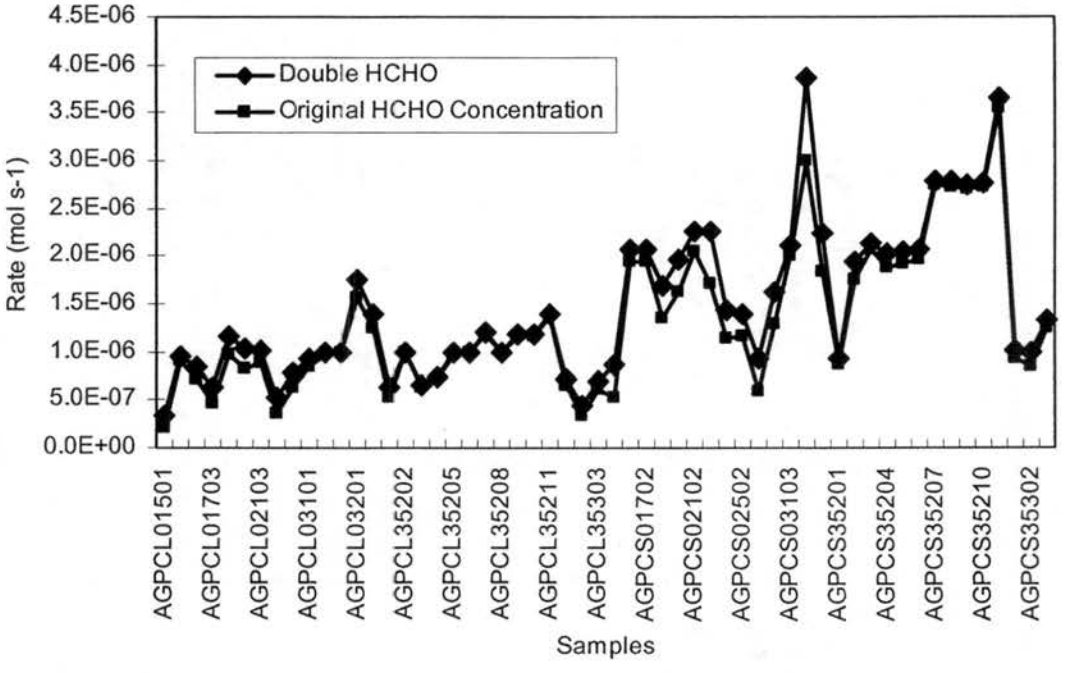

Figure 4-37. Sensitive test of rate of HMS formation to HCHO concentrations.

For S(IV) oxidation rates, Figure 4-36 shows that oxidation by ozone accounts for approximately 80% of the oxidation in the large drops, and approximately 90% in the small drops. Oxidation by hydrogen peroxide contributed for 20% in the large drops and 10% in the small drops. Hydrogen peroxide as S(IV) oxidant shows greater importance in large drops (20%), in contrast to previous studies (Reilly et al., 2001). Reilly et al. (2001) found that hydrogen peroxide showed greater importance as a S(IV) oxidant in small drops, due largely to the lower pH values found in small drops. Here the pH difference

between drop size classes is negligible. Figure 4-38 shows the sensitivity of the rate of the hydrogen peroxide S(IV) oxidation pathway to the hydrogen peroxide concentration. Doubling the H_2O_2 concentration almost doubles the oxidation rate, which means that the hydrogen peroxide oxidation rate is sensitive to the H_2O_2 concentration. Similarly, Figure 4-39 shows sensitivity test results for ozone. Doubling ozone concentrations also almost doubles ozone oxidation rates.

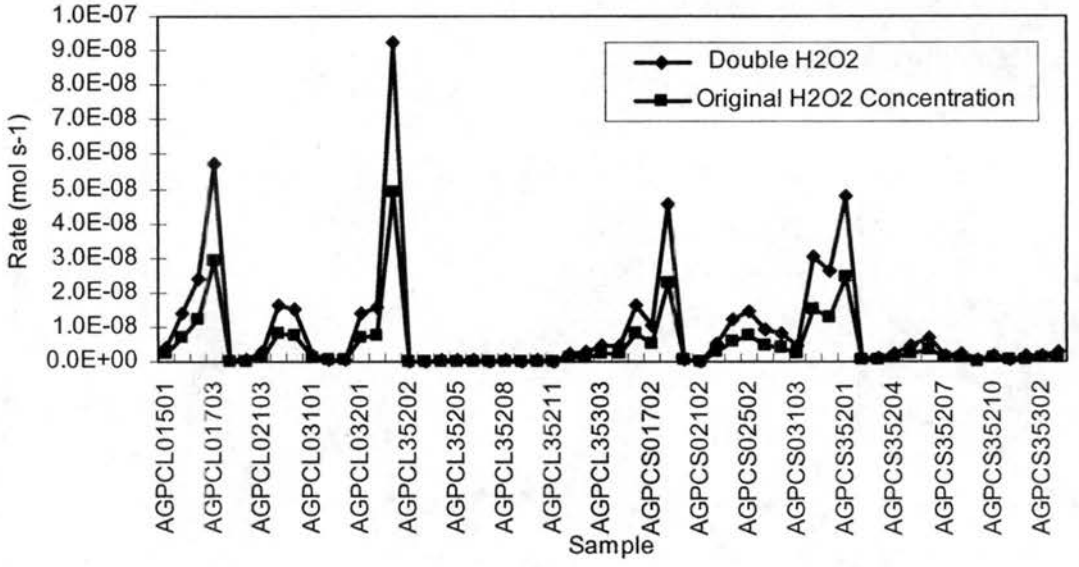

Figure 4-38. Sensitivity test of rate of the H_2O_2-S(IV) oxidation pathway to H_2O_2 concentrations.

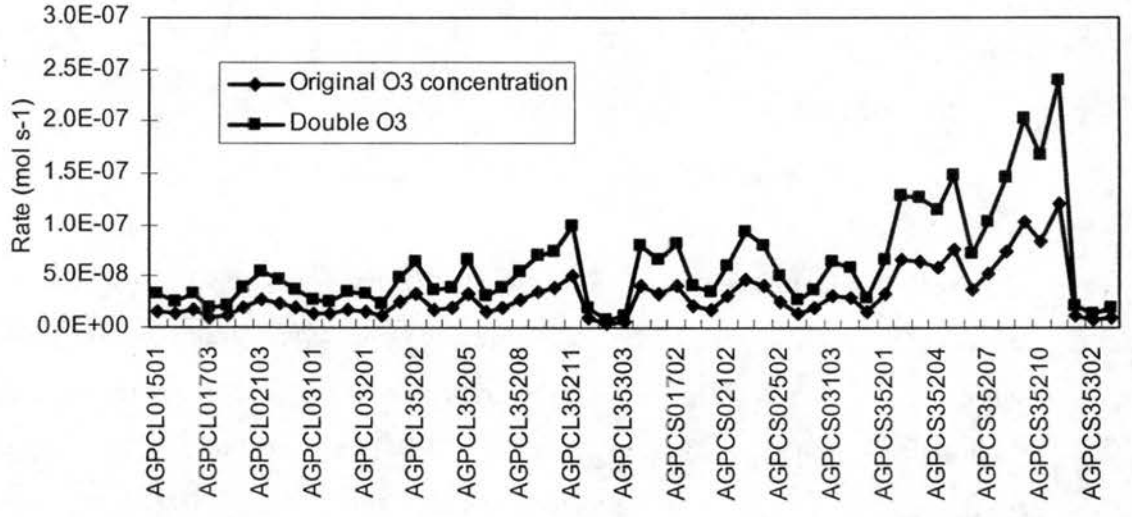

Figure 4-39. Sensitivity test of the rate of the O_3-S(IV) oxidation pathway to O_3 concentrations.

4.3.4.2 Theoretical S(IV) reaction rates

Table 4-11. Theoretical oxidation rate and HMS formation rate for all fog samples.

Sample Name	Oxidation by H_2O_2 ($M\ s^{-1}$)	Oxidation by O_3 ($M\ s^{-1}$)	HMSA prod. ($M\ s^{-1}$)	Sample Name	Oxidation by H_2O_2 ($M\ s^{-1}$)	Oxidation by O_3 ($M\ s^{-1}$)	HMSA prod. ($M\ s^{-1}$)
AGPCL01501	5.97E-09	3.73E-07	2.56E-07	AGPCS01501	5.97E-09	1.03E-06	7.06E-07
AGPCL01701	1.28E-07	3.27E-06	8.92E-06	AGPCS01701	1.28E-07	8.61E-06	1.68E-05
AGPCL01702	8.66E-08	1.76E-06	2.65E-06	AGPCS01702	8.66E-08	1.06E-05	1.73E-05
AGPCL01703	1.17E-07	4.91E-07	9.14E-07	AGPCS01703	1.17E-07	1.42E-06	3.72E-06
AGPCL02101	1.81E-09	7.39E-07	3.05E-06	AGPCS02101	1.81E-09	9.30E-07	4.62E-06
AGPCL02102	1.38E-09	1.16E-06	1.90E-06	AGPCS02102	1.38E-09	3.49E-06	1.16E-05
AGPCL02103	1.09E-08	3.06E-06	3.55E-06	AGPCS02103	1.09E-08	1.65E-06	3.57E-06
AGPCL02501	2.92E-08	1.42E-06	5.99E-07	AGPCS02501	2.92E-08	2.58E-06	2.74E-06
AGPCL02502	4.34E-08	1.96E-06	1.75E-06	AGPCS02502	4.34E-08	2.14E-06	3.40E-06
AGPCL03101	1.32E-08	1.75E-06	5.32E-06	AGPCS03101	1.32E-08	1.75E-07	7.46E-07
AGPCL03102	1.90E-08	6.53E-06	2.16E-05	AGPCS03102	1.90E-08	5.96E-07	2.88E-06
AGPCL03103	5.93E-08	2.73E-05	7.39E-05	AGPCS03103	5.93E-08	6.54E-06	2.52E-05
AGPCL03201	6.41E-08	1.66E-06	7.31E-06	AGPCS03201	6.41E-08	8.32E-07	6.57E-06
AGPCL03202	6.98E-08	1.09E-06	5.82E-06	AGPCS03202	6.98E-08	5.70E-07	5.16E-06
AGPCL35201	4.95E-07	3.46E-06	2.66E-06	AGPCS35201	4.95E-07	9.97E-06	8.91E-06
AGPCL35202	7.37E-09	3.02E-03	2.82E-03	AGPCS35202	7.37E-09	9.11E-06	9.10E-06
AGPCL35203	2.40E-08	5.95E-05	6.54E-05	AGPCS35203	2.40E-08	3.93E-05	4.32E-05
AGPCL35204	1.70E-08	2.60E-05	3.17E-05	AGPCS35204	1.70E-08	1.19E-05	1.37E-05
AGPCL35205	4.63E-08	1.29E-04	1.33E-04	AGPCS35205	4.63E-08	2.05E-05	1.90E-05
AGPCL35206	6.88E-08	6.75E-05	1.56E-04	AGPCS35206	6.88E-08	9.33E-06	1.87E-05
AGPCL35207	6.78E-08	1.66E-04	3.99E-04	AGPCS35207	6.78E-08	5.26E-05	1.05E-04
AGPCL35208	8.60E-08	1.68E-04	2.05E-04	AGPCS35208	8.60E-08	6.39E-05	9.13E-05
AGPCL35209	1.39E-08	2.70E-04	3.40E-04	AGPCS35209	1.39E-08	1.29E-04	1.17E-04
AGPCL35210	8.93E-08	2.92E-04	3.25E-04	AGPCS35210	8.93E-08	9.67E-05	1.34E-04
AGPCL35211	1.77E-08	2.93E-04	3.03E-04	AGPCS35211	1.77E-08	5.86E-05	7.90E-05
AGPCL35301	1.08E-08	1.19E-06	3.23E-06	AGPCS35301	1.08E-08	1.56E-06	6.34E-06
AGPCL35302	6.26E-09	1.65E-07	7.06E-07	AGPCS35302	6.26E-09	4.55E-07	2.90E-06
AGPCL35303	1.82E-08	5.70E-07	2.44E-06	AGPCS35303	1.82E-08	1.37E-06	8.73E-06

Rates of S(IV) reaction were also computed directly using the rate expressions for oxidation by ozone and by hydrogen peroxide, as well as for HMS formation, given above. These calculations assume all species attain phase equilibrium and that, consequently, there is no reactant limitation due to finite rates of mass transport inside or

outside of the droplets. Results of these calculations, termed here to be "theoretical" reaction rates, are shown in Table 4-11.

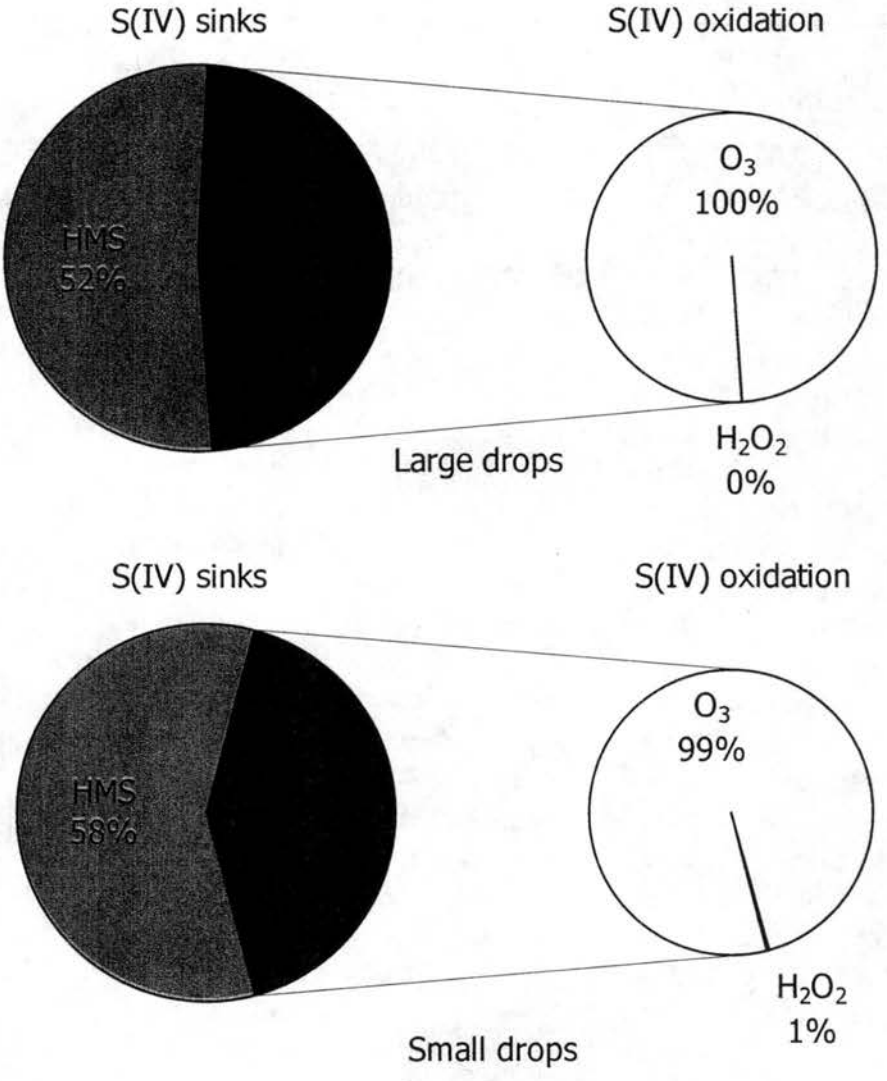

Figure 4-40. Theoretical rates of ozone and hydrogen peroxide oxidation and HMS formation averaged for all the large drop and small drop fog samples.

Based on Table 4-10, Figure 4-40 shows the average rates for the large and small drop classes as pie diagrams. In these calculations, both HMS formation and S(IV) oxidation by ozone are important components of dissolved sulfur dioxide. For small droplets, HMS

formation accounts for about 58%, which is slightly higher than in large droplets. O_3 oxidation pathway is still the dominant pathway for all large and small drops.

4.3.4.3 Comparison of theoretical and modeled rates

Comparing Figure 4-36 and Figure 4-40, we see a very large difference between modeled and theoretical rates. The modeled rates predicted that over 97% of the S(IV) reacts with HCHO to form HMS; while the theoretical rate calculations suggest this value to be somewhat below 60%. Further, S(IV) oxidation is clearly dominated by ozone in the theoretical rate calculations.

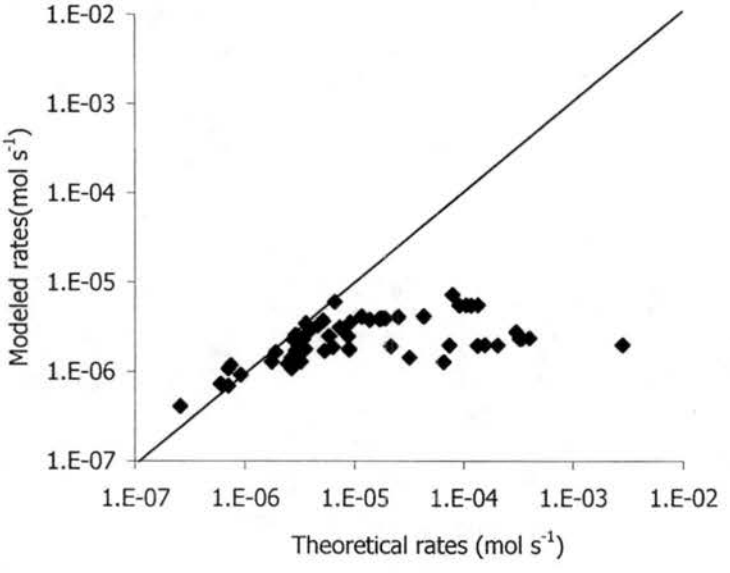

Figure 4-41. Comparison of HMS formation modeled rates and theoretical rates.

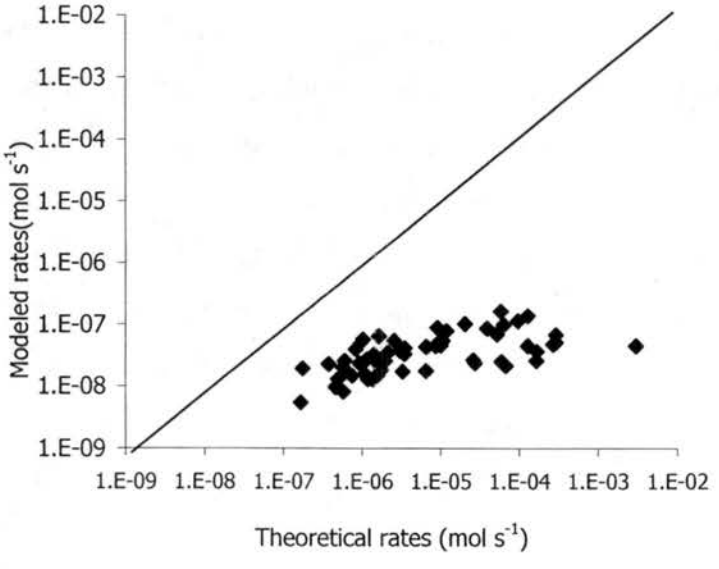

Figure 4-42. Comparison of ozone oxidation modeled rates and theoretical rates.

Figures 4-41 and 4-42 show scatter plots of modeled vs. theoretical rates for HMS formation and ozone oxidation. We can see again quite clearly that theoretical rates are nearly always much higher than modeled rates. Together, these analyses clearly indicate the importance of considering mass transport limitations to rates of reaction in these highly reactive systems.

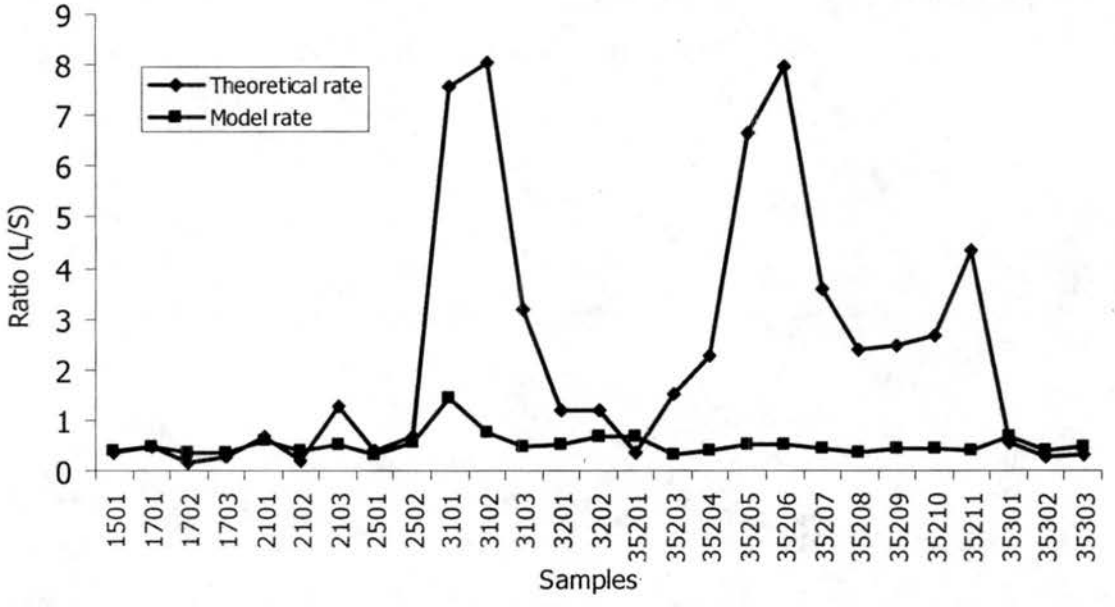

Figure 4-43. Theoretical and model rate comparison to large/small ratios for all fog sample periods.

Figure 4-43 shows large drop/small drop ratios vs. total rate (S(IV) oxidation plus HMS formation) for CRPAQS fog sample periods. Sample 35302 is not shown because the ratio is too large to fit in the plot. Rate ratios are shown both for the model results and the direct theoretical rate calculations. Nearly all model predicted ratios are below one, indicating that the total rate of reaction of dissolved SO_2 is higher in small drops. This is a consequence of the reduced mass transport limitations for smaller drops. The theoretical rate ratios, by contrast, vary widely. Again, the difference between these two sets of results illustrates the importance of considering mass transport limitations to aqueous phase reaction rates.

4.4 Overall effects of fog on atmospheric species concentrations

Based on Table 4-2, the deposition removal rates of each species for all fog events are listed in Table 4-12. Figure 4-44 plots the removal rates for the fog events on 12/17 and 12/18/00.

Table 4-12. Deposition removal rates of each species for all fog events.

Sample Start Date	Start Time	End Time	Cl^- ($\mu g/m^2/h$)	NO_3^- ($\mu g/m^2/h$)	NO_2^- ($\mu g/m^2/h$)	SO_4^{2-} ($\mu g/m^2/h$)	Na^+ ($\mu g/m^2/h$)	NH_4^+ ($\mu g/m^2/h$)	K^+ ($\mu g/m^2/h$)	Mg^{2+} ($\mu g/m^2/h$)	Ca^{2+} ($\mu g/m^2/h$)	TOC ($\mu g/m^2/h$)
12/17/2000	11:00 PM	1:00 AM	8.56	144.65	5.67	47.13	2.74	113.69	3.10	2.18	19.96	66.61
12/18/2000	1:00 AM	3:10 AM	16.66	281.89	14.11	100.67	6.06	233.67	8.35	5.83	57.29	119.05
12/18/2000	3:10 AM	6:10 AM	20.21	360.69	14.46	110.76	4.20	344.17	8.78	5.28	27.60	117.12
12/18/2000	6:10 AM	8:15 AM	22.35	255.74	17.31	192.67	16.41	425.29	6.21	4.37	27.61	115.90
12/18/2000	8:15 AM	10:00 AM	21.00	157.75	13.48	134.79	14.25	261.14	10.04	3.19	26.12	94.22
12/18/2000	10:00 AM	12:00 PM	5.94	70.59	9.19	77.12	8.70	73.81	5.05	3.03	3.45	45.45
12/19/2000	5:15 AM	7:35 AM	6.15	54.59	5.72	21.54	3.50	86.92	3.18	1.48	10.61	30.91
1/15/2001	1:00 AM	3:00 AM	6.49	25.68	4.12	10.88	2.78	35.45	2.99	1.07	5.54	37.31
1/17/2001	12:15 AM	2:00 AM	7.57	55.39	17.16	21.25	3.28	69.60	5.49	1.42	13.18	56.51
1/17/2001	2:00 AM	3:55 AM	8.98	76.01	23.85	28.92	2.60	95.32	4.60	1.84	10.44	87.57
1/17/2001	4:00 AM	6:00 AM	5.31	32.87	22.61	18.07	1.68	51.01	2.43	1.24	7.58	52.95
1/17/2001	6:00 AM	8:00 AM	8.07	48.70	32.04	24.96	2.76	67.48	3.33	1.60	7.93	--
1/21/2001	6:15 AM	7:15 AM	7.56	247.33	20.17	39.44	4.99	131.22	7.39	1.59	9.37	82.05
1/21/2001	7:15 AM	9:15 AM	8.66	263.16	32.20	66.83	6.36	158.40	5.94	2.51	19.78	135.47
1/25/2001	5:00 AM	6:00 AM	16.88	14.78	3.78	11.86	10.02	27.67	6.23	1.56	19.98	67.42
1/25/2001	6:00 AM	7:30 AM	13.00	14.93	5.42	9.55	6.57	28.51	2.09	1.08	4.85	43.00
1/31/2001	5:15 AM	7:00 AM	22.91	338.56	43.69	143.36	13.77	264.68	7.76	3.99	42.31	258.10
1/31/2001	7:00 AM	9:05 AM	5.17	139.53	30.04	52.97	4.33	119.44	3.21	0.87	5.82	110.56
2/1/2001	2:15 AM	3:55 AM	10.06	57.38	23.63	42.63	5.47	60.38	4.72	1.50	12.00	67.66

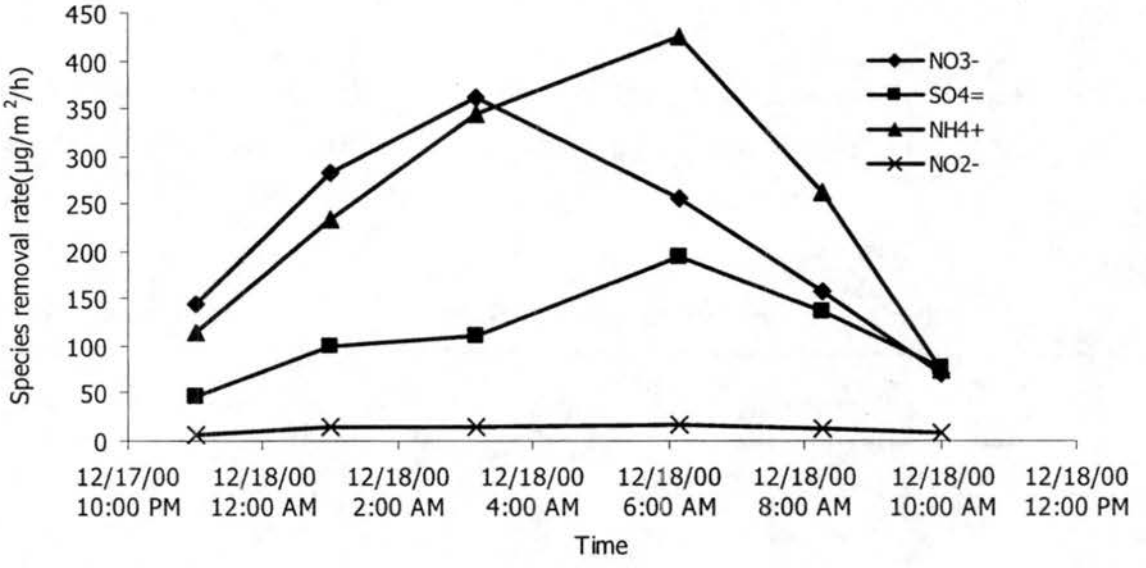

Figure 4-44. Timelines of deposition removal rates of four major ions in the 12/17/00 - 12/18/00 fog event.

Figure 4-44 clearly shows that during an extended fog episode, fog can remove significant quantities of atmospheric pollutant species by occult deposition. The overall removal rate also can vary with time and depends on the species' concentration in the fog, its enrichment in different size fog droplets, and its replenishment via emission or atmospheric production.

Table 4-13. Total mass removal of species by fog episodes during CRPAQS.

Sample Start Date	Sample Time (hour)	NO_3^- ($\mu g/m^2$)	SO_4^{2-} ($\mu g/m^2$)	NH_4^+ ($\mu g/m^2$)	TOC ($\mu gC/m^2$)
12/18/2000	9.0	2246	1223	2627	952
12/19/2000	2.3	127	50	203	72
1/15/2001	2.0	51	22	71	75
1/17/2001	7.8	393	174	526	309
1/21/2001	3.0	774	173	448	312
1/25/2001	2.5	37	26	70	66
1/31/2001	3.8	592	251	463	452
2/1/2001	1.7	96	71	101	113

Table 4-13 shows computed species mass removals for each CRPAQS fog event. Longer fog events tend to produce greater mass removal amounts. Taking into account fog duration and measured fluxes, a typical fog episode in CRPAQS removed approximately

- Sulfate: 46 $\mu g/m^2$/hour
- Nitrate: 108 $\mu g/m^2$/hour
- Ammonium: 105 $\mu g/m^2$/hour
- TOC: 66 $\mu gC/m^2$/hour

Table 4-14. Estimated reduction in ground level ambient concentrations by fog episodes during CRPAQS assuming a 100 m fog depth.

Sample Start Date	Sample Time (hour)	NO_3^- ($\mu g/m^3$/h)	SO_4^{2-} ($\mu g/m^3$/h)	NH_4^+ ($\mu g/m^3$/h)	TOC ($\mu gC/m^3$/h)
12/18/2000	9.00	22.46	12.23	26.27	9.52
12/19/2000	2.30	1.27	0.50	2.03	0.72
1/15/2001	2.00	0.51	0.22	0.71	0.75
1/17/2001	7.75	3.93	1.74	5.26	3.09
1/21/2001	3.00	7.74	1.73	4.48	3.12
1/25/2001	2.50	0.37	0.26	0.70	0.66
1/31/2001	3.80	5.92	2.51	4.63	4.52
2/1/2001	1.70	0.96	0.71	1.01	1.13

In CRPAQS study, the typical fog layer was less than 50m high. If we consider a conservative case where the measured fluxes of material are removed from a column 100m deep, we can estimate the effects of CRPAQS fog episodes on boundary layer pollutant concentrations. The results are shown, by fog episode, in Table 4-14. For a typical CRPAQS fog episode, we estimate ambient concentration reductions of approximately:

- Sulfate: 0.46 $\mu g/m^3$/hour

- Nitrate: 1.08 $\mu g/m^3$/hour
- Ammonium: 1.05 $\mu g/m^3$/hour
- TOC: 0.66 $\mu gC/m^3$/hour

These numbers are quite significant and indicate the effective role these fogs can play as atmospheric cleansers. It is important to keep in mind, however, that some of the deposited material may be volatile (but water soluble) and subject to emission back into the atmosphere as the wetted ground dries off following fog evaporation.

Chapter 5

Determination of Organic composition

5.1 Overview

This chapter focuses on observations of the organic composition of Central California radiation fogs, on improvement of techniques for characterizing organic species concentrations, and on issues related to organic aerosol and trace gas processing by these fogs.

5.1.1 TOC and DOC

Figure 5-1. Average fraction of TOC and DOC for CRPAQS samples.

Figure 5-1 shows the average split between total and dissolved organic carbon for CRPAQS fog samples. Results are shown for bulk fog samples collected with the ss-CASCC. It can be seen that an average of 75% of the organic material is dissolved, as operationally defined by the relative fractions of organic carbon in fog samples which

were passed through a quartz fiber filter. The results indicate that insoluble matter is an important part of the organic carbon burden of the CRPAQS fog drops and should not be ignored. A more detailed breakdown by sample is shown by Herckes et al. (2002). This finding should caution those who routinely filter fog and cloud samples, looking only at the soluble fraction, as it is clear that a significant amount of insoluble carbon is also being processed by the fog. The insoluble fraction probably contains a wide variety of organic material, perhaps including a significant amount of biological material (Bauer et al., 2002).

5.1.2 MW analysis of DOC

Molecular weight (MW) analyses of DOC in six fog samples were performed using ultrafiltration, which allows the classification of dissolved organic matter in different molecular weight classes. Results of the technique give an approximate idea of the molecular weight distribution of the DOC, but should not be over-interpreted as molecular structure, in addition to molecule size, influences the observed partitioning.

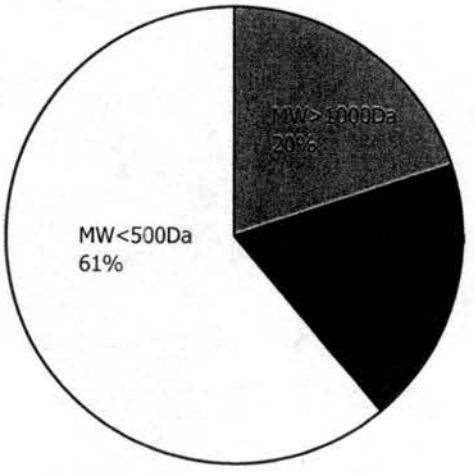

Figure 5-2. Molecular weight analysis of DOC for six fog water samples.

Figure 5-2 shows the average molecular weight distribution as a pie diagram. On average approximately 61% of the DOC is comprised of organic compounds with MW less than 500Da. The remaining 39% of the DOC is approximately evenly split between compounds with MW between 500Da and 1000Da and compounds with MW > 1000Da.

The presence of this large amount of high molecular weight material, reported in greater detail by Herckes et al. (2002), came as something of a surprise and necessitates a change in future approaches to characterizing the organic speciation of fog organics.

5.1.3 DOC composition

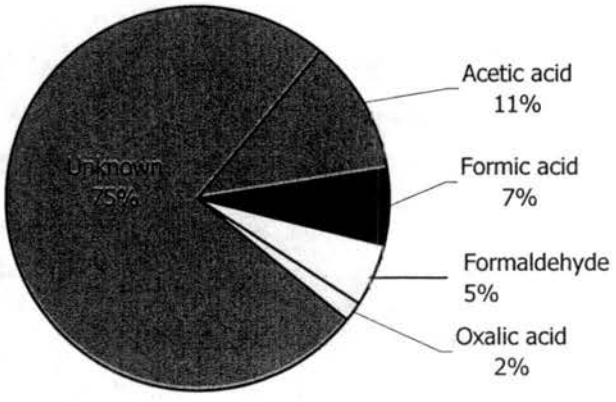

Figure 5-3. Mass fractions of CRPAQS fog DOC comprised by several key low MW species.

Past studies have found that several low molecular weight organic compounds can comprise a significant fraction of the organic burden in clouds and fogs. Figure 5-3 shows the average contributions of acetic acid, formic acid, oxalic acid, and formaldehyde to CRPAQS fog DOC. On a carbon mass basis, acetic acid is the dominant compound, comprising on average 11% of the fog DOC. Formic acid (7%), and formaldehyde (5%) follow in importance. Oxalic acid, the simplest dicarboxylic acid, makes up only 2%, on average, of the fog DOC. The relatively small contribution by oxalic acid stands in contrast to traditional use of dicarboxylic acids as model compounds for organic aerosol interactions with clouds and fogs. Together, the four compounds depicted here comprise only about one-fourth of the fog DOC, but make up nearly half of the DOC with MW < 500Da. The importance of these four compounds is consistent with earlier observations of the organic speciation of SJV fogs shown in Chapter 3.

Clearly there remains a significant fraction of fog borne organics that need to be identified, even in the lower MW range. One class of compounds worth investigating is carbonyls and dicarbonyls. Collett et al. (1990) found that glyoxal and methyl glyoxal,

two simple dicarbonyl compounds, had significant concentrations in clouds intercepting the slopes of the Sierra Nevada downwind of the Central Valley. Certainly, then, it seems worthwhile measuring concentrations of these compounds in the valley fogs. Also, functional group analysis, proposed by others to characterize water soluble organic compounds (WSOC) in fogs and aerosols, will help us better understand the profiles and abundance of soluble organic matter in fog water.

Measurement of carbonyl compounds is challenging because of their trace concentrations and interferences arising from other pollutants in fog water. Carbonyl compounds are directly emitted from a variety of sources including automotive, stationary source, and other industrial emissions, as well as from natural biogenic sources. Secondary production via atmospheric oxidation of other volatile organic compounds (VOC) can also be important sources. A review of atmospheric hydrocarbon oxidation mechanisms reveals many that are initiated by hydroxyl radical attack and eventually result in production of a variety of carbonyl and dicarbonyl compounds. Carbonyls themselves are also quite reactive and exert an important influence on NO_x and ozone chemistry in the troposphere (Fung et al., 1981; Seinfeld et al., 1998; Finlayson-Pitts et al., 2000). Problems previously identified in measurement of atmospheric carbonyls and dicarbonyls include 1) incomplete collection of carbonyls, 2) loss of carbonyl compounds by physical processes, vaporization, or by reactions with other pollutants in fog water, and 3) variable blanks resulting from contamination of reagents and/or sampling equipment.

5.2 Determination of carbonyl compounds by HPLC

5.2.1 Overview

Carbonyl compounds in fog samples were measured using a revised version of U.S. EPA Method 8315(A). It provides procedures for the determination of free carbonyl and dicarbonyl compounds in solid and liquid (aqueous) samples by derivatization with 2,4-dinitrophenylhydrazine (DNPH), and application of high performance liquid

chromatography (HPLC) with ultraviolet (UV) detection.

Derivatization of carbonyl compounds by the DNPH method is based on the acid-catalyzed derivatization of carbonyls by nucleophilic addition of DNPH to a C=O bond, followed by 1,2-elimination of water to form 2,4-dinitrophenylhydrazone. (The DNPH-hydrazones formed during sample derivatization are non-volatile).

The yellow to deep-orange colored DNPH-hydrazones have UV absorption maxima in the 360-375 nm range (for carbonyls) and near 430nm (for dicarbonyls), and can be analyzed by a high performance liquid chromatography (HPLC) method coupled with UV absorbance detection.

The water soluble low molecular weight (C_1-C_7) carbonyl compounds that can be quantified by this approach include formaldehyde, acetaldehyde, acrolein, acetone, propionaldehyde, crotonaldehyde, butyraldehyde, benzaldehyde, isovaleraldehyde, valeraldehyde, tolualdehyde, hexaldehyde, glyoxal and methyl glyoxal.

5.2.2 Instruments and reagents

5.2.2.1 HPLC conditions

HPLC operating conditions were adjusted to optimize chromatographic conditions for our particular analytical needs.

- Column: C18, 25 cm x 4.6 mm , 5 μm particle size. Supelco
- Mobile Phase Gradient: 50/50 acetonitrile/water (v/v), hold for 20 min. 50/50 acetonitrile/water to 95% acetonitrile in 15 min, 95% acetonitrile for 5 min. Total is 40 minutes plus 6 minutes flush time.
- Temperature: 40.0°C
- Flow Rate: 1.5 ml/min
- Detector: Ultraviolet absorption, monitored at 360 nm for mono-carbonyls,

430nm for dicarbonyls (Glyoxal and Methyl Glyoxal)

- Injection Volume: 20μl

5.2.2.2 Reagents

Table 5-1 shows the reagents used for carbonyls analysis. Standards are expected to be stable for about 6 weeks. All standards should be checked frequently for signs of degradation or evaporation. The lowest standard concentration should be at or just above the minimum detection limits when low concentration samples are anticipated. The other concentrations of the calibration curve should correspond to the expected range of concentrations in target samples.

Table 5-1. Required reagents to carbonyl and di-carbonyl analysis.

Methylene chloride	CH_2Cl_2 - HPLC grade or equivalent, Fisher Scientific
Acetonitrile	CH_3CN - HPLC grade or equivalent. Fisher Scientific
Sodium hydroxide solutions	NaOH, 6M,
Hydrochloric acid	HCl, 6M, J.T.Baker
Sodium sulfate	Na_2SO_4 - granular, anhydrous. Chempure
Citric acid	$C_8H_8O_7$, 1.0 M solution, Fisher Scientific
Sodium citrate	$C_6H_5Na_3O_7 \cdot 2H_2O$, 1.0 M trisodium salt dihydrate solution. Fisher Scientific
Citrate buffer	1 M, pH 3.0 - Prepare by adding 80ml of 1 M citric acid solution to 20 ml of 1 M sodium citrate solution. Mix thoroughly. Adjust pH with NaOH or HCl as needed. Fisher Scientific
DNPH	2,4-Dinitrophenylhydrazine, $[2,4\text{-}(O_2N)_2C_6H_3]NHNH_2$(DNPH), 70% in organic-free reagent water (w/w), Sigma. Add 428.7mg recrystallized 70% (w/w) DNPH solution in 100ml of acetonitrile to make a 3.00mg/ml solution.
Aldehyde stock standard	Commercial product: TO11/IP6A Carbonyl-DNPH Mix, Supelco Company, including 15 aldehyde compounds. Part# 47285-U. Analytical concentrations are 15μg/ml.
Calibration standards	A minimum of 5 concentrations (range from 0.02μg/ml to 0.45μg/ml of carbonyls) in acetonitrile from the stock standard. Store all standard solutions at 4℃ in a glass vial with a PTFE-lined cap, leaving minimum headspace, and in the dark.

5.2.3 Procedures

Glassware must be scrupulously cleaned. Glassware should be rinsed as soon as possible after use with the last solvent used. This should be followed by detergent washing with hot water and rinses with DI water. After washing, the glassware should then be drained, dried, and heated in a laboratory oven at 450°C for two to three hours before reuse. Solvent rinses with acetonitrile may be substituted for the oven heating. After drying and cooling, glassware should be stored in a clean environment to prevent accumulation of dust or other contaminants.

NOTE: Do not rinse glassware with acetone or methanol. These solvents react with DNPH to form interferences.

1. A measured volume of fog water sample (usually 20 ml or less, depending on the amount of real sample) is buffered to pH=3 and derivatized with 2,4-dinitrophenylhydrazine (DNPH): Transfer sample into reaction vessel, add 4 ml of citrate buffer and adjust the pH to 3.0 ± 0.1 with 6M HCl or 6M NaOH. Add 6 ml of DNPH reagent, seal the container, and place on a heated (40°C), stirring plate for about 2 hour. Adjust the agitation to produce a gentle swirling of the reaction solution.

   Note: An emulsion might appear. It will disappear/melt upon extraction in the next step.

2. **The derivatized compound is serially extracted three times with methylene chloride.** Serially extract the solution with three 20 ml portions of methylene chloride using a 125 ml or 250 ml separatory funnel. Combine the methylene chloride layers in a flask and add ~5.0 grams of anhydrous sodium sulfate. Swirl contents to complete the extract drying process.

3. **The methylene chloride extracts are concentrated.** Pour the extract into the evaporator flask, being careful to minimize transfer of sodium sulfate granules. Wash the flask with 3~4 ml of methylene chloride three times and combine wash to the

evaporator flask to complete quantitative transfer.

Note: be careful to prevent sodium sulfate from being transferred to the flask because hydrous sodium sulfate will make the solution opaque in the next step (although an opaque solution won't affect the detection and results). During each wash, the sodium sulfate granules will change color from yellow to white or very light yellow. If the color remains bright after three washes, one or more additional washes are required.

4. **Exchange with acetonitrile prior to HPLC analysis.** Concentrate the extract to a final volume of ~1ml, and exchange the solvent to acetonitrile prior to analysis.

   Note: In this step, carefully flushing the flask is necessary. Try to minimize the amount of acetonitrile, using a pipette to flush the flask from top to bottom, and accurately transfer it to the storage vial by pipette. Repeat until the acetonitrile flush solution is white, which means all the products are dissolved and transferred to the vial. Record the amount of acetonitrile used.

5.2.4 HPLC method results

5.2.4.1 Chemical structures of carbonyls and dicarbonyls

Numerous carbonyl and dicarbonyl compounds can be analyzed by this method. Table 5-2 lists several compounds analyzed in this study, along with their chemical structures.

Table 5-2. Chemical Structures of carbonyls and dicarbonyls.

Name	Formaldehyde	Acetaldehyde	Acrolein	Acetone	Propionaldehyde
Formula	HCHO	C_2H_4O	C_3H_4O	C_3H_6O	C_3H_6O
Molecular weight	30.0262	44.053	56.064	58.0798	58.0798
Structure	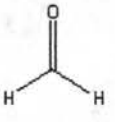	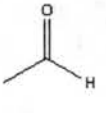	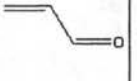	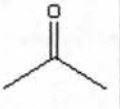	

Name	Crotonaldehyde	Butyraldehyde	Benzaldehyde	Isovaleraldehyde
Formula	C_4H_6O	C_4H_8O	C_7H_6O	$C_5H_{10}O$
Molecular weight	70.0908	72.1066	106.1238	86.1334
Structure	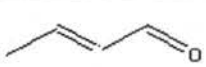		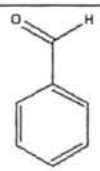	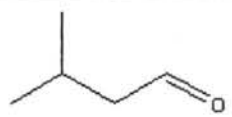

Name	Valeraldehyde	o-Tolualdehyde	m-Tolualdehyde	p-Tolualdehyde
Formula	$C_5H_{10}O$	C_8H_8O		
Molecular weight	86.1334	120.1506		
Structure		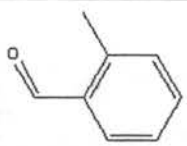	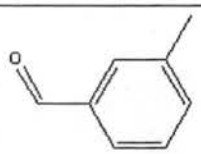	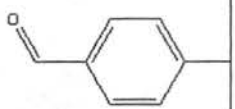

Name	Hexaldehyde	Glyoxal	Methyl glyoxal
Formula	$C_6H_{12}O$	$C_2H_2O_2$	$C_3H_4O_2$
Molecular Weight	100.1602	58.0366	72.0634
Structure		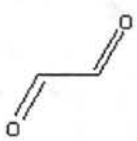	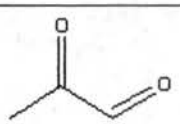

5.2.4.2 Example chromatograms

Figure 5-4 depicts 2-D and 3-D views of one example chromatogram showing retention times of several carbonyls in an analyzed standard. From left to right, the peaks in the 2D chromatogram are formaldehyde, acetaldehyde, acrolein+acetone, propionaldehyde, crotonaldehyde, butyraldehyde, benzaldehyde, isovaleraldehyde, valeraldehyde, o-tolualdehyde, m-tolualdehyde, p-tolualdehyde and hexaldehyde. The analytical separation occurs over approximately 30 minutes. During our testing of the method we were unable to separate acrolein and acetone, which co-elute as indicated.

Even strong changes to the separation method resulted in little improvement in the separation of these two compounds, Therefore, all results presented below consider these two compounds together.

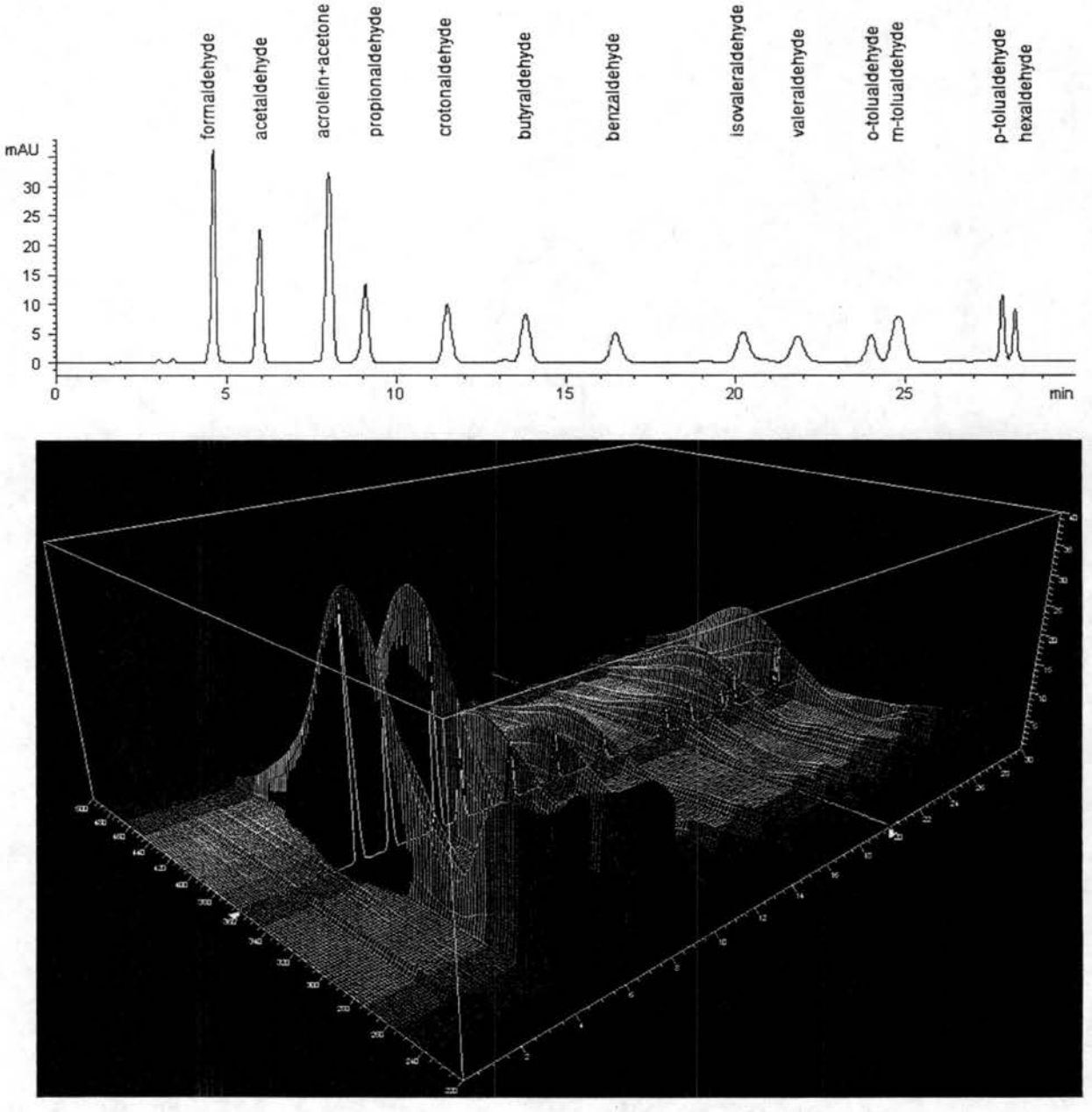

Figure 5-4. 2-D and 3-D views of an example chromatogram showing retention times and wavelength dependent absorption for several carbonyls in a standard.

In the 3-D chromatogram view, the x axis indicates retention time, the y axis indicates the detection wavelength (from 220 nm to 500 nm), and the z-axis indicates the measured

absorbance. The white curve bisecting the figure at 360nm is the 2-D view of the chromatogram discussed above. It is clear that 360 nm is close to the absorption maximum for many of the carbonyls, while several of the more complex carbonyls tend to absorb most strongly at longer wavelengths.

5.2.4.3 Carbonyl calibration results

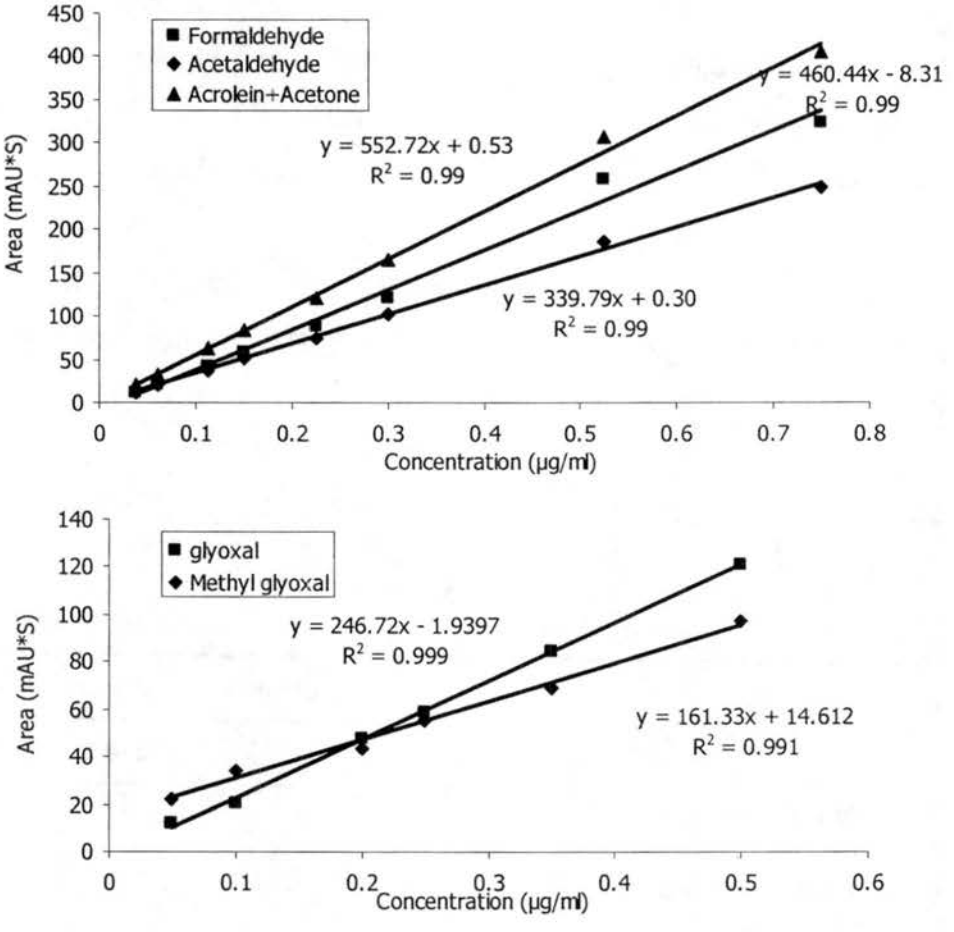

Figure 5-5. Several example calibration curves. Calibration curves of formaldehyde, acetaldehyde, acrolein+acetone were based on standards analyzed on 01/25/04 with absorbance monitored at 360 nm. Glyoxal and methyl glyoxal calibration curves were constructed on the same date, but absorbance of these compounds was monitored at 430 nm.

Method calibration curves were constructed based on injection of dilute standards prepared from a commercial stock standard containing DNPH-derivatized carbonyls.

The stock includes fifteen aldehyde compounds with 15.0 μg/ml concentrations. During each measurement period, standard solutions were made freshly from this stock solution. In order to make the standards consistent with samples, DNPH was also added to these standards which were treated the same way as samples.

Dicarbonyls analyzed in the work include glyoxal and methyl glyoxal. There is no commercial DNPH-derivatized standard available for either compound. Therefore, stock calibration solutions were manually made by adding proper amounts of glyoxal and methyl glyoxal into DI water and derivatizing. All the calibration standards for dicarbonyls were derivatized by DNPH and treated the same way as samples.

Figure 5-5 shows the calibration results for three abundant aldehydes as well as for glyoxal and methyl glyoxal. The calibration results for the other compounds reported here exhibit a similar linear relation between concentration and absorption.

5.2.4.4 Blank and Minimum Detection Limit (MDL)

Table 5-3. Carbonyl and dicarbonyl concentrations in blanks (20 ml DI water).

Species	Concentration (μg/ml)					
	BLK1	BLK2	BLK3	BLK4	BLK5	BLK6
Formaldehyde	0.01	0.01	0.02	0.01	0.01	0.01
Acetaldehyde	0.01	0.01	--	--	--	--
Acrolein+Acetone	0.02	0.01	0.02	0.02	0.02	0.02
Propionaldehyde	--	--	--	--	--	--
Crotonaldehyde	--	--	--	--	--	--
Butyraldehyde	--	--	--	--	--	--
Benzaldehyde	--	--	--	--	--	--
Isovaleraldehyde	--	--	--	--	--	--
Valeraldehyde	--	--	--	--	--	--
o-Tolualdehyde	--	--	--	--	--	--
m-Tolualdehyde	--	--	--	--	--	--
p-Tolualdehyde	--	--	--	--	--	--
Hexaldehyde	--	--	--	--	--	--
Glyoxal	--	--	--	--	--	--
Methyl Glyoxal	--	--	--	--	--	--

-- means the compound was not detected

Table 5-4. Minimum detection limits of aldehydes based on replicate low level (0.015 μg/ml) standard analyses

Species	Concentration (μg/ml)									
	A*	B	C	D	E	F	G	H	***MDL***	***Published MDL***
Formaldehyde	0.023	0.021	0.021	0.021	0.021	0.024	0.022	0.021	0.025	0.02
Acetaldehyde	0.013	0.012	0.012	0.012	0.012	0.012	0.012	0.011	0.013	0.11
Acrolein+Acetone	0.011	0.011	0.011	0.011	0.011	0.012	0.011	0.011	0.013	--
Propionaldehyde	0.011	0.011	0.010	0.011	0.011	0.012	0.010	0.011	0.012	0.008
Crotonaldehyde	0.013	0.012	0.013	0.013	0.012	0.013	0.013	0.014	0.015	0.006
Butyraldehyde	0.014	0.013	0.012	0.013	0.014	0.013	0.013	0.013	0.015	0.008
Benzaldehyde	0.010	0.012	0.009	0.010	0.012	0.007	0.011	0.009	0.014	--
Isovaleraldehyde	0.014	0.012	0.012	0.014	0.013	0.012	0.013	0.011	0.015	--
Valeraldehyde	0.011	0.010	0.009	0.011	0.013	0.010	0.009	0.010	0.013	--
o-Tolualdehyde	0.009	0.010	0.011	0.014	0.012	0.012	0.011	0.010	0.015	--
m-Tolualdehyde	0.011	0.011	0.010	0.011	0.011	0.012	0.011	0.010	0.012	--
p-Tolualdehyde	0.012	0.011	0.011	0.011	0.012	0.013	0.011	0.011	0.013	--
Hexaldehyde	0.012	0.012	0.011	0.011	0.012	0.013	0.010	0.011	0.014	0.012

* A to H are parallel replicate samples

Table 5-3 shows the carbonyl and dicarbonyl concentrations measured in six blanks (20 ml organic-free DI water). Since many compounds were not detected in these blanks, method detection limits were calculated by replicate analyses of a low concentration standard. Table 5-4 lists the MDL determined for each species, based on analyzing eight replicate samples (A to H). The minimum detection limits are comparable to published MDLs in EPA method 8315A, with some carbonyl MDLs slightly exceeding the published MDLs. The MDL for a specific sample may differ from the listed value, depending upon interferences from the sample matrix and the volume of sample used in the procedure. In the EPA method 8315A, the MDLs were obtained using 100 ml DI water, while 20 ml samples were used in our methods (we use 20 ml instead of 100 ml to be consistent with our 20 ml fog water samples – larger volumes are hard to obtain and dedicate just for this analysis). Generally, using larger sample volumes will lower the detection limits. Therefore, slightly higher MDLs in our results are very reasonable.

The concentrations of most carbonyls and dicarbonyls in the blanks are below the Minimum Detection Limit. For formaldehyde, acetaldehyde, acrolein+acetone, the concentrations are also very low.

5.2.4.5 DNPH Recrystallization

Formaldehyde contamination of the DNPH reagent is frequently encountered due to its widespread occurrence in the environment. In order to ensure acceptable results, the DNPH reagent must be purified by multiple recrystallizations in HPLC-grade acetonitrile. Recrystallization is accomplished, at 40-60°C, by slow evaporation of the solvent to maximize crystal size. The purified DNPH crystals are stored under HPLC-grade acetonitrile. Impurity levels of carbonyl compounds in the DNPH are determined prior to sample analysis and should be less than 25 μg/ml. Detailed DNPH recrystallization procedures can be found in EPA method 8315A. A brief description follows.

NOTE: This procedure should be performed in a properly ventilated hood. Inhalation of acetonitrile can result in nose and throat irritation (brief exposure at 500 ppm) or more serious effects at higher concentration and/or longer exposures.

1 Prepare a saturated solution of DNPH by boiling excess DNPH in 200 ml of acetonitrile for approximately 1 hour.
2 After 1 hour, remove and transfer the supernatant to a covered beaker on a hot plate and allow gradual cooling to 40 to 60°C. Maintain this temperature range until 95% of the solvent has evaporated, leaving crystals.
3 Decant the solution to waste and rinse the remaining crystals twice with three times their apparent volume of acetonitrile.
4 Transfer the crystals to a clean beaker, add 200 ml of acetonitrile, heat to boiling, and again let the crystals grow slowly at 40 to 60°C until 95% of the solvent has evaporated. Repeat the rinsing process as in step 3.
5 Take an aliquot of the second rinse, and analyze by HPLC. An acceptable impurity level is less than 0.025 μg/ml of formaldehyde in recrystallized DNPH reagent or

below the MDL listed in Table 5-4.

6 If the impurity level is not satisfactory, decant the solution to waste, repeat the recrystallization as in step 4 but rinse with two 25 ml portions of acetonitrile. Prepare and analyze the second rinse as in step 5.

7 When the impurity level is satisfactory, place the crystals in an all-glass reagent bottle, add another 25 ml of acetonitrile, stopper, and shake the bottle. Use clean pipets when removing the saturated DNPH stock solution to reduce the possibility of contaminating the solution. Maintain only a minimum volume of the saturated solution adequate for day to day operation to minimize waste of the purified reagent.

Table 5-5. DNPH recrystallization results.

Species	Original concentration (μg/ml)	First recrystallization (μg/ml)	Second recrystallization (μg/ml)
Formaldehyde	0.02	---*	---
Acetaldehyde	0.08	0.15	0.01
Acrolein+Acetone	2.15	0.53	0.03
Propionaldehyde	0.01	---	---
Crotonaldehyde	---	---	---
Butyraldehyde	---	---	---
Benzaldehyde	---	---	---
Isovaleraldehyde	---	---	---
Valeraldehyde	---	---	---
o-Tolualdehyde	---	---	---
m-Tolualdehyde	---	---	---
p-Tolualdehyde	---	---	---
Hexaldehyde	---	---	---
Glyoxal	---	---	---
Methyl Glyoxal	---	---	---

--- the compound is not detected

Table 5-5 shows the results of blank tests using original and recrystallized (once and two times respectively) 2,4-dinitrophenylhydrazine (DNPH). We can see that after the first recrystallization the concentrations of detectable compounds have already dropped to below 25 μg/l, but are still higher than blank concentrations listed in Table 5-3. After a second recrystallization the concentrationa are below or comparable to the blanks listed

in Table 5-3.

5.2.4.6 HPLC Uncertainty (RSD)

Table 5-6. Precision of carbonyl analyses based on replicate standard (0.15μg/ml).

Species	Concentration of Standard (μg/ml)					RSD (%)
	1st*	2nd	3rd	4th	5th	
Formaldehyde	0.16	0.16	0.18	0.17	0.16	4
Acetaldehyde	0.16	0.16	0.16	0.16	0.16	2
Acrolein+Acetone	0.16	0.16	0.16	0.16	0.16	2
Propionaldehyde	0.15	0.16	0.16	0.16	0.16	2
Crotonaldehyde	0.16	0.16	0.16	0.16	0.15	2
Butyraldehyde	0.16	0.16	0.16	0.16	0.16	2
Benzaldehyde	0.15	0.15	0.15	0.16	0.15	2
Isovaleraldehyde	0.15	0.15	0.16	0.15	0.16	2
Valeraldehyde	0.15	0.16	0.16	0.15	0.16	2
o-Tolualdehyde	0.15	0.15	0.16	0.16	0.16	3
m-Tolualdehyde	0.15	0.15	0.16	0.16	0.16	2
p-Tolualdehyde	0.15	0.15	0.16	0.16	0.15	2
Hexaldehyde	0.15	0.15	0.16	0.16	0.15	2

* 1^{st} to 5^{th} are replicate analyses.

Table 5-6 shows the precision of carbonyl measurements for a standard solution (carbonyl concentrations: 0.15 μg/ml), which was prepared by diluting 100 μl aldehyde stock standard solution into 10 ml. This sample was measured 5 times repeatedly by HPLC to test method precision. All the uncertainties are smaller than 5% (relatives standard deviation, RSD).

5.2.4.7 Standard Accuracy

In order to test if this method has good/stable recovery ratios (efficiencies) for each compound, parallel samples (STD1 to STD4) were made from the stock standard solution, which contained identical concentration (about 0.11 μg/ml) of DNPH derivatized

carbonyls. These were processed by the same method as fog water samples. Table 5-7 shows the measured sample concentrations and measurement accuracy of each species. Some species, such as formaldehyde, have greater error due to widespread occurrence in the environment leading to contamination during processing.

Table 5-7. Accuracy for carbonyls analysis.

Species	Concentration(μg/ml)					Theoretical value	Error
	STD1*	STD2	STD3	STD4	Average	(μg/ml)	(%)
Formaldehyde	0.13	0.14	0.14	0.13	0.14	0.11	+21
Acetaldehyde	0.13	0.12	0.12	0.12	0.12	0.11	+9
Acrolein+aceton	0.10	0.10	0.10	0.09	0.10	0.11	-11
Propionaldehyde	0.11	0.12	0.11	0.11	0.11	0.11	-0.4
Crotonaldehyde	0.10	0.10	0.10	0.10	0.10	0.11	-12
Butyraldehyde	0.09	0.09	0.09	0.09	0.09	0.11	-18
Benzaldehyde	0.09	0.08	0.09	0.08	0.09	0.11	-23
Isovaleraldehyde	0.09	0.09	0.09	0.09	0.09	0.11	-20
Valeraldehyde	0.11	0.11	0.11	0.11	0.11	0.11	-3
o-Tolualdehyde	0.11	0.11	0.11	0.11	0.11	0.11	-2
m-Tolualdehyde	0.11	0.11	0.11	0.11	0.11	0.11	-2
p-Tolualdehyde	0.08	0.08	0.07	0.07	0.08	0.11	-34
Hexaldehyde	0.11	0.11	0.11	0.10	0.11	0.11	-5

* STD1 to STD4 were replicate analyses.

5.2.4.8 Artificial fog water samples

Artificial fog water samples were used to test the derivatization process with DNPH. These samples yield an overview of the validity of the method. A one liter stock artificial fog water solution was made, by adding known amounts of formaldehyde, acetone and benzaldehyde, and kept in the refrigerator. The theoretical concentrations in the stock solution are 11 μg/ml formaldehyde and 20 μg/ml each for acetone and benzaldehyde. The theoretical concentration of formaldehyde was obtained by fluorescence measurement (Dong et al., 1987). Formaldehyde can form a stable compound, HMS, in the presence of bisulfite. HMS can later be decomposed to formaldehyde to be analyzed.

After decomposition, formaldehyde is reacted with 2.4-pentanedione and ammonia to quantitatively form a yellow product, diacetyldihydrolutidine (DDL), which is measured by fluorescence. With excess 2,4-pentanedione and ammonia, the amount of DDL produced equals the amount of formaldehyde present in solution. Therefore, the formaldehyde concentration can be determined from the amount of DDL. Theoretical concentrations of acetone and benzaldehyde were calculated based on the amount added to the solution.

Sample solution was made freshly each time before reaction by adding 1ml stock solution into a 100ml volumetric flask and diluting with DI water.

Table 5-8. Concentrations of artificial fog water parallel samples.

Species	Concentration (μg/ml)							Theoretical concentration* (μg/ml)
	Artifog -1	Artifog -2	Artifog -3	Artifog -4	Artifog -5	Artifog -6	Average	
Formaldehyde	0.11	0.10	0.11	0.10	0.13	0.12	0.11	0.11
Acetone	0.06	0.08	0.07	0.09	0.06	0.08	0.07	0.20
Benzaldehyde	0.20	0.18	0.20	0.19	0.20	0.20	0.20	0.20

*formaldehyde theoretical concentration were measured by RF-1501 spectrofluorotometer; Acetone and benzaldehyde theoretical concentrations were calculated based on the amount added to the solution.

Table 5-8 shows the concentrations of six artificial fog sample replicates analyzed in parallel. We can see that for formaldehyde and benzaldehyde, the theoretical concentration and measured concentration fit very well. But for acetone, the measured concentration is much smaller than the calculated concentration. This reflects the significant volatility of acetone resulting in loss from the prepared solution. A similar loss phenomena was observed for formaldehyde. The target concentration was supposed to be 0.20 μg/ml when I made the artificial fog water solution by weighing the formaldehyde added to the solution, while the real/theoretical concentration measured by a fluorescence method was only 0.11 μg/ml.

5.2.4.9 Stability of samples

We have noticed that the concentrations of carbonyls in stored, unpreserved fog water samples (CRPAQS samples, collected in winter 2000/2001 and analyzed in summer 2003) are very low. Formaldehyde concentrations in some samples were even close to DI water blank values, inconsistent with large amounts of formaldehyde measured in preserved fog water aliquots soon after the samples had been collected. The loss of aldehydes can be explained by chemical instability of aldehydes in fog water, volatilization, microbial degradation, etc. Therefore, a stability test is extremely important for determining appropriate sample collection, preservation, and handling processes. If fog samples are stable after collection, we can transfer them back to the main lab in Fort Collins for analysis, which will save limited and valuable time and effort on site. If they are not stable, we then have to treat samples on site immediately after collection and/or send them back to the lab as soon as possible for analysis.

Two kinds of solutions were made to compare carbonyl stability. One is artificial fog water samples, with DI water as the base matrix, adding appropriate amounts of carbonyl and dicarbonyl compounds; the other uses a real fog water base matrix.

Table 5-9. Comparison of concentrations of artificial fog water samples.

Species	Concentration (μg/ml)						Theoretical concentration (μg/ml)*
	Artifog-1 (03/22/03)	Artifog-2 (03/22/03)	Artifog-1 (05/23/03)	Artifog-2 (05/23/03)	Artifog-7 (05/22/03)	Artifog-8 (05/22/03)	
Formaldehyde	0.11	0.10	0.11	0.11	0.10	0.11	0.11
Acetone	0.06	0.08	0.06	0.08	0.06	0.05	0.20
Benzaldehyde	0.20	0.18	0.20	0.20	0.20	0.19	0.20

*formaldehyde theoretical concentration were measured by RF-1501 spectrofluorotometer; Acetone and benzaldehyde theoretical concentrations were calculated based on the amount added to the solution.

Table 5-9 lists the concentrations of four parallel artificial fog water samples prepared using a DI water base matrix. Two samples (artifog-1 and artifog-2) were made and analyzed on 03/22/03, then re-analyzed on 05/23/03. The other two samples (artifog-7 and artifog-8) were freshly made on 05/22/03. We can see that there is no significant

difference among them. For the first two samples (artifog-1 and artifog-2), we can conclude that after derivatization with DNPH, it is stable for two months, which is long enough for the samples to be transferred back to the lab and be analyzed. Comparing the first two parallel samples (artifog-1 and artifog-2) with the second parallel samples (artifog-7 and artifog-8), we can also conclude that the artificial fog samples were also stable without derivatization (the next table will show that real fog matrix were not stable in similar conditions). This is probably because the matrix of the artificial fog water is DI water, and nothing in the solutions like microorganisms can react with aldehydes and degrade the solutions.

Table 5- 10. Stability test in a real fog water matrix.

Species	9/15/03 (μg/ml)	9/18/03 (μg/ml)	9/22/03 (μg/ml)	9/29/03 (μg/ml)	10/7/03 (μg/ml)	10/15/03 (μg/ml)
Acetone	0.33	0.32	0.29	0.25	0.27	0.32
Benzaldehyde	1.11	0.72	0.53	<0.02	<0.02	<0.02
Glyoxal	0.94	0.83	0.84	0.71	0.67	0.59
Methyl Glyoxal	1.19	1.06	0.84	0.47	0.25	0.07

Table 5-10 shows stability results for two carbonyl and two dicarbonyl compounds prepared and analyzed in an authentic fog water matrix (left over of California fog samples). Figure 5-6 shows the data in Table 5-10. We can see that even though the samples prepared with a DI water base matrix were stable, the samples with a real fog water base matrix were not. The concentrations of carbonyls except acetone began dropping within a few days. After one month, all the carbonyls except acetone and glyoxal were gone from the samples. EPA method 8315A indicates "Aqueous samples must be derivatized and extracted within 3 days of sample collection. All derivatized sample extracts should be analyzed within 3 days after preparation." However, this EPA recommended schedule is a conservative one since the method considers various samples, whose matrix, containers, preservation, analysis techniques and holding times are all different (please refer to EPA method 8315A and the introductory material, Organic Analytes, Sec 4.1). Our results confirm that it is necessary to derivatize samples on site because carbonyls in fog water sample will degrade fast, but our results shows that

derivatized samples are stable for at least two months and do not need to be analyzed within 3 days. For our Fresno fog campaign, the fog samples were derivatized on site, then transfer back to main lab in Fort Collins at the end of the whole fog campaign (Jan 13th 2004), and analyzed from Jan 21st to 26th, 2004.

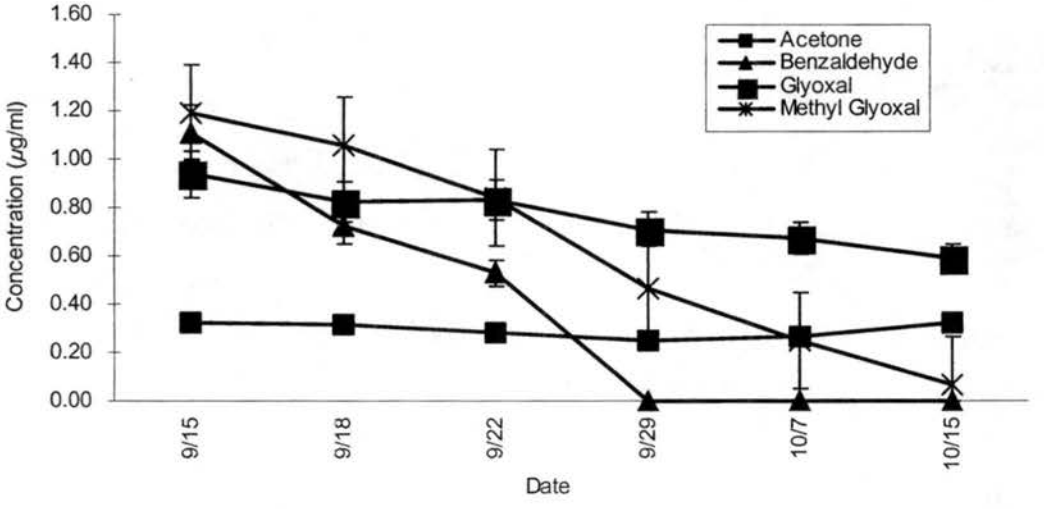

Figure 5-6. Carbonyl stability test in real fog water base matrix.

5.2.5 California SJV fog water samples analysis

Nineteen CRPAQS fog water samples have been analyzed by the method above. Analyses were completed in Sept 2003. These samples were collected during the Angiola CRPAQS campaign by CASCC and sf-CASCC collectors, and include twelve samples of one fog event from 12/17/2000 night to 12/18/2000 noon, four samples of large fog droplets from the same fog event, and three samples from a fog event on 12/19/2000. Table 5-11 shows the concentrations of detectable carbonyl and dicarbonyl compounds. For most of the samples except AGCC35201 (first Angiola ground sample, collected by CASCC collector on 12/17/08), the concentrations of carbonyls and dicarbonyls are very low. For example, based on the formaldehyde analysis by spectrophotometer, the average concentration of Formaldehyde in California Angiola fog samples is 20.6 μN, while the concentrations of formaldehyde in these nineteen fog water samples are all less than 1 μM. These samples have been stored in the refrigerator for over two years. Stability test

shows that the samples will degrade very fast (less than one month to reach detection limit) if not derivatized on site. This strongly suggests that the samples have been significantly degraded during the long storage time, and most of the original carbonyls and dicarbonyls were lost. For sample AGCC35201, there are still fairly large concentrations of glyoxal and methyl glyoxal in it. This result is surprising.

5.2.6 Fresno fog water analysis

Twenty one fog water samples collected during the Fresno fog campaign were analyzed. These samples were collected by ss-CASCC and ss-sf-CASCC. These samples were derivatized on-site first then transferred back to CSU for analysis. Analyses were finished about ten days after the campaign (From Jan 21st to 26th, 2004). These samples were collected during three fog events:

- 12/31/03- 01/01/04

  A fog event lasted from 3:52pm to 6:30am, one sample was collected (FSC36401).
- 01/10/04- 01/11/04

  A fog event lasted from 9:30pm to 11:40am next day. Four bulk fog water (FSC01001, 01002, 01003, 01004), four large fog drop samples (FSCL01001, 01002, 01003, 01004) and three small fog drop samples (FSCS01001, 01002, 01003) were collected.
- 01/11/04- 01/12/04

  A fog event lasted from 6:00pm to 10:00am next day. Three bulk fog water samples (FSC01101, 01102, 01103), three large fog droplets samples (FSCL01101, 01102, 01103) and three small fog droplets samples (FSCS01101, 01102, 01103) were collected.

Table 5-12 shows the sampling information including date, time, sample weight, pH and concentrations of detectable carbonyls and dicarbonyls. Two dicarbonyls we are interested in were found in the bulk fog samples, but not all fifteen carbonyls we looked for were found. Formaldehyde, acetaldehyde, acrolein+acetone, isovaleraldehyde,

glyoxal and methyl glyoxal had larger concentrations than butyraldehyde, o-tolualdehyde, m-tolualdehyde, p-tolualdehyde and hexaldehyde.

5.2.6.1 Fresno fog sample pH and pH size distribution

From Table 5-12, we can see that for Fresno bulk fog water samples, the pH ranged from 6.58 to 7.23, averaging 6.90, similar to Angiola CRPAQS fog samples and previous SJV fog studies. Again, as we recall, the unique characteristic of California San Joaquin valley fogs is that fog water contains large inputs of ammonia which is the main factor making the fogs alkaline.

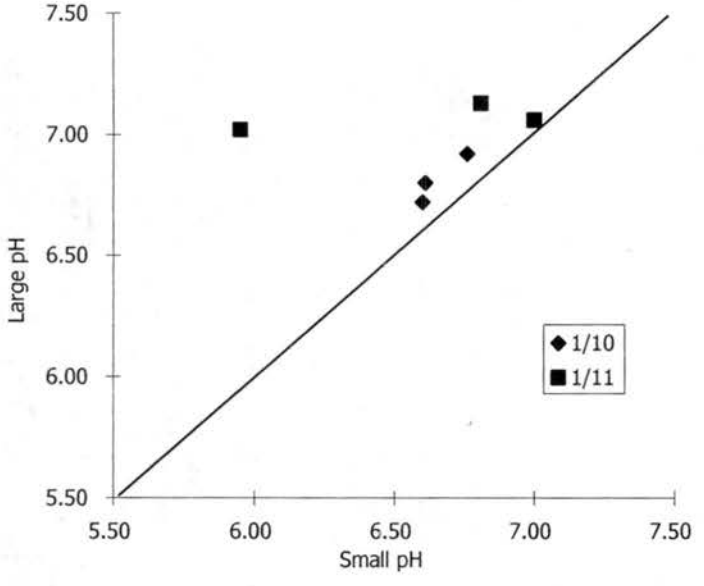

Figure 5-7. Comparison of pH between large and small fog drops.

Figure 5-7 plots the pH values in large and small fog droplets according to Table 5-12. All the data points are above the 1:1 line, implying that pH in small drops is lower than in large drops. The first pair of size fractioned samples (FSCL01101 and FSCS01101) of the fog event on 01/11/04, shows a large difference (5.95 small vs. 7.02 large). This result contrasts with the other samples examined here and with most Angiola CRPAQS fog samples. Earlier SJV fog studies, including those in Davis (Moore et al., 2000, Moore et al., 2004b), often determined that small fog drops were more acidic than large fog drops.

Table 5-11. Carbonyl and dicarbonyl concentrations of California SJV fog samples.

Samples	Sample Start Date	Sample Start Time	Sample End Time	Formaldehyde (μM)	Acetaldehyde (μM)	Acrolein+ acetone (μM)	Crotonaldehyde (μM)	Glyoxal (μM)	Methyl Glyoxal (μM)
AGCC35201*	12/17/2000	10:15 PM	11:00 PM	0.86	0.41	0.34	--**	25.42	14.76
AGCC35202	12/17/2000	11:00 PM	12:00 AM	0.47	0.62	0.63	--	--	0.73
AGCC35303	12/18/2000	12:00 AM	1:00 AM	0.56	--	0.19	--	--	--
AGCC35204	12/18/2000	1:00 AM	2:00 AM	0.45	0.51	0.60	--	--	1.00
AGCC35206	12/18/2000	3:00 AM	4:00 AM	0.53	0.59	0.54	--	--	0.77
AGCC35207	12/18/2000	4:00 AM	5:00 AM	0.66	0.59	0.76	--	--	0.91
AGCC35208	12/18/2000	5:00 AM	6:00 AM	0.60	0.54	0.66	--	--	0.75
AGCC35209	12/18/2000	6:00 AM	7:00 AM	0.51	0.59	0.68	--	--	1.04
AGCC35210	12/18/2000	7:00 AM	8:00 AM	0.52	0.57	0.57	--	--	0.79
AGCC35211	12/18/2000	8:00 AM	9:00 AM	0.54	0.92	0.35	--	--	0.14
AGCC35212	12/18/2000	9:00 AM	10:00 AM	0.51	0.56	0.70	--	--	0.90
AGCC35213	12/18/2000	10:00 AM	11:00 AM	0.54	0.63	0.55	--	--	1.20
AGPCL35201	12/18/2000	12:00 AM	1:00 AM	0.95	0.58	0.17	0.64	--	0.50
AGPCL35205	12/18/2000	4:00 AM	6:00 AM	0.84	1.22	0.32	0.88	0.13	4.76
AGPCL35207	12/18/2000	7:00 AM	8:00 AM	0.81	0.58	0.20	0.45	0.12	0.81
AGPCL35208	12/18/2000	8:00 AM	9:00 AM	0.60	1.03	0.37	--	--	0.14
AGCC35302	12/19/2000	1:20 AM	3:00 AM	0.78	0.55	0.17	--	--	0.42
AGCC35303	12/19/2000	3:05 AM	5:05 AM	0.73	0.49	0.19	--	0.09	0.37
AGCC35304	12/19/2000	5:05 AM	7:35 AM	0.74	0.54	0.19	0.36	0.11	0.59

*Sample nomenclature: AG: Angiola ground; CC: plastic CASCC collector; PCL: plastic sf-CASCC collector

352: 12/17/00; 353: 12/18/00; The last two digits are sample sequence.

**-- means the concentration is below detection limit.

Table 5-12. Sampling information and concentrations of detectable carbonyls and dicarbonlys in Fresno fog samples.

Sample Name	Sample Start Date	Sample Start Time	Sample End Time	Sample Weight (g)	pH	Formaldehyde (μM)	Acetaldehyde (μM)	Acrolein +acetone (μM)	Butyraldehyde (μM)	Isovaleraldehyde (μM)	o-Tolualdehyde (μM)	m-Tolualdehyde (μM)	p-Tolualdehyde (μM)	Hexaldehyde (μM)	Gloxyal (μM)	Methyl Glyoxal (μM)
FSC36401*	12/31/03	3:52 AM	6:30 AM	73.3	6.63	24.59	4.18	1.71	--**	2.76	--	0.10	0.00	0.18	8.81	10.73
FSC01001	1/10/04	9:30 PM	11:37 PM	255.38	6.71	13.47	3.64	1.10	--	1.82	--	0.07	0.08	0.17	9.64	9.63
FSC01002	1/10/04	11:38 PM	2:00 AM	238.04	6.58	17.40	5.42	1.62	--	3.34	--	0.14	0.17	0.42	26.65	16.59
FSC01003	1/10/04	2:00 AM	9:30 AM	760.10	6.89	16.76	2.83	1.05	--	1.16	--	0.05	0.08	0.20	5.19	5.87
FSC01004	1/11/04	9:30 AM	11:40 AM	96.9	7.1	24.08	3.51	2.45	--	1.83	--	0.10	0.21	0.34	12.33	12.53
FSC01101	1/11/04	6:00 PM	1:00 AM	183.7	6.91	38.16	5.49	4.60	--	5.75	--	0.28	0.45	0.38	28.02	24.60
FSC01102	1/11/04	1:00 AM	7:00 AM	213.15	7.18	28.21	3.34	3.03	--	1.81	--	0.08	0.34	1.18	10.82	8.94
FSC01103	1/11/04	7:00 AM	10:00 AM	83.5	7.23	36.69	3.87	2.13	--	1.97	--	0.09	0.37	1.31	11.29	10.00
FSCL01001	1/10/04	9:30 PM	1:30 AM	849.17	6.72	18.27	3.18	0.87	--	1.96	--	0.04	0.08	0.12	6.32	9.81
FSCL01002	1/10/04	1:30 AM	5:30 AM	897.42	6.8	18.62	2.88	0.94	--	1.15	--	0.05	0.08	0.22	4.18	6.83
FSCL01003	1/10/04	5:30 AM	9:30 AM	759.40	6.92	16.20	2.61	0.75	--	0.94	--	0.04	0.07	0.15	3.26	4.77
FSCL01004	1/11/04	9:30 AM	11:40 AM	215.2	7.05	20.04	2.50	2.54	--	1.42	--	0.09	0.13	0.28	8.21	11.33
FSCL01101	1/11/04	6:00 PM	1:00 AM	559.75	7.02	40.80	3.32	2.70	--	3.55	--	0.14	0.15	0.21	15.86	19.39
FSCL01102	1/11/20	1:00 AM	7:05 AM	574.42	7.13	21.21	1.86	1.03	--	1.11	--	0.04	0.05	0.06	4.23	4.42
FSCL01103	1/11/04	7:05 AM	10:05 AM	264.37	7.06	36.51	2.36	2.21	--	1.55	--	0.08	0.28	0.19	7.40	9.16
FSCS01001	1/10/04	9:30 PM	1:30 AM	65.01	6.6	21.84	3.03	1.13	--	2.96	0.31	0.11	0.12	0.31	10.11	14.18
FSCS01002	1/10/04	1:30 AM	5:30 AM	81.11	6.61	17.25	4.25	1.33	--	2.69	--	0.10	0.14	0.47	17.36	11.01
FSCS01003	1/10/04	5:30 AM	9:30 AM	100.12	6.76	14.33	3.25	1.26	--	1.83	--	0.07	0.13	0.33	12.19	7.43
FSCS01101	1/11/04	6:00 PM	1:00 AM	44.1	5.95	30.72	9.22	5.86	3.16	9.83	--	0.39	0.60	3.21	79.19	36.91
FSCS01102	1/11/04	1:00 AM	7:05 AM	65.66	6.81	27.73	9.28	4.94	2.04	6.32	--	0.24	0.84	3.12	53.15	23.94
FSCS01103	1/11/04	7:05 AM	10:05 AM	32.01	7	27.98	6.16	2.98	--	3.14	--	0.12	0.67	2.31	27.25	13.60

*Sample nomenclature: F: Fresno;SC: ss-CASCC collector; SCL: large cut-size fraction of ss-sf-CASCC collector;

SCS: small cut-size fraction of ss-sf-CASCC collector; 364, 010, 011: 352: 12/30/00, 01/10/04, 01/11/04;

The last two digits are sample sequence.

**-- means the concentration is below detection limit.

5.2.6.2 Fresno bulk fog samples' carbonyl and dicarbonyl concentrations

Formaldehyde concentrations in the Fresno fogs ranged from 13.5 μM to 38.2 μM, averaging 24.9 μM. Formaldehyde is a highly soluble gas, because of its gem-diol formation in water, and is often abundant in urban atmospheres. It is directly emitted from combustion sources and produced via photochemical oxidation of many hydrocarbons. The background level of gas phase formaldehyde is reported to be in the range of 0.5-2 ppb, while in urban areas the value can be up to 10 times higher (Munger et al., 1984).

Table 5-13 shows the summary of pH and bulk organic fog sample composition. Acetaldehyde concentrations range from 2.8 μM to 5.5 μM, averaging 4.0 μM; acrolein+acetone ranges from 1.0 μM to 4.6 μM, averaging 2.2 μM; isovaleraldehyde ranges from 1.2 μM to 5.8 μM, averaging 2.6 μM; concentrations of m-tolualdehyde, p-tolualdehyde and hexaldehyde were smaller than other carbonyls, but still above the blanks.

Table 5-13. Summary of Fresno bulk organic fog sample composition.

Species	Number of samples	Concentration Range	Median
pH (pH units)	8	6.58-7.23	6.90
Formaldehyde (μM)	8	13.47-38.16	24.92
Acetaldehyde (μM)	8	2.83-5.49	4.04
acrolein+acetone (μM)	8	1.05-4.60	2.21
Isovaleraldehyde (μM)	8	1.16-5.75	2.55
Glyoxal (μM)	8	5.19-28.02	14.10
methyl glyoxal (μM)	8	5.87-24.60	12.36
m-tolualdehyde (μM)	8	0.05-0.28	0.11
p-tolualdehyde (μM)	8	0.08-0.45	0.24
Hexaldehyde (μM)	8	0.17-1.31	0.52

Two dicarbonyls had higher concentrations than all carbonyls except formaldehyde. Glyoxal concentrations range from 5.2 μM to 28.0 μM, averaging 14.1 μM. Methyl glyoxal concentrations range from 5.9 μM to 24.6 μM, averaging 12.4 μM. These

relatively high concentrations indicate the importance of considering dicarbonyls when looking at carbonyl concentrations or the general makeup of fog DOC.

5.2.6.3 Fresno bulk fog sample composition

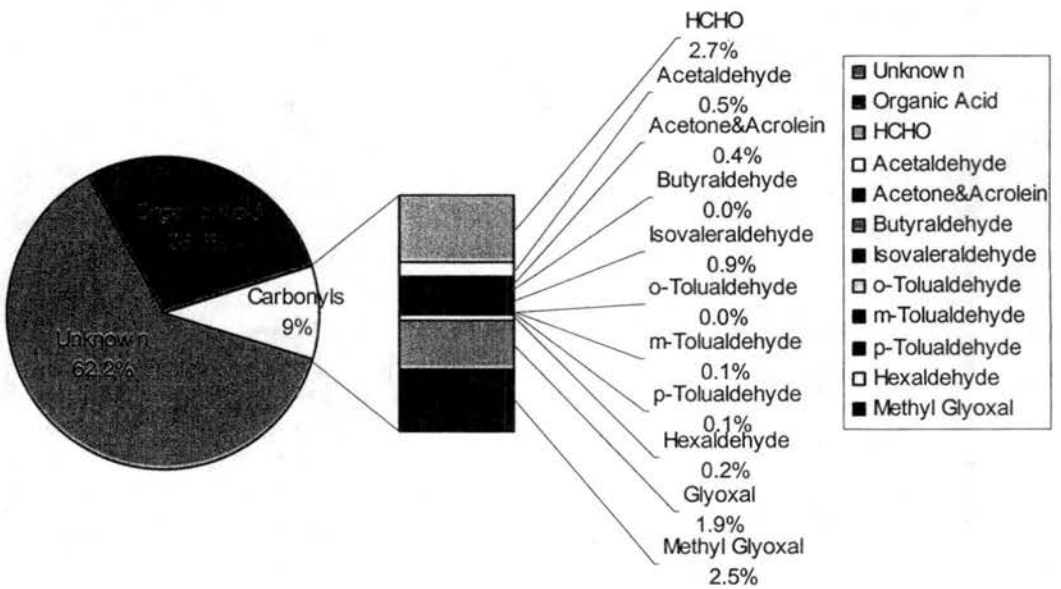

Figure 5-8. Typical composition of carbonaceous material comprising the total dissolved organic carbon (DOC) content observed for several California Fresno radiation fog samples.

Figure 5-8 shows the average/typical composition of organic material comprising the total DOC in the Fresno fog samples. Organic acids (including formate, acetate, propionate, pyruvate, glutarate, succinate, malonate and oxalate) comprise 28.5% of the total DOC, while carbonyls comprise 9% of the total DOC. Among the carbonyls, formaldehyde, glyoxal and methyl glyoxal are the most abundant carbonyls in fog samples, comprising together an average of 7.1% of total DOC in the fog samples. Appendix-G plots the composition of DOC for individual Fresno fog samples.

5.2.6.4 Comparison of HCHO measurement techniques

As seen above, HPLC can be used to measure formaldehyde concentrations in fog

water samples, and the results can be compared with the fluorescence spectrophotometer method (Dong et al., 1987) described earlier. Table 5- 14 compares results from the two measurement methods.

Table 5-14. Comparison of two HCHO measurements.

Sample Name	HCHO by HPLC (μM)	HCHO by Fluorescence (μM)	Ratio (%) (HPLC/Fluorescence)
FSC36401	24.59	35.72	69
FSC01001	13.47	21.77	62
FSC01002	17.40	31.62	55
FSC01003	16.76	25.05	67
FSC01004	24.08	36.57	66
FSC01101	38.16	61.82	62
FSC01102	28.21	46.11	61
FSC01103	36.69	52.62	70
FSCL01001	18.27	24.5	75
FSCL01002	18.62	26.63	70
FSCL01003	16.20	24	67
FSCL01004	20.04	33.39	60
FSCL01101	40.80	56.43	72
FSCL01102	21.21	40.09	53
FSCL01103	36.51	52.83	69
FSCS01001	21.84	33.55	65
FSCS01002	17.25	38.08	45
FSCS01003	14.33	27.97	51
FSCS01101	30.72	81.33	38
FSCS01102	27.73	60.67	46
FSCS01103	27.98	51.94	54

We can see that concentrations of HCHO measured by HPLC were lower than concentrations measured by the fluorescence technique, with a ratio ranging from about 38% to 75%. This difference might be related to HMS present in the fog. As mentioned before, formaldehyde can form stable HMS in the presence of sulfite or bisulfite in solution, and in SJV fog samples, HMS is often important (Rao et al., 1995; Munger et al., 1996). A test of the detection of HMS by the HPLC method is necessary.

An interesting feature of HMS chemistry is that the high pH condition that favors its production is not good for its preservation. EPA method 8315A recommends another buffer solution if formaldehyde is the only aldehyde of interest. This new buffer solution

is 5 M sodium acetate/ 5 M acetic acid (pH=5), while the normal buffer for analyses of all aldehydes is 1.0 M sodium citrate/1.0 M citric acid (pH=3). The acetate buffer solution was tested and the results compared with results using the normal citrate buffer. Also, we used a DI water base matrix and a real fog water base matrix separately to test if a different matrix affects the results.

Table 5-15. Free HCHO and HMS measurement.

	0.75 μg/ml Free HCHO solution (DI matrix)		10.45μM HMS solution (DI matrix)		10.45μM HMS solution (real fog matrix)	
	Citrate buffer (μg/ml) (%)	Acetate buffer (μg/ml) (%)	Citrate buffer (μM) (%)	Acetate buffer (μM) (%)	Citrate buffer (μM) (%)	Acetate buffer (μM) (%)
HCHO/ HMS	0.73 (97)	0.73 (97)	0.64 (6)	9.98 (96)	0.63 (6)	10.21(98)

Table 5-15 summarizes results of testing free HCHO and HMS measurement with different buffer solution and sample matrix. First we used two parallel samples with 0.75 μg/ml free formaldehyde to compare the two buffer solutions. Second, we used parallel 10.45 μM HMS solution (DI water matrix) to compare the results also using two buffer solutions. Third, we used parallel 10.45 μM HMS solutions in a real fog water matrix to test any matrix effects.

The results using different buffer solutions with free formaldehyde solutions were the same, and very close to the theoretical concentration value (0.73 μg/ml vs. 0.75 μg/ml), with 97% of the expected free formaldehyde measured. This suggests there is no selectivity of free HCHO in the solution using the different buffer solutions at different pH.

HMS test solutions produced very different results. For the parallel DI water matrix samples, the citric/citrate (pH=3) buffer failed to give the right concentration, with only 6% HMS determined. Citrate buffer also failed to determine the right concentration in real fog water matrix samples. No matter what matrix, the citrate buffer protocol only yields 6% of the total HMS in solution, while the protocol acetic/acetate (pH=5) buffer

successfully determined the right concentration (9.98 μM and 10.21 μM vs. 10.45 μM), with an average 97% of HMS determined.

This series of tests shows that both buffer solutions can determine free HCHO in fog water without problem, but the normal citrate buffer protocol significantly underestimates HMS originally in the solution. Rao et al. (1995) measured formaldehyde and HMS concentration in several sites within the US, and Table 5-16 below is the chemical compositions of cloudwater and fogwater collected by size-fractionating CASCC in California (this table is part of table 1 adopted from Rao et al. (1995)). We can see that when pH was about 3, HMS only accounted for a negligible part of total formaldehyde. But when pH was around 6, then HMS can account for up to 22% (29.8 μM vs. 133.8 μM) of the total formaldehyde. Guiang et al. (1984) reported 0-9.5 μM HMS in rain water in rural Minnesota area; Fuzzi (1992) found 8-820 μM HMS in fog water in Po Valley, Italy. The pH of our Fresno fog samples ranged from 5.95 to 7.23, averaging 6.84, Therefore, HMS is expected to account for an important part of total formaldehyde. Our results, taking into account the fractions of formaldehyde forming HMS in SJV fogs, can explain why the HPLC method (with citrate buffer) only accounted for 38%~75% of the fluorescence HCHO measurements which determine the sum of free HCHO and HMS.

Based on these findings, the difference between HCHO concentrations measured by the fluorescence and HPLC methods could approximate the HMS concentrations originally in the fog. Using this approach we estimate the HMS concentrations in the Fresno fog samples ranged from 6.2 to 50.2 μM, averaging 16.8 μM. 0.46 ppmC HCHO.

Now Figure 5-8 can be modified to include the contribution of estimated HMS. Original HCHO contribution (2.7% of total DOC) can be broken down to 1.9% HCHO and 0.8% HMS (average concentration: 0.46 ppmC HCHO vs. 0.20 ppmC HMS). This amount of HMS is comparable with isovaleraldehyde, which is 0.9% of total DOC, but only about 50% of glyoxal.

Table 5-16. Chemical compositions of cloudwater and fogwater collected by size-fractionating CASCC (Adapted from Rao et al., 1995).

Sampling site	Local time	pH		Total HCHO (μM)		HMS (μM)	
		Small drops	Large drops	Small drops	Large drops	Small drops	Large drops
La Jolla Peak, CA	00:50-01:50	3.33	3.90	18.4	11.1	1.0	0.5
07/01/1993	01:56-02:29	3.46	3.64	17.6	9.3	1.1	0.5
	02:31-03:34	3.54	3.76	16.0	9.4	1.2	ND*
	03:38-04:05	3.82	3.75	16.5	8.6	0.9	0.5
	04:06-05:20	3.45	3.57	16.3	10.9	1.0	0.8
	05:26-05:46	3.33	3.35	17.4	14.8	0.8	0.5
Bakersfield, CA	02:50-07:00	5.89	6.48	133.8	82.4	29.8	6.5
01/15/1994	07:45-09:45	6.40	6.67	183.3	118.4	37.8	0.5
	09:50-10:10	6.21	6.91	162.5	97.4	NA	1.8
	10:10-11:20	6.10	6.76	175.6	111.5	NA	3.1

*ND: not detected. NA, sample not available

5.2.6.5 Species size distribution of Fresno fog samples

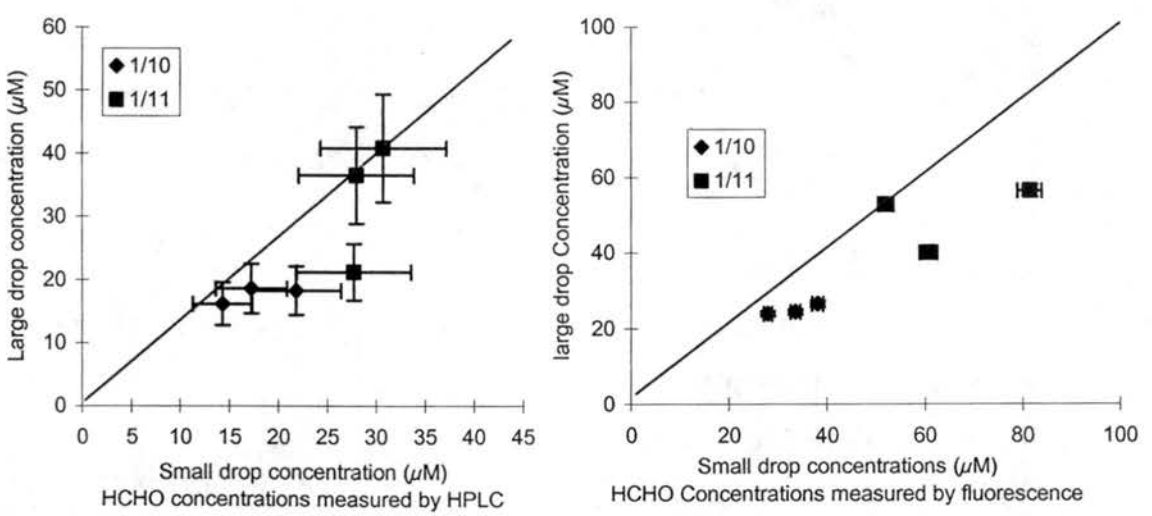

Figure 5-9. Concentrations of HCHO measured by the HPLC method and fluorescence in large and small drop samples collected with the ss-sf-CASCC in Fresno radiation fogs on the night started from Jan 10-Jan 11, 2004.

Figures 5-9 to 5-17 shows the size distributions of carbonyls and dicarbonyls based on

information from Table 5-12. HCHO didn't show a strong size dependence; it was approximately evenly distributed between small and large drops. Other carbonyls and dicarbonyls were more or less all enriched in small drops.

Formaldehyde didn't show significant differences between large and small drops within uncertainty range. HCHO in drops is taken up from the gas phase and similar partitioning to small and large drops is expected if equilibrium is attained. Most of the available HCHO remains in the gas phase inside typical fogs and clouds (Seinfeld et al., 1998). If total HCHO (free HCHO + HMS) as measured by the fluorescence technique is examined, there still is little indication of enrichment in large or small drops.

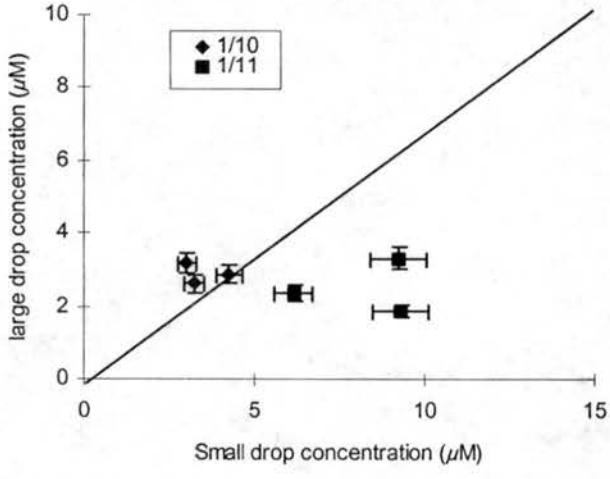

Figure 5-10. Concentrations of acetaldehyde measured by the HPLC method in large and small drop samples collected with the ss-sf-CASCC in Fresno radiation fogs on the night started from Jan 10-Jan 11, 2004.

Typical sources of acetaldehyde include emissions from combustion processes such as motor vehicles, incomplete combustion in fireplaces, industry, etc. In California, photochemical oxidation is the largest source - as high as 41 to 67 percent of acetaldehyde concentrations in the ambient air (Seinfeld et al., 1998). Acetaldehyde exists in the atmosphere in the gas phase. From Figure 5-10 we see a tendency for acetaldehyde to be enriched in smaller fog drops in the Jan. 11th samples but little size-dependence for the Jan. 10th samples.

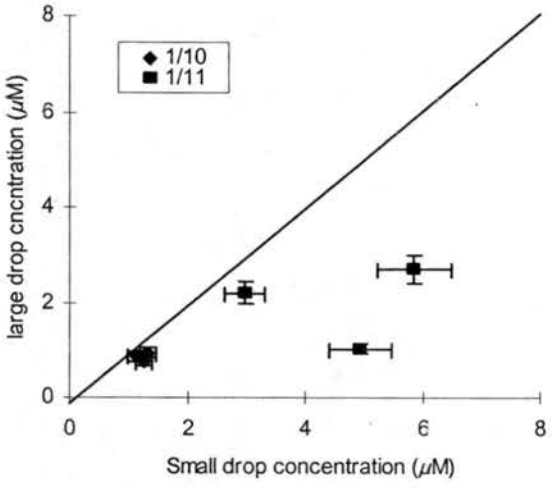

Figure 5-11. Concentrations of acrolein and acetone measured by the HPLC method in large and small drop samples collected with the ss-sf-CASCC in Fresno radiation fogs on the night started from Jan 10-Jan 11, 2004.

Acrolein can be formed from the breakdown of certain pollutants, such as heterogeneously catalyzed gas-phase oxidation of propene. Acrolein can also be from burning tobacco, or from burning gasoline. Acetone is the simplest representative of the ketones. The major source of acetone is from industrial emission where it is produced or used. Acetone is also found in plants, forest etc. As illustrated in Figure 5-11, acrolein and acetone also appear to be enriched in smaller fog drops on Jan. 11th but not on the 10th.

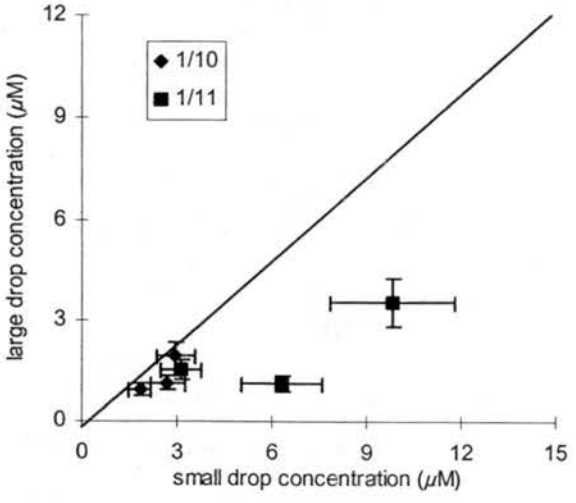

Figure 5-12. Concentrations of isovaleraldehyde measured by the HPLC method in large and small drop samples collected with the ss-sf-CASCC in Fresno radiation fogs on the night started from Jan 10-Jan 11, 2004.

Isovaleraldehyde was enriched in small drops collected on Jan. 11th as seen from

Figure 5-12. It is a compound with an apple-like odor which can be derived from natural sources such as honey or the rain forest. It also comes from industrial emissions, such as those associated with the food and fragrance industry, and contributes to the aromatic qualities of coffee.

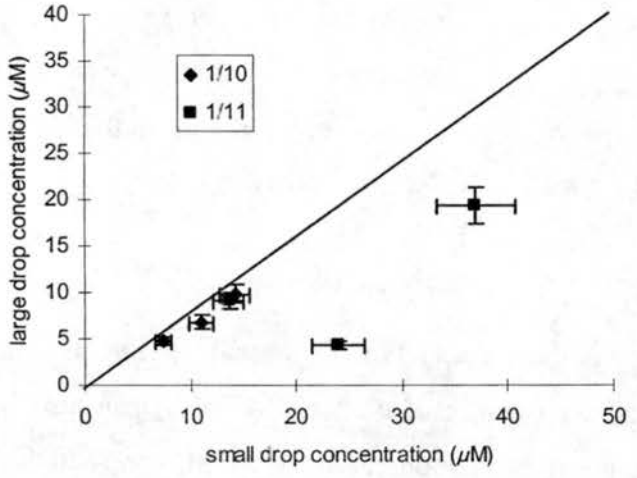

Figure 5-13. Concentrations of glyoxal measured by the HPLC method in large and small drop samples collected with the ss-sf-CASCC in Fresno radiation fogs on the night started from Jan 10-Jan 11, 2004.

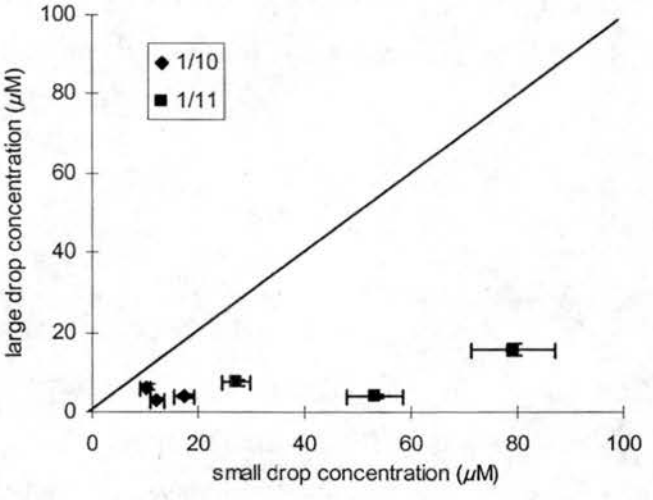

Figure 5-14. Concentrations of methylglyoxal measured by the HPLC method in large and small drop samples collected with the ss-sf-CASCC in Fresno radiation fogs on the night started from Jan 10-Jan 11, 2004.

Glyoxal and methyl glyoxal are present in tobacco smoke and are also products of ring opening reactions of PAHs. For example, toluene and other aromatics, after reaction with hydroxyl radical and oxygen in the environment, will generate ring-fragmentation products including glyoxal and methyl glyoxal (Seinfeld et al., 1998). Also some □,□-unsaturated carbonyls, for example, acrolein, can react with ozone and OH radical,

and ultimately give rise to □-dicarbonyls such as glyoxal and methyl glyoxal. Figure 5-13 and 5-14 show that glyoxal and methyl glyoxal are somewhat enriched in smaller drops with generally greater enrichment for glyoxal. This strong enrichment in small drops mirrors patterns often seen in SJV fogs for TOC and inorganic solutes and suggests these species are probably associated with scavenged particles.

Figures 5-15, 5-16 and 5-17 show size-distributions of tolualdehyde (m-, p-) and hexaldehyde. Only trace concentrations of tolualdehyde (m-, p-) and hexaldehyde were observed. They were also enriched in small drops. These compounds, known to be carcinogenic and mutagenic, are oxidation products of emission of motor vehicles.

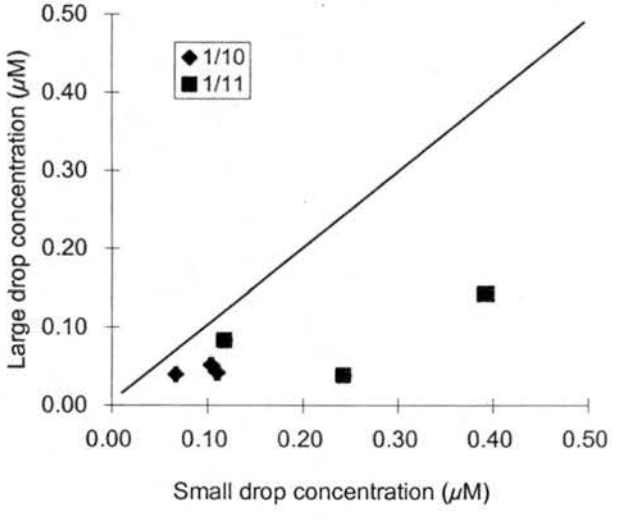

Figure 5-15. Concentrations of m-Tolualdehyde measured by the HPLC method in large and small drop samples collected with the ss-sf-CASCC in Fresno radiation fogs on the night started from Jan 10-Jan 11, 2004.

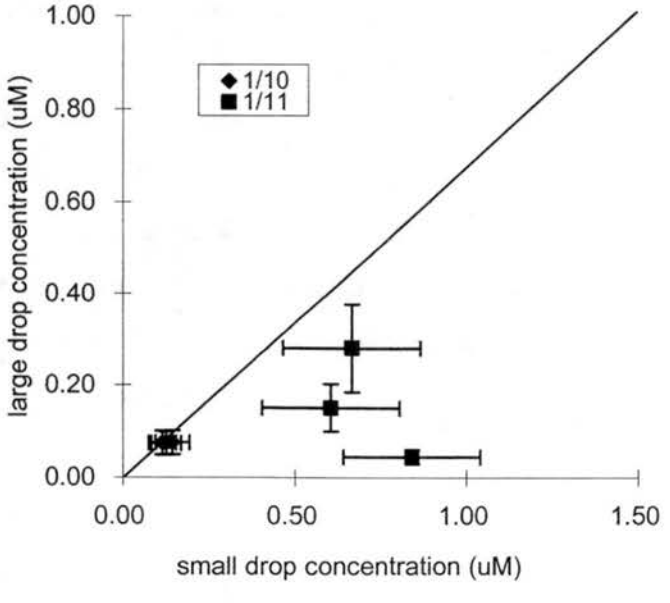

Figure 5-16. Concentrations of p-Tolualdehyde measured by the HPLC method in large and small drop samples collected with the ss-sf-CASCC in Fresno radiation fogs on the night started from Jan 10-Jan 11, 2004.

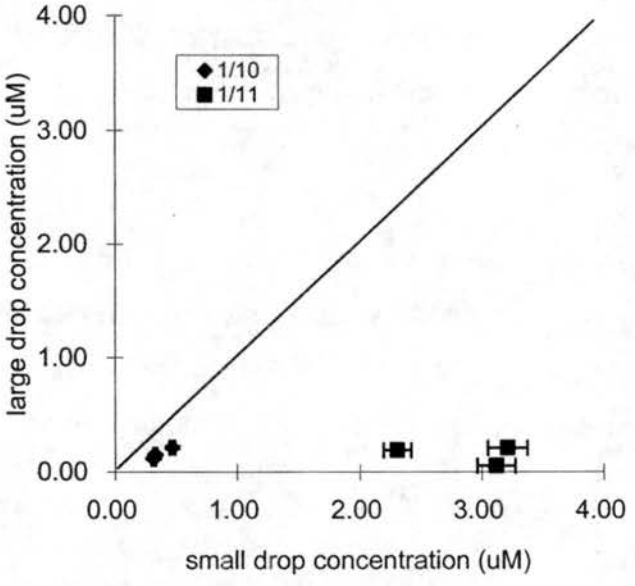

Figure 5-17. Concentrations of hexaldehyde measured by the HPLC method in large and small drop samples collected with the ss-sf-CASCC in Fresno radiation fogs on the night started from Jan 10-Jan 11, 2004.

5.3 Functional group characterization of organic acids.

5.3.1 Overview

Several investigations (Gundel et al., 1993; Gundel et al., 1994; Saxena et al., 1996; Suzuki et al., 1998; Facchini et al., 1999; Zappoli et al., 1999; Blando et al., 2000; Decesari et al., 2000) have found that mono-, di-, and polyfunctional carboxylic acids are important contributors to water soluble organic carbon in fogs and aerosol particles. Here we utilize a different HPLC method to provide a functional group separation of organic acids. The method was first described by Fuzzi et al. (2000). It is designed to separate organic compounds in aqueous samples into several compound classes by separation on an HPLC ion exchange column with UV detection. This method provides a complementary way to investigate the form of the carbonaceous fraction (water-soluble organic compounds, WSOC) in fog water.

5.3.2 Instruments and reagents

5.3.2.1 HPLC conditions

The following conditions were used for the analysis by HPLC.

- Column: Toso-Haas TSK DEAE-5PW gel column, 7.5 cm x 7.5 mm, 10 μ.
- Mobile Phase Gradient: the initial mobile phase is DI water. From 0.2 to 2 minutes, the solvent composition was linearly changed to 100% eluent B: 0.02 M $NaClO_4$, 0.02 M Tris-hydroxymethyl-aminomethane (TRIS) and 10% methanol. Keep this solution from 2 to 10 minutes. From 10 to 15 minutes, eluent phase was linearly changes from 100% eluent B to 100% eluent C, which is 0.4 M $NaClO_4$, 0.02 M TRIS and 10% methanol. Keep 100% eluent C from 15 to 20 minutes. During the post run period (6 minutes), the column was flushed by DI water.
- Temperature: 30.0°C
- Flow Rate: 1.0 ml/min for first 20 minutes, then 1.2 ml/min for the rest of time.
- Detector: Diode Array Detector, Absorbance operated at 254 nm.
- Injection Volume: 100μl

5.3.2.2 Reagents

$NaClO_4$	Crystal, analytical grade, Fisher Scientific
0.02M TRIS	Tris-hydroxymethyl-aminomethane - HPLC grade or equivalent. Aldrich
methanol	HPLC grade or equivalent. Fisher Scientific

5.3.3 Procedures

1. No pre-treatment is required for the fog water samples. Refrigerated samples were allowed to warm to room temperature. 430 μl was pipetted into a 1.5 ml glass auto sampler screw cap vial with a 500 μl insert.
2. Prepare three eluent solutions.
   (1). DI water; (2). 0.02 M $NaClO_4$, 0.02 M Tris-hydroxymethyl-aminomethane (TRIS) and 10% methanol. (3). 0.4 M $NaClO_4$, 0.02 M Tris-hydroxymethyl-aminomethane

(TRIS) and 10% methanol.

Note: it takes a long time for TRIS to dissolve in the water. Ultrasonication is necessary to quicken the process. Weigh the TRIS in a small beaker, and add an appropriate amount of DI water then put the beaker in an ultrasonic bath for over an hour. Transfer the solution into volumetric flask. Add other required compounds to complete making the eluent.

3. Turn on HPLC, run the method first to ensure there is no leak in the connections, and wait for the baseline to stabilize.
4. Inject 100 μl samples.

   Note: generally, 20 μl injection volume may be sufficient if you have high concentrations of DOC in the fog water. If your samples contain mainly aliphatic oxygenated compounds, and they have relatively small absorption efficiencies, 100 μl injection volume is better to get good peak shape and larger area of absorption.

5.3.4 Results

5.3.4.1 Method Test

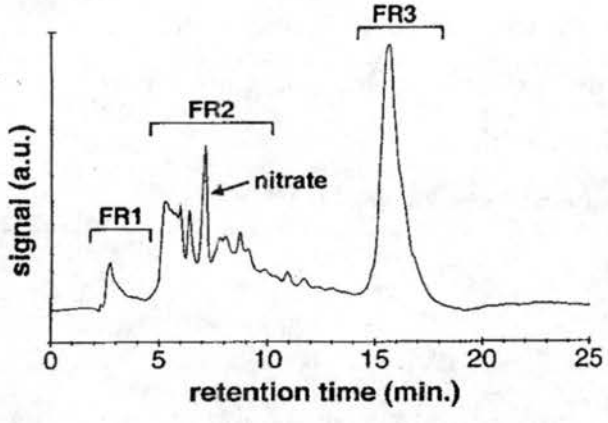

Figure 5-18. HPLC chromatograms of fog water. The three fractions defined in the test (FR1, FR2 FR3) are indicated by the horizontal bars above the chromatogram. The peak due to nitrate is also evidenced. (taken from Decesari et al. (2000)).

This method uses gradient elution by increasing the ionic strength of the eluent buffer solution to separate the WSOC in fog water. Uncharged (neutral) compounds are expected to elute the quickest because the separation method relies on ion exchange. One expects compounds with a greater number of charges (e.g., poly-functional carboxylic

acids) to bind more strongly and elute later. Figure 5-18 (taken from Decesari et al. (2000)) shows that the method separates the WSOC in fog water into three organic fractions, with a nitrate peak in between (nitrate appears in the chromatogram due to its UV absorption characteristics). Chromatographic separation was performed on an anion exchange DEAE-TSK gel column (Toso-Haas, 7.5 mm ID × 7.5 cm length), and detected by a Varian 2550 UV detector at 254 nm. The HPLC conditions used are the same as we used. They also quantitatively analyzed the three classes of compounds derived from total organic carbon (TOC) analysis by using a preparative scale packed column filled with a DEAE-cellulose gel. A volume of sample corresponding to ~1 mg of organic carbon content was eluted through the column and a stepwise elution was performed at 1.0 ml min^{-1} with water, then with buffer solutions of NH_4HCO_3 0.05 and 1.0 M at pH=8.0. They found that the three fractions account for 77% carbon of the total WSOC concentration in a fog water sample.

Overall, Fuzzi and co-workers describe the three organic fractions as the following, and their typical amount in Fuzzi's samples (aerosol and fog water samples taken from station of S. Pietro Capofiume in the Po Valley, northern Italy) are:

1. Neutral/ Basic compounds, comprised about 26±4% of total WSOC;
2. mono- and di-carboxylic compounds, comprised about 37±5% of total WSOC;
3. polyacidic organic compounds, comprised about 23±7% of total WSOC.

Spectroscopic techniques have been used to identify functional groups for a long time. Approaches include IR spectroscopy, UV spectroscopy, fluorescence and nuclear magnetic resonance. These approaches have been used to identify some aerosol and fog water organic characteristics (Blando et al., 1998; Havers et al., 1998; Suzuki et al., 1998). While spectroscopic techniques can shed light on the major characteristics of organic species in aerosol and fog water samples, they cannot generally provide detailed information about the particular compounds present in a sample. HPLC, as one of the most effective chromatographic separation techniques, can separate organic compounds into different classes based on their functional groups, and often can distinguish between

compounds of the same family with similar structures.

However, because of the complex mixtures of organic species in the environment, a universal separation method, that works in some areas for certain types of samples might not function well in a different area or with different samples. Therefore, before using this HPLC method on our fog samples collected in California, some tests are necessary. Based on the abundance of organic compounds we suspect in the region, we chose aldehydes, ketones, aromatic compounds (PAHs), aliphatic oxygenated compounds, and amines and amino acids as test compounds for the HPLC DEAE separation. Among each compound family we started testing from the simplest compound and avoid using those compounds that have two different functional groups in the molecule. Our first goal is to test if this method can be used on California fog samples without modification. Also, the peaks in the HPLC chromatogram are broad and likely include several individual compound responses different than normal HPLC chromatogram with a single diagnostic peak/retention time for each compound. Therefore, our second goal is to try to identify some strong peaks corresponding to certain compounds.

Figures 5-19 to 5-24 show HPLC analyses of several individual compounds, including sodium nitrate (110 μg/ml), sodium nitrite (105 μg/ml), methyl glyoxal (120 μg/ml), benzene (100 μg/ml), phenol(100 μg/ml) and vanillin (110 μg/ml). Sodium nitrate and sodium nitrite are included because they have strong UV absorptions and nitrate and nitrite are important compounds in SJV fogs. We can see that nitrate and nitrite show strong peaks at retention times of 6.8min and 6.0min, respectively. These two peaks are in fraction 2, labeled by previous investigators as mono/di-carboxylic acids. The occurrence of a nitrate peak in this region of the chromatogram has been widely reported. Methyl glyoxal has a somewhat surprising chromatogram, with three large peaks and one smaller peak. The first three peaks fall into the right fraction (neutral/basic), but the fourth peak is in fraction 2 corresponding to mono/di-carboxylic acids. Since methyl glyoxal has fairly small absorption efficiency, its net effect on the UV absorption chromatogram may be relatively small, although we saw above that methyl glyoxal can be present at large concentrations. Benzene elutes in the polyacidic organic compound

fraction, instead of neutral/basic compounds fraction as we expected. Phenol, one of the simplest aromatic compounds with only one hydroxyl group attached to a benzene ring, elutes in the mono-/di-carboxylic acid fraction, rather than the neutral/basic fraction. Vanillin, a compound associated with wood smoke, has a higher absorption efficiency and also appears in the mono-/di-carboxylic acid fraction instead of the neutral/basic fraction.

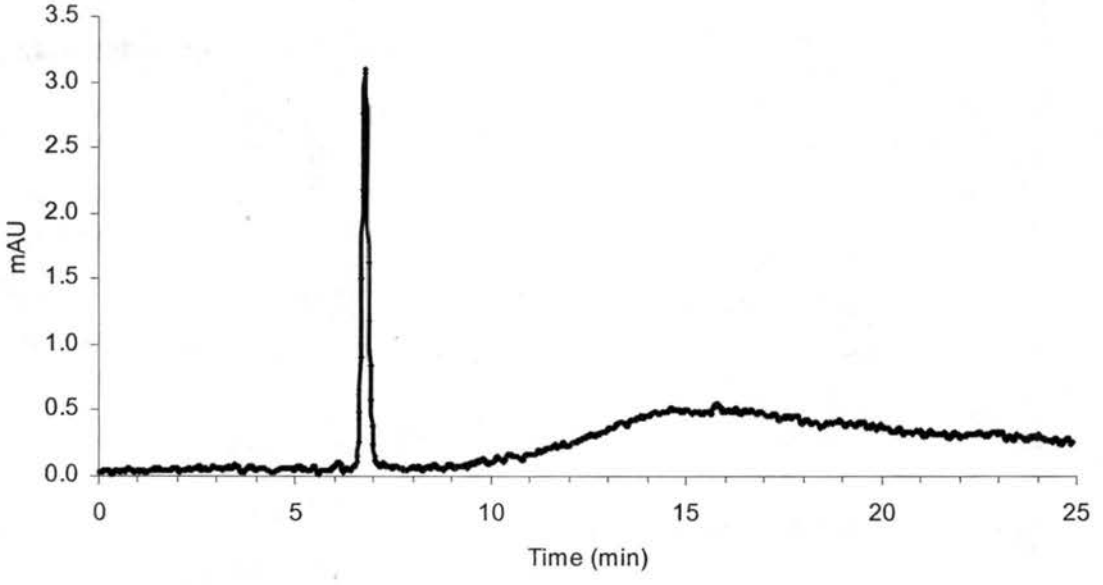

Figure 5-19. HPLC chromatogram of sodium nitrate using DEAE method.

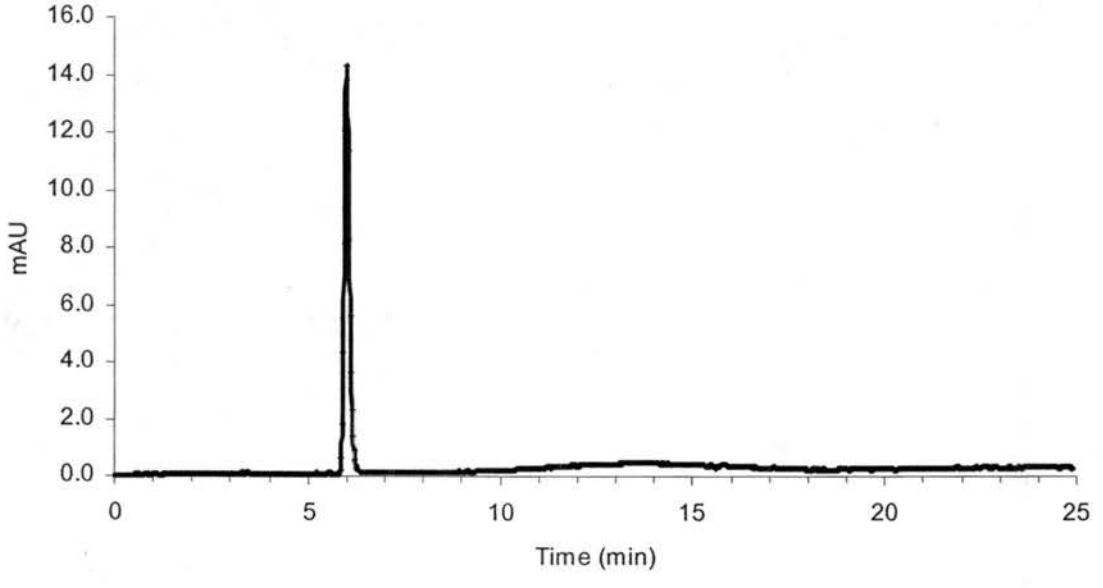

Figure 5-20. HPLC chromatogram of sodium nitrite using DEAE method.

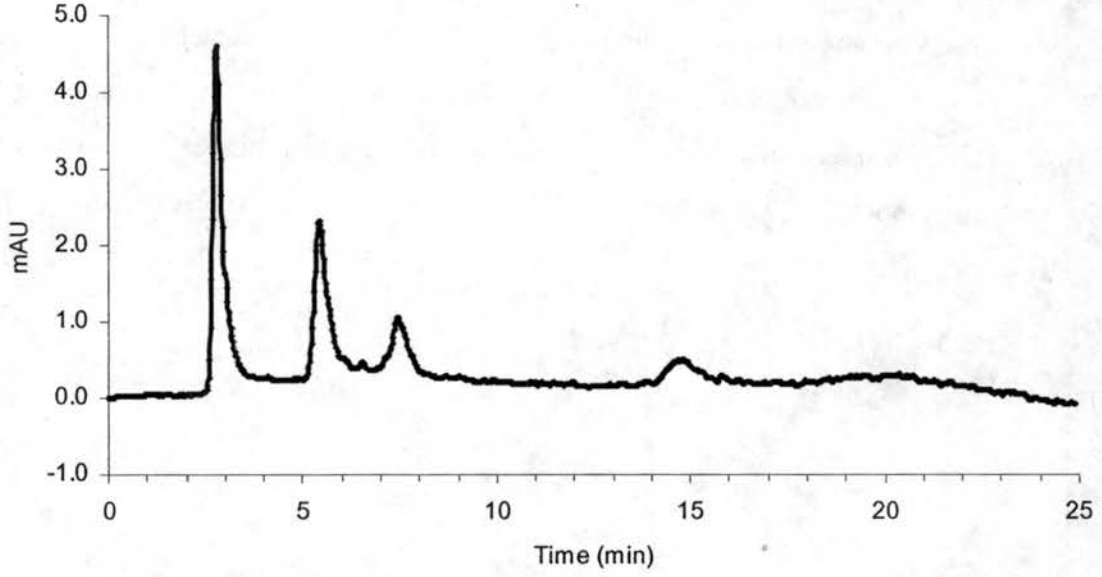

Figure 5-21. HPLC chromatogram of methyl glyoxal using DEAE method.

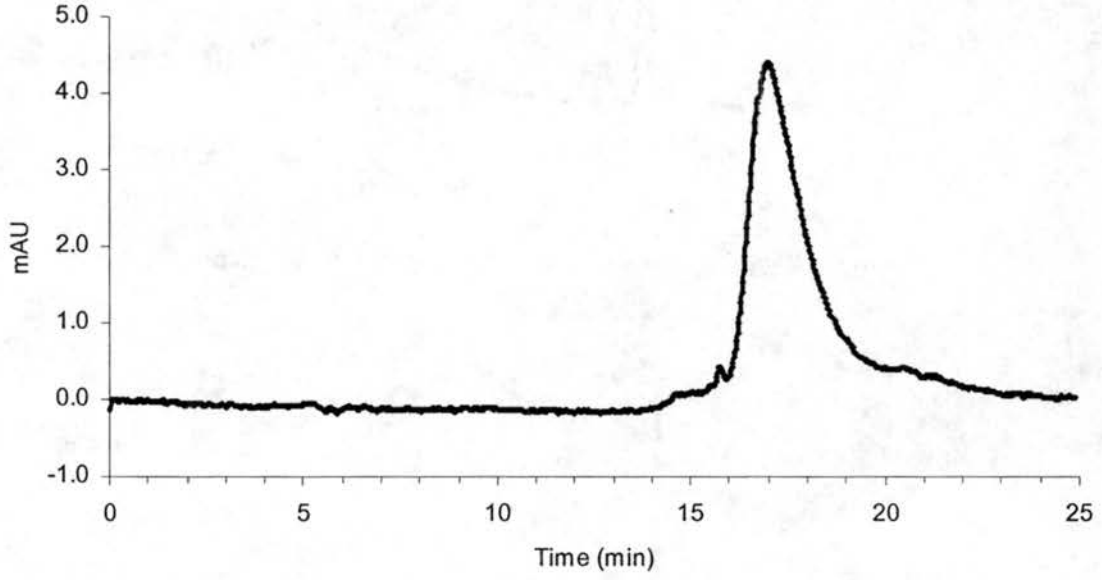

Figure5-22. HPLC chromatogram of benzene using DAEA method.

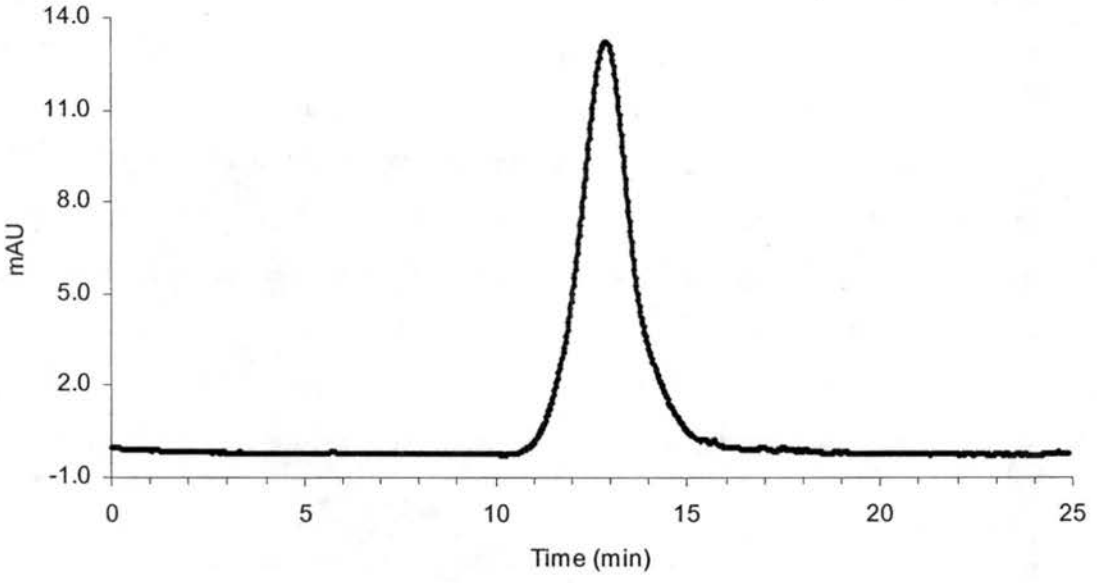

Figure 5-23. HPLC chromatogram of phenol using DEAE method.

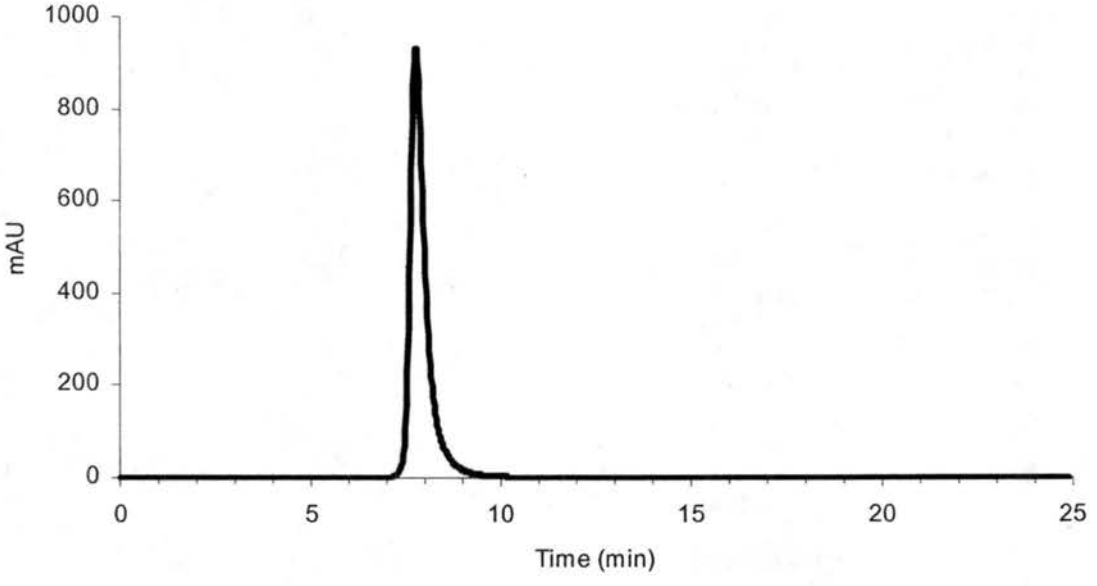

Figure5-24. HPLC chromatogram of vanillin using DEAE method.

Table 5- 17A shows the summary of the individual compound tests. This table only lists compounds which absorb at 254nm. Some compounds we tested turned out to have no absorption in the UV range and thus could not be monitored. These compounds are listed in table 5-17B. In table 5- 17A the compounds are organized by aldehyde, ketone,

"normal" organic acids (non-aromatic) and aromatic compounds, based on their expected separation fraction assigned based on the functional group present. For example, acetone has no carboxylic acid group and is expected to elute in fraction 1, neutral/basic compounds. Pyruvic acid, however, has one carboxylic acid group, so it belongs to fraction 2, mono- and di-carboxylic acids. Observed fractions are the fractions where compounds actually appear in the test chromatograms. The retention times observed for each compound are shown in Table 5-17A as well.

Table 5-17A. Expected and observed separation regions of some organic compounds.

	Compounds	Retention time (min)	Expected Fraction	Real Fraction	Absorption Efficiency (Area/concentration) mAU*S / µg/ml (mAU*S / µgH/ml)
	Neutral/basic				
Aldehyde	methyl glyoxal	2.8, 5.4, 7.4, 14.8	1	1, 2	0.71, 0.39, 0.17, 0.12
Aldehyde	benzaldehyde	11.9	1	2	111 (1961)
Ketone	Acetone	2.9	1	1	0.43 (4.16)
Aromatic	acridine	4.5	1	1	<0.68 (13.5)
Aromatic	4-hydroxy-3,5-dimethoxy benzaldehyde	7.5	1	2	227 (4131)
Aromatic	vanillin	7.8	1	2	243 (4617)
Aromatic	2,6-dimethoxy-phenol	9.0	1	2	53.6 (825)
Aromatic	aniline	9.4	1	2	91.3 (1213)
Aromatic	guaiacol	10.6	1	2	85.5 (1325)
Aromatic	o-nitrophenol	11.7	2	2	34.2 (951)
Aromatic	phenol	12.9	1	2	12.8 (201)
Aromatic	Benzene	17.0	1	3	4.14 (538)
Aromatic	4-ethylguaiacol	17.4	1	3	118 (1495)
Aromatic	m-cresol	17.9	1	3	96.7 (1305)
	Mono-carboxylic acid				
	pyruvic	5.5	2	2	7.03 (155)
Aromatic	Salicylic	13.2	2	2	9.61 (221)
	Di-carboxylic acid				
	Oxalic	7.8	2	2	0.28 (12.6)
Aromatic	succinic	8.7	2	2	0.52 (10.2)
Aromatic	Phthalic	8.7	2	2	12.8 (354)
	Polyacidic organics				
	Humic	15.5	3	3	5.54
	Tannic	16.3	3	3	4.88
	Inorganic Reference groups				
	Nitrite	6.0	--	--	1.34
	Nitrate	6.8	--	--	0.34

Table 5-17B. Organic compounds, tested with the HPLC DEAE separation but yielding no absorption.

Compounds		Retention time (min)	Expected Fraction
Neutral/basic			
Aldehyde	HCHO	--	1
	dodecyl aldehyde	--	1
	nonyl aldehyde	--	1
	decyl aldehyde	--	1
	glyoxal	--	1
Aromatic	toluene	--	1
	naphthalene	--	1
	benz[a]anthracene	--	1
Mono-carboxylic acid			
chain	Oleic	--	2
Aromatic	abietic	--	2
Di--carboxylic acid			
chain	glutaric	--	2
	citrate	--	2
	suberic	--	2

The absorption efficiency of each compound was obtained by dividing the area of the peak of each compound in each chromatogram by its concentration. For compounds with multiple peaks such as methyl glyoxal, the absorption efficiency was calculated for each peak and listed respectively. This absorption efficiency can be used to qualitatively define the relative sensitivity of the method to different compounds. For instance, benzaldehyde has a much higher absorption efficiency than acetone (111mAU*S/μg/ml vs. 0.43mAU*S/μg/ml). Consequently, for equal concentrations of benzaldehyde and acetone, benzaldehyde will have a much bigger impact on the observed chromatogram. Similarly, shown in brackets is another hydrogen-normalized absorption efficiency, where the area of the peak is divided by hydrogen concentrations in the solutions. Hydrogen concentrations were calculated based on the fraction of hydrogen in the molecules of one compound, and the concentration of the compound. The hydrogen

absorption efficiency will be used later to estimate the impact of misidentified compound types on the chromatograms based on H-NMR analyses of the functional group classes comprising fog DOC.

From the tables and figures above, we can see that many compounds which belong in theory to fraction 1 (neutral/basic compounds) appear in fraction 2 (mono-/di-carboxylic acid), some even in fraction 3 (polyacidic compounds). Compounds whose peaks appear in the wrong fraction are mainly aromatic compounds. Complicating matters, their absorption efficiencies are much higher than most non-aromatic compounds.

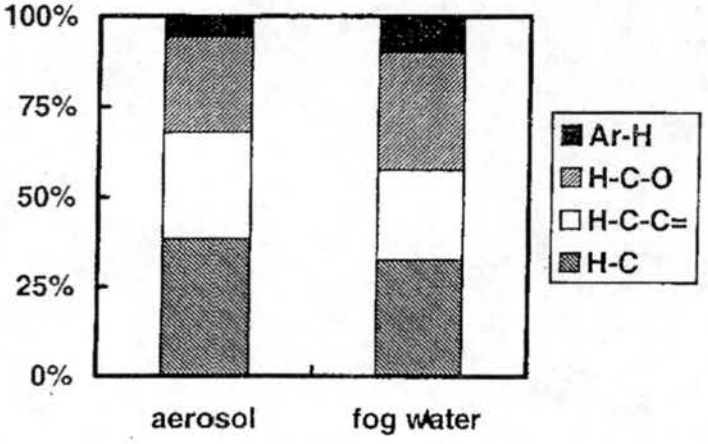

Figure 5-25. Normalized abundance in the aerosol water extract and fog sample of nonexchangeable protons in the four categories (Taken from Decesari et al. (2000)).

This method is not as simple as claimed in the literature. The classification of the observed fractions as neutral/basic, mono and di-carboxylic acids and polyacids appears inaccurate. Charge-based separation might not be the only factor determining retention times as indicated by the long retention times of cresol and 4-ethylguaiacol. Methyl glyoxal, one major component in California fog samples, may react with the eluent mixture thus shows multiple retention times in the spectrum. Single compound tests above show that compounds without carboxyl groups often elute in the second or third fractions, probably because some compounds such as phenolic compounds, can partly dissociate at elution pH=8 (pKa ~ 7) and elute in the mono- and di-carboxylic acid fractions. Also, some aromatic compounds, such as phenols, appear in the wrong fraction with very high absorption efficiencies at 254 nm, making it hard to get useful quantitative, and even qualitative, information about the composition of WSOC according to the

compound classes typically associated with this method in the literature. Nuclear magnetic resonance (NMR) analyses of fog water obtained by Fuzzi et al. (2000) can be used to estimate the importance of this bias by giving a basic idea of the speciation of organic compound in the fog water. NMR is a phenomenon which occurs when the nuclei of certain atoms are immersed in a static magnetic field and exposed to a second oscillating magnetic field. Whether the nuclei experience this phenomenon or not depends upon whether they possess a spin. NMR spectroscopy of hydrogen (H-NMR) is routinely used to study chemical structure, since the intensity and chemical shifts of peaks in the spectrum can be used to identify protons in different environments and quantify molecular structures.

Hydrogens are connected to different functional groups, which affect the chemical shifts of hydrogen dramatically. While the mass concentrations attributable to different functional groups can not be inferred directly from H-NMR, we can obtain normalized abundances. Figure 5-25 (Taken from Decesari et al. (2000)) shows representative categories of functional groups of fog water and aerosol samples determined by H-NMR spectra: Ar-H are aromatic protons; H-C-O are protons on carbon atoms singly bound to oxygen atoms; H-C-C= are aliphatic protons on carbon atoms adjacent to carbonyl groups or aromatic rings; H-C are aliphatic protons.

Read from the figure above, we can roughly get: Ar-H: ~10%; H-C-O: ~25%; H-C-C=: ~30%; H-C: ~35%. We can therefore evaluate how important aromatic compounds can be in terms of influencing the HPLC chromatograms. The influence of aromatic compounds is estimated by calculating the percentage of aromatic compounds in the chromatograms. Absorption efficiencies for different functional group classes were roughly estimated based on Table 5-17A. These absorption efficiencies were then multiplied by the estimated concentrations of each functional group. This is a rough estimate because (1) to calculate the influence percentage, we assume here that all the compounds have absorptions in UV range, while Table 5-17B has shown that some compounds like HCHO, which is abundant in the fog water, don't have UV absorption. (2) absorption efficiency varies a lot for individual compounds. (3) organic composition may vary significantly for

different fog samples.

Table 5-18 shows that for fog samples from the Po Valley in Italy, the influence of aromatic compounds can be from 22% to 33% based on the HNMR analysis. High organic acid contents were found in California's Central Valley fog samples (Ervens et al., 2003), with 20% of TOC comprised by acetic acid. Therefore, the errors that come from aromatic compounds will make the results inaccurate.

Table 5-18. Evaluation of effects of aromatic compounds on DEAE HPLC chromatogram

Absorption efficiency* (mAU*S/μgH/ml)	Minimum influence	Maximum influence
2000	10% aromatic compounds (whole single Ar-H)	10% aromatic compounds (whole Ar-H plus H-C-C=)
200	25% mono/di-acids or polyacids (whole H-C-O)	55% mono/di-acids or polyacids (whole H-C-O and H-C-C=)
1000	65% neutral compounds (assuming neutral compounds comprise alkane and alkene mainly)	35% neutral compounds (assuming neutral compounds comprise alkane mainly)
Influence by Aromatic compounds	22%	33%

*Absorption efficiencies of compounds are read and roughly evaluated from table 5- 17A.

5.3.5 Sample results

5.3.5.1 Blanks

Figure 5-26 shows a typical HPLC spectrum of DI water used in California. There were some unknown strong absorptions at around 15 minutes. Overall, the absorption is not high. All the spectrums shown below will be the net spectrum with blank absorption correction.

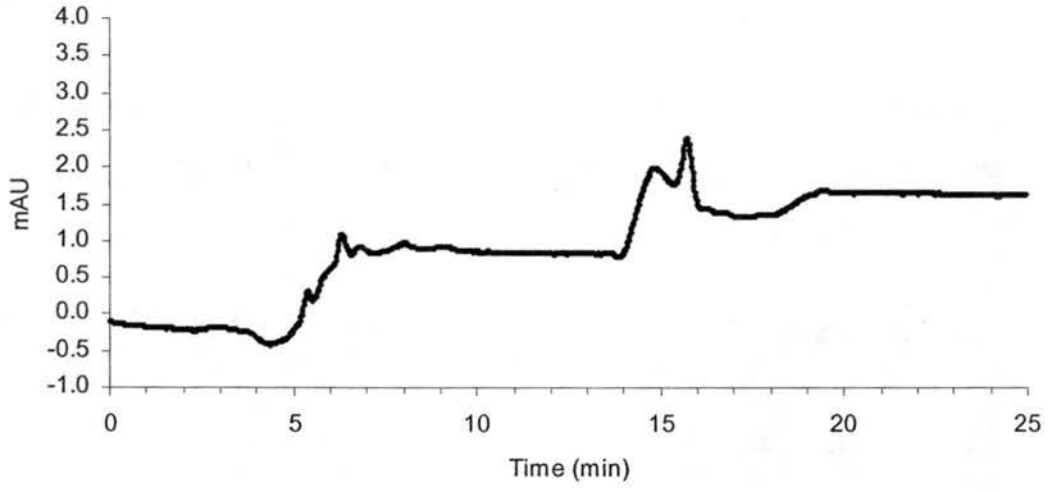

Figure 5-26. HPLC chromatogram of DI water using DEAE method.

5.3.5.2 California fog samples (Angiola)

Several Angiola fog samples were analyzed by the HPLC DEAE method on Oct 2003. In many of these samples, little response was observed, probably reflecting compound degradation during the long storage period. Figure 5-27 shows a representative spectrum for sample AGCC35204, the fourth fog sample colleted on 12/17, 2002 by a CASCC collector. The peak at 6.8 min apparently is sodium nitrate. The remainder of the chromatogram is not much different from blanks on Figure 5-26.

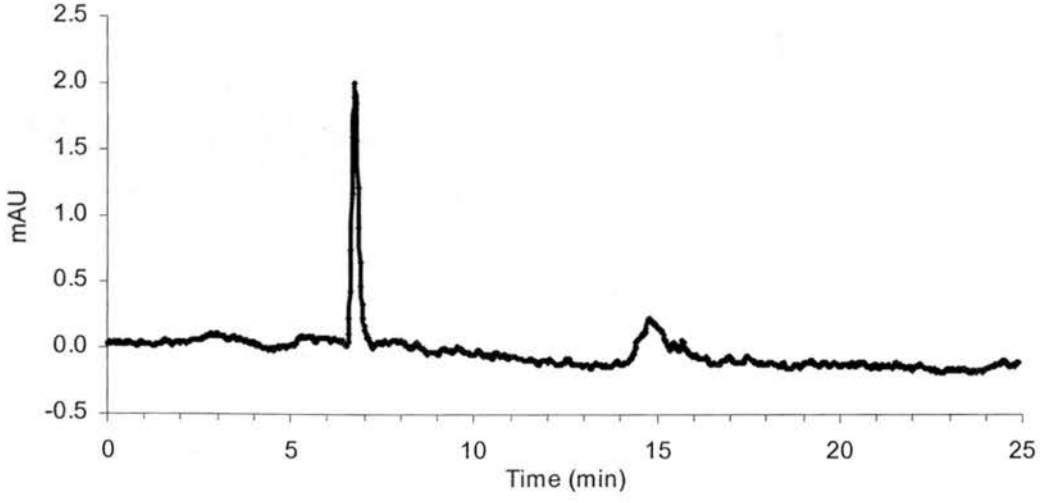

Figure 5-27. HPLC chromatogram of one real California sample using DEAE method.

Four samples were found to be different from the other samples (AGCC03101, AGPCL03101, AGPCL03102 and AGPCL03103). These are bulk and large drop fog samples from a Jan 31st fog event. They all show multiple peaks with strong absorptions in the UV.

Figures 5-28 to 5-31 shows the results for these four samples. Their chromatograms are very similar to the example shown by in Fuzzi et al. (2000). We can clearly see the nitrite and nitrate peaks, and three organic fractions as well.

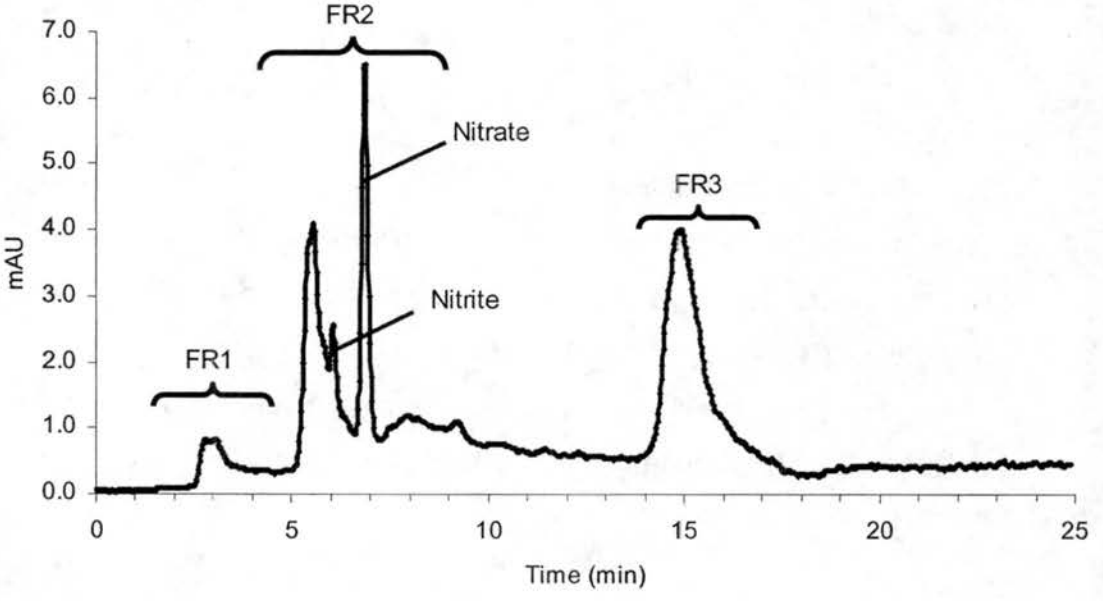

Figure 5-28. HPLC chromatogram of California sample AGCC03101 using DEAE.method

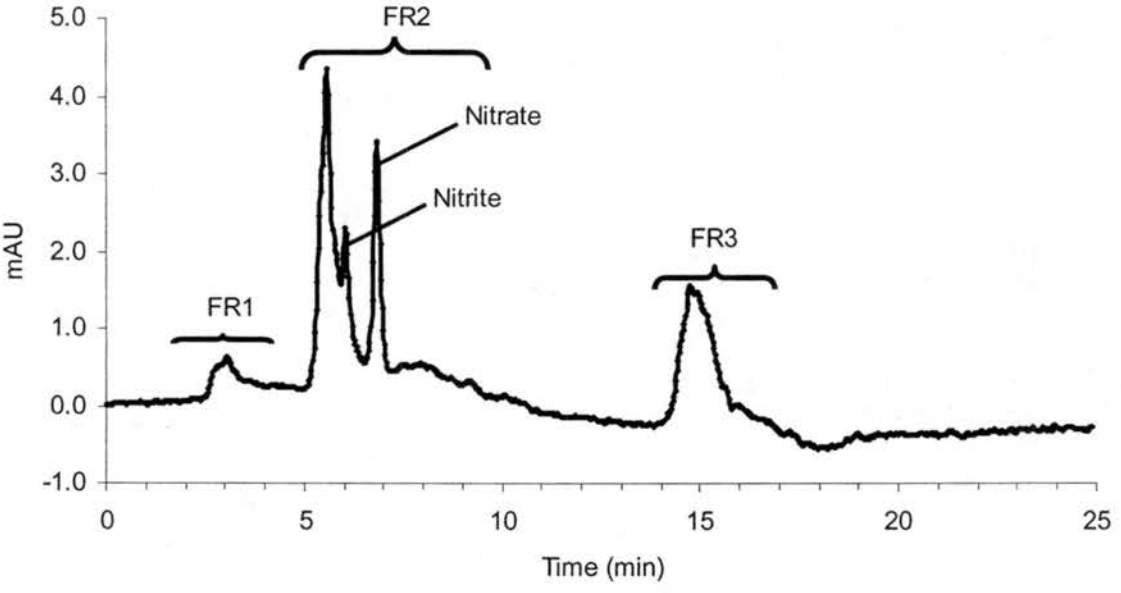

Figure 5-29. HPLC chromatogram of California sample AGPCL03101 using DEAE. method

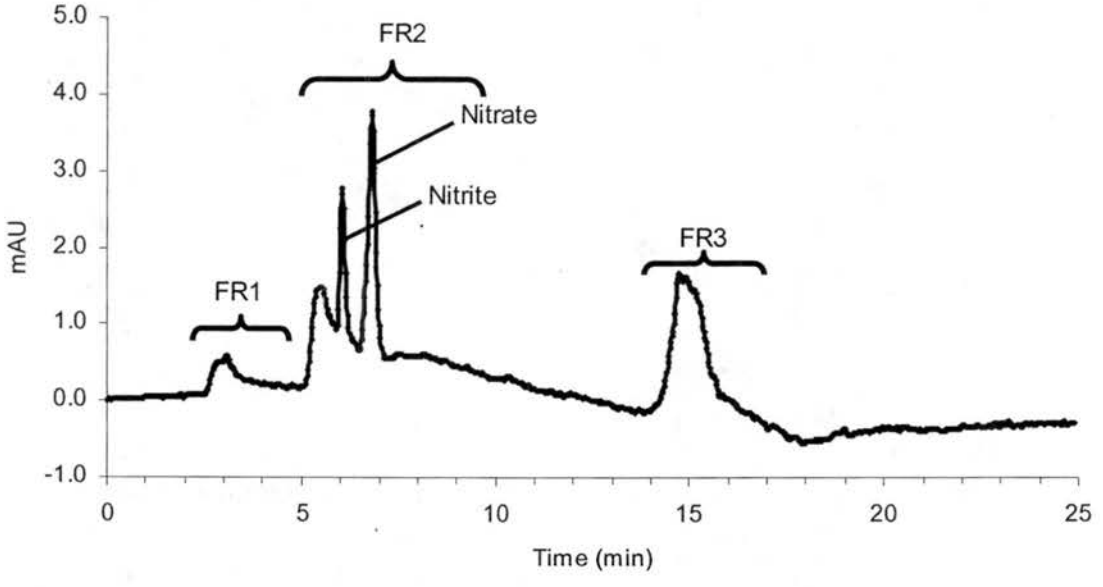

Figure 5-30. HPLC chromatogram of California sample AGPCL03102 using DEAE method.

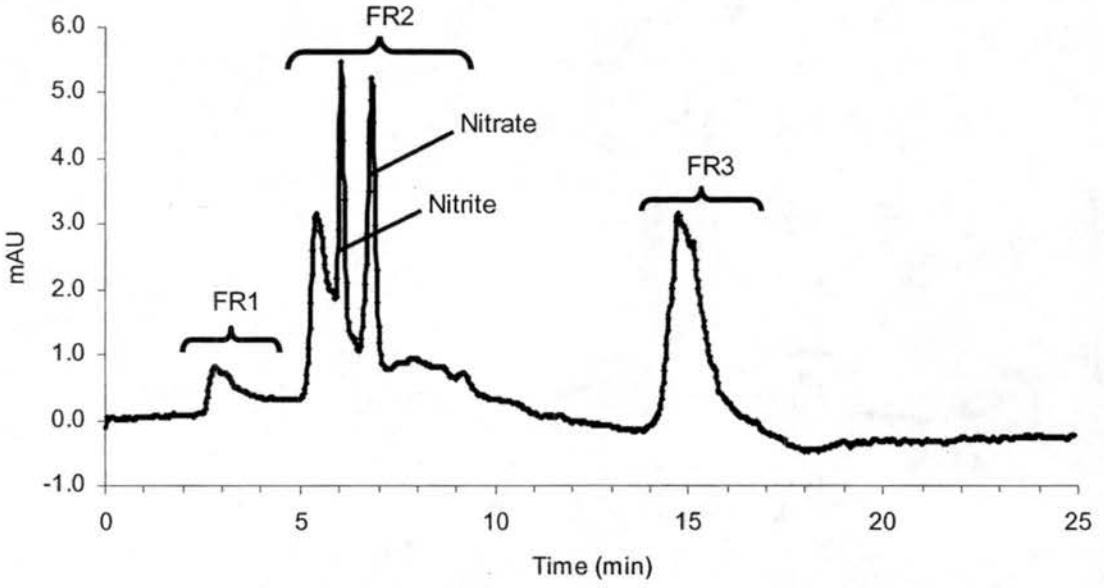

Figure 5-31. HPLC chromatogram of California sample AGPCL03103 using DEAE method.

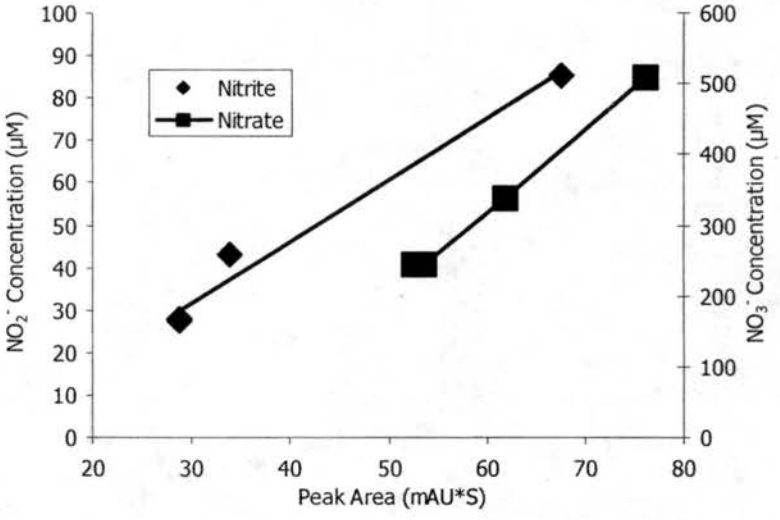

Figure 5-32. Peak areas vs. concentrations for nitrite and nitrate.

Figure 5-32 plots the concentrations of nitrite and nitrate in these four fog water samples (measured by ion chromatography) with the peak areas in the HPLC chromatograms. It is apparent that concentrations in the aqueous phase vary linearly with peak area. It is doubtful that such a strong relationship exists between the concentration sums of organics in each of the three categories and the HPLC chromatogram peak areas,

since the mix of organics with varying 254 nm absorption efficiencies probably varies substantially from sample to sample.

5.3.5.3 Fresno fog samples

Samples from the Jan. 2004 fog campaign in Fresno were tested by the same separation method within a few weeks of collection. Fresno fog sample chromatograms differ from those measured long after collection from the rural Angiola fog samples. The Fresno fog sample chromatograms also show different patterns than the example in Fuzzi et al. (2000). In particular, more distinct peaks are observed in the Fresno sample chromatograms. We can identify two or three peaks in the spectrum. One is nitrite, a second is nitrate, and a third is from methyl glyoxal.

Figures 5-33 to 5-35 show HPLC chromatograms of three bulk fog samples from a Fresno fog event beginning on Jan. 11th. Specifically, Figure 5-33 shows the breakdown by peak and fraction for sample FSC01101. We can see materials eluting as part of fraction 1 (neutral/basic compounds, retention time at ~3 to 5 min), fraction 2 (mono-/di-carboxylic acid, retention time at 5 to 10 min) and fraction 3 (polyacidic compounds, retention time at 13 to 19 min) clearly. Two typical peaks that were found in each chromatogram have retention time at 6.0 min and 6.8 min, respectively. These two peaks are likely nitrite and nitrate, since we observed high amounts of nitrite and nitrate from IC analysis. Also, methyl glyoxal was found by HPLC carbonyl analysis, and may contribute to the peak in fraction 1. In order to try and confirm the identity of certain peaks in the DEAE chromatograms, four test solutions were prepared and analyzed by HPLC:

(1) 50% FSC01101 plus 50% DI water as reference;
(2) 50% 110μg/ml nitrate plus 50% FSC01101;
(3) 50% 105 μg/ml nitrite plus 50% FSC01101;
(4) 50% 140μg/ml methyl glyoxal plus 50% FSC01101.

Figure 5-36 depicts chromatograms for these four solutions. We can see that after adding nitrate, the peaks at 6.8 min increased and became the biggest peak, confirming the this as a nitrate peak. Similarly, the nitrite addition confirms that the peak at 6.0 min corresponds to nitrite. As for methyl glyoxal, since methyl glyoxal has very small absorption efficiencies for its four characteristic peaks, the chromatogram changes are small. Comparing with 50% FSC01101:50% DI water chromatogram with the chromatogram of 50% methyl glyoxal plus 50% FSC01101, we can see that the peaks at ~3.0 min increased slightly and shift slightly to earlier retention times. Since methyl glyoxal is observed to show a peak eluting at 2.8 min we can conclude that methyl glyoxal probably contributed to the peak at 3.0 min.

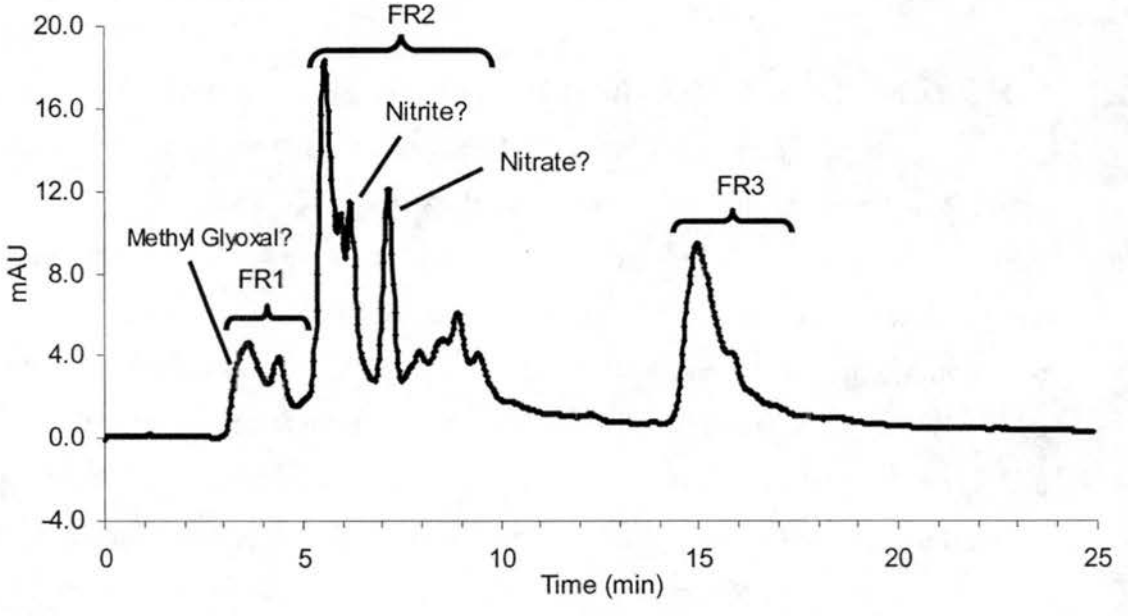

Figure 5-33. HPLC chromatogram of FSC01101 using DEAE method.

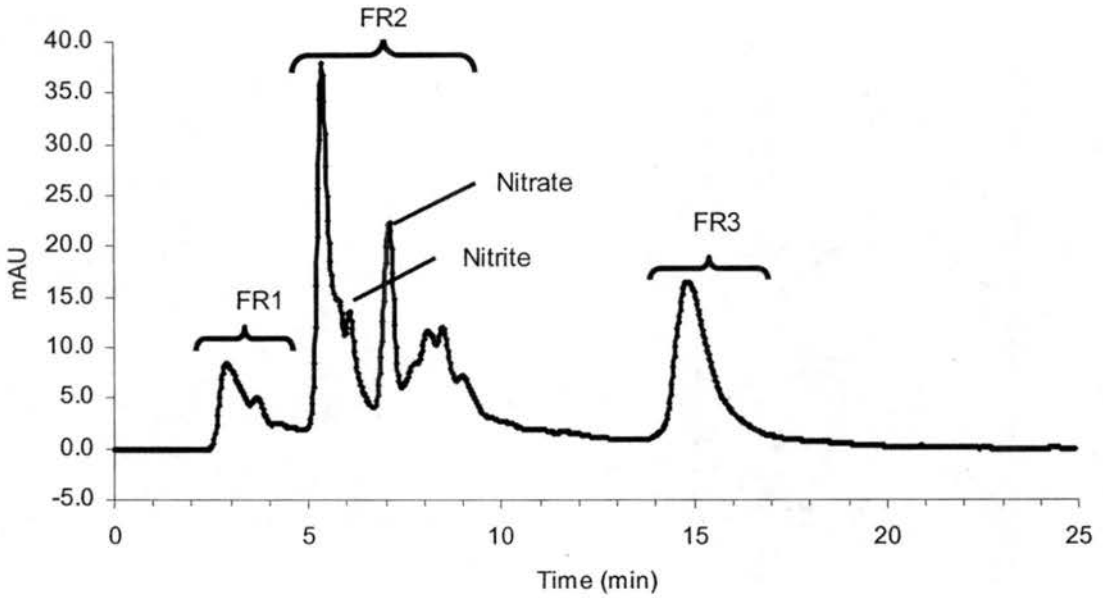

Figure 5-34. HPLC chromatogram of FSC01102 using DEAE method.

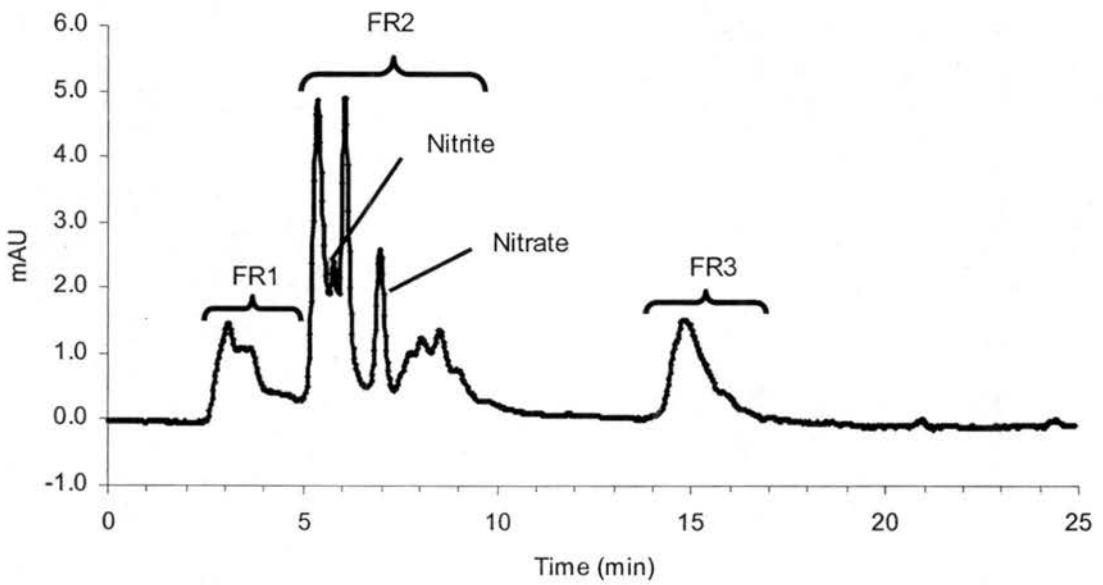

Figure 5-35. HPLC chromatogram of FSC01103 using DEAE method.

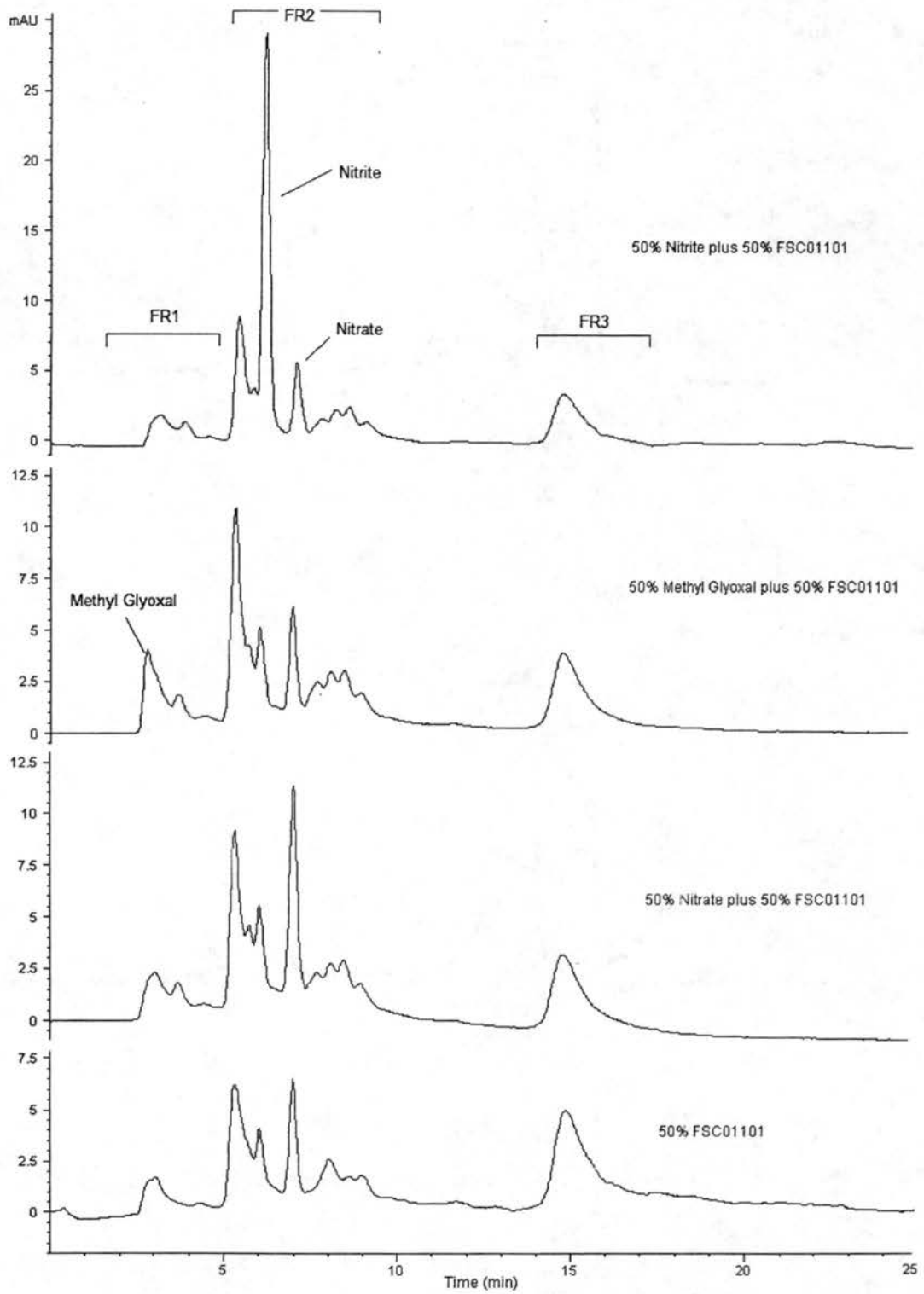

Figure 5-36. HPLC chromatograms of (1) 50% FSC01101 with 50% DI (2) 50% Nitrate plus 50% FSC01101 (3) 50% Methyl Glyoxal plus 50% FSC01101 (4) 50% Nitrite plus 50% FSC01101, using DEAE method.

Chapter 6

Conclusions and future work

As a result of the data analyses conducted during this study, combined with results of previous studies of fogs in California's Central Valley, some conclusions have been reached and some recommendations for future work are made.

6.1 Conclusions

- Consistent with previous studies, there were large amounts of ammonium in the fog drops. Ammonia can neutralize the acid species and make fog samples alkaline. The dominant species measured were ammonium, nitrate, nitrite, sulfate, formate, acetate.
- Consistent with previous studies, we observed that droplet composition varies with drop size. Most of the inorganic species measured were enriched in small drops relative to their large drop concentrations. For the organic species that we measured, all of them were enriched in small drops. No large pH differences were observed between large and small drops. Results from the CSU 5-stage collector show more detailed size distributions of some major ions than are obtained using the 2-stage sf-CASCC collector. Ammonium and nitrate concentrations, in particular, showed a very strong size dependence.
- Theoretical analysis of the fog chemistry and microphysics observations indicates that aqueous reactions of S(IV) species are important in SJV fogs. Formation of hydroxymethanesulfonate (HMSA) is the dominant fate for dissolved sulfur dioxide, due to the high concentrations of HCHO in the fog water. Ozone oxidation of dissolved S(IV) is the most important pathway for sulfate production in the fogs despite low ozone concentrations observed in conjunction with the fog events. S(IV)

oxidation by ozone contributed an average of 80% to sulfate production in small droplets and an average of 90% in large droplets. Model simulations predicted no significant difference between large and small drops S(IV) oxidation rates, due to the absence of significant pH differences. This result is in contrast to previous studies.

- Measurements of fog water deposition using Teflon deposition plates and recording balances are capable of providing estimates of fog water and fog solute fluxes in low wind speed radiation fog. Results from paired deposition plates agreed reasonably well. A comparison of fog water fluxes to rough (artificial grass) and smooth (metal) deposition surfaces revealed some enhancement of deposition to the rougher surface.
- Enrichment of ion concentrations in small drops, which settle to the ground slowly, reduces removal rates via sedimentation. Deposition velocity calculations show that the species dependent trend in average deposition velocities is $NH_4^+ > SO_4^{2+} \sim TOC > NO_3^-$, consistent with preferential enrichment of these species in small fog drops. All of these species exhibit average deposition velocities lower than observed for fog water. Nitrite, by contrast, exhibited an average deposition velocity higher than observed for fog water. This is consistent with the observed enrichment of nitrite in large fog drops.
- Organic carbon is an important component of the fog solute loading. The majority of the organic carbon in the collected fog drops is dissolved, although ~ 25% of the organic carbon is typically undissolved. Because the fog processes both dissolved and undissolved forms (e.g., via deposition), it is important to consider both reservoirs when analyzing droplet composition.
- Formaldehyde, formate, and acetate were once again observed to be dominant contributors to fog organic carbon. Analysis of higher molecular weight carbonyls revealed important organic carbon contributions also from other species, including glyoxal and methylglyoxal. Contributions of formaldehyde, glyoxal, and methyl glyoxal to fogs sampled in Fresno averaged 2.7, 1.9 and 2.5%, respectively. Studies of carbonyl and dicarbonyl compound stability in fog water revealed that many of these compounds are lost over periods of days to weeks, necessitating their on-site preservation immediately following sample collection.
- We obtained anion exchange chromatograms (DEAE cellulose column separation

with mobile phase including $NaClO_4$, TRIS and methanol) for our California fog samples very similar to the example shown by Decesari et al. (2000). Tests of this method using individual compound standards, however, revealed a tendency for the method to mis-classify important classes of organic compounds (e.g., phenolic compounds) as acids. Care is certainly required for appropriate interpretation of these chromatograms.

6.2 Recommendations for future work

- Size distribution studies of fog water composition have a trade off between sampling time/sample amount and the sharpness of collector size cuts. The current 2-stage sf-CASCC collector permits sufficient fog water collections within a short time, but only yields composition information for two drop size classes. The CSU 5-stage collector features a lower flow rate, due to technical limitations in jet impactor design, and often yields insufficient sample volumes for detailed chemical composition analysis. Development of a high volume sampler with the capability of collecting at least three drop size fractions is recommended. This should be possible using the strand/rod collection design employed in the sf-CASCC.
- Additional work is needed to examine the contributions of carbonyl and dicarbonyl compounds to fog and cloud composition. In particular, it would be useful to look at gas/drop partitioning of these compounds, their fate in sunlight illuminated droplets, their distributions across the drop size spectrum, and their occurrence in clouds collected in other types of environments.
- Additional work is needed to more fully speciate organic matter in fog drops, including developing a better understanding of the composition of the high molecular weight organic fractions identified in this study. One goal of such work should be to develop improved models of the composition of organic molecules present in cloud condensation nuclei. Examples of promising techniques to be applied to this problem include H-NMR, ^{13}C-NMR, FTIR, and various fractionation/detection schemes (e.g., size-exclusion/TOC, acidity/NMR).

References

Anastasio, C. and McGregor, K.G., 2000. Photodestruction of dissolved organic nitrogen species in fog waters. Aerosol Science and Technology, 32(2): 106 - 119.

Anastasio, C. and McGregor, K.G., 2001. Chemistry of fog water in California's central valley: 1. in situ photoformation of hydroxyl radical and singlet molecular oxygen. Atmospheric Environment, 35: 1079 - 1089.

Aumont, B., Madronich, S., Bey, I. and Tyndall, G.S., 2000. Contribution of secondary VOC to the composition of aqueous atmospheric particles: A modeling approach. Journal of Atmospheric Chemistry, 35(1): 59-75.

Bator, A. and Collett, J.L., 1997. Cloud chemistry varies with drop size. Journal of Geophysical Research-Atmospheres, 102(D23): 28071-28078.

Bauer, S.E. and Langmann, B., 2002. An atmosphere-chemistry model on the meso-gamma scale: model description and evaluation. Atmospheric Environment, 36(13): 2187-2199.

Blando, J. D., R. J. Procja, T.-H. Li, D. Bowman, P. J. Lioy, B. J. Turpin, 1998. Secondary formation and the Smoky Mountain organic aerosol: An examination of aerosol polarity and functinalgroup composition during SEAVS. Environ. Sci. Technol., 32: 604-613.

Blando, J.D. and Turpin, B.J., 2000. Secondary organic aerosol formation in cloud and fog droplets: a literature evaluation of plausibility. Atmospheric Environment, 34: 1623 - 1632.

Bower, Keith N., Choularton, Thomas W., Gallagher, Martin W., Colville, R. N., Beswick, K. M., Inglis, D. W. F., Bradbury, C., Martinsson, B. G., Swietlicki, E., Berg, O. H., Cederfelt, Sven-Inge, Frank, G., Zhou, J., Cape, J. N., Sutton, M. A., McFadyen, G. G., Milford, C., Birmili, W., Yuskiewicz, Brett, Wiedensohler, Alfred, Stratmann, Frank, Wendisch, Manfred, Berner, A., Ctyroky, P., Galambos, Zsuzsanna, Mesfin, S. H., Dusek, Ulrike, Dore, C. J., Lee, D. S., Pepler, S. A.,

Bizjak, M. and Divjak, B., 1999. The Great Dun Fell experiment 1995: an overview. Atmospheric Research, 50: 151 - 184.

Boyce, S.D. and Hoffmann, M.R., 1984. Kinetics and mechanism of the formation of hydroxymethanesulfonic acid at low pH. Journal of Physical Chemistry, 88: 4740-4746.

Burkhard, R., Eugster, W. and Thalmann, E., 2000. A direct method for fog and cloud droplet deposition flux measurements. EOS, transactions, 81(48): F64 - F65.

Calvert, J. G., Lazrus, A. L., Kok, G., Heikes, B., Walega, J., Lind, J. and Cantrell, C. A., 1985. Chemical mechanisms of acid generation in the troposphere. Nature, 317(6032): 27-35.

Capel, P.D., Gunde, R., Zürcher, F. and Giger, W., 1990. Carbon speciation and surface tension of fog. Environmental Science and Technology, 24(5): 722 - 727.

Carpenter, A. and Provorse, C., 1998. The World almanac of the U.S.A. Copyright 1998.

Carrillo, J.H., Emert, S.E., Sherman, D.E. and Collett, J.L.J., 2004. An Economical Optical Fog Detector. Atmospheric Environment, in preparation.

Cereceda, P. and Schemenauer, R.S., 1991. The occurrence of fog in Chile. J. Appl. Meteor., 30: 1095-1105.

Chameides, W.L. and Davis, D.D., 1983. Aqueous-phase source of formic acid in clouds. Nature, 304: 427 - 429.

Choularton, T. W., Colvile, R. N., Bower, K. N., Gallagher, M. W., Wells, M., Beswick, K. M., Arends, B. G., Mols, J. J., Kos, G. P. A., Fuzzi, S., Lind, J. A., Orsi, G., Facchini, M. C., Laj, P., Gieray, R., Wieser, P., Engelhardt, T., Berner, A., Kruisz, C., Moller, D., Acker, K., Wieprecht, W., Luttke, J., Levsen, K., Bizjak, M., Hansson, H. C., Cederfelt, S. I., Frank, G., Mentes, B., Martinsson, B., Orsini, D., Svenningsson, B., Swietlicki, E., Wiedensohler, A., Noone, K. J., Pahl, S., Winkler, P., Seyffer, E., Helas, G., Jaeschke, W., Georgii, H. W., Wobrock, W., Preiss, M., Maser, R., Schell, D., Dollard, G., Jones, B., Davies, T., Sedlak, D. L., David, M. M., Wendisch, M., Cape, J. N., Hargreaves, K. J., Sutton, M. A., StoretonWest, R. L., Fowler, D., Hallberg, A., Harrison, R. M. and Peak, J. D., 1997. The Great Dun Fell cloud experiment 1993: An overview. Atmospheric Environment, 31(16): 2393-2405.

Collett, J., Oberholzer, B. and Staehelin, J., 1993. Cloud chemistry at Mt Rigi, Switzerland - dependence on drop size and relationship to precipitation chemistry. Atmospheric Environment, 27(1): 33-42.

Collett, J.L., Bator, A., Rao, X. and Demoz, B.B., 1994a. Acidity variations across the cloud drop size spectrum and their influence on rates of atmospheric sulfate production. Geophysical Research Letters, 21(22): 2393-2396.

Collett, J.L., Daube, B.C., Gunz, D. and Hoffmann, M.R., 1990. Intensive studies of Sierra-Nevada cloudwater chemistry and its relationship to precursor aerosol and gas concentrations. Atmospheric Environment, 24(7): 1741-1757.

Collett, J.L.J., Bator, A., Demoz, B.B. and Rao, X., 1994b. Cloud chemistry varies with drop size. Air & Waste Management Association (94-RA105.02).

Collett, J.L.J., Hoag, K.J. and Pandis, S.N., 1998. The influence of drop size-dependent fog chemistry on aerosol production and deposition in San Joaquin Valley fogs, Department of Atmospheric Science, Colorado State University, Fort Collins, CO.

Collett, J.L.J., Hoag, K.J., Rao, X. and Pandis, S.N., 1999a. Internal acid buffering in San Joaquin Valley fog drops and its influence on aerosol processing. Atmospheric Environment, 33: 4833 - 4847.

Collett, J.L.J., Hoag, K.J., Sherman, D.E., Bator, A. and Richards, L.W., 1999b. Spatial and temporal variations in San Joaquin Valley fog chemistry. Atmospheric Environment, 33: 129 - 140.

Collett, J.L.J., Iovinelli, R.J. and Demoz, B.B., 1995. A three-stage cloud impactor for size-resolved measurement of cloud drop chemistry. Atmospheric Environment, 29(10): 1145 - 1154.

Collett, J.L.J., Sherman, D.E., Moore, K.F., Hannigan, M.P. and Lee, T., 2001. Aerosol particle processing and removal by fogs: observations in chemically heterogeneous central California radiation fogs. Water, Air and Soil Pollution, Focus:1: 303-312.

Dasgupta, P.K., DeCesare, K. and Ullrey, J.C., 1980. Determination of atmospheric sulfur dioxide without tetrachloromercurate(II) and the mechanism of the Schiff reaction. Analytical Chemistry, 52: 1912 - 1922.

Daugherty, R.L. and Franzini, J.B., 1965. Fluid mechanics. New York: McGraw-Hill:

162-165.

Daum, P.H., Schwartz, S.E. and Newman, L., 1984. Acidic and related constituents in liquid water stratiform clouds. Journal of Geophysical Research, 89(D1): 1447 - 1458.

Davis, E.J., 1983. Transport phenomena with single aerosol particles. Aerosol and Science Technology, 2: 121-144.

Decesari, S., Facchini, M.C., Fuzzi, S. and Tagliarini, E., 2000. Characterization of water-soluble organic compounds in atmospheric aerosol: a new approach. Journal of Geophysical Research, 105(D1): 1481 - 1489.

Demoz, B. B., Bator, A., Rao, X. and Collett, J. L., Jr. (1995) Field evaluation of new size-fractionating fog and cloudwater collectors, Proceedings of the American Meteorological Society Conference on Cloud Physics, Dallas, Texas, 2 pp.

Dlugi, R., 1989. Chemistry and deposition of soot particles in moist air and fog. Aerosol Science and Technology, 10: 93 - 105.

Dollard, G.J. and Unsworth, M.H., 1983. Field measurements of turbulent fluxes of wind-driven fog drops to a grass surface. Atmospheric Environment, 17(4): 775 - 780.

Dong, S. and Dasgupta, P.K., 1987. Fast fluorometric flow injection analysis of formaldehyde in atmospheric water. Environmental Science and Technology, 21: 581 - 588.

Emert, S.E., 2001. Design, construction, and evaluation of the CSU optical fog detector. MS Thesis, Colorado State University.

Erel, Y., Pehkonen, S.O. and Hoffmann, M.R., 1993. Redox chemistry of iron in fog and stratus clouds. Journal of Geophysical Research, 98(D10): 18423 - 18434.

Ervens, B., P. Herckes, G. Feingold, T. Lee, J. L. Collett, Jr. and S. M. Kreidenweis, 2003. On the drop-size dependence of organic acid and formaldehyde concentrations in fog,. Journal of Atmospheric Chemistry, 46: 239-269.

Eugster, W., Burkhard, R., Klemm, O. and Wrzesinsky, T., 2001. Fog deposition measurements with the eddy covariance method. In: R.S. Schemenauer and H. Puxbaum (Editors), 2nd International Conference on Fog and Fog Collection, St. John's, Newfoundland, Canada, pp. 193 - 196.

Facchini, M.C., Decesari, S., Mircea, M., Fuzzi, S. and Loglio, G., 2000. Surface tension

of atmospheric wet aerosol and cloud/fog droplets in relation to their organic carbon content and chemical composition. Atmospheric Environment, 34: 4853 - 4857.

Facchini, M.C., Fuzzi, S., Lind, J. A., Fierlinger, H., Kalina, M., Puxbaum, H., Winiwarter, W., Arends, B. G., Wobrock, W., Jaeschke, Wolfgang, Berner, A. and Kruisz, Christian, 1992. Phase-partitioning and chemical reactions of low molecular weight organic compounds in fog. Tellus, 44B: 533 - 544.

Facchini, M.C., Fuzzi, S., Zappoli, Sergio, Andracchio, Antonella, Gelencsér, A., Kiss, Gyula, Krivácsy, Z., Mészáros, E., Hansson, H.C., Alsberg, T. and Zebühr, Y., 1999a. Partitioning of the organic aerosol component between fog droplets and interstitial air. Journal of Geophysical Research, 104(D21): 26821 - 26832.

Facchini, M.C., Mircea, M., Fuzzi, S. and Charlson, R.J., 1999b. Cloud albedo enhancement by surface-active organic solutes in growing drops. Nature, 401: 257 - 259.

Facchini, M. C., Mircea, M., Fuzzi, S. and Charlson, R.J., 2001. Comments on "Influence of soluble surface properties on the activation of aerosol particles containing inorganic solute". Journal of the Atmospheric Sciences, 58: 1465 - 1467.

Finlayson-Pitts, B.J. and Pitts, J.N.J., 2000. Chemistry of the upper and lower Atmosphere: theory, experiments, and applications. Academic Press, San Diego, CA, 969 pp.

Fitzjarrald, D.R. and Lala, G.G., 1986. Observed fine structure in radiation fog, 23rd conference on radiation meteorology and conference on cloud physics. American Meteorological Society, Snowmass, CO, pp. P226 - P228.

Forkel, R., Seidl, W., Dlugi, R. and Deigele, E., 1990. A one dimensional numerical model to simulate formation and balance of sulfate during radiation fog events. Journal of Geophysical Research: Atmospheres, 95(D11): 18501 - 18515.

Fuchs, N.A. and Sutugin, A.G., 1971. High-dispersed aerosols. Int. Rev. Aerosol Phys. Chem, 2: 1-60.

Fung and D, Grosjean., 1981. Determination of nanogram amounts of carbonyls as 2,4-dinitrophenylhydrazones by high-performance liquid-chromatography. Analytical Chemistry, 53(2): 168-171.

Fuzzi, S., 1988. Fog chemistry and deposition in the Po Valley, Italy. In: M.H. Unsworth and D. Fowler (Editors), Acid deposition at high elevations. Kluwer Academic Publishers, Dordrecht, pp. 443 - 452.

Fuzzi, S., 1995. The multiphase chemistry of clouds in the atmosphere. life chemistry reports, 13: 29-38.

Fuzzi, S., Decesari, S., Facchini, M.C., Matta, E., Mircea, M. and Tagliavini, E., 2001. A simplified model of the water soluble organic component of atmospheric aerosols. Geophysical Research Letters, 28(21): 4079-4082.

Fuzzi, S., Facchini, M.C., Schell, D., Wobrock, W., Winkler, Peter, Arends, B. G., Kessel, M., Möls, J. J., Pahl, S., Schneider, T., Berner, A., Solly, I., Kruisz, Christian, Kalina, M., Fierlinger, H., Hallberg, A., Vitali, P., Santoli, L. and Tigli, G., 1994. Multiphase chemistry and acidity of clouds at Kleiner-Feldberg. Journal of Atmospheric Chemistry, 19(1-2): 87-106.

Fuzzi, Sandro, Laj, Paolo, Ricci, Loretta, Orsi, Giordano, Heintzenberg, Jost, Wendisch, Manfred, Yuskiewicz, Brett, Mertes, Stephan, Orsini, Douglas, Schwanz, Marina, Wiedensohler, Alfred, Stratmann, Frank, Berg, Olle H., Swietlicki, Erik, Frank, Goran, Martinsson, Bengt G., Günther, Armin, Dierssen, Jens Peter, Schell, Dieter, Jaeschke, Wolfgang, Berner, Axel, Dusek, Ulrike, Galambos, Zsuzsanna, Kruisz, Christian, Mesfin, Nigatu S., Wobrock, Wolfram, Arends, Beate and Ten Brink, H., 1998. Overview of the Po Valley fog experiment 1994 (CHEMDROP). Contributions to Atmospheric Physics, 71(1): 3-19.

Fuzzi S, Facchini M.C., Orsi G, Lind Ja, Wobrock W., Kessel M., Maser R., Jaeschke W., Enderle K.H., Arends B.G., Berner A, Solly I, Kruisz C, Reischl G, Pahl S, Kaminski U, Winkler P, Ogren Ja, Noone K.J., Hallberg A., Fierlingeroberlinninger H., Puxbaum H., Marzorati A., Hansson H.C., Wiedensohler A., Svenningsson Ib, Martinsson B.G., Schell D. and Georgii H.W., 1992. The Po Valley fog experiment 1989- an overview. Tellus, 44B: 448-468.

Gerber, H., 1991. Direct measurement of suspended particulate volume concentration and far-infrared extinction coefficient with a laser-diffraction instrument. Applied Optics, 30(33): 4824 - 4831.

Gerber, H., B. G. Arends, and A. S. Ackerman, 1994: New microphysics sensor for

aircraft use. Atmos. Res., 31, 235–252.

Gerber, H., Frick, G. and Rodi, A.R., 1999. Ground-based FSSP and PVM measurements of liquid water content. Journal of Atmospheric and Oceanic Technology, 16: 1143-1149.

Geshen, Z., 2000. Modern weather measurement and detection. Beijing University Publication, Beijing: 114-115.

Guiang, S.F., Sagar, I., Krupa. V. and Pratt, G.C., 1984. Measurements of S(IV) and organic anions in Minnesota rain. Atmospheric Environment, 18(8): 1677-1682.

Gundel, L.A., Benner, W.H. and Hansen, A.D.A., 1994. Chemical-composition of fog water and interstitial aerosol in Berkeley, California. Atmospheric Environment, 28(16): 2715-2725.

Gundel, L.A., Dalsey, J.M., Carvalho, L.R.F.d., Kado, N.Y. and Schuetzle, D., 1993. Polar organic matter in airborne particles: chemical characterization and mutagenic activity. Environ. Sci. Technol., 27: 2112-2119.

Gurciullo, C.S. and Pandis, S.N., 1997. Effect of composition variations in cloud droplet populations of aqueous-phase chemistry. Journal of Geophysical Research: Atmospheres, 102(D8): 9375-9385.

Hanel, G., 1976. The properties of atmospheric aerosol particles as functions of relative humidity at thermodynamic equilibrium with the surrounding moist air. Adv. Geoph., 19: 73-188.

Havers, N., Burba, P., Lambert, J. and Klockow, D., 1998. Spectroscopic characterization of humic-like substances in airborne particulate matter. Journal of Atmospheric Chemistry, 29(1): 45-54.

Heintzenberg, J., Ogren, J.A., Noone, K.J. and Gärdneus, L., 1989. The size distribution of submicrometer particles within and about stratocumulus cloud droplets on Mt. Åreskutan, Sweden. Atmospheric Research, 24: 89 - 101.

Herckes, P., Hannigan, M.P., Trenary, L., Lee, T. and Collett, J., J.L, 2002a. Organic compounds in radiation fogs in Davis (California). Atmos. Res., 64: 99-108.

Herckes, P., Hannigan, M.P., Trenary, L., Lee, T. and Collett, J.L.J., 2002b. Organic compounds in radiation fogs in Davis (California). Atmos. Res., 64: 99-108.

Herckes, P., Lee, T., Trenary, L., Kang, G. G., Chang, H., Collett, J. L., 2002c. Organic

matter in central California radiation fogs. Environmental Science & Technology, 36(22): 4777-4782.

Herckes, P., Trenary, L., Hannigan, M.P., Lee, T. and Collett, J.L.J., 2001. Cloud and fog processing of atmospheric organic compounds. In: R.S. Schemenauer and H. Puxbaum (Editors), 2nd International Conference on Fog and Fog Collection, St. John's, Newfoundland, Canada, pp. 13 - 16.

Hitzenberger, R. and Berner, A., 2002. Surface tension of rax cloud water and its relation to the concentration of organic material. Journal of Geophysical Research, 107: No. D24, 4752.

Hoag, K.J., Collett, J.L. and Pandis, S.N., 1999a. The influence of drop size-dependent fog chemistry on aerosol processing by San Joaquin Valley fogs. Atmospheric Environment, 33(29): 4817-4832.

Hoag, K.J., Collett, J.L.J. and Pandis, S.N., 1999b. The influence of drop size-dependent fog chemistry on aerosol processing by San Joaquin Valley fogs. Atmospheric Environment, 33: 4817-4832.

Hoffmann, M.R., 1984. Comment on "acid fog". Environmental Science and Technology, 18(1): 61 - 64.

Hoffmann, M.R., 1986. On the kinetics and mechanism of oxidation of aquated Sulfur Dioxide by Ozone. Atmos. Environ., 10: 1145-1154.

Hoffmann, M.R. and Calvert, J.G., 1985. Chemical transformation modules for eulerian acid deposition models, vol. 2, The aqueous-phase chemistry. EPA/600/3-85/017, U.S. Environ. Prot. Agency, Research Triangle Park, N. C.

Holets, S. and Swanson, R.N., 1981. High inversion fog episodes in central California. Journal of Applied Meteorology, 20: 890 - 899.

Husain, L., 1989. A technique for determining in-cloud formation of SO_4. Geophysical Research Letters, 16(1): 57 - 60.

Ibusuki, T. and Takeuchi, A., 1987. Sulfur dioxide oxidation by oxygen catalyzed by mixtures of manganese (II) and iron (III) in aqueous solutions at environmental reaction conditions. Atmos. Environ, 21: 1555-1560.

Jacob, D.J., 1986. Chemistry of OH in remote clouds and its role in the production of formic acid and peroxymonosulfate. Journal of Geophysical Research, 91(D9):

9807 - 9826.

Jacob, D.J., F.H., S., J.M., W., Munger, J.W. and Hoffmann, M.R., 1987. Transport and oxidation of SO_2 in a stagnant foggy valley. Atmos. Environ., 21: 1305-1314.

Jacob, D.J., Munger, J.W., Waldman, J.M. and Hoffmann, M.R., 1986a. The H_2SO_4-HNO_3-NH_3 system at high humidities and in fogs 1. spatial and temporal patterns in the San Joaquin Valley of California. Journal of Geophysical Research, 91(D1): 1073 - 1088.

Jacob, D.J., Waldman, J.M., Munger, J.W. and Hoffmann, M.R., 1984. A field investigation of physical and chemical mechanisms affecting pollutant concentrations in fog droplets. Tellus, 36B: 272 - 285.

Jacob, D.J., Waldman, J.M., Munger, J.W. and Hoffmann, M.R., 1986b. The H_2SO_4-HNO_3-NH_3 system at high humidities and in fogs 2. comparisons of field data with thermodynamic calculations. Journal of Geophysical Research, 91(D1): 1089 - 1096.

Kulmala, M., Laaksonen, A., J. Charlson, R. and Korhonen1, P., 1997. Clouds without supersaturation. Nature, 388(336-337).

Laaksonen, A., Korhonen, P., Kulmala, M. and Charlson, R.J., 1998. Modification of the Kohler equation to include soluble trace gases and slightly soluble substances. Journal of the Atmospheric Sciences, 55: 853 - 862.

Laj, P. et al., 1997. Cloud processing of soluble gases. Atmospheric Environment, 31(16): 2589 - 2598.

Lazrus, A.L., Kok, G.L., Gitlin, S.N. and Lind, J.A., 1985. Automated fluorometric method for hydrogen peroxide in atmospheric precipitation. Analytical Chemistry, 57: 917 - 922.

Lazrus, A. L., Kok, G. L., Lind, J. A., Gitlin, S. N., Heikes, B. G., Shetter, R. E., 1986. Automated fluorometric method for H_2O_2 in air. Analytical Chemistry, 58: 594 - 597.

Lee, T.F., 1987. Urban clear islands in California Central Valley. Monthly Weather Review, 115: 1794-1796.

Li, Z.D., Williams, A.L. and Rood, M.J., 1998. Influence of soluble surfactant properties on the activation of aerosol particles containing inorganic solute. Journal of the

Atmospheric Sciences, 55(10): 1859-1866.

Likens, G.E., Edgerton, E.S. and Galloway, J.N., 1983. The composition and deposition of organic-carbon in precipitation. Tellus, 35: 16-24

Lillis, D., Cruz, C.N., Collett, J., Richards, L.W. and Pandis, S.N., 1999. Production and removal of aerosol in a polluted fog layer: model evaluation and fog effect on PM. Atmospheric Environment, 33(29): 4797-4816.

Limbeck, A. and Puxbaum, H., 2000. Dependence of in-cloud scavenging of polar organic aerosol compounds on the water solubility. Journal of Geophysical Research, 105(D15): 19857 - 19867.

Luttke, J. and Levsen, K., 1997. Phase partitioning of phenol and nitrophenols in clouds. Atmospheric Environment, 31(16): 2649-2655.

Luttke, J. et al., 1997. Occurrence and formation of nitrated phenols in and out of cloud. Atmospheric Environment, 31(16): 2637-2648.

Maahs, H.G., 1983. Kinetics and mechanism of the oxidation of S(IV) by ozone in aqueous solution with particular reference to SO_2 conversion in non-urban tropospheric clouds. Journal of Geophysical Research, 88: 10721-10732.

Martin, L., 1994. Aqueous sulfur(IV) oxidation revisited. Environmental Oxidants (J. O. Nriagu and M. S. Simmons, Eds.): 221-268.

Martin, L.R., 1984. Kinetic studies of sulfite oxidation in aqueous solution in SO_2, NO and NO_2 oxidation mechanism: atmospheric considerations, edited by J. G. Calvert. (Butterworth-Heinemann, Woburn, Mass): 63-100.

McArdle, J.V. and Hoffmann, M.R., 1983. Kinetics and mechanism of the oxidation of aquated sulfur dioxide by hydrogen peroxide at low pH. Journal of Physical Chemistry, 87: 5425-5429.

McGregor, K.G. and Anastasio, C., 2001. Chemistry of fog waters in California's central valley: 2. photochemical transformations of amino acids and alkyl amines. Atmospheric Environment, 35: 1091 - 1104.

Mircea, M., Facchini, M.C., Decesari, S., Fuzzi, S. and Charlson, R.J., 2002. The influence of the organic aerosol component on CCN supersaturation spectra for different aerosol types. Tellus, 54B: 74-81.

Moore, K.F., 2001. Ph.D. dissertation Thesis, Colorado State University, Fort Collins, CO.

Moore, K.F., Sherman, D.E., Reilly, J.E. and Collett, J.L., 2002. Development of a multi-stage cloud water collector Part 1: design and field performance evaluation. Atmospheric Environment, 36(1): 31-44.

Moore, Katharine F., Sherman, D. Eli, Reilly, Jill E., Hannigan, Michael P., Lee, Taehyoung and Collett, Jeffrey L. Jr., 2004. Drop size-dependent chemical composition of clouds and fogs. II. relevance to interpreting the aerosol/trace gas/fog system. Atmos. Res., 38(10): 1403-1415.

Munger, J.W., Collett, J., Daube, B. and Hoffmann, M.R., 1990. Fogwater chemistry at Riverside, California. Atmospheric Environment, 24(2): 185-205.

Munger, J.W., Collett, J.L., Jr., Daube, B.C., Jr. and Hoffmann, M.R., 1989a. Carboxylic acids and carbonyl compounds in southern California clouds and fogs. Tellus, 41B: 230 - 242.

Munger, J.W., Collett, J.L.J., Daube, B.C.J. and Hoffmann, M.R., 1989b. Chemical composition of coastal stratus clouds: dependence on drop size and distance from the coast. Atmospheric Environment, 23(10): 2305 - 2320.

Munger, J.W., Jacob, D.J. and Hoffmann, M.R., 1984. The occurrence of bisulfite-aldehyde addition products in fog- and cloudwater. Journal of Atmospheric Chemistry, 1: 335 - 380.

Munger, J.W., Jacob, D.J., Waldman, J.M. and Hoffmann, M.R., 1983a. Fogwater chemistry in an urban atmosphere. Journal of Geophysical Research, 88(C9): 5109 - 5121.

Munger, J.W., Tiller, C. and Hoffmann, M.R., 1986. Identification of hydroxymethanesulfonate in fog water. Science, 231: 247 - 249.

Munger, J.W., Waldman, J.M., Jacob, D.J. and Hoffmann, M.R., 1983b. Vertical variability and short-term temporal trends in precipitation chemistry. In: H.R. Pruppacher, R.G. Semonin and W.G.N. Slinn (Editors), Precipitation Scavenging, Dry Deposition, and Resuspension. Elsevier, New York, pp. 275 - 282.

Noone, K.J., Charlson, R.J., Covert, D.S., Ogren, J.A. and Heintzenberg, J., 1988. Cloud droplets: solute concentration is size-dependent. Journal of Geophysical Research, 93(D8): 9477 - 9482.

Ogren, J.A., Heintzenberg, J., Zuber, Z., Noone, K.J. and Charlson, R.J., 1989.

Measurements of the size-dependence of solute concentrations in cloud droplets. Tellus, 41B: 24 - 31.

Pandis, S.N. and Seinfeld, J.H., 1989a. Mathematical modeling of acid deposition due to radiation fog. Journal of Geophysical Research, 94(D10): 12911 - 12923.

Pandis, S.N. and Seinfeld, J.H., 1989b. Sensitivity analysis of a chemical mechanism for aqueous-phase atmospheric chemistry. Journal of Geophysical Research, 94(D1): 1105 - 1126.

Pandis, S.N., Seinfeld, J.H. and Pilinis, C., 1990. Chemical composition differences in fog and cloud droplets of different sizes. Atmospheric Environment, 24A: 1957 - 1969.

Pandis, S.N., Seinfeld, J.H. and Pilinis, C., 1992. Heterogeneous sulfate production in an urban fog. Atmospheric Environment, 26A(14): 2509 - 2522.

Penkett, S.A., Jones, B.M.R., Brice, K.A. and Eggleton, A.E., 1979. The importance of atmospheric ozone and hydrogen peroxide in oxidizing sulphur dioxide in cloud and rainwater. Atmospheric Environment, 13: 123-137.

Pinnick, R.G. and Auvermann, H.J., 1979. Response characteristics of Knollenberg light-scattering aerosol counters. Journal of Aerosol Science, 10: 55-74.

Rao, X., 1997. Cloud chemical heterogeneity and its influence on aqueous sulfur(IV) oxidation. Ph.D. Thesis, University of Illinois at Urbana-Champaign, Urbana-Champaign, IL, 231 pp.

Rao, X. and Collett, J.L.J., 1995. Behavior of S(IV) and formaldehyde in a chemically heterogeneous cloud. Environmental Science and Technology, 29: 1023-1031.

Rao, X. and Collett, J.L.J., 1998. The Drop size-dependence of iron and manganese concentrations in clouds and fogs: implications of sulfate production. Journal of Atmospheric Chemistry, 30: 273-289.

Rattigan, O. V., Reilly, J., Judd, C. D., Moore, K. F., Das, M., Sherman, D. E., Dutkiewicz, V. A., Collett, J. L. and Husain, L., 2001. Sulfur dioxide oxidation in clouds at Whiteface mountain as a function of drop size. Journal of Geophysical Research-Atmospheres, 106(D15): 17347-17358.

Raymond, T.M. and pandis, S.N., 2002. Cloud activation of single-component organic aerosol. Journal of Geophysical Research, 107: NO.D24, 4787.

Reible, D.D., 1982. Investigation of transport in complex atmospheric flow systems. Ph.D. Dissertation, California Institute of Technology.

Reilly, J.E., 2000. Application of a tracer technique to study sulfur dioxide oxidation in cloud drops as a function of drop size. M.S. Thesis, Colorado State University, Fort Collins, CO.

Reilly, J. E., Rattigan, O. V., Moore, K. F., Judd, C., Sherman, D. E., Dutkiewicz, V. A., Kreidenweis, S. M., Husain, L. and Collett, J. L., Jr., 2001. Drop size-dependent S(IV) oxidation in chemically heterogeneous radiation fogs. Atmospheric Environment, 35(33): 5717-5728.

Roach, W.T., 1976. On the effect of radiative exchange on the growth by condensation of a cloud or fog droplet. Quarterly Journal of the Royal Meteorological Society, 102: 361 - 372.

Rodhe, H., 1999. Clouds and climate. Nature, 401: 223-225.

Rood, M.J. and Williams, A.L., 2001. Comments on "Influence of soluble surfactant properties on the activation of aerosol particles containing inorganic solute" - Reply. Journal of the Atmospheric Sciences, 58: 1468 - 1473.

Saxena, P. and Hildemann, L.M., 1996. Water-soluble organics in atmospheric particles: a critical review of the literature and application of thermodynamics to identify candidate compounds. Journal of Atmospheric Chemistry, 24: 57 - 109.

Saxena, P., Hildemann, L.M., McMurry, P.H. and Seinfeld, J.H., 1995. Organics alter hygroscopic behavior of atmospheric particles. Journal of Geophysical Research, 100(D9): 18755 - 18770.

Seinfeld, J.H., 1986. Atmospheric chemistry and physics of air pollution. (Wiley, New York).

Seinfeld, J.H. and Pandis, S.N., 1998. Atmospheric chemistry and physics. John Wiley and Son, Inc, New York.

Shulman, M.L., Jacobson, M.C., Carlson, R.J., Synovec, R.E. and Young, T.E., 1996. Dissolution behavior and surface tension effects of organic compounds in nucleating cloud droplets. Geophysical Research Letters, 23(3).

Silva, P.J., Liu, D.Y., Noble, C.A. and Prather, K.A., 1999. Size and chemical characterization of individual particles resulting from biomass burning of local

southern California species. Environ Sci Technol, 33: 3068-3076.

Straub, D.J. and Collett, J.L., 2002. Development of a multi-stage cloud water collector Part 2: numerical and experimental calibration. Atmospheric Environment, 36(1): 45-56.

Suzuki, Y., Imai, S., Kawakami, M., Masuda, Y. and Akasaka, K., 1998. Identification and determination of low-molecular weight organic compounds in contaminated fog water using proton nuclear magnetic resonance spectroscopy. Environ. Contam. Toxicol., 60: 355-362.

Waldman, J.M. and Hoffmann, M.R., 1987. Depositional aspects of pollutant behaviour in fog and intercepted clouds. In: R.A. Hites and S.J. Eisenreich (Editors), Sources and Fates of Aquatic Pollutants. Advances in Chemistry Series #216. American Chemical Society, pp. 79 - 129.

Waldman, J.M., Munger, J.W., Jacob, D.J. and Hoffmann, M.R., 1983. Fogwater composition in Southern California. In: H.R. Pruppacher, R.G. Semonin and W.G.N. Slinn (Editors), Precipitation Scavenging, Dry Deposition, and Resuspension. Elsevier, New York, NY, pp. 137 - 145.

Wark, K., Warner, C.F. and Davis, W.T., 1998. Air Pollution: Its Origin and Control. Addison-Wesley, Menlo Park, CA, 573 pp.

Welch, R.M. and Wielicki, B.A., 1986. The stratocululus nature of fog. J. clim. Appl., 25: 101-111.

Wendisch, M., 1998. A quantitative comparison of ground-based FSSP and PVM measurements. Journal of Atmospheric and Oceanic Technology, 15: 887-900.

Whitby, K.T., 1978. The physical characteristics of sulfur aerosols. Atmos. Environ, 12: 135-159.

Whiteaker, J.R. and Prather, K.A., 2003. Hydroxymethanesulfonate as a tracer for fog processing of individual aerosol particles. Atmospheric Environment, 37(8): 1033-1043.

Wobrock, W., Schell, D., Maser, R., Jaeschke, W., ,Georgii, H. W., Wieprecht, W., Arends, B. G., Mols, J. J., Kos, G. P. A., Fuzzi, S., Facchini, M. C., Orsi, G., Berner, A., Solly, I., Kruisz, C., Svenningsson, I. B., Wiedensohler, A., Hansson, H. C., Ogren, J. A., Noone, K. J., Hallberg, A., Pahl, S., Schneider, T., Winkler, P., Winiwarter,

W., Colvile, R. N., Choularton, T. W., Flossmann, A. I. and Borrmann, S., 1994. The Kleiner-Feldberg cloud experiment 1990 - an overview. Journal of Atmospheric Chemistry, 19(1-2): 3-35.

Wrzesinsky, T., Thalmann, E., Burkhard, R., Eugster, W. and Klemm, O., 2001. Fog deposition of nutrients and pollutants to a montane forest site. In: R.S. Schemenauer and H. Puxbaum (Editors), 2nd International Conference on Fog and Fog Collection, St. John's, Newfoundland, Canada, pp. 169 - 172.

Xu, G., Sherman, D. E., Andrews, E., Moore, K., Straub, D., Hoag, K. and Collett, J. L. Jr., 1999. The influence of chemical heterogeneity among cloud drop populations on processing of chemical species in winter clouds. Atmospheric Research(51): 119-140.

Zappoli, S., Andracchio, A., Fuzzi, S., Facchini, M. C., Gelencser, A., Kiss, G., Krivacsy, Z., Molnar, A., Meszaros, E., Hansson, H. C., Rosman, K. and Zebuhr, Y., 1999. Inorganic, organic and macromolecular components of fine aerosol in different areas of Europe in relation to their water solubility. Atmospheric Environment, 33(17): 2733-2743.

Zhang, Q. and Anastasio, C., 2001. Chemistry of fog waters in California's central valley - Part 3: concentrations and speciation of organic and inorganic nitrogen. Atmospheric Environment, 35(32): 5629-5643.

Zhou, X. and Lee, Y.N., 1992. Aqueous solubility and reaction kinetics of hydroxymethyl hydroperoxide. J. Phys. Chem., 96: 265-272.

Appendix A

Collector flow measurements and size cut calculations

The fog collectors (CASCC, sf-CASCC and 5-stage etc.) collect fog water droplets by inertial impaction. The performance of the collector is a function of its geometry and the air sample rate. If the performance is well characterized, we can use the amount of collected fog water to determine the ambient liquid water content (LWC) for each sampling period. This can be compared to independent LWC measures (e.g., from the PVM). In the CRPAQS study, the voltages applied to the CASCC fans was not measured and adjusted. Later measurements of applied voltage in the lab at CSU indicated it was generally too low, resulting in slower then designed fan speeds and, consequently, smaller than expected water collection rates for a given LWC. The change in fan speed and air sampling rate also affects stage collection efficiencies, since collection efficiency is a function of drop velocity.

In order to account for different fan voltages, the relationship between fan voltage and real air velocity is needed. We can also get another relationship between fan voltage and its revolution speed since fan voltage is easier to be measured on-site. We can measure the revolution speed of each fan in main site, and we will know the real air velocity through the collector, which will be use to calculate the real volumetric flow. In the later part of this summary, size cut calculations for the CASCC, first stage of sf-CASCC, first stage and main inlet of ss-sf-CASCC will also be summarized.

A.1 Fan Law

We use two different fans for the collectors. For CASCC and sf-CASCC, the fans are

DC 12V BOSCH blower fans. For CHRCC, the fans are AC 115V 60Hz Nidec ALPHA-V fans.

The most important factor for a fan is its rotation velocity, typically expressed in rpm (Revolutions Per Minute), which determines the forced air flow, typically expressed in CFM (Cubic Feet Per Minute). We determined that the voltage applied to the fan of the CASCC in CRPAQS was 10.6V, lower than the theoretical value of 13.3V. This difference can significantly reduced fan rpm. The following discussion explains and evaluates this effect.

A.1.1 The relationship between revolution speed of a fan and air velocity

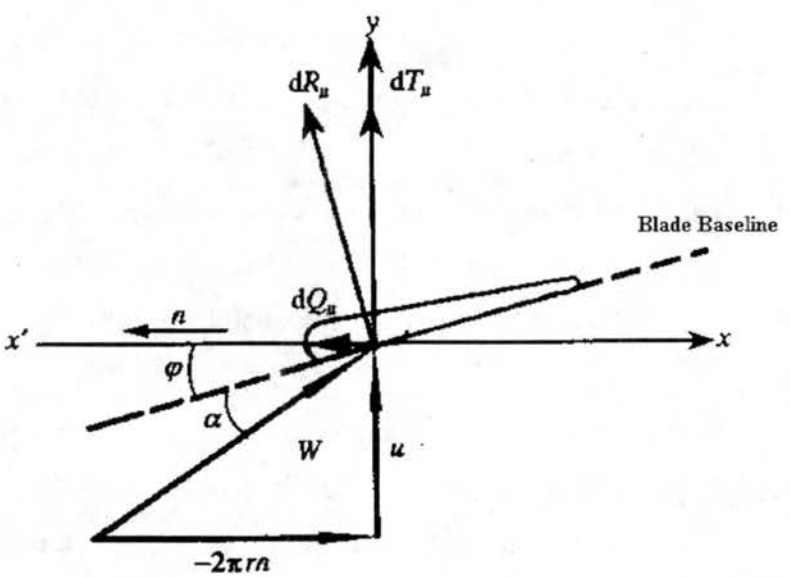

Figure A-1. The principle of fan's blade with wind speed. (Geshen, 2000)

Fans are powered by a motor and rotating blades will generate a pressure difference in front and behind the fan, which will push the air to go through the fan. The principle of an anemometer is very similar to this except that the torque is generated by wind not by electricity. In Figure A-1 (taken from Geshen, 2000), the irregular object is the cross section of a fan's blade, xx' is rotation plane. φ is the angle between rotation plane and blade baseline. y axis is perpendicular to rotation plane and the point of intersection is the origin of this coordinate. u is air flow speed. n is the rotation direction. line velocity is

$2\pi rn$. r is distance between gravity center of the blade and the axle center. When the fan is being rotating by the electrical power, the air flow will exert a net pressure to the blade. The composite force is determined by the relative velocity W between the blade and air flow, which is the composite vector of air flow speed u and rotation speed $2\pi rn$.

In order to simplify this question, we assume:

1. The blade is flat and thin, and when the air flow is parallel to the blade baseline, no net force is exerted on the blade.
2. We can ignore the friction resistance force.
3. No rotation or turbulence flow when the fan is working.
4. air flow speed u is a constant.

Under the assumption above, noticing there is an angle α between the baseline and the composite speed W, we can write down the force, which is exerted on the blade:

$$dR_u = a_u \frac{1}{2} \rho W^2 c\alpha \qquad \text{(A-1)}$$

where c is the chord of the blade; a_u is pressure coefficient.

This force dR_u can break up into two component forces, one is push force dT_u, the other is torque force dQ_u. This torque force will generate a torsional moment dM_Q:

$$dM_Q = a_u \frac{1}{2} \rho W^2 c\alpha \bullet r \sin\varphi \quad . \qquad \text{(A-2)}$$

Therefore, when and only when the angle α=0, the torsional moment is zero, and the fan will rotate at a constant rate. That is:

$$\frac{2\pi rn}{u} = \cot\varphi \quad . \qquad \text{(A-3)}$$

Therefore, the revolution speed of a fan has a linear function with air flow speed.

A.2 Experimental Approach

Because the cross section of collector is a square (ss-sf-CASCC is rectangle) and air velocity changes at different position inside the collector, measurements were taken at sixteen points that are evenly distributed inside the collector cross section (ss-sf-CASCC used 24 holes). These sixteen points were determined as follows:

1. Choose the top side, drill four holes (labeled name as "1, 2, 3, 4") to separate this side into five segments. For ss-sf-CASCC, drill six holes (labeled as "1, 2, 3, 4, 5, 6").
2. Carefully measured the length of the other perpendicular side, mark four points (labeled as "A, B, C, D") along the side to separate it into five segments as well.
3. Those points form a net, and the cross points are the measuring points we need.
4. Insert a hot wire anemometer through each hole, measured the air velocity at each point.
5. Thus the average air velocity is determined as:

$$V = \frac{\sum_{i=1}^{16} V_i}{16} \tag{A-4}$$

All the measurements were taken in the SimLab, Fort Collins Colorado. Because the hotwire performance depends on mass air flow, a pressure correction is needed to obtain the actual air velocity from the value reported by the probe.

A.3 Results and Discussion

A.3.1 CASCC collector

Table A-1 shows the air velocity vs. fan voltage of the CASCC, which was measured in the SimLab. Front voltage is the voltage measured right after the power supply and

before the wire; and back voltage is the voltage right before the collector fan. Table A-2 shows the average air velocity and revolution speed of the fan vs. back voltage. Since this data was measured in the SimLab, which is about 1500m higher than sea level, corrected average air velocity is calculated to represent the actual air velocity. The lower pressure in Fort Collins must be accounted for since the hot wire cooling rate is calibrated for standard conditions.

Table A-1. Uncorrected air velocity vs. voltage of CASCC fan.

Front Voltage (V)	Current (A)	Back Voltage (V)	Uncorrected air velocity (m/s)				Front Voltage (V)	Current (A)	Back Voltage (V)	Uncorrected air velocity (m/s)			
6.3	3.3	6.0	1	2	3	4	7.7	4.2	7.0	1	2	3	4
		A	3.6	3.6	3.8	3.6			A	4.6	4.2	4.3	4.2
		B	4.5	4.5	4.9	4.5			B	5.5	5.1	6	5.1
		C	4.3	4.2	4.6	4.4			C	6.3	5.1	5.1	5.3
		D	4.9	4	4.2	4.8			D	5.7	5	5.2	5.5
8.9	5.2	8.0	1	2	3	4	10.1	6.4	9.0	1	2	3	4
		A	4.7	5.2	4.8	4.9			A	5.7	5.2	5.5	5.1
		B	5.9	6.7	6.1	6.3			B	7.1	7	7.2	6.6
		C	6.2	6.3	6.2	6.4			C	7.3	7.1	7	7.1
		D	6.4	6.3	6.3	6.5			D	7	7	7.1	7.1
11.7	7.6	10.0	1	2	3	4	12.1	8.0	10.5	1	2	3	4
		A	6.7	6.3	6.7	6.3			A	6.8	6.7	6.8	6.7
		B	8	7.8	8	8			B	8.7	9.1	8.9	9.2
		C	8.7	8	7.7	8.2			C	8.9	9.4	8.6	9
		D	8.7	7.9	7.7	8.2			D	9.2	9	8.8	8.8
13.0	9.0	11.0	1	2	3	4	14.3	10.2	12.0	1	2	3	4
		A	7	6.8	7.3	6.8			A	8	8.1	8.1	8
		B	8.8	9.1	9.2	9			B	9.9	10	10.2	11.1
		C	9.9	9.5	9.2	9.3			C	10.7	10.1	9.6	10.5
		D	9.6	9	9.7	9.1			D	10.7	9.4	10.3	10.5
16.1	11.8	13.3	1	2	3	4							
		A	9.2	9.5	9.4	9							
		B	12.1	11.8	12.3	11.9							
		C	12.2	11.1	11.1	12.1							
		D	11.8	10.8	11.5	11.4							

These results are plotted in Figure A-2. The red curve is revolution speed vs. voltage;

the black curve is corrected air velocity vs. voltage. Tendency curves and R^2 value were also shown in Figure A-2.

Table A-2. Corrected average air velocity and fan revolution speed vs. voltage.

Back Voltage (V)	Current (A)	Revolution Speed (RPM)	Average air velocity (m/s)	Corrected average air velocity (m/s)
6	3.3	1410	4.28	5.04
7	4.2	1682	5.14	6.05
8	5.2	1910	5.95	7.00
9	6.4	2105	6.63	7.80
10	7.6	2328	7.68	9.04
10.5	8	2447	8.41	9.89
11	9	2597	8.71	10.25
12	10.2	2804	9.7	11.41
13.3	11.8	3073	11.1	13.06

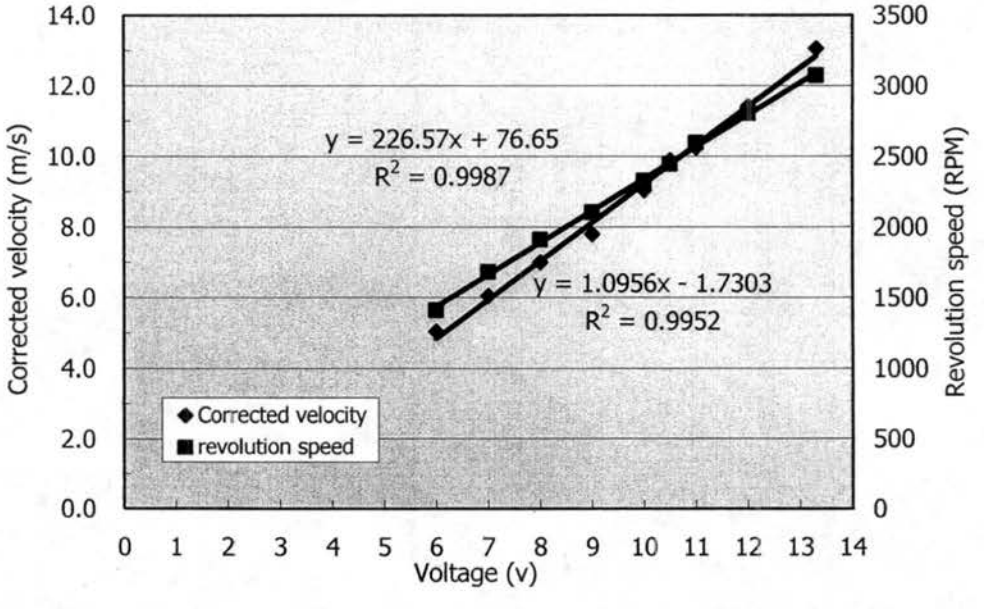

Figure A-2. Corrected air velocity and revolution speed vs. voltage on CASCC.

We can see that both air velocity and revolution speed have linear functions with voltage, and both R^2 value are close to one, which means the linear relationships are

really strong. These results agree well with aerodynamic calculations, which shows that revolution speed of a fan and the air velocity through the collector should have a direct proportional relationship. The DC fan can be treated as an electromotor and some power will be consumed by the fan's internal resistance. This power consumption is negligible, since the collector fans are relatively small. Therefore, the curve of air velocity vs. voltage is also essentially a straight line.

A.3.2 sf-CASCC collector

Similar to CASCC collector measurement, Table A-3 lists the result of flow measurement of sf-CASCC. Table A-4 shows the corrected air velocity and fan revolution speed vs. voltage. Figure A-3 depicts the plots and tendency curves of these relationships.

Table A-3. Uncorrected air velocity vs. voltage of sf-CASCC fan.

Front Voltage	Current (A)	Back Voltage	Uncorrected air velocity (m/s)				Front Voltage	Current (A)	Back Voltage	Uncorrected air velocity (m/s)			
6.3	3.4	6.0	1	2	3	4	7.6	4.3	7.0	1	2	3	4
		A	1.9	1.8	2.3	2.2			A	2.2	2.4	2.4	2.8
		B	3.2	2.8	3.1	3.2			B	3.8	3.5	3.9	3.9
		C	3.6	3.3	3.5	3.6			C	4	4	4.2	4.3
		D	3.5	3.3	3.5	3.4			D	4	3.9	4.1	4.2
8.9	5.4	8.0	1	2	3	4	10.0	6.6	9.0	1	2	3	4
		A	2.5	2.5	2.4	3.3			A	3.4	2.9	3	3
		B	4.4	4.1	4.6	4.7			B	5.4	5.1	5.4	5.4
		C	4.8	4.9	5	5.3			C	5.7	5.6	5.7	6
		D	5	4.9	5	5.2			D	5.6	5.4	5.9	5.9
11.7	7.6	10.0	1	2	3	4	12.1	8.5	10.5	1	2	3	4
		A	3.8	3.6	3.6	3.7			A	4.2	4.2	4.1	4.1
		B	6	5.4	6.1	6.3			B	6.4	5.9	6.7	6.6
		C	6.5	6.4	6.5	6.8			C	6.9	6.6	6.9	7
		D	6.3	6	6.5	6.6			D	6.6	6.4	7	6.8
12.9	9.2	11.0	1	2	3	4	14.5	10.8	12.0	1	2	3	4
		A	4.1	4.4	4.8	5			A	4.1	4.1	5.4	5
		B	6.7	6.4	6.7	7			B	7.4	7.2	7.4	7.6
		C	7	7	7.3	7.5			C	7.8	7.5	8.2	8.2
		D	6.9	6.7	7.2	7.3			D	7.8	7.3	8	8.1
16.1	12.5	13.3	1	2	3	4							
		A	5	5.2	5	5.1							
		B	8.1	7.8	8	8.6							
		C	8.4	8.5	8.9	9.3							
		D	8.4	8.4	8.6	9							

Table A-4. Corrected Air velocity and fan revolution speed vs. voltage.

Back Voltage (V)	Current (A)	Revolution Speed (RPM)	Average air velocity (m/s)	Corrected average air velocity (m/s)
6	3.4	1394	3.01	3.54
7	4.3	1613	3.6	4.24
8	5.4	1855	4.29	5.05
9	6.6	2113	4.96	5.84
10	7.6	2326	5.63	6.62
10.5	8.5	2439	6.03	7.09
11	9.2	2548	6.38	7.51
12	10.8	2783	6.94	8.16
13.3	12.5	3042	7.64	8.99

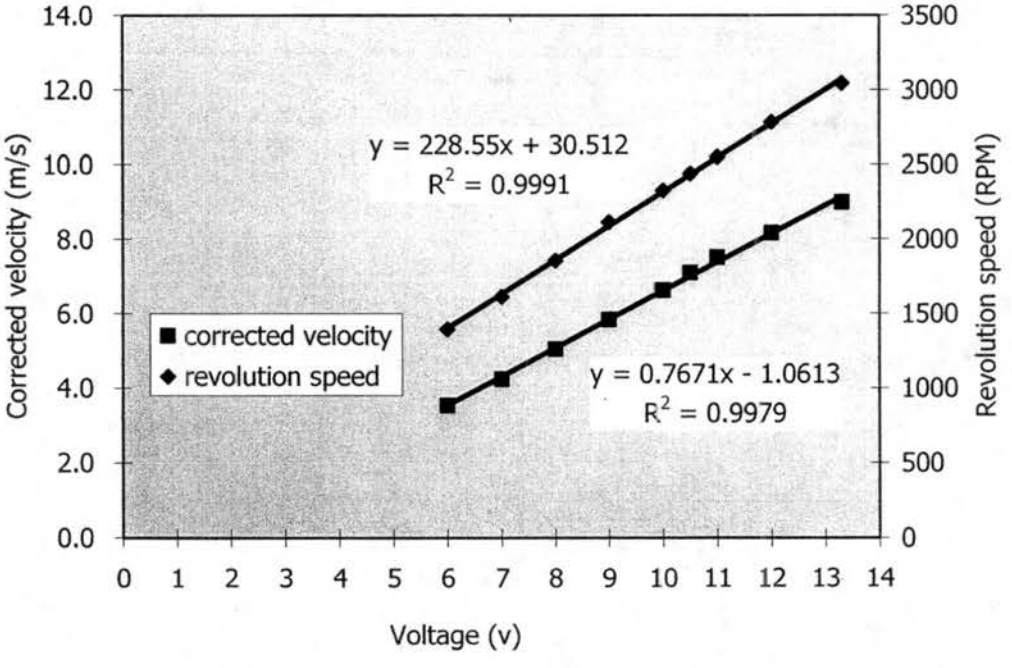

Figure A-3. Corrected air velocity and revolution speed vs voltage on sf-CASCC.

From the data and Figure A-3, we see the relationships are also linear, and R^2 values are near to one. Compared with CASCC results, sf-CASCC air velocities are lower for the same voltage. This is because sf-CASCC has two collection stages with rods/strands, increases the pressure drop through the whole collector.

A.3.3 Stainless Steel (ss-) CASCC collector

Table A-5. Uncorrected air velocity vs. voltage of the ss-CASCC.

Front Voltage (V)	Current (A)	Back Voltage (V)	Uncorrected air velocity (m/s)				Front Voltage (V)	Current (A)	Back Voltage (V)	Uncorrected air velocity (m/s)			
6.3	3.4	6.0	1	2	3	4	7.5	4.2	7.0	1	2	3	4
		A	4	3.8	3.7	4			A	4.4	4.4	4.5	4.9
		B	4.3	4.3	4.4	4.3			B	4.9	5	5	5.4
		C	4.4	4.3	4.6	4.8			C	5.1	4.9	5.3	5.6
		D	4.4	4.2	4.5	4.7			D	4.8	5.1	5.4	5.8
8.8	5.2	8.0	1	2	3	4	10.1	6.4	9.0	1	2	3	4
		A	5.4	5.1	5.1	5.6			A	5.8	6.1	6.2	6.2
		B	5.7	5.9	5.8	6.5			B	6.2	7	7.1	7.3
		C	5.7	6	6.2	6.4			C	6.5	7.2	7.3	7.4
		D	5.6	5.8	6	6.2			D	6.2	6.7	6.7	7.1
11.3	7.3	10.0	1	2	3	4	12.9	8.5	11.0	1	2	3	4
		A	6.1	6.4	6.7	6.9			A	6.6	7.6	7.6	8.3
		B	7.4	7.5	7.6	7.9			B	8.2	8.4	9.1	9.5
		C	7.4	7.5	7.8	8.4			C	8.3	9	9.4	9.7
		D	7.2	7.6	7.7	7.7			D	8	8.5	8.9	8.5
14.1	9.8	12.0	1	2	3	4	15.9	11.4	13.3	1	2	3	4
		A	8.1	8.2	8.5	9.5			A	9	9.2	9.5	9.5
		B	9.4	9.6	9.7	10.6			B	10.4	10.5	10.7	12.3
		C	9.6	9.8	9.6	10.7			C	10.7	11.2	11	12.4
		D	9.5	9.6	9.4	9.4			D	10.6	10.4	10.6	11.3

Table A-6 Air velocity and fan revolution speed vs. voltage of the ss-CASCC

Back Voltage (V)	Current (A)	Revolution Speed (RPM)	Average air velocity (m/s)	Corrected average air velocity (m/s)
6	3.3	1476	4.29	5.05
7	4.2	1719	5.03	5.92
8	5.2	1942	5.81	6.84
9	6.4	2181	6.69	7.87
10	7.6	2401	7.36	8.66
11	9	2629	8.48	9.98
12	10.2	2867	9.45	11.12
13.3	11.8	3112	10.57	12.44

Table A-5 shows the result of flow measurement of the ss-CASCC. Table A-6 shows measured average air velocity, corrected air velocity and revolution speed vs. back voltage. Figure A-4 plots the data in Table A-6.

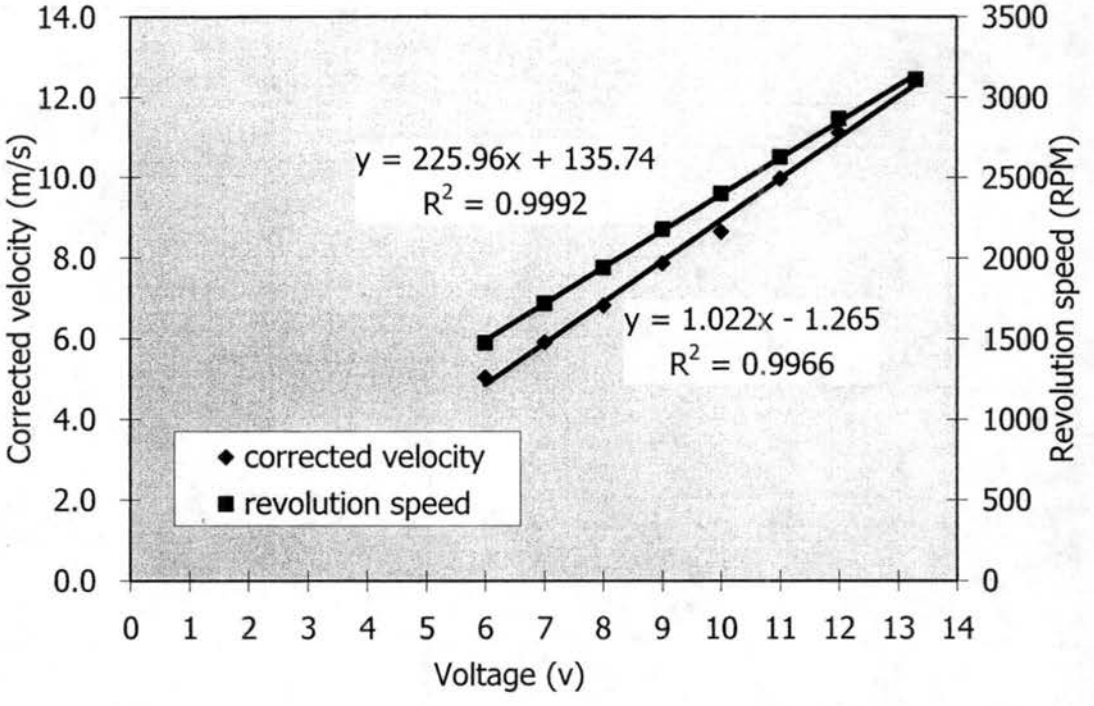

Figure A-4. Corrected air velocity and revolution speed vs voltage on the ss-CASCC

A.3.4 ss-sf-CASCC collector

The ss-sf-CASCC has two fans and the cross section is a rectangle not a square. Therefore, revolution speed is measured for each fan. "Average revolution speed" is the average revolution speed of the two fans. Table A-7 and Table A-8 list the results of flow measurement of the ss-sf-CASCC. Figure A-5 lists the corrected air velocity and average revolution speed vs. voltage.

Although the cross section of ss-sf-CASCC is almost twice as big as the CASCC and sf-CASCC, the air velocity is higher than the sf-CASCC and lower than the CASCC. And also because of the two fans, the current is as almost two times higher than for the CASCC.

Table A-7 Uncorrected air velocity vs. voltage of ss-sf-CASCC

Front Voltage (V)	Current (A)	Back Voltage (V)	Uncorrected air velocity(m/s)						Front Voltage (V)	Current (A)	Back Voltage (V)	Uncorrected air velocity(m/s)					
6.2	6.7	6.0	1	2	3	4	5	6	7.8	8.6	7.0	1	2	3	4	5	6
		A	3.4	3.3	3.2	3.2	3.3	3			A	4.2	3.9	4	3.9	4	3.9
		B	3.4	3.3	3.3	3.3	3.3	3.3			B	4	4.1	4	3.9	4	4.2
		C	3.2	3.4	3.3	3.2	3.3	3.4			C	3.9	4.1	4.1	3.9	3.9	4
		D	3.2	3.2	3.3	3.2	3.2	3.3			D	3.9	4	4.1	3.9	3.8	3.6
8.9	10.2	8.0	1	2	3	4	5	6	10.1	12.5	9.0	1	2	3	4	5	6
		A	4.9	4.5	4.8	4.4	4.7	4.4			A	5.4	5.3	5.4	5.3	5.4	5.3
		B	4.8	4.6	4.8	4.6	4.6	4.6			B	5.5	5.5	5.7	5.5	5.5	5.5
		C	4.7	4.7	4.8	4.6	4.6	4.7			C	5.5	5.4	5.6	5.3	5.3	5.2
		D	4.7	4.7	4.6	4.5	4.4	4.7			D	5.4	5.3	5.3	5.2	5.1	4.9
10.8	14.9	10.0	1	2	3	4	5	6	12.2	16.4	10.5	1	2	3	4	5	6
		A	6.4	6.2	6.3	6.2	6.3	6			A	6.6	6.6	6.7	6.7	6.6	6.5
		B	6.3	6.3	6.5	6.5	6.3	6.5			B	6.9	6.7	7.1	7.1	6.7	6.8
		C	6.3	6.3	6.7	6.5	6.2	6.2			C	6.8	6.7	6.8	6.6	6.7	6.5
		D	6.3	6.2	6.2	6.2	5.8	5.7			D	6.7	6.3	6.6	6.2	6.1	5.8
13.1	17.6	11.0	1	2	3	4	5	6	14.7	19.8	12.0	1	2	3	4	5	6
		A	7	6.9	7	6.9	7.2	6.7			A	7.7	7.5	7.7	7.4	8	7.6
		B	7	7.2	7.5	7.3	7.3	7.1			B	7.6	7.4	8	8.1	8	7.8
		C	7.3	7.3	7.7	7.2	7	7			C	7.7	7.5	7.9	7.9	7.7	7.5
		D	6.9	7.1	7.1	6.8	6.9	6.2			D	7.7	7.3	7.6	7.6	7.4	6.8
16.2	23.1	13.3	1	2	3	4	5	6									
		A	8.4	8.3	8.4	8.2	8.5	8.2									
		B	8.4	8.5	8.8	8.7	8.3	8.6									
		C	8.4	8.4	8.6	8.4	8.3	8.2									
		D	8.4	8.2	8.1	8	7.8	8.5									

Table A-8. Air velocity and fan revolution speed vs. voltage of ss-sf-CASCC.

Back Voltage (V)	Current (A)	Revolution Speed of left fan (RPM)	Revolution Speed of right fan (RPM)	Average revolution speed (RPM)	Average air velocity (m/s)	Corrected Average air velocity (m/s)
6	6.7	1330	1412	1371	3.27	3.85
7	8.6	1585	1632	1609	3.97	4.67
8	10.2	1826	1796	1811	4.64	5.46
9	12.5	2082	2046	2064	5.37	6.32
10	14.9	2320	2287	2304	6.27	7.38
10.5	16.4	2458	2443	2451	6.62	7.79
11	17.6	2564	2553	2559	7.01	8.25
12	19.8	2744	2736	2740	7.64	8.99
13.3	23.1	2991	2990	2991	8.36	9.84

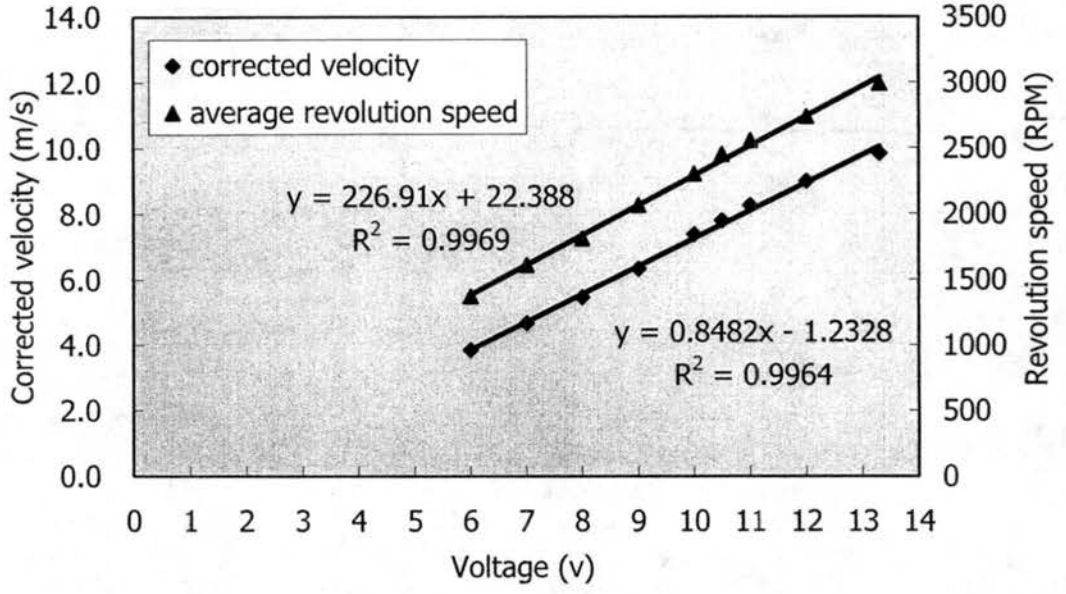

Figure A-5. Corrected air velocity and revolution speed vs. voltage on ss-sf-CASCC.

A.3.5 CASCC2 collector

Table A-9. Plastic CASCC2 flow measurement

Revolution speed (RPM)	Position	Air velocity (m/s)				Average air velocity (m/s)	Corrected average air velocity (m/s)
		1	2	3	4		
3360	A	12.4	11.8	11.5	12.2	12.17	14.32
	B	12.3	11.5	11.8	12.2		
	C	11.9	11.9	11.8	12.9		
	D	12.8	12.5	12.6	12.6		

The CASCC2 collector is smaller than the regular CASCC. It also uses an AC fan (~110V, 60Hz), so it is not necessary to get relationship between voltage and air velocity. Table A-9 lists the flow measurement of the plastic CASCC2. Table A-10 lists the same measurement for the Al-CASCC2.

The revolution speed of the AC fan is about 3360 rpm for the plastic CASCC2, and 3380 rpm for the metal CASCC2. These collectors use different fans, from different

manufacturers, but the fan performance is similar. The ultimate corrected air velocity for both collectors is similar to the CASCC. However, since the cross section of CASCC2 is much smaller than that of CASCC, the volume flow rate is much smaller than that of CASCC.

Table A-10 Al-CASCC2 flow measurement

Revolution speed (RPM)	Position	Air velocity (m/s)				Average air velocity (m/s)	Corrected average air velocity (m/s)
		1	2	3	4		
3380	A	11.6	9.5	10.2	9.8	12.35	14.53
	B	12.4	11.3	11.2	11.8		
	C	12.9	12.9	12.6	12.9		
	D	14.9	14.6	14.9	14.1		

A.4 Size cut calculation

The efficiency curves are calculated based upon information presented by Demoz et al. (1996). The major processes are:

A. Calculate Stokes number of single strand collection efficiency.
B. Calculate the efficiency of the strands.
C. Calculate the theoretical collection efficiency for each stage.
D. If necessary, repeat the steps above for different air velocity.

A.4.1 CASCC collector

Table A-11 shows results of collection efficiency calculations for the CASCC. The beginning of this table lists all the parameters that are needed. Detailed definitions can be found in the Demoz et al. (1996) paper. When calculating the theoretical collection efficiency for each stage, a parameter called *fr*, which is the fractional coverage per row (cross-sectional area of the strands in a row divided by the total cross sectional area of the collector), was measured manually.

Table A-11. Collection efficiency calculations for CASCC.

	Droplet Diameter (μm)	Air velocity (m/s)												
		4	4.5	5	5.5	6	6.5	7	7.5	8	8.5	9	9.5	10
St	2	0.17	0.19	0.21	0.23	0.25	0.27	0.29	0.31	0.33	0.35	0.38	0.40	0.42
	3	0.38	0.42	0.47	0.52	0.56	0.61	0.66	0.70	0.75	0.80	0.85	0.89	0.94
	4	0.67	0.75	0.83	0.92	1.00	1.09	1.17	1.25	1.34	1.42	1.50	1.59	1.67
	5	1.04	1.17	1.30	1.43	1.57	1.70	1.83	1.96	2.09	2.22	2.35	2.48	2.61
	6	1.50	1.69	1.88	2.07	2.25	2.44	2.63	2.82	3.01	3.19	3.38	3.57	3.76
	7	2.05	2.30	2.56	2.81	3.07	3.32	3.58	3.83	4.09	4.35	4.60	4.86	5.11
	8	2.67	3.01	3.34	3.67	4.01	4.34	4.67	5.01	5.34	5.68	6.01	6.34	6.68
	9	3.38	3.80	4.23	4.65	5.07	5.49	5.92	6.34	6.76	7.18	7.61	8.03	8.45
	10	4.17	4.70	5.22	5.74	6.26	6.78	7.30	7.83	8.35	8.87	9.39	9.91	10.43
	11	5.05	5.68	6.31	6.94	7.58	8.21	8.84	9.47	10.10	10.73	11.36	11.99	12.63
	15	9.39	10.57	11.74	12.91	14.09	15.26	16.43	17.61	18.78	19.96	21.13	22.30	23.48
	20	16.70	18.78	20.87	22.96	25.04	27.13	29.22	31.30	33.39	35.48	37.57	39.65	41.74
	25	26.09	29.35	32.61	35.87	39.13	42.39	45.65	48.91	52.17	55.44	58.70	61.96	65.22
	30	37.57	42.26	46.96	51.65	56.35	61.04	65.74	70.44	75.13	79.83	84.52	89.22	93.91
	35	51.13	57.52	63.91	70.31	76.70	83.09	89.48	95.87	102.26	108.65	115.04	121.44	127.83
	40	66.78	75.13	83.48	91.83	100.17	108.52	116.87	125.22	133.57	141.91	150.26	158.61	166.96
	45	84.52	95.09	105.65	116.22	126.78	137.35	147.91	158.48	169.05	179.61	190.18	200.74	211.31
	50	104.35	117.39	130.44	143.48	156.52	169.57	182.61	195.65	208.70	221.74	234.79	247.83	260.87
	55	126.26	142.04	157.83	173.61	189.39	205.18	220.96	236.74	252.52	268.31	284.09	299.87	315.66
	60	150.26	169.05	187.83	206.61	225.39	244.18	262.96	281.74	300.52	319.31	338.09	356.87	375.66
Single strand Efficiency	2	0.02	0.02	0.02	0.02	0.03	0.03	0.04	0.04	0.04	0.05	0.05	0.06	0.06
	3	0.05	0.06	0.08	0.09	0.10	0.11	0.13	0.14	0.15	0.17	0.18	0.20	0.21
	4	0.13	0.15	0.18	0.21	0.23	0.26	0.28	0.30	0.33	0.35	0.37	0.39	0.41
	5	0.24	0.28	0.32	0.36	0.39	0.42	0.45	0.48	0.50	0.53	0.55	0.57	0.59
	6	0.37	0.42	0.46	0.50	0.54	0.57	0.60	0.62	0.64	0.66	0.68	0.70	0.72
	7	0.50	0.54	0.58	0.62	0.65	0.68	0.70	0.72	0.74	0.76	0.77	0.79	0.80
	8	0.60	0.64	0.68	0.71	0.74	0.76	0.78	0.79	0.81	0.82	0.83	0.84	0.85
	9	0.68	0.72	0.75	0.78	0.80	0.81	0.83	0.84	0.85	0.86	0.87	0.88	0.89
	10	0.75	0.78	0.80	0.82	0.84	0.85	0.87	0.88	0.88	0.89	0.90	0.91	0.91
	11	0.80	0.82	0.84	0.86	0.87	0.88	0.89	0.90	0.91	0.91	0.92	0.92	0.93
	15	0.90	0.91	0.92	0.93	0.94	0.94	0.95	0.95	0.95	0.96	0.96	0.96	0.96
	20	0.95	0.95	0.96	0.96	0.97	0.97	0.97	0.97	0.98	0.98	0.98	0.98	0.98
	25	0.97	0.97	0.97	0.98	0.98	0.98	0.98	0.98	0.98	0.99	0.99	0.99	0.99
	30	0.98	0.98	0.98	0.98	0.99	0.99	0.99	0.99	0.99	0.99	0.99	0.99	0.99
	35	0.98	0.99	0.99	0.99	0.99	0.99	0.99	0.99	0.99	0.99	0.99	0.99	0.99
	40	0.99	0.99	0.99	0.99	0.99	0.99	0.99	0.99	0.99	0.99	0.99	1.00	1.00
	45	0.99	0.99	0.99	0.99	0.99	0.99	0.99	1.00	1.00	1.00	1.00	1.00	1.00
	50	0.99	0.99	0.99	0.99	1.00	1.00	1.00	1.00	1.00	1.00	1.00	1.00	1.00
	55	0.99	0.99	1.00	1.00	1.00	1.00	1.00	1.00	1.00	1.00	1.00	1.00	1.00
	60	0.99	1.00	1.00	1.00	1.00	1.00	1.00	1.00	1.00	1.00	1.00	1.00	1.00
Total strand Efficiency	2	0.02	0.03	0.03	0.03	0.04	0.04	0.05	0.06	0.06	0.07	0.07	0.08	0.09
	3	0.07	0.09	0.10	0.12	0.14	0.15	0.17	0.19	0.20	0.22	0.24	0.25	0.27
	4	0.17	0.20	0.23	0.26	0.29	0.32	0.34	0.37	0.39	0.41	0.43	0.45	0.47
	5	0.30	0.34	0.38	0.41	0.44	0.47	0.50	0.52	0.54	0.56	0.57	0.59	0.60
	6	0.43	0.47	0.51	0.54	0.56	0.58	0.60	0.62	0.63	0.65	0.66	0.67	0.68
	7	0.53	0.57	0.60	0.62	0.64	0.66	0.67	0.68	0.69	0.70	0.71	0.71	0.72
	8	0.61	0.63	0.66	0.67	0.69	0.70	0.71	0.72	0.73	0.73	0.74	0.74	0.75
	9	0.66	0.68	0.70	0.71	0.72	0.73	0.74	0.74	0.75	0.75	0.76	0.76	0.76
	10	0.69	0.71	0.72	0.73	0.74	0.75	0.75	0.76	0.76	0.76	0.77	0.77	0.77
	11	0.72	0.73	0.74	0.75	0.76	0.76	0.76	0.77	0.77	0.77	0.78	0.78	0.78
	15	0.77	0.77	0.78	0.78	0.78	0.79	0.79	0.79	0.79	0.79	0.79	0.79	0.79
	20	0.79	0.79	0.79	0.79	0.79	0.80	0.80	0.80	0.80	0.80	0.80	0.80	0.80
	25	0.80	0.80	0.80	0.80	0.80	0.80	0.80	0.80	0.80	0.80	0.80	0.80	0.80
	30	0.80	0.80	0.80	0.80	0.80	0.80	0.80	0.80	0.80	0.80	0.80	0.80	0.80
	35	0.80	0.80	0.80	0.80	0.80	0.80	0.80	0.80	0.80	0.80	0.80	0.80	0.81
	40	0.80	0.80	0.80	0.80	0.80	0.80	0.80	0.81	0.81	0.81	0.81	0.81	0.81
	45	0.80	0.80	0.80	0.80	0.81	0.81	0.81	0.81	0.81	0.81	0.81	0.81	0.81
	50	0.80	0.80	0.81	0.81	0.81	0.81	0.81	0.81	0.81	0.81	0.81	0.81	0.81
	55	0.81	0.81	0.81	0.81	0.81	0.81	0.81	0.81	0.81	0.81	0.81	0.81	0.81
	60	0.81	0.81	0.81	0.81	0.81	0.81	0.81	0.81	0.81	0.81	0.81	0.81	0.81

Droplet Density 1000 kg/m^3; Angle: 35°; Air viscosity: 1.72×10^{-5} kg/m.s; Strand diameter 5.08×10^{-4} m

Figure A-6 shows collection efficiency curves for the CASCC at various air velocities. It is very similar to the efficiency curve of CASCC2, which is in figure 2 in Demoz et al., (1996) paper, but the highest efficiency is slightly lower than that of CASCC2. Furthermore, we can see that changing sampling air velocity can also change the flow rate but will not change the droplet collection efficiency very much. For example, changing air velocity from 6m/s to 10m/s will only change the size cut from 6 to 4 μm. This agrees well with Demoz et al. (1996).

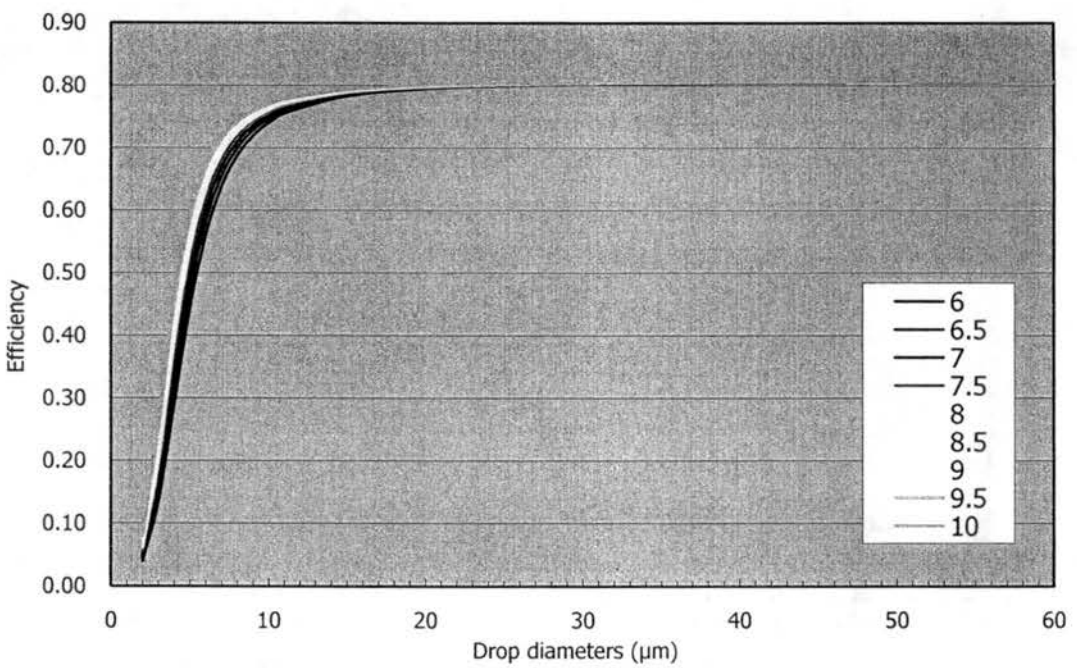

Figure A-6. Efficiency curves for the CASCC at various air velocities.

A.4.2 sf-CASCC first stage.

Table A-12 shows the collection efficiency calculations for the sf-CASCC first stage. The calculation method is the same as for the CASCC. Figure A-7 shows the efficiency curves for the sf-CASCC first stage at various speeds.

Table A-12. Collection efficiency calculations for sf-CASCC first stage.

	Droplet Diameter (um)	Air speed (m/s)												
		4	4.5	5	5.5	6	6.5	7	7.5	8	8.5	9	9.5	10
St	2	0.01	0.01	0.01	0.01	0.01	0.01	0.01	0.01	0.01	0.01	0.02	0.02	0.02
	3	0.02	0.02	0.02	0.02	0.02	0.02	0.03	0.03	0.03	0.03	0.03	0.04	0.04
	4	0.03	0.03	0.03	0.04	0.04	0.04	0.05	0.05	0.05	0.06	0.06	0.06	0.07
	5	0.04	0.05	0.05	0.06	0.06	0.07	0.07	0.08	0.08	0.09	0.09	0.10	0.10
	6	0.06	0.07	0.08	0.08	0.09	0.10	0.11	0.11	0.12	0.13	0.14	0.14	0.15
	7	0.08	0.09	0.10	0.11	0.12	0.13	0.14	0.15	0.16	0.17	0.18	0.19	0.20
	8	0.11	0.12	0.13	0.15	0.16	0.17	0.19	0.20	0.21	0.23	0.24	0.25	0.27
	9	0.14	0.15	0.17	0.19	0.20	0.22	0.24	0.25	0.27	0.29	0.30	0.32	0.34
	10	0.17	0.19	0.21	0.23	0.25	0.27	0.29	0.31	0.33	0.35	0.38	0.40	0.42
	11	0.20	0.23	0.25	0.28	0.30	0.33	0.35	0.38	0.40	0.43	0.45	0.48	0.51
	15	0.38	0.42	0.47	0.52	0.56	0.61	0.66	0.70	0.75	0.80	0.85	0.89	0.94
	20	0.67	0.75	0.83	0.92	1.00	1.09	1.17	1.25	1.34	1.42	1.50	1.59	1.67
	25	1.04	1.17	1.30	1.43	1.57	1.70	1.83	1.96	2.09	2.22	2.35	2.48	2.61
	30	1.50	1.69	1.88	2.07	2.25	2.44	2.63	2.82	3.01	3.19	3.38	3.57	3.76
	35	2.05	2.30	2.56	2.81	3.07	3.32	3.58	3.83	4.09	4.35	4.60	4.86	5.11
	40	2.67	3.01	3.34	3.67	4.01	4.34	4.67	5.01	5.34	5.68	6.01	6.34	6.68
	45	3.38	3.80	4.23	4.65	5.07	5.49	5.92	6.34	6.76	7.18	7.61	8.03	8.45
	50	4.17	4.70	5.22	5.74	6.26	6.78	7.30	7.83	8.35	8.87	9.39	9.91	10.43
	55	5.05	5.68	6.31	6.94	7.58	8.21	8.84	9.47	10.10	10.73	11.36	11.99	12.63
	60	6.01	6.76	7.51	8.26	9.02	9.77	10.52	11.27	12.02	12.77	13.52	14.27	15.03
Single strand Efficiency	2	0.00	0.00	0.00	0.00	0.00	0.00	0.00	0.00	0.00	0.00	0.00	0.00	0.00
	3	0.00	0.00	0.00	0.00	0.00	0.00	0.00	0.00	0.00	0.00	0.00	0.00	0.00
	4	0.00	0.00	0.00	0.00	0.00	0.00	0.00	0.00	0.00	0.00	0.01	0.01	0.03
	5	0.00	0.00	0.00	0.00	0.01	0.04	0.06	0.02	0.02	0.01	0.01	0.01	0.01
	6	0.01	0.03	0.03	0.02	0.01	0.01	0.01	0.01	0.01	0.01	0.01	0.01	0.01
	7	0.02	0.01	0.01	0.01	0.01	0.01	0.01	0.01	0.02	0.02	0.02	0.02	0.02
	8	0.01	0.01	0.01	0.01	0.02	0.02	0.02	0.02	0.02	0.02	0.03	0.03	0.03
	9	0.01	0.01	0.02	0.02	0.02	0.02	0.03	0.03	0.03	0.03	0.04	0.04	0.04
	10	0.02	0.02	0.02	0.02	0.03	0.03	0.04	0.04	0.04	0.05	0.05	0.06	0.06
	11	0.02	0.02	0.03	0.03	0.04	0.04	0.05	0.05	0.06	0.07	0.07	0.08	0.08
	15	0.05	0.06	0.08	0.09	0.10	0.11	0.13	0.14	0.15	0.17	0.18	0.20	0.21
	20	0.13	0.15	0.18	0.21	0.23	0.26	0.28	0.30	0.33	0.35	0.37	0.39	0.41
	25	0.24	0.28	0.32	0.36	0.39	0.42	0.45	0.48	0.50	0.53	0.55	0.57	0.59
	30	0.37	0.42	0.46	0.50	0.54	0.57	0.60	0.62	0.64	0.66	0.68	0.70	0.72
	35	0.50	0.54	0.58	0.62	0.65	0.68	0.70	0.72	0.74	0.76	0.77	0.79	0.80
	40	0.60	0.64	0.68	0.71	0.74	0.76	0.78	0.79	0.81	0.82	0.83	0.84	0.85
	45	0.68	0.72	0.75	0.78	0.80	0.81	0.83	0.84	0.85	0.86	0.87	0.88	0.89
	50	0.75	0.78	0.80	0.82	0.84	0.85	0.87	0.88	0.88	0.89	0.90	0.91	0.91
	55	0.80	0.82	0.84	0.86	0.87	0.88	0.89	0.90	0.91	0.91	0.92	0.92	0.93
	60	0.83	0.85	0.87	0.88	0.89	0.90	0.91	0.92	0.92	0.93	0.93	0.94	0.94
Total strand Efficiency	2	0.00	0.00	0.00	0.00	0.00	0.00	0.00	0.00	0.00	0.00	0.00	0.00	0.00
	3	0.00	0.00	0.00	0.00	0.00	0.00	0.00	0.00	0.00	0.00	0.00	0.00	0.00
	4	0.00	0.00	0.00	0.00	0.00	0.00	0.00	0.00	0.01	0.01	0.01	0.02	0.05
	5	0.00	0.00	0.00	0.01	0.02	0.07	0.10	0.04	0.03	0.02	0.02	0.02	0.02
	6	0.01	0.06	0.06	0.03	0.02	0.02	0.02	0.02	0.02	0.02	0.02	0.02	0.03
	7	0.03	0.02	0.02	0.02	0.02	0.02	0.02	0.03	0.03	0.03	0.03	0.04	0.04
	8	0.02	0.02	0.02	0.03	0.03	0.03	0.03	0.04	0.04	0.04	0.05	0.05	0.06
	9	0.02	0.03	0.03	0.03	0.04	0.04	0.05	0.05	0.06	0.06	0.07	0.07	0.08
	10	0.03	0.03	0.04	0.04	0.05	0.06	0.06	0.07	0.08	0.09	0.09	0.10	0.11
	11	0.04	0.04	0.05	0.06	0.07	0.08	0.09	0.10	0.11	0.12	0.13	0.14	0.15
	15	0.09	0.11	0.13	0.15	0.17	0.19	0.21	0.24	0.26	0.28	0.30	0.32	0.34
	20	0.22	0.26	0.29	0.33	0.36	0.40	0.43	0.46	0.48	0.51	0.53	0.55	0.57
	25	0.38	0.43	0.47	0.51	0.55	0.58	0.61	0.63	0.66	0.68	0.69	0.71	0.72
	30	0.53	0.58	0.62	0.65	0.68	0.70	0.73	0.74	0.76	0.77	0.78	0.79	0.80
	35	0.65	0.69	0.72	0.74	0.76	0.78	0.79	0.80	0.81	0.82	0.83	0.84	0.84
	40	0.73	0.76	0.78	0.80	0.81	0.82	0.83	0.84	0.85	0.85	0.86	0.86	0.87
	45	0.78	0.80	0.82	0.83	0.84	0.85	0.86	0.86	0.87	0.87	0.87	0.88	0.88
	50	0.82	0.83	0.84	0.85	0.86	0.87	0.87	0.88	0.88	0.88	0.88	0.89	0.89
	55	0.84	0.85	0.86	0.87	0.87	0.88	0.88	0.88	0.89	0.89	0.89	0.89	0.89
	60	0.86	0.87	0.87	0.88	0.88	0.89	0.89	0.89	0.89	0.90	0.90	0.90	0.90

Droplet Density 1000 kg/m^3; Angle: 35°; Air viscosity: 1.72×10^{-5} kg/m.s; Strand diameter 1.27×10^{-2} m

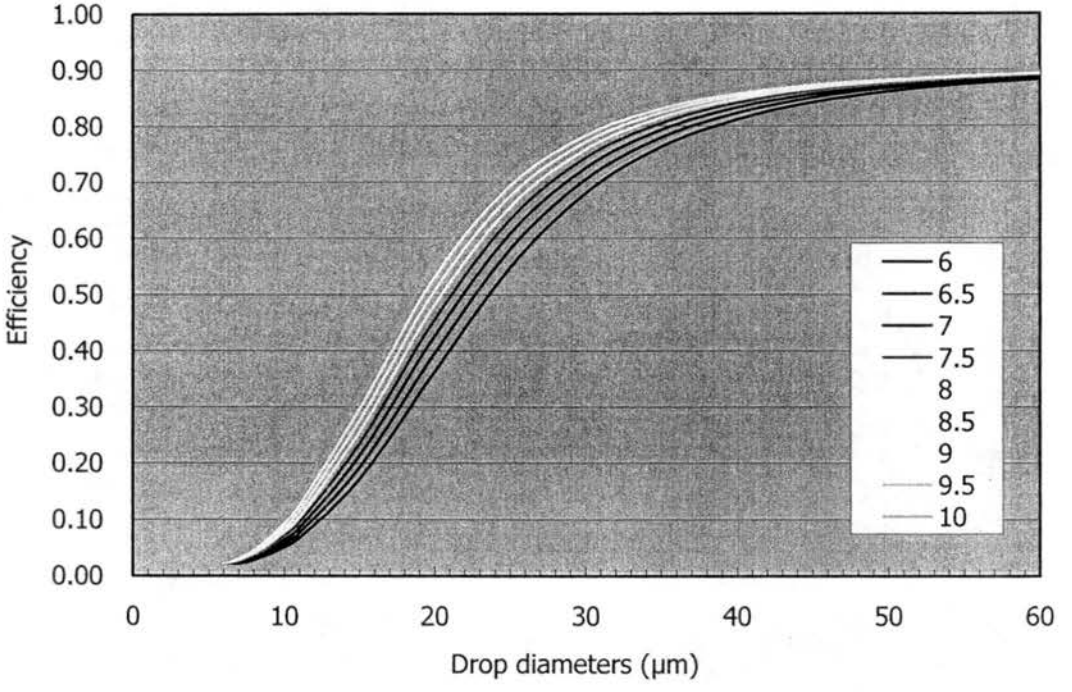

Figure A-7. Efficiency curves for the sf-CASCC first stage at various air velocities.

Scott Emert measured the working voltages of the fans used in CRPAQS, which were 11.12V for sf-CASCC and 10.65V for CASCC. From Table A-4, corrected air velocity is about 7.5 m/s when voltage equals 11.12V. Based on Figure A-6, the 50% cut size is about 21 μm for 7.5 m/s air velocity. Figure A-6 is also consistent with figure 2 in Demoz et al., (1996). It is important to keep in mind that these calculations do not include airflow focusing effects caused by air passage through a row being accelerated onto the downstream row. Numerical modeling of this effect demonstrates that it can significantly decrease the 50% cut size due to higher drop velocities following the first row of a stage (Moore, 2002).

A.4.3 ss-sf-CASCC collector

Scott Emert measured the working voltage of ss-sf-CASCC, which is about 11V. From Table A-8, corrected air velocity should be 8.25 m/s. Taking 8.25 m/s as the air velocity,

we can calculate efficiency curves for first and second stage of ss-sf-CASCC. Figure A-8 shows the efficiency curves of ss-sf-CASCC.

Although the ss-sf-CASCC has two fans and its cross section is a rectangle, these efficiency curves are similar to those for the ASCC and ss-CASCC, because the equations we used don't depend on the physical structure of a collector.

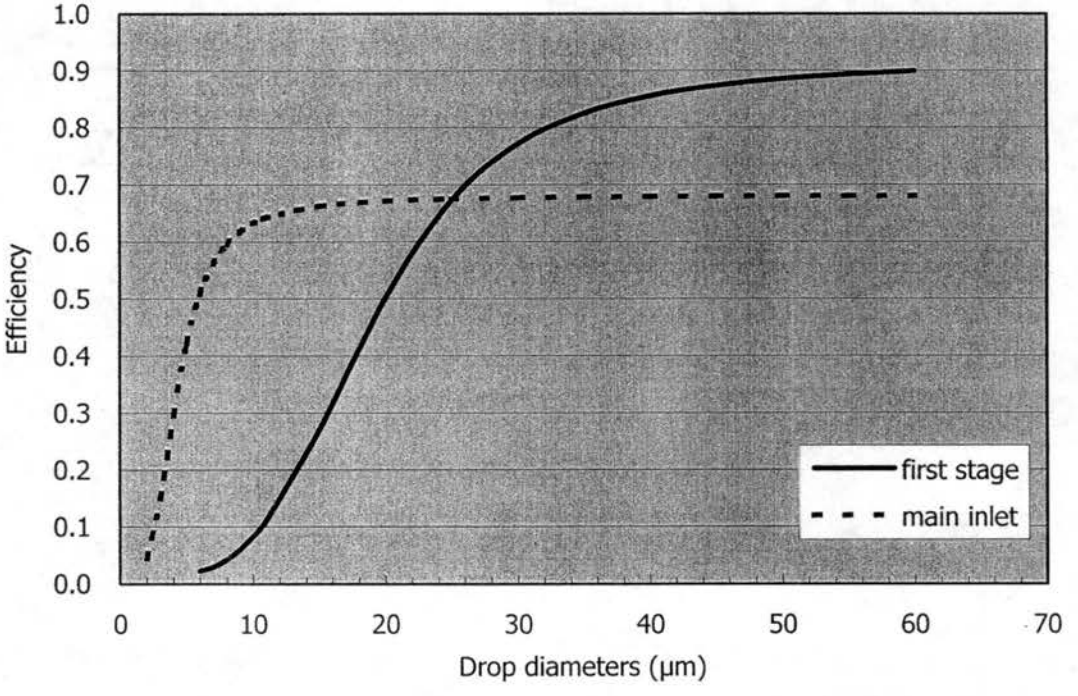

Figure A-8. Efficiency curves for the sf-CASCC first and second stage at 8.25 m/s air velocity.

Appendix B

Simulated air flow and particle tracks in sampling tube of CSASP

B.1 Introduction

One of the most important parameters for characterizing clouds and fogs is Liquid Water Content (LWC). Currently, the PVM and Classical scattering aerosol spectrometer probe (CSASP) are both being used to measure LWC. However, large differences were found between LWC values reported by these instruments in some studies. Differences of up to 650% in LWC measured by the CSASP and PVM, are much larger than the expected accuracies given for both instruments (Gerber et al. 1994).

The CSASP uses a fan to accelerate air to go through a horn-like tube and the particles in the air were measured by a laser illuminating a sensing volume at the center of the tube. Figure B-1 (planform) show the schematic view of the CSASP. There is an axial fan on the back of the CSASP which is not shown in figure B-1. The fan draws the air through the accelerator, which is also called the sampling tube. On the air flow pathway, the laser will emit a beam of light to illuminate the water droplets in the air flow. Collecting optics receive scattered light, and generate an electrical signal, which will be recorded by computer. If the droplets were focused by the inlet toward the center of the sampling tube, the CSASP would overestimate LWC.

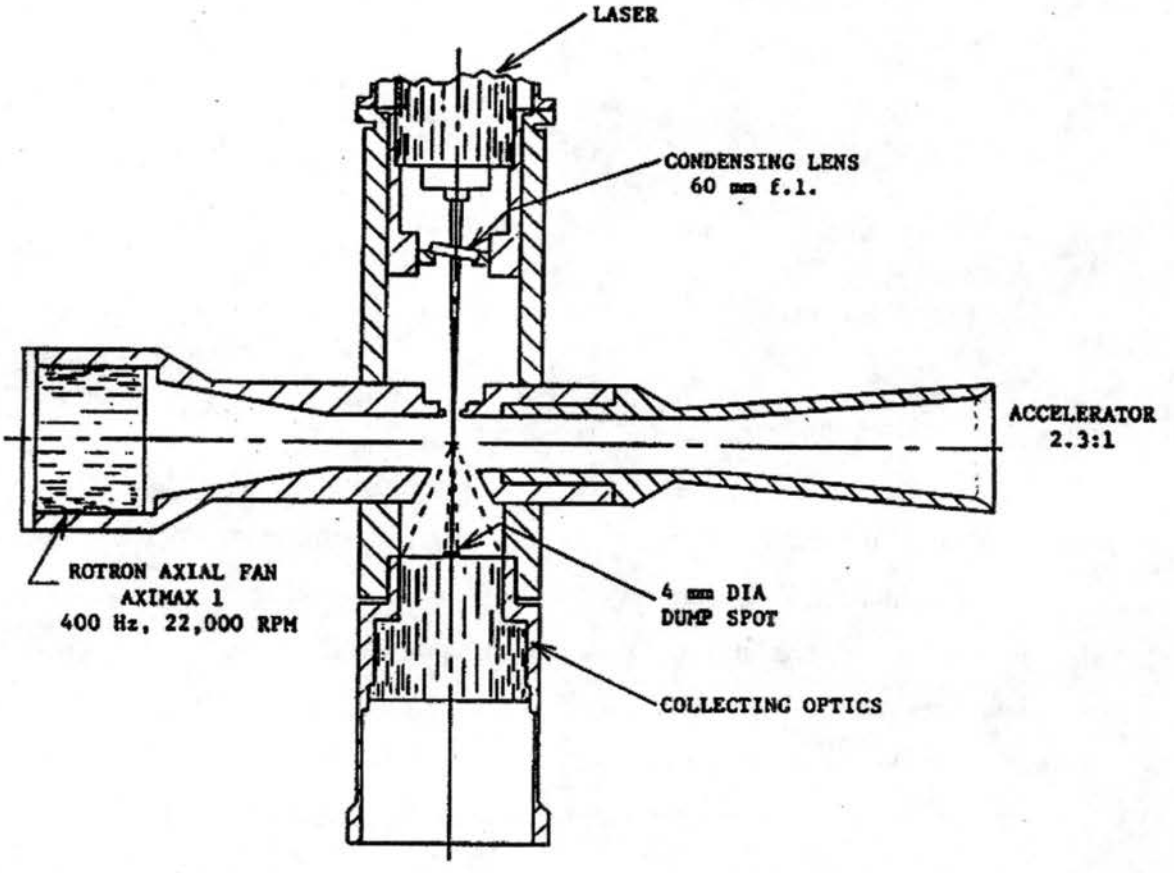

Figure B-1. The schematic view of the CSASP inlet (accelerator) and optical laser source. The fan draws air and droplets through accelerator and the droplets are measured by a laser source (collecting optics in the figure).

B.2 Experimental approach

A 2-D numerical flow modeling of the sampling tube of CSASP and its mesh file are generated by using GAMBIT 1.1 software, and CFD software package FLUENT 5.5 were used to simulate the air flow and trajectories of released particles (from rakes). FLUENT's multiphase functions allow us to investigate the continuous phase (air) and discrete phase (water droplet). A simple droplet trajectory model was used to show if suction used to draw droplets into the sampling tube of the CSASP can cause changes of the droplet concentration at the point in the tube where the laser beam interacts with the droplets.

B.2.1 Mesh file generation

Since the sampling tube is symmetric along its centerline, only half of the tube is generated with GAMBIT, with symmetry applied to the outer boundaries to avoid the excessively fine mesh needed to resolve flow features. Inside the sampling tube, boundary layers were used to better simulate the flow near the walls. The rest of the tube inside was meshed by hex method.

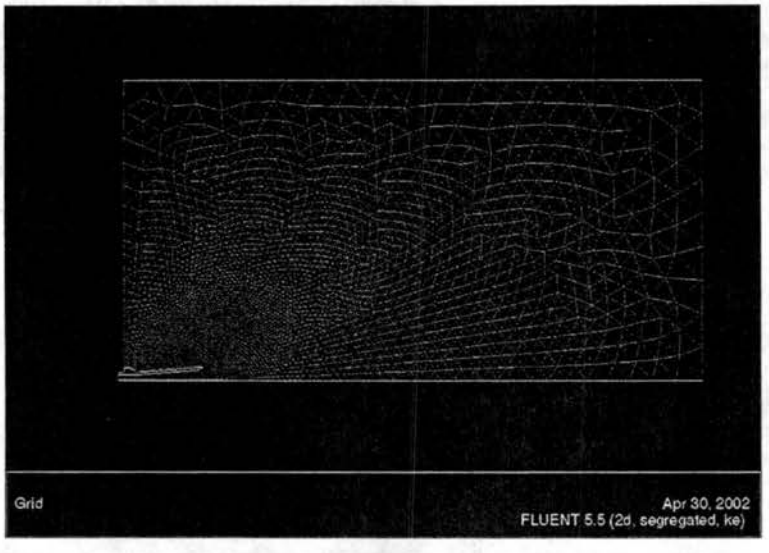

Figure B-2. Final mesh of CSASP sampling tube with environment.

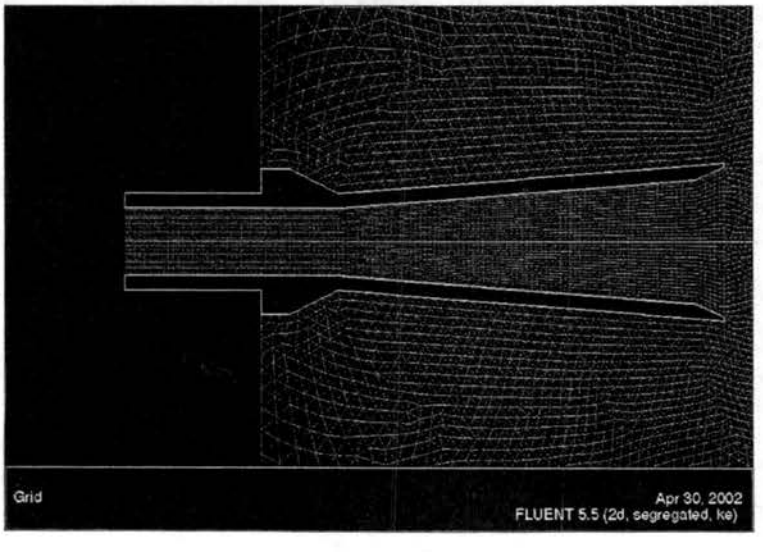

Figure B-3. Detail view of the mesh inside sampling tube (symmetry boundary are the centerline), the mesh in the walls of the tube were set as invisible.

A broader space was meshed to simulate the flow outside the tube. A square area was created, whose sides are 20 times longer that the tube maximum diameter. This is to make sure the out space is large enough, and won't affect the air flow. For this area, Tri/Pave

method was used to mesh it, so the final mesh is hybrid. The final mesh is shown in Figure B-2 and B-3.

B.2.2 Numerical approach

There are several ways to model two-phase flows in Fluent (for cloud collectors, the two phases are air and water drops). These include the volume of fluid model, the cavitation model, the algebraic slip model, and the discrete phase model. The most useful model for looking at cloud drop trajectories is the discrete phase model. This model tracks individual particles or drops as they move through the computational domain so that you can determine which surfaces they impact on.

The following steps were processed:

1. Keep the default solver settings.
2. Turn on the standard k-ε turbulence model.
3. Use air to be the default material.
4. Set the boundary conditions:

   Set the main outlet as pressure outlet. Since the air terminal velocity should be 26.5m/s, which is written on the operation manual of CSASP, a fixed pressure was used as initial conditions.

   Set outer space as pressure inlet. Set the walls of sampling tube as walls, and set discrete phase model condition as "escape", so that the water droplets will escape when they hit the walls of the sampling tube.
5. It is enough to keep the default solution setting. Second order solution was tried, but didn't change the results very much.
6. For residual monitors, check the box "plot" under options.
7. Iterate under the solution reached convergence.

   After having a converged solution for the air flow (the continuous phase), then define the cloud drop (the discrete phase) properties and initial conditions. Based on an equation of motion for the cloud drops, their motion through the continuous phase will be then calculated.

8. Create a Rake surface near the inlet of the sampling tube. Set particle number to 30.
9. Make injections. Choose the "Inert" particle type, and select "water-liquid" as working material. Set the drop size in the range of 1 to 50 micrometers (1e-6 to 5e-5 meters) in diameter. The Stochastic Tracking section is to include the effects of turbulence on drop motion. Start out without the stochastic model activated.
10. From "display" ->"particle tracks", release the particles and look at their tracks.

B.3 Results and discussion

B.3.1 Continuous phase (air flow)

Figure B-4 shows the pressure contour of the sampling tube. Figure B-5A shows the velocity contour. We can see that the outer space is big enough and will not affect the flow. Figure B-5B is the amplified velocity contour near the wall boundary. It is very clear that there is a boundary layer near the walls of sampling tube, which is fit what we expected.

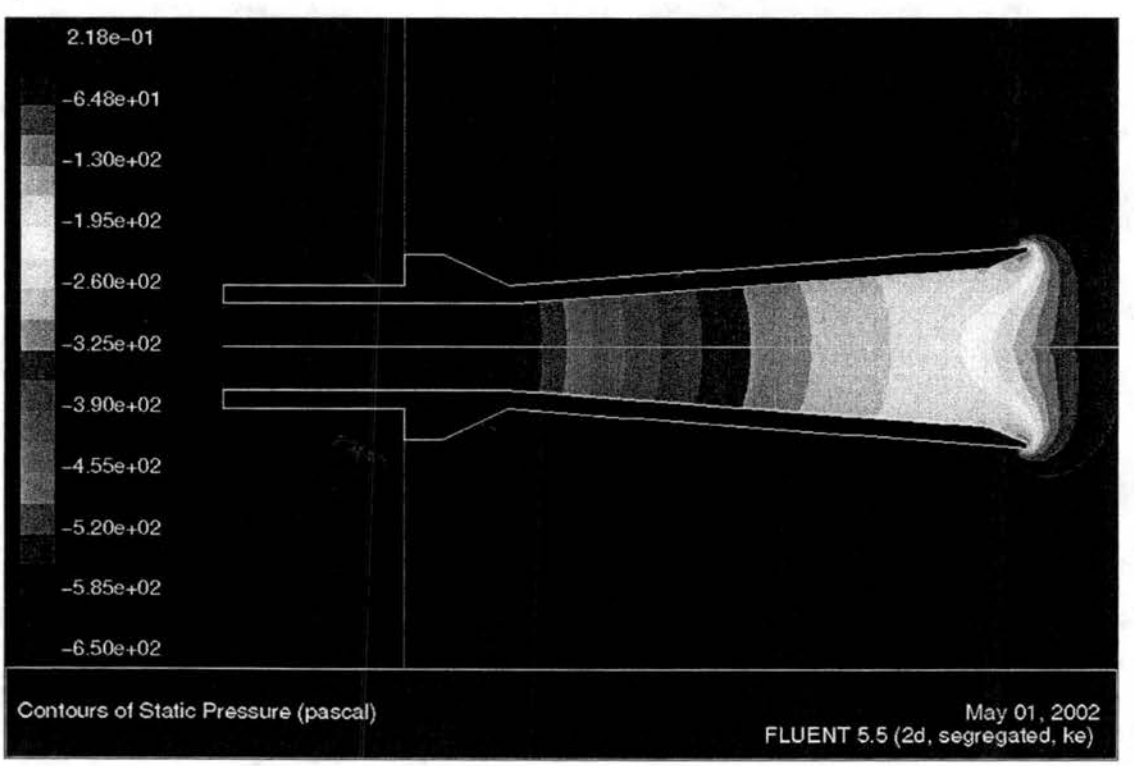

Figure B-4. Pressure contour of the sampling tube.

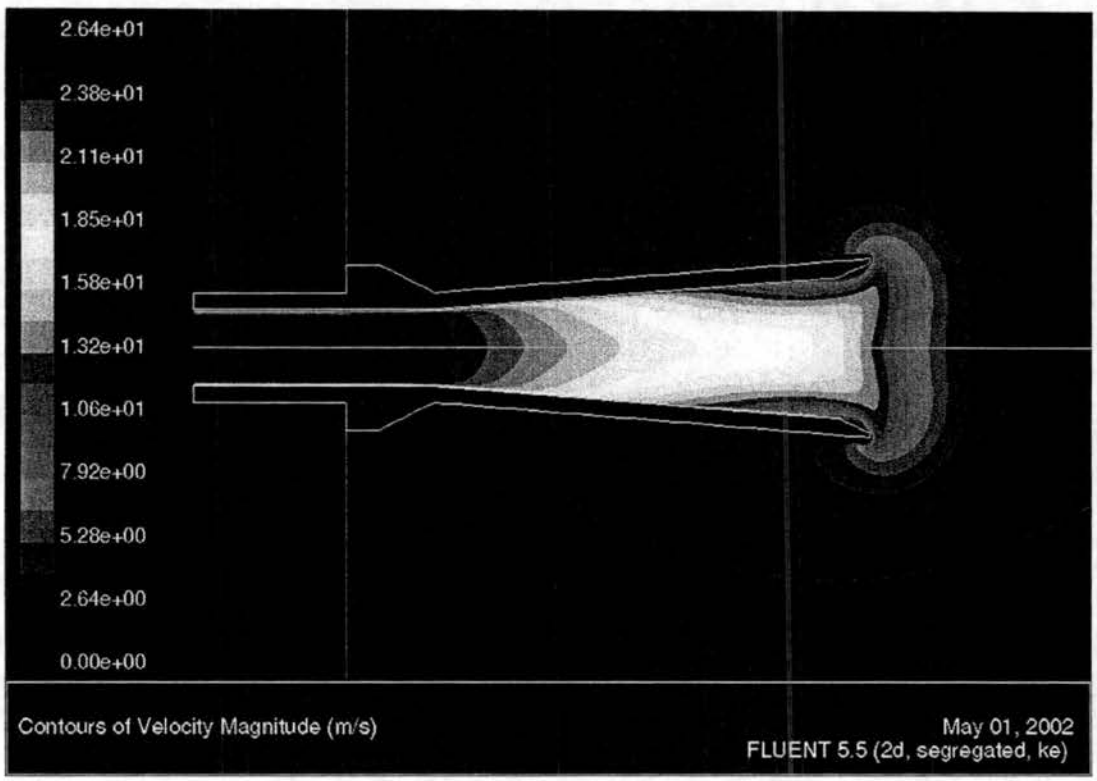

Figure B-5A. velocity contour of the sampling tube.

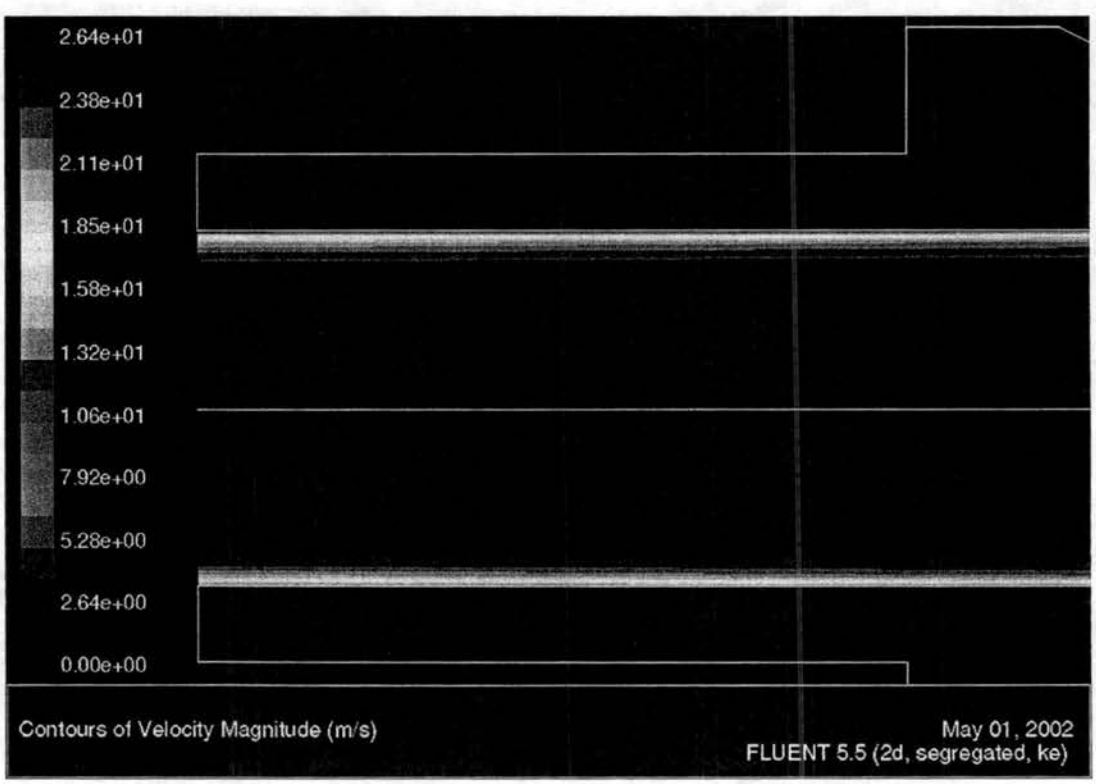

Figure B-5B. Amplified velocity contour near the wall boundary.

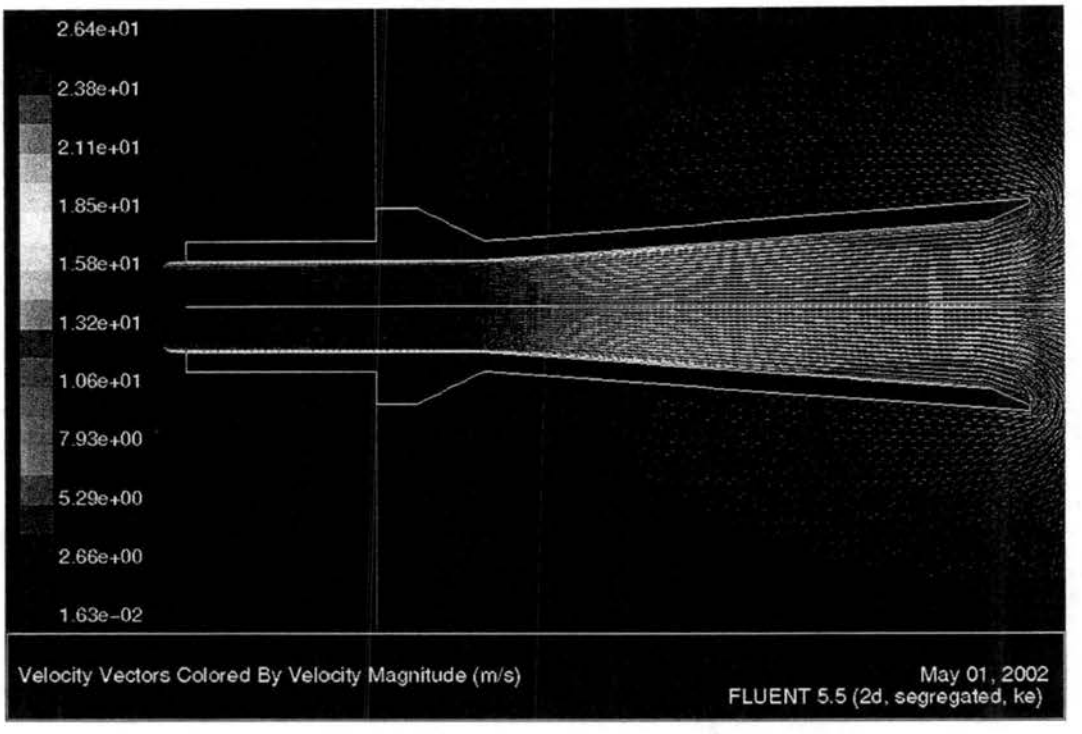

Figure B-6. Velocity vector of the sampling tube.

Figure B-6 shows the velocity vectors of the sampling tube. From the vector distribution, we can see that first the air passed the entrance of the tube, and then was accelerated to go through the tube. The terminal velocity is about 26.4m/s, which agrees well with theoretical value. Based on figure B-4~6, the resulting air flow distribution satisfies and fits what we expected: 1) Terminal velocity is about 26.5m/s. 2) Boundary layers near the walls are good. 3) Outer space is big enough. 4) Air flow pattern is very similar to what it should be.

B.3.2 Discrete phase (water droplets)

Figure B-7, B-8 and B-9 show the calculated droplet trajectories of 5 μm, 25 μm and 50 μm diameter particles in sampling tube respectively. The droplets are introduced into the right end of the sampling tube.

The velocity vector contour (Figure B-6) can also be seen as the streamline that all the particles should follow. The curvature of the streamline in contact with the inside wall of

the converging part of the insert has the same shape with that of the insert wall. But from Figures B-7, B-8 and B-9, only particles whose diameter is 5um can follow the streamline and doesn't change the size distribution; 25 μm and 50 μm droplets are unable to follow the curved streamlines, and due to the droplets inertia, accumulate near the centerline of the tube where the laser-sensitive volume is located.

Another interesting phenomenon is that the inertia of 50μm diameter droplets is so strong, that the particles not only fail to follow the streamline, but also pass the centerline.

The results above agree well with what Gerber et al. (1999) found. Gerber et al. (1999) used a different sampling tube, which is purely a cylinder with polished edges. They found that the FSSP-100 overestimates LWC for large droplets because these droplets are unable to follow the curved streamlines of the flow generated by drawing air into the FSSP-100's sensitive volume at 25 m/s. This inertial effect causes droplets to accumulate near the active volume of the instrument's laser beam and to produce large LWC values for the largest droplets.

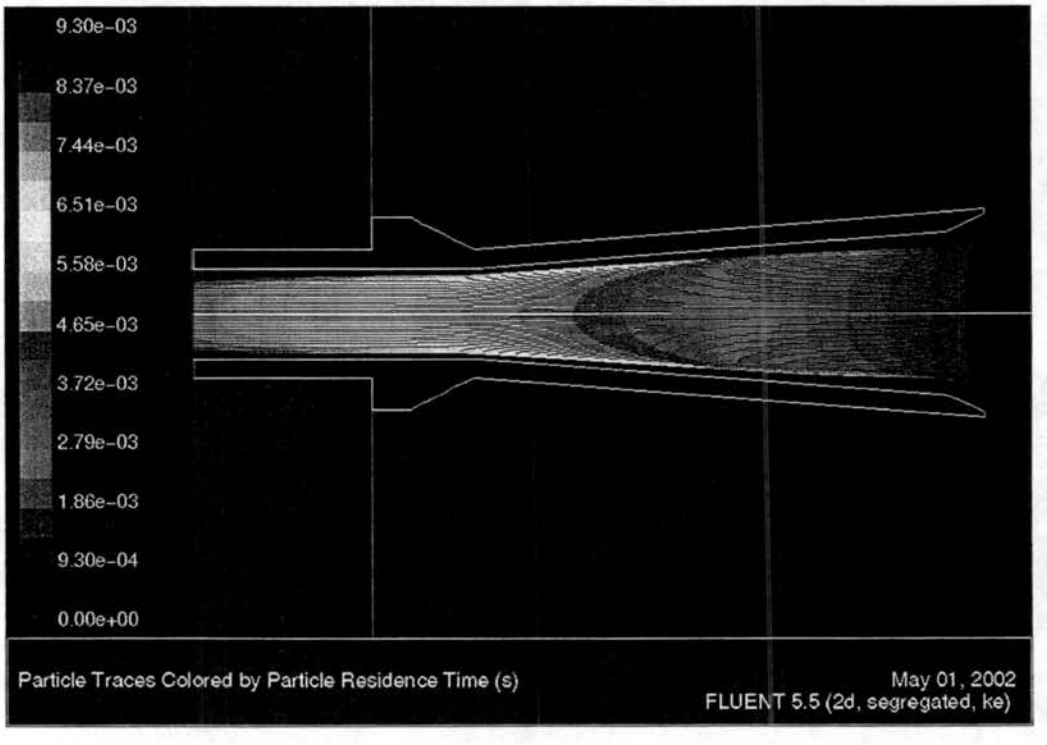

Figure B-7. Particle tracks of 5um diameter particles in sampling tube.

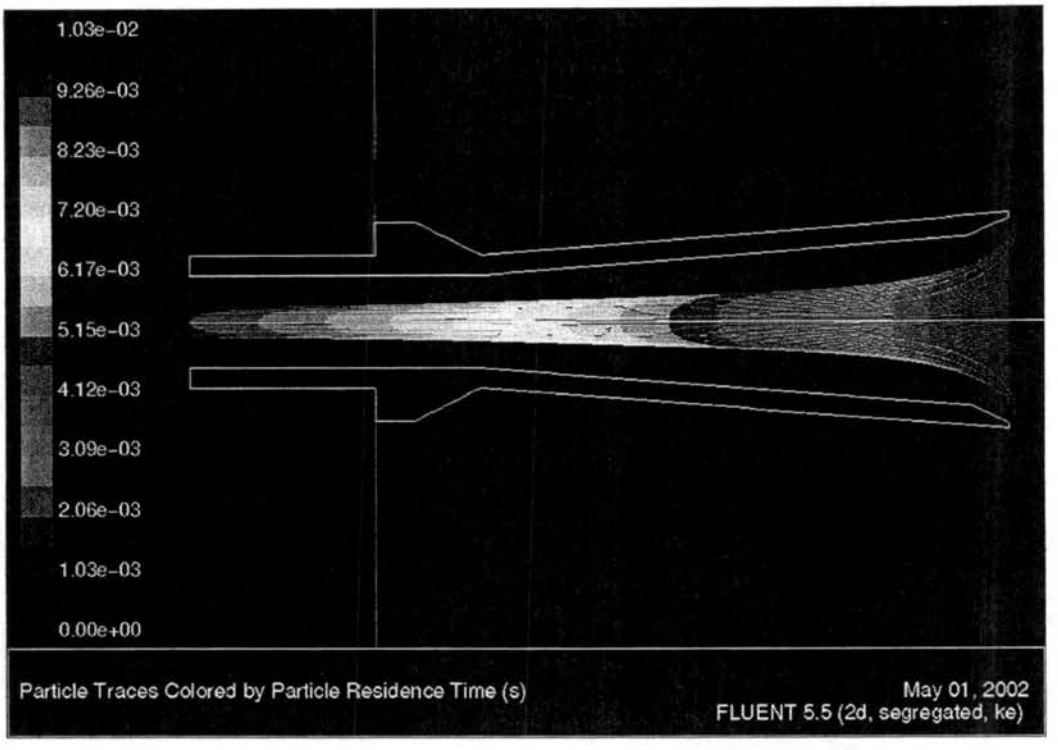

Figure B-8. Particle tracks of 25um diameter particles in sampling tube.

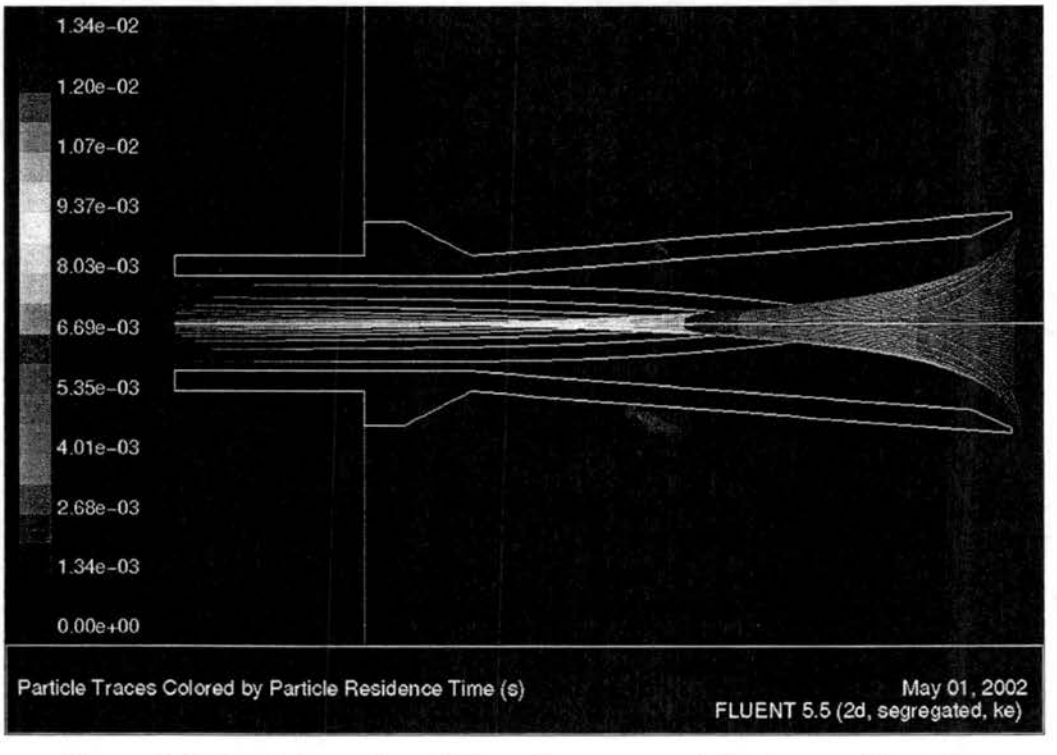

Figure B-9. Particle tracks of 50um diameter particles in sampling tube.

B.4 Conclusion

We conclude that the large observed differences in ground-based LWC measurements made with the CSASP and the PVM may partially result from the CSASP behaving as an inertial droplet concentrator that accelerates the flow and measured LWC values much larger than ambient values. This source of CSASP error, apparently overlooked until now, is predicted to be small for droplet sizes less than about 5 μm radius, but thereafter increases rapidly with increasing droplet size. Thus the suggestion that the PVM underestimates LWC when droplets are large may be mitigated because another possible reason for the difference is the overestimate of LWC by the CSASP due to this inertial effect. This conclusion is supported by the present modeling effort that shows that the ground-based use of the CSASP, where a flow-accelerator tube is used, is vulnerable to droplet inertial effects.

Appendix C

CSASP data treatment procedures

C.1 Output file structure

The detail about the output file structure can be found in SPP-100 manual. What we need are:

1. Particle diameters for cells 1 through 20: 18th line
2. Particle peak counts in cells 1 through 20: 19th line, from 3rd to 23rd data
3. Interval: 19th line, 2nd data
4. Beam diameter: 15th Line, 2nd data from right
5. Depth of field: 7th Line, 1st data from right
6. Reject average transit counts: 20th line, 2nd data
7. Lost particles; 20th line, 4th data
8. Air speed; 20th line, 6th data

Beam diameter, depth of field, reject average transit counts, lost particles and air velocity are used to calculate the sampling volumes, so that we can get number distributions as well as mass distributions.

C.2 How to extract data from output data file

The code use to extract data was attached. First, extract interval and particle peak

counts. Second, delete those illogical data using Microsoft excel (some data are extremely high probably due to electrical turbulence). Third, average them to 5-minute interval. Fourth, extract beam diameter, depth of field, reject average transit counts, lost particles and air speed to calculate the sample volumes.

C.3 Data treatment

1. Average data to 5 minute interval

   Since the data was recorded every second, which was a very huge data set and not very useful. So the data was shrunken to 5-minute interval. This process was done by two small C codes. The first code is to extracted data from original output files, and the other one is to average the data.

2. Calculate sampling volumes

   Beam diameter, depth of field, reject average transit counts, lost particles and air speed are used to calculate the sampling volume, so that we can get number distributions as well as mass distributions.

3. Get number distribution and mass distribution.

   Assuming the droplets are spherical and the density of water is a constant, from counts on each bin, we can get number concentration for each bin. The unit of number concentration is cm^{-3}. the equation is:

$$C_{in} = \frac{Counts}{volume} \quad . \tag{C-1}$$

   Each bin represents a certain diameter region. Center diameter (or 50% cut diameter)

was used to calculate mass concentration for each bin. The unit of mass concentration is g m^{-3}. The equation is:

$$C_{im} = \frac{1}{6} \times 10^{-6} \times \pi \times D^3 \times C_{in} \times \rho_{water} \qquad \text{(C-2)}$$

where C_{im} is mass concentration for each bin (g m^{-3}), D is diameter for each bin (μm), C_{in} is number concentration for the i^{th} bin, P_{water} is density of water (g m^{-3}).

4. Calculate LWC

   There are 20 bins whose diameters are from 0 to 47 μm. All the mass concentration of these 20 bins were added up to be the LWC at that time:

$$LWC = \sum_{i=1}^{20bins} C_{im} \qquad \text{(C-3)}$$

5. Plot these distributions for each sampling hour (so each plot should have 12 curves).
6. Calculate average diameter and mass weighted diameter, and effective diameter.

C.4 Computer code (C language)

1. Retrieve data

```
#include "stdio.h"
#include "math.h"
#include "io.h"
int main(int argc, char* argv[])
{ FILE *in,*out;
 in = fopen( "c:/AG352.dat", "rb" );    //change to corresponding file name
```

```
 out = fopen( "c:/352.dat", "wb" );      //change to corresponding file name
 char read_ch;
 long int lines=0;
 do
 {fscanf( in, "%c", &read_ch);
 if (read_ch=='\n')
   {lines++;}
if (lines>=18)                  // because 1 to 17 lines are some remark, just ignore them
{if (fmod(lines,3)==0)          // because particle peak counts recorded every three lines
 { fprintf(out, "%c",read_ch); }
 }
 }
 while (!feof(in));
fclose(in);
fclose(out);
}
```

2. Average data to 5-minute interval

```
#include "stdio.h"
#include "math.h"
#include "io.h"
int main(int argc, char* argv[])
{ FILE *in,*out;
 in = fopen( "c:/352.dat", "rb" );              //change to corresponding file name
 out = fopen( "c:/352x.dat", "wb" );        //change to corresponding file name
 int number[20][300];
```

```
float interval;
char time[]="00:00:00.00";
char waste[]="sp";
long int sum=0;
int i,j;
float sumtime;
do
  {interval=0.00;
   sumtime=0.00;
   sum=0;
   for (j=0;j<300;j++)                          //read file
       {fscanf(in,"%s",waste);
        fscanf(in,"%s",time);
        fscanf(in,"%f",&interval);
sumtime+=interval;              //get sample time (should be about 300 seconds)
        if (j==0)
       { fprintf(out, "%s ",time); }
        for (i=0;i<20;i++)
     {number[i][j]=0;
      fscanf(in,"%d",&number[i][j]);}
  }
   fprintf(out,"%3.2f ",sumtime);
   for (i=0;i<20;i++)                           //average process
       { sum=0;
       for (j=0;j<300;j++)
   { sum+=number[i][j];}
         sum=sum/sumtime;
```

```
            fprintf(out,"%d ",sum);
          }
    fprintf(out,"\n");
    }
  while (!feof(in));
fclose(in);
fclose(out);
}
```

3. Retrieve 20th line date (used to calculate sample volume)

```
#include "stdio.h"
#include "math.h"
#include "io.h"
int main(int argc, char* argv[])
{ FILE *in,*out;
 in = fopen( "c:/AG352.dat", "rb" );
 out = fopen( "c:/352.dat", "wb" );
 char read_ch;
 long int lines=0;
 do
 {   fscanf( in, "%c", &read_ch);
  if (read_ch=='\n')
  {   lines++;}
  if (lines>=19)
  {if (fmod(lines-1,3)==0)
        {fprintf(out, "%c",read_ch);
```

```
        }
      }
    }
  while (!feof(in));
  fclose(in);
  fclose(out);
  }
```

4. average the sample volume to 5-minute interval

```
  #include "stdio.h"
  #include "math.h"
  #include "io.h"
  int main(int argc, char* argv[])
  { FILE *in,*out;
   in = fopen( "c:/352SV.dat", "rb" );
   out = fopen( "c:/352x.dat", "wb" );
   float number[7][300];
   float sum=0;
   int i,j;
   do
     { sum=0;
       for (j=0;j<300;j++)
           { for (i=0;i<7;i++)
       {number[i][j]=0;
        fscanf(in,"%f",&number[i][j]);
//      fprintf(out,"%3.0f ",number[i][j]);
     }
```

```
//     fprintf(out, "\n");
          }
     for (i=1;i<7;i=i+2)
          { sum=0;
            for (j=0;j<300;j++)
     {sum+=number[i][j];
     }
            sum=sum/300;
            fprintf(out,"%10.1f ",sum);
          }
     fprintf(out,"\n");
   }
   while (!feof(in));
fclose(in);
fclose(out);
}
```

Appendix D

Discussion and correction of drop size distribution data at Angiola

At Angiola main site during the winter of 2000 and spring of 2001, cloud drop size distribution data was obtained by using CSASP. However, due to the principle deficiencies of CASAP as well as the sampling conditions, some corrections might need to be applied to the drop size distribution data. The following corrections are some uncertainties and corrections that often seen in fog measurement by CSASP or FSSP. Some corrections were applied to the CSASP data.

1. *Particle Shape.* We take spherical shape water droplets as granted, thus some irregularly-shaped drops may not be counted properly. There is no correction for this effect as this is one of the basic assumptions applied to corresponding calculations.

2. *Gravitational losses* can be ignored since there is only 3% loss for 30 μm diameter drops in the inlet of CSASP, which is only 15 cm long, plus, the sampling velocity is 20 m/s.

   Particle undercounting due to dead-time. New electrical parts of CSASP were installed by DMT Inc. They also installed new control software. In the manual and output files, these particles are called lost particles, which are rejected when the First-in-first-out memory (FIFO) did not get cleared quickly enough in very high concentrations. These values were used to correct the calculated concentrations:

$$CF = \frac{N(n_t + n_l)}{n_t} \quad \text{..... (D-1)}$$

where N is number concentration, n_t is total number of measured particles. n_l is lost particles in the output file. This correction were applied to the data set.

3. *Coincidence errors.* If two or more drops are close to each other while passing through the spectrometer probes, they might be counted as one particle by mistake. This effect can significantly distort drop size distribution when N_{drops}>500 cm^{-3}, but not important if N_{drops}<100 cm^{-3}. In our cases, the total number concentration rarely exceeded 500 cm^{-3}. For example, on 12/17/00, there are only 15 data points out of 181 (22:00pm to 12:55pm next day, 5 min interval) whose total number concentrations are slightly higher than 500 cm^{-3}. This error was corrected together with dead-time problem above. In CSASP manual, the equation to correct this error is:

$$N = \frac{N'}{1 - 0.0065 \bullet A} \quad \text{..... (D-2)}$$

where N is actual number concentration per unit time for any bin in a given range, N' is observed number concentration, A is the activity in percent for a given range, which is the percentage of time during which the instrument is busy analyzing particles.

From this equation, we can see coincidence error has relationship with dead time since A is also the percentage of dead time to total time, because the busier the instrument, the easier coincidence errors occur. If there is no dead time or the particle number concentration is low, A could be zero, and N=N'. The values of lost particles are always zero in our data since our instrument can handle it under the sampling conditions.

Note: Equation (D-2) is for the old electrical parts, Equation (D-1) is for the new ones. It is important to use right equation since 0.0065 is an empirical value for old electrical parts.

4. *Laser inhomogeneities*. DMT also installed a new laser source. In general, the magnitude of the reference voltage should be greater than 6V and it should vary with time less than 0.5V. The Laser Reference Voltage is +9.7V. From the output files on 12/17/00 (fog event was from 12/17/00 22:00 to 12/18/00 12;00), for the first 12 minutes, the voltage gradually increased from 9.00 to 9.30, showing the voltage is not stable during sampling period. Taking 0.5V as maximum change, 0.5/9.7=5%, it means laser power can have maximum 5% variation.

5. *Velocity Acceptance Ratio(VAR).* Not all the particles will be counted. They have to take at least an "average" time to pass through the system to be counted. If some particles pass through the edge of the sensing annulus, they might be counted to a wrong size bin because the signal is not accurate. This correction is NOT a drop size-dependent correction. For our new software, they apply this correction by modify the sampling volume. The equation is:

Sampling Volume (SV)=DOF*Beam diameter*(GS/TS)*Air Speed*Sample time. (D-3)

where *DOF* is Depth of Field, *GS* is Gated strobes, velocity accepted particles, *TS* is Total strobes, total particles regardless of whether they are velocity accepted or not.

In output file, Beam diameter, depth of field, reject average transit counts (TS-GS), lost particles and air speed are used to calculate the real sampling volume.

6. *Wind ramming*. The volumetric sampling rate can change if sampling is not in

still air. Two empirical correction equation has been used. The first equation is:

$$V_i' = V_i \times \frac{C}{f_i} \quad \text{..... (D-4)}$$

where V_i' is actual sample volume, V_i is manufacture's quoted sample volume, C is an empirical constant for specified FSSP, f_i is frequency factor generated from particle transit times. The second equation is:

$$\text{Windramming} \propto (1+\frac{U_a}{U_b}) \quad \text{..... (D-5)}$$

where U_a is the component of the ambient wind down the FSSP throat, U_b is the fan induced velocity in the FSSP's sensing volume.

These two equations are both empirical. For equation (D-4), it needs an empirical constant that is instrument dependent. For equation (D-5), this correction depends on the ambient wind speed. In our case, the ambient wind speed is low (less than 2 m/s during the most of the sample time), so this correction is not necessary.

7. *Saturation errors.* If N_{drop} is very high, for example, 1000~2500 per cubic centimeter, saturation errors are serious. Our drop number distribution is low, so this errors can be ignored.

8. *Measured size distribution "spread".* FSSP might over-size small particles (D_p<14 μm) and under-size large particles. FSSP might spread large particles over 4 bins. These effects can spread the spectrum and result in wrong LWC calculation.

Appendix E

Timelines of temperature and wind speed for CRPAQS

Besides Figure 3-1 to 3-5 in chapter 3, which shows effective diameter and LWC profiles for fog events, Figure E-1 to E-5 show temperature and wind speed timelines for fog events. We can see that the temperatures are stable during the fog events, with only several degree changes. Wind speeds were less than 2m/s except fog event on 01/21/01, but was still less than 3m/s. this atmosphere conditions favors the radiation fog formation.

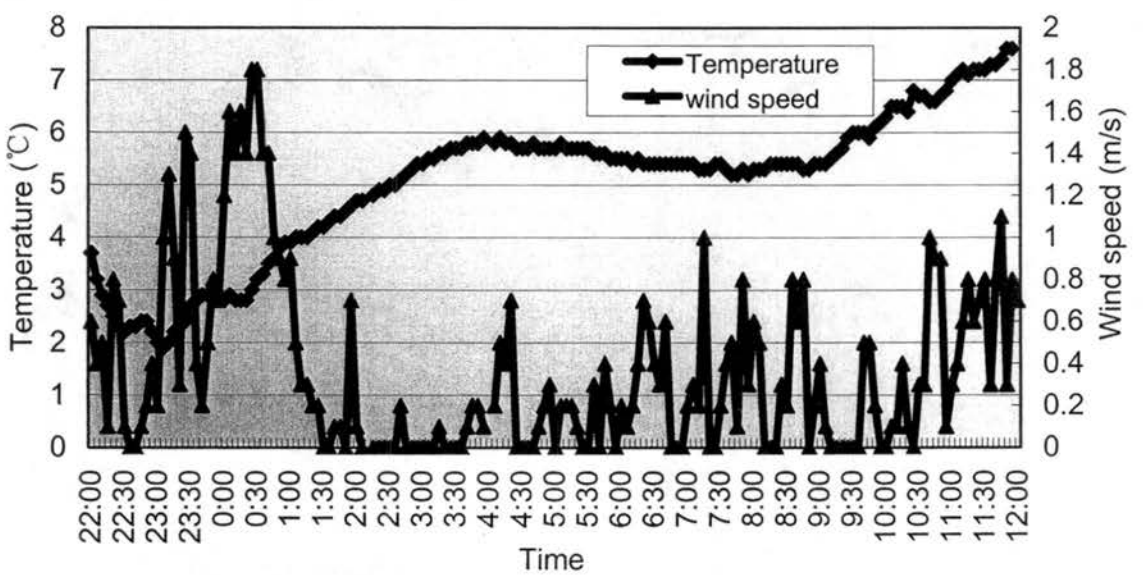

Figure E-1. Temperature and wind speed on 12/18/00.

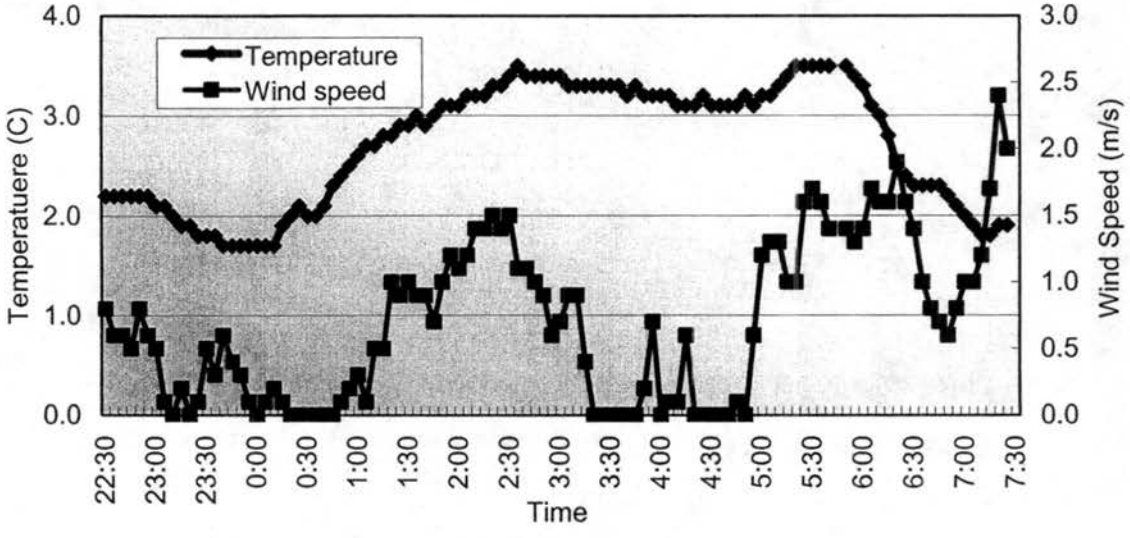

Figure E-2. Temperatureand wind speed on 12/18 & 12/19/00.

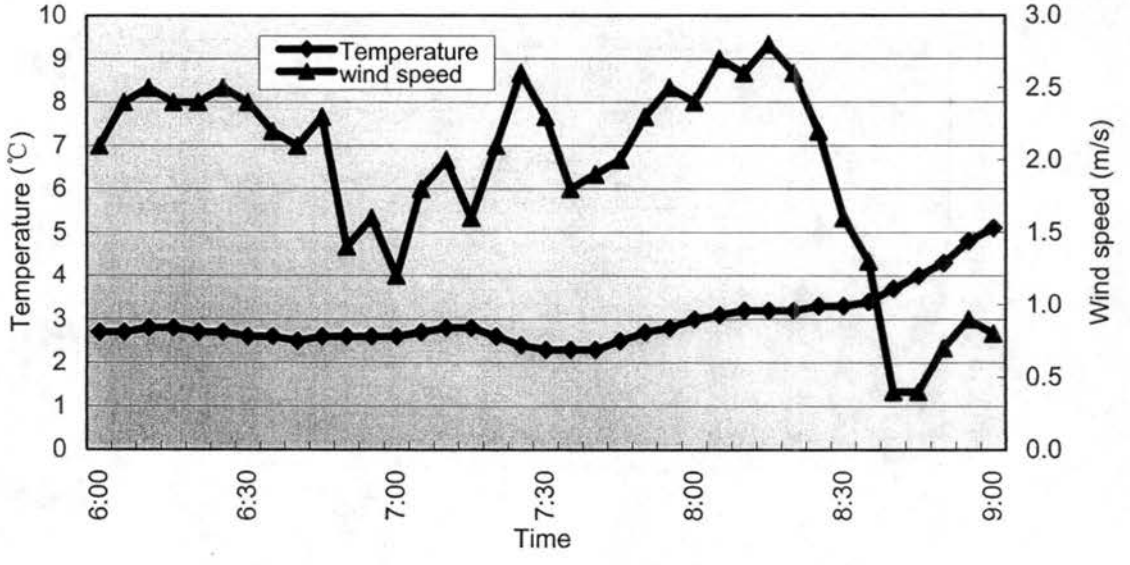

Figure E-3. Temperature and wind speed on 01/21/00.

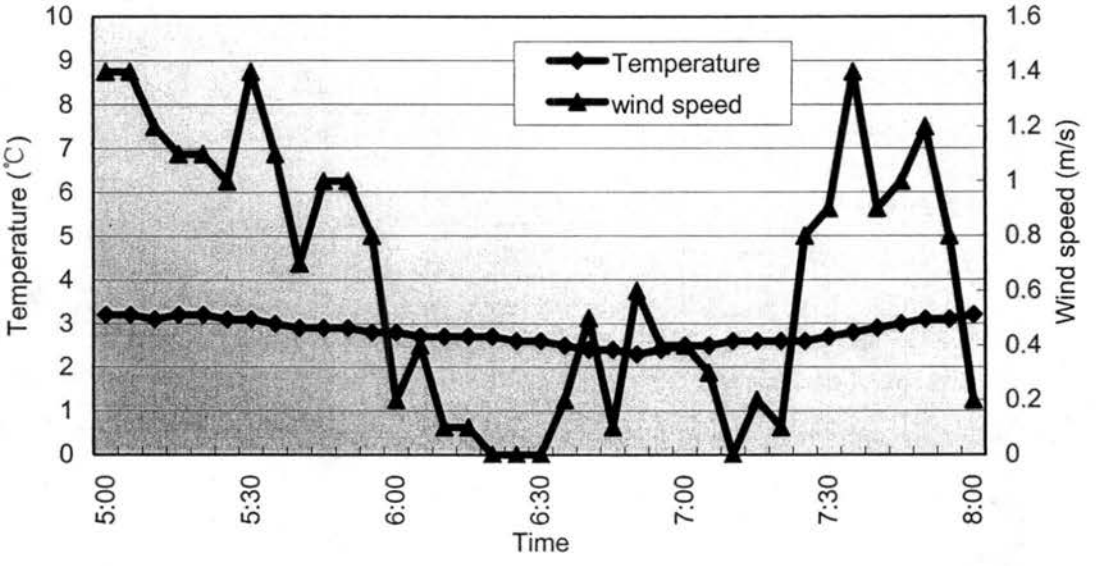

Figure E-4. Temperature, LWC and wind speed on 01/25/00.

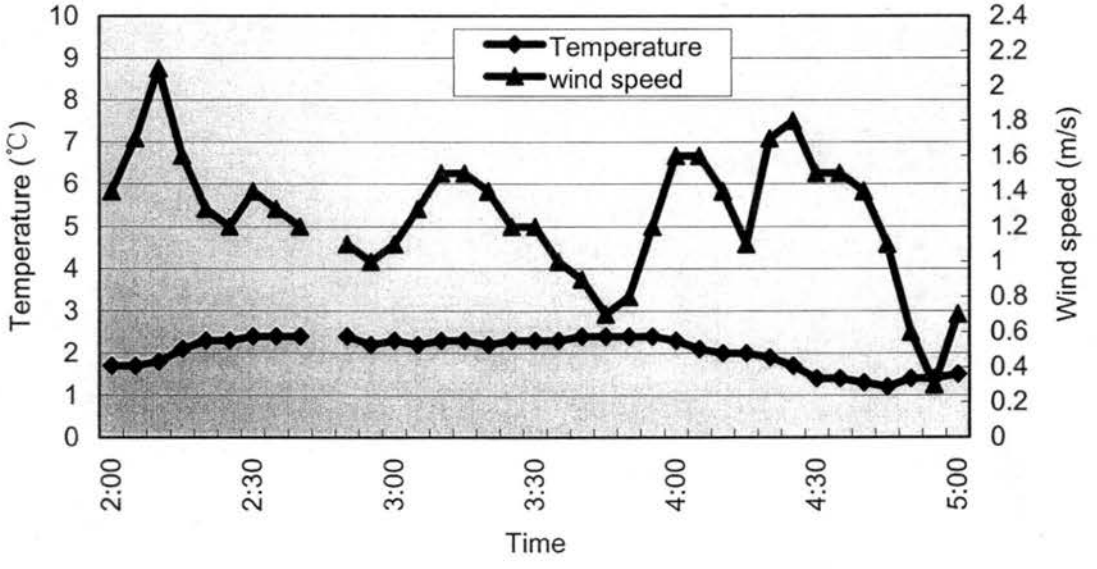

Figure E-5. Temperature and wind speed on 02/01/00.

Appendix F

Aqueous chemistry model code

This is the aqueous chemistry model code used in chapter 4. Here, only the major program and important sub routines are listed. The integration subroutines are not included due to length.

```
c program AQCHEM.FOR:
c                       Sonia Kreidenweis and John Hobson, October 1991
c  modified:
c        Sonia Kreidenweis, 29 Sept 1995, as follows:
c        this version had been worked on by Wendy Richardson
c        to work with VODE rather than EDRIV.
c        some aqinp input was changed
c        also 'nt' not allowed on HP for output
c
c SK and Jill Reilly, June 00:
c        add Q for S(IV), O3 and H2O2
c        add HMS reactions
c
c SK and Hui Chang, Apr 04:
c        used new equation to calculate k_mt, the mass transfer coefficient.
c        numcase needs to be manually input now.
c        input filename is "inputc"
c
c  References:
c    Pandis and Seinfeld, JGR 94(D1), 1105-1126, 1989.
c    Chameides, JGR 89(D3), 4739-4755, 1984.
c    Lelieveld and Crutzen, J. Atm. Chem. 12, 229-267, 1991.
c
c         Computes both rate of transfer of species between aqueous
c          and gas phases, and rate of reaction in aqueous
c          Gas-phase sources may be specified by user
c
        include 'dropcl'
      external diffun,jac
c
c First read text from input file that gives nature of problem, and
c specifies species and their numbering.
c Next, read initial values for all species.
c
c  UNITS: gas-phase species are to be given in mol/L gas
```

```
c         aqueous-phase species are to be given in mol/L water
c         unit conventions follow Pandis and Seinfeld
c Read in external conditions: temperature in K, liquid water content
c (L water/L air), droplet radius (cm), mean free path (cm),
c diffusivity (cm2/s), gas constant (L atm/mol K).
c
c Read in information for ODE solver, including number of ODEs to solve
(NEQNS0)

      parameter (lrw = 22 + 9*neqn + 2*neqn**2)
        parameter(liw = 30 + neqn)
      dimension rwork(lrw), iwork(liw)

c SK and JR: Add rsrc dimension for output

      dimension rsrc(14)
      character*132 filename

c        call dropfile(0)

c        call ioscale
        nt = 5
c        call msglink(nt,1)
        open(20,file='aqout1',status='unknown')
        open(21,file='aqout2',status='unknown')
c Sk and JR: new files for derivatives and Q
        open(23,file='rates',status='unknown')
        open(24,file='Qvalues',status='unknown')
c new file for summary information at end time of each case
        open(28,file='summary',status='unknown')
c new file with names of input files to be read
        open(27,file='filenames',status='unknown')
c new file to write Kmt of two equations
      open(88, file='Kmt',status='unknown')

c header for summary file

        write(28,335)
  335    format(1x,"input file",2x,"rad", 7x,"temp",6x,
     1      "LWC",7x,"pH",7x,
     1      "SO2",7x,"O3",7x,"H2O2",7x,"S(IV)",7x,"HCHO",5x,
     1      "S(VI)",4x,"PF,S(IV)",3x,"PF,O3",3x,"PF,H2O2",5x,
     1      "Q_O3",5x,"Q_H2O2",5x,"Q_SIV",4x,
     1      "r_O3ox",4x,"r_H2O2ox",3x,
     1      "r_HMS", 4x, "r_totS(IV)")


c please manually input how many cases will be run

      numcase=

c now read which file is to be read (contains multiple cases)

c     filename=inputc
        open(10,file='inputc',status='unknown')

c an outer loop opens each new input line and starts a new case
```

```
c (now they are all in the same file)

      do 777 icases=1,numcase
c
c each case is called 'sample' so add that to dropcl and print out
c in output
c
c zero all species concentrations in case they are not set in input
c file
c
        do 444 k =1,14
      ya(k) = 0.
 444  continue

c        call rdinput(ya)
        call rdinput2(ya)

      neqns = neqn
      rtolc = rtol
      atolc = atol
c
c
c Call subroutine that contains accommodation coefficients to be used
c (user supplies this subroutine)
c
        call accoeff
        write(20,'(1x,"etas",14(1pe10.3))') (eta(i),i=1,neqn)
c
c Call subroutine that computes the mass-transfer coefficients
c
        call xkmcoef
        write(20,'(1x,"kmt",14(1pe10.3))') (xkmt(i),i=1,neqn)
c
c Call subroutine to calculate the equilibrium constants, ek(nspec)
c
        call eqcon
        write(20,'(1x,"ek",13(1pe10.3))') (ek(i),i=1,neql)
c
c pH is now an input variable and will remain fixed.
c
        h=10.**(-1.*pH)

        call henry(h)
        call partfcn(ya)
c

c Print out all initial information: copy all input files to
c  the output file. Also write out initial conc and initial pH as
c  t=0 values in time-history part of output file.
      write(20,'(3x,"time",7x,"y1",8x,"y2",8x,"y3",8x,"y4",8x,"y5",
     1           8x,"y6",8x,"y7",8x,"y8",8x,"y9",7x,"y10",7x,"y11",
     1           8x,"y12",8x,"y13",8x,"y14",
     1          6x,"pH")')
c       ph = -dlog10(h)
       write(20,'(16(1pe10.3))') xo,(ya(i),i=1,neqn),ph
       write(21,'(3x,"time",7x,"ph",8x,"h1",8x,"h2",8x,"h3",8x,"h4",
     1           8x,"h5",8x,"h6",8x,"p1",8x,"p2",8x,"p3",8x,"p4",8x,
```

```
     1              "p5",8x,"p6")')
      write(21,'(14(1pe10.3))') xo,ph,(heff(i),i=1,6),(pf(i),i=1,6)

c SK and JR: new file for rates

      write(23,'("rates of change")')
      write(23,'(5x,"time",8x,"ph",9x,"S[IV]",9x,"O3",9x,"H2O2",
     1 9x,"r1",9x,"r2",9x,"r3",9x,"S[VI]",9x,"HMS")')

      write(24,'("Q values")')
      write(24,'(5x,"xend",7x,"pH",10x,"xkO3",5x,"qO3",7x,"bigQO3",
     1       5x,"xkH2O2",5x,"qH2O2",5x,"bigQH2O2",5x,"xkSIV",5x,
     1       "qSIV",5x,"bigQSIV")')

c
c Call the ODE solver, updating timestep:
c

        xend=xo+xstp
        do 1000 j=1,iter
c      do 1000 j=1,5
c     print *, ' '
c     print *, 'iter',j
c
c Update a stored initial guess for [H+] that goes into common block
c (keep this line, but now pH is fixed so hconc should be constant too)
c
        hconc=h
c
c
c     rtol = 1.0d-5
      itol = 1
c     atol = 1.0d-20
      itask = 1
      istate = 1
      iopt = 0
c
c
c call to vode:  (  F   , neq , y , T , tout, itol, rtol, atol,..)
      call vode(diffun, neqn, ya, xo, xend, itol, rtolc, atolc,
     1    itask, istate, iopt, rwork, lrw, iwork, liw, jac, mf,
     2   rpar, ipar)
c
c
c     print *, 'line 112, post vode'
c       write(*,'("step= ",i3," last h used= ",e12.5)') j,ho
        if(istate.lt.0)then
        write(20,2)istate
        write(*,2)istate
 2      format(//,' istate=', i6,16h problem stopped,//)
        stop
        endif
c
c upon return, print out all species concentration information
c
      write(20,'(16(1pe10.3))') xend,(ya(i),i=1,neqn),ph
c
```

```
c compute the partition function for gaseous species (PF=1 indicates
c that it is in equilibrium with the aqueous phase according to Henry's
c Law)
c
        call henry(h)
        call partfcn(ya)
c
c SK and JR: write out the derivatives for all species here
c call diffun to compute them at current conditions
c
c Compute current values of chemical source rates
c SK and JR: rsrc will now be modified by Q!
c the values of Q and r1,r2,r3 are now in the common block
c so that we can output right after the call to rsource
c
        rt=gasc*temp
        call rsource(ya,rsrc,h,xend)

      do 20 i=7,12
       yderiv(i)=xkmt(i)*(ya(i-6)-(ya(i)/(heff(i-6)*rt)))
     1   + (rsrc(i))
 20     continue

        yderiv(13)=rsrc(13)
        yderiv(14)=rsrc(14)
c
c Sk and JR: write out the derivatives for all species
c
         write(23,'(10(1pe12.3))') xend,pH,(yderiv(i),i=7,9),
     1     r1, r2, r3, yderiv(13), yderiv(14)
c
c SK and JR: write out q and Q to files
c
         write(24,'(11(1pe11.3))') xend,pH,xkO3,qO3,bigQO3,
     1       xkH2O2,qH2O2,bigQH2O2,xkSIV,qSIV,bigQSIV
c
c following was for debug (uncomment if needed)
c         write(26,'(3(1pe11.3))') xk5, xk6, hcho
c
c write out values of the partition function
      write(21,'(14(1pe10.3))') xend,ph,(heff(i),i=1,6),(pf(i),i=1,6)
c write out times to flag the pHcalc debug file
c      write(22,'(14(1pe10.3))') xend,ph,(heff(i),i=1,6),(pf(i),i=1,6)
c
c Update timestep and continue
c
 1000   xend=xend+xstp

c done with this case; write output and then return to next case

      print *, 'done with this case - used file: ', sample

        write(28,334) sample,rad*1.e4,temp,wl,pH,ya(1),ya(2),
     1     ya(3),ya(7),
     1     ya(12),ya(13),pf(1),pf(2),pf(3),bigQO3,bigQH2O2,bigQSIV,
     1     r1,r2,r4,r3
c  334    format(a12,1pe10.3,f6.2,1x,1pe10.3,1x,1pe10.3,1x,13(1pe10.3))
```

```
  334     format(a18,f6.2,1x,f6.2,1x,2(1pe10.3),1x,16(1pe10.3))

  777   continue

        stop
        end
c
c
SSSSSSSSSSSSSSSSSSSSSSSSSSSSSSSSSSSSSSSSSSSSSSSSSSSSSSSSSSSSSSSSSSSSSSS
c
        subroutine accoeff
        include 'dropcl'
      dimension aw(14)
c
c subroutine specifies accomodation coefficients to be used and
computes
c transition formula, eta, for each species.
c in this run, default accommodation coefficients are set equal to 0.05
c ---------------------------------------------------------------------
-
c **NOTE: to change accommodation coefficient, go into this subroutine,
c change value of ÒawÓ and recompile code. Mean free path and radius
are
c input in ÒaqinpÓ file.
c ---------------------------------------------------------------------
-
c
        xkn=xmfp/rad
        xkni=1./xkn
      t1=(1.33+(0.71*xkni))/(1.+xkni)

        awd=0.05
        t2=4*(1.-awd)/(3.*awd)
        t3=(t1+t2)*xkn
        eta(1)=1./(1.+t3)
        do 100 i=2,14
        eta(i)=eta(1)
100     continue

c enter values for sticking coeffs

        aw(1)=0.035
        aw(2)=5.4e-4
        aw(3)=0.18
        aw(4)=0.06
        aw(5)=0.2
        aw(6)=0.05

        do 200 i=1,6
        t2=4*(1.-aw(i))/(3.*aw(i))
        t3=(t1+t2)*xkn
        eta(i)=1./(1.+t3)
200     continue

c symmetry for aqueous phase

      do 300 j=7,12
```

```
        eta(j)=eta(j-6)
300     continue

        return
        end
c
c
SSSSSSSSSSSSSSSSSSSSSSSSSSSSSSSSSSSSSSSSSSSSSSSSSSSSSSSSSSSSSSSSSSSSSSSSSSS
c
        subroutine xkmcoef
        include 'dropcl'
        dimension aw2(14)
        dimension vi(14)
        dimension xkmtn(14)
c compute mass-transfer coefficients. In this problem, all are equal.
c
        aw2(1)=0.035
        aw2(2)=5.4e-4
        aw2(3)=0.18
        aw2(4)=0.06
        aw2(5)=0.2
        aw2(6)=0.05

        do 50 i=7,12
        aw2(i)=aw2(i-6)
 50     continue
        aw2(13)=0.05
        aw2(14)=0.05


        vi(1)=100*sqrt(8*8.314*temp/3.1415926/.064)
        vi(2)=100*sqrt(8*8.314*temp/3.1415926/.048)
        vi(3)=100*sqrt(8*8.314*temp/3.1415926/.034)
        vi(4)=100*sqrt(8*8.314*temp/3.1415926/.017)
        vi(5)=100*sqrt(8*8.314*temp/3.1415926/.063)
        vi(6)=100*sqrt(8*8.314*temp/3.1415926/.030)
        vi(7)=100*sqrt(8*8.314*temp/3.1415926/.064)
        vi(8)=100*sqrt(8*8.314*temp/3.1415926/.048)
        vi(9)=100*sqrt(8*8.314*temp/3.1415926/.034)
        vi(10)=100*sqrt(8*8.314*temp/3.1415926/.017)
        vi(11)=100*sqrt(8*8.314*temp/3.1415926/.063)
        vi(12)=100*sqrt(8*8.314*temp/3.1415926/.030)
        vi(13)=100*sqrt(8*8.314*temp/3.1415926/.032)
        vi(14)=100*sqrt(8*8.314*temp/3.1415926/.112)


        do 100 i=1,14
        xkmtn(i)=1.0/((rad**2/3/diff)+(4*rad/3/vi(i)/aw2(i)))
c       write     (88,*) xkmt(i)
        xkmt(i)=3.*eta(i)*diff/(rad**2)
        write (88,*) xkmtn(i),xkmt(i)
100     continue
c       xkmt(10)=1.d2*xkmt(10)
        return
        end
c
```

```
c
SSSSSSSSSSSSSSSSSSSSSSSSSSSSSSSSSSSSSSSSSSSSSSSSSSSSSSSSSSSSSSSSSSSSSS
c
        subroutine eqcon
        include 'dropcl'
c
c subroutine gets equilibrium constants using temperature input.
c these values are from Pandis and Seinfeld.
c ------------------------------------------------------------------
-
c. To add equilibirum reactions, go into this subroutine and add the
c equation in the form ÒK = Ò, as shown. Remember to change to correct
c value of 'neql' to be used in code (in the file Ódropcl Ó).
c ------------------------------------------------------------------
-
c
        delt=(1./temp)-(1./298.)
        ek(1)=1.23*exp(3120.*delt)
        ek(2)=1.29e-2*exp(1960.*delt)
        ek(3)=6.4e-8*exp(1431.*delt)
        ek(4)=1000.
        ek(5)=1.02e-2*exp(2720.*delt)
        ek(6)=7.45e4*exp(6620.*delt)
        ek(7)=2.1e5
        ek(8)=15.4*exp(8700.*delt)
        ek(9)=1.13e-2*exp(2300.*delt)
        ek(10)=75.*exp(3400.*delt)
        ek(11)=1.75e-5*exp(-450.*delt)
        ek(12)=1.0e-14*exp(-6710.*delt)
c
c next one is new for HCHO Henry's Law
c
      ek(13)=2.5*exp(644.*delt)

c
        return
        end
c
c
SSSSSSSSSSSSSSSSSSSSSSSSSSSSSSSSSSSSSSSSSSSSSSSSSSSSSSSSSSSSSSSSSSSSSS
c
        subroutine partfcn(ya)
        include 'dropcl'
c
c subroutine to compute the partition function for each gas-phase
species
c ------------------------------------------------------------------
-
c This is set up to have 6 gas-phase species; if increased, need to
c come into this subroutine and add in the appropriate equations.
c Also remember to change dimension of partfn in Ódropcl Ó.
c ------------------------------------------------------------------
-
c
        do 100 j=1,6
        if(ya(j).eq.0)pf(j)=0.
 100    continue
```

```
        if(ya(1).ne.0.)pf(1)=ya(7)/(ya(1)*heff(1)*gasc*temp)
        if(ya(2).ne.0.)pf(2)=ya(8)/(ya(2)*heff(2)*gasc*temp)
        if(ya(3).ne.0.)pf(3)=ya(9)/(ya(3)*heff(3)*gasc*temp)
        if(ya(4).ne.0.)pf(4)=ya(10)/(ya(4)*heff(4)*gasc*temp)
        if(ya(5).ne.0.)pf(5)=ya(11)/(ya(5)*heff(5)*gasc*temp)
        if(ya(6).ne.0.)pf(6)=ya(12)/(ya(5)*heff(5)*gasc*temp)
c
c species 13 and 14 are S(VI) and HMS, respectively: no
c  gas-aqueous equilibria
c
        return
        end
c
c SSSSSSSSSSSSSSSSSSSSSSSSSSSSSSSSSSSSSSSSSSSSSSSSSSSSSSSSSSSSSSSSSSSSSSS
c
      subroutine rdinput2(ya)
c
c -----------------------------------------------------------------------
-
c new code to read in Excel files for Collett and Reilly data
c -----------------------------------------------------------------------
-
      include 'dropcl'
      character msg*72
      parameter (maxi=70)
      character*8 iout
      character*132 line
c
c     fixed numbers for all runs
c
      xmfp = 0.065e-4
      diff = 0.1
      gasc = 0.082058
      xo = 0.
      ho = .0001
      xstp = 10.
      iter = 120
      mf = 22
      atol = 1.e-20
      rtol = 1.e-5
c
c now read in from Excel file
c
c      read (10, *) sample,pH,rad,temp,fjunk,fjunk,
c     1   ya(1),fjunk,ya(2),fjunk,ya(3),fjunk,ya(12),
c     1   wl

      read (10,888) sample,pH,rad,temp,fjunk1,fjunk2,
     1      ya(1),fjunk3,ya(2),fjunk4,ya(3),fjunk5,ya(12),wl
      write (*,888) sample,pH,rad,temp,fjunk1,fjunk2,
     1     ya(1),fjunk3,ya(2),fjunk4,ya(3),fjunk5,ya(12),wl

 888  format(a10,1x,f4.2,1x,f6.4,1x,f6.2,1x,f7.2,1x,f4.2,1x,
     1  e8.2,1x,f4.2,1x,e8.2,1x,f7.5,1x,e8.2,1x,
     1  f5.2,1x,e8.2,1x,e8.2,1x)
      return
      end
```

```
c
c
SSSSSSSSSSSSSSSSSSSSSSSSSSSSSSSSSSSSSSSSSSSSSSSSSSSSSSSSSSSSSSSSSSSSSS
c
        subroutine diffun(neqns,t,ya,yderiv,rpar,ipar)
        include 'dropcl'
c     double precision t,yderiv,ya,rpar
      dimension rpar(*),Ipar(*)
        dimension rsrc(nspec)
c
c Compute the current value of h using the input value of pH
c
       h=10.**(-1.*pH)
c
c Use pH to compute the current values of the modified Henry's Law
coeff
c
        call henry(h)
c
c Compute current values of chemical source rates
c SK and JR: rsrc will now be modified by Q!
c
        call rsource(ya,rsrc,h,t)
c
c Species conservation equations: gas-phase
c
c ---------------------------------------------------------------------
-
c Note that 6 gas-phase species are hard-wired in here. If this is to
be
c changed, remember to carry changes into this subroutine
c Same idea for aqueous-phase species and S(VI)
c ---------------------------------------------------------------------
-
c
        rt=gasc*temp
        do 10 i=1,6
c
c following is normal conservation equation:
c
c             yderiv(i)=xkmt(i)*wl*((ya(i+6)/(heff(i)*rt))-ya(i))+rsrc(i)
c
c following is to keep gas phase concentrations constant (open system)
c 3-22-00 JR and SK: make gases constant
c
          yderiv(i)=0.
c
  10    continue
c
c change this later; for now make all reaction rates zero
c
c     rsrc(mm)=0.

 33     continue

c Species conservation equations: aqueous-phase
c
```

```
        do 20 i=7,12
c
c below is usual expression.
c
         yderiv(i)=xkmt(i)*(ya(i-6)-(ya(i)/(heff(i-6)*rt)))
     1       + (rsrc(i))
  20     continue
c
c SK and JR: species 12 is HCHO total in aqueous phase.
c for use with field data, make this constant at input
c (i.e., set derivative to zero)
c
         yderiv(12)=0.

c      write(*,21)yderiv(10), heff(5), ya(5), ya(10)
 21      format(1x,'yderiv(10) = ', 1x, e12.5, 1x, 'h=', e7.2,
     1    1x, 'y5 and 10 = ', 2e12.5)
c
c      write(*,22)yderiv(9), xkmt(1), ya(4), ya(9)
 22      format(1x,'yderiv(9) = ', 1x, e12.5, 1x, 'k=', e7.2,
     1    1x, 'y4 and 9= ', 2e12.5)
c
c species without gas-liquid equilibrium: S(VI) and HMS
c
        yderiv(13)=rsrc(13)
        yderiv(14)=rsrc(14)
c
        return
        end
c
c
SSSSSSSSSSSSSSSSSSSSSSSSSSSSSSSSSSSSSSSSSSSSSSSSSSSSSSSSSSSSSSSSSSSSSSS
c
        subroutine henry(h)
c
c Needs 13 equilibrium constants to do calculation; these are ek(i)
c
        include 'dropcl'
c
c h is the concentration of [H+]. heff is the effective Henry's Law
constant
c -----------------------------------------------------------------
-
c Right now 5 HenryÕs Law coefficients are hardwired in. Input more
c equaitons into this subroutine and change dimension in Òdropcl Ó
c -----------------------------------------------------------------
-
c
        heff(1)=ek(1)*(1+(ek(2)/h)+(ek(2)*ek(3)/(h**2)))
        heff(2)=ek(9)
        heff(3)=ek(6)
        heff(4)=ek(10)*(1+(ek(11)*h/ek(12)))
        heff(5)=ek(7)*(1+(ek(8)/h))
      heff(6)=ek(13)*(1+2530)
c
        return
        end
```

```
c
c
SSSSSSSSSSSSSSSSSSSSSSSSSSSSSSSSSSSSSSSSSSSSSSSSSSSSSSSSSSSSSSSSSSSSSS
c
      subroutine rsource(ya,rsrc,h,t)
c
c Needs to have rate constants passed to it; also, for
c computing reaction rates, needs current conc's of reactants
c
      include 'dropcl'
      dimension rsrc(14)
c ---------------------------------------------------------------------
-
c User supplies this subroutine according to reaction rates desired
c Change dimension of rsrc(i) if this is modified
c ---------------------------------------------------------------------
-
c
c Compute the source rates of each species for which conservation eqn
written
c Can be constant sources, zero sources (closed system), or chemical
reaction
c
c Species numbering:
c    1 SO2(g)            7 S(IV)(aq)
c    2 O3(g)             8 O3(aq)
c    3 H2O2(g)           9 H2O2(aq)
c    4 NH3(g)           10 N(III)(aq)
c    5 HNO3(g)          11 N(V)(aq)
c    6 HCHO(g)          12 HCHO(aq)
c                       13 S(VI)(aq)
c                       14 HMS(aq)
c
c source of S(VI) is reactions 1 and 2 in aqueous phase, due to O3 and
H2O2
c
        hso3=ya(7)/(1.+(h/ek(2))+(ek(3)/h))
        so3=ek(3)*hso3/h
        so2=ya(7)-hso3-so3
c
c HCHO is the non-gem-diol portion of total HCHO(aq)
c
        if (ya(12).gt.0.) then
      hcho=ya(12)/(1.+2530.)
      else
      hcho = 0.
      endif
c
c next are temp-dep rate constants for reactions
c
          xk1=2.4e4
     xk2=3.7e5*exp((-46000./8.3145)*(1./temp - (1./298.15)))
     xk3=1.5e9*exp((-43900./8.3145)*(1./temp - (1./298.15)))
     xk4=7.45e7*exp((-39500./8.3145)*(1./temp - (1./298.15)))
     xk5=7.9e2*exp((-4900./1.)*(1./temp - (1./298.15)))
     xk6=2.5e7*exp((-1800./1.)*(1./temp - (1./298.15)))
c
```

```
c SK and JR: include an estimate of Q for S(IV) here; need to iterate
to get
c   consistent Q's for all species
c
c first guess: Q(S(IV)) = 1.
c
         iters = 1.
         bigQSIV = 1.
         bigQO3 = 1.
         bigQH2O2 = 1.
c
c label next line: this is where we will return to for iterations on
QSIV

 21      r1=ya(8)*((xk1*so2)+(xk2*hso3)+(xk3*so3))*bigQSIV*bigQO3
         r2=xk4*h*ya(9)*hso3/(1.+(13.*h))*bigQSIV*bigQH2O2
       r4=hcho*((xk5*hso3)+(xk6*so3))*bigQSIV
c
c SK and JR: now add in the Q's for other species
c
c diffO3 is the diffusivity for ozone; should make more general

        if (ya(8).gt.0.) then

        diffO3 = 1.e-5

        xkO3 = r1/(ya(8)*bigQO3)
        qO3 = rad * (xkO3/diffO3)**0.5
          bigQO3new = 3.*(((1./tanh(qO3))/qO3)-(1./(qO3**2.)))

        r1 = r1 * bigQO3new / bigQO3
        bigQO3 = bigQO3new

         else
         r1 = 0.
         xkO3 = 0.

        endif

          if (ya(9).gt.0.) then

        diffH2O2 = 1.e-5
        xkH2O2 = r2/(bigQH2O2*ya(9))
        qH2O2 = rad * (xkH2O2/diffH2O2)**0.5
          bigQH2O2new = 3.*(((1./tanh(qH2O2))/qH2O2)-(1./(qH2O2**2.)))

        r2 = r2 * bigQH2O2new / bigQH2O2

         else
         r2 = 0.
         xkH2O2 = 0.

        endif
c
c update the QSIV here and check for convergence
c the rate of comsumption of S(IV) is due to
c ozone (r1), H2O2 (r2), and HMS production (r4)
```

```
c
          r3 = (r1 + r2 + r4)

          if (ya(7).gt.0.) then

        diffSIV = 1.e-5
        xkSIV = r3/(ya(7)*bigQSIV)
        qSIV = rad * (xkSIV/diffSIV)**0.5
          bigQSIVnew = 3.*(((1./tanh(qSIV))/qSIV)-(1./(qSIV**2.)))

        r3 = r3 * bigQSIVnew / bigQSIV
        endif
c
c test for convergence
c
        testQ = abs((bigQSIVnew/bigQSIV)-1.)
c
c SK and JR: debug the iterations
c
        write(25,10) iters, r3, bigQO3, bigQH2O2, bigQSIVnew, testQ
 10       format('iters, r3, QO3, QH2O2, QSIV, test: ', i5, 5e13.3)


         if (iters.gt.100) then
           print *,'iters > 100: stop '
           stop
           endif

        if (testQ. gt. 0.01) then
           bigQSIV = bigQSIVnew
           iters = iters+1
           go to 21
          else
           bigQSIV = bigQSIVnew
          endif

c if no reactions are to be included, use following:
c
c        r1=0.
c        r2=0.
c
c following is gas source for open system:
c Note: unit conversion needed; aqueous is mol/l water; gas is mol/l
air
c
c        rsrc(1)=(r1+r2)*wl
c        rsrc(2)=r1*wl
c        rsrc(3)=r2*wl
c
c Following is for closed system:
c JR and SK: set to zero for our fixed gas phase case too
c
          rsrc(1)=0.
          rsrc(2)=0.
          rsrc(3)=0.
c
c these do not react chemically:
```

```
          rsrc(4)=0.
          rsrc(5)=0.
          rsrc(6)=0.
c
c always use the ones below - they are the aqueous-phase rxns:
c SK and JR: for Q's use r3 for S(IV)
c
c         rsrc(7)=-r1-r2
         rsrc(7)=-r3
         rsrc(8)=-r1
         rsrc(9)=-r2
         rsrc(10)=0.
         rsrc(11)=0.
c
c         rsrc(12)=r1+r2
c
c Next: r(12) is loss of HCHO(aq)
c r(13) is production of S(VI)
c r(14) is production of HMS
c
         rsrc(12)=-r4
         rsrc(13)=r1+r2
         rsrc(14)=r4
c
         return
         end
c
```

Appendix G

The composition of DOC for individual Fresno fog samples

Twenty one fog water samples (including replicates and duplicates) collected during the Fresno fog campaign were analyzed. These samples were collected by ss-CASCC and ss-sf-CASCC.

One sample was collected on 12/31/03- 01/01/04 fog events (FSC36401). Four bulk fog water (FSC01001, 01002, 01003, 01004), four large fog drop samples (FSCL01001, 01002, 01003, 01004) and three small fog drop samples (FSCS01001, 01002, 01003, 01004) were collected in 01/10/04- 01/11/04 fog event. Three bulk fog water samples (FSC01101, 01102, 01103), three large fog droplets samples (FSCL01101, 01102, 01103) and three small fog droplets samples (FSCS01101, 01102, 01103) were collected in 01/11/04- 01/12/04 fog event.

Organic acids were still observed to be dominant contributors to fog organic carbon, but it can be seen that carbonyls and dicarbonyls cannot be ignored as important fog components. The concentrations of each carbonyls and dicarbonyls various with samples. The total amount of carbonyls and dicarbonyls various from 5% to 15% of the total DOC.

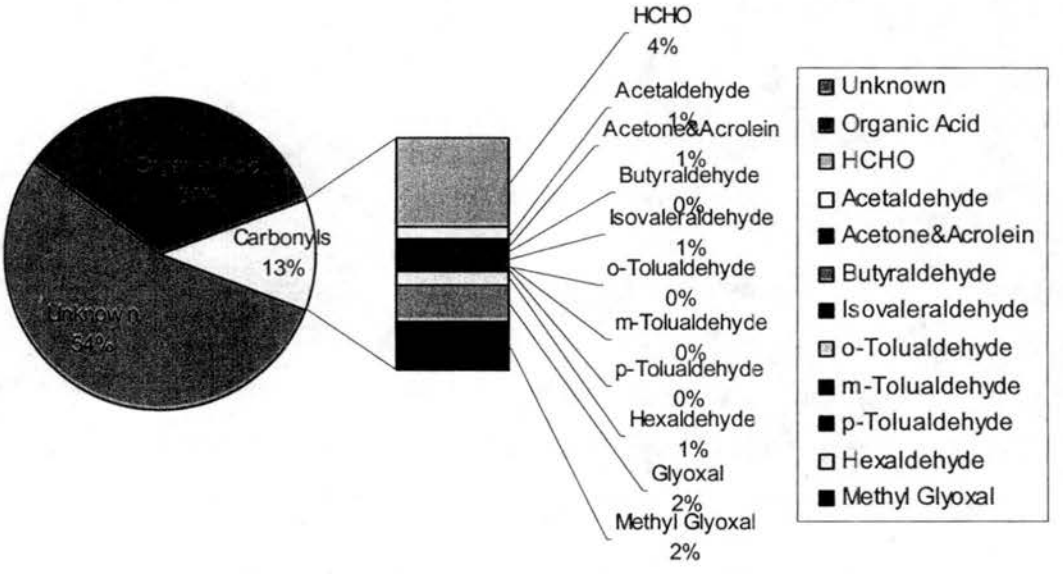

Figure G-1. Composition of carbonaceous material comprising the total dissolved organic carbon (DOC) content observed for FSC01001

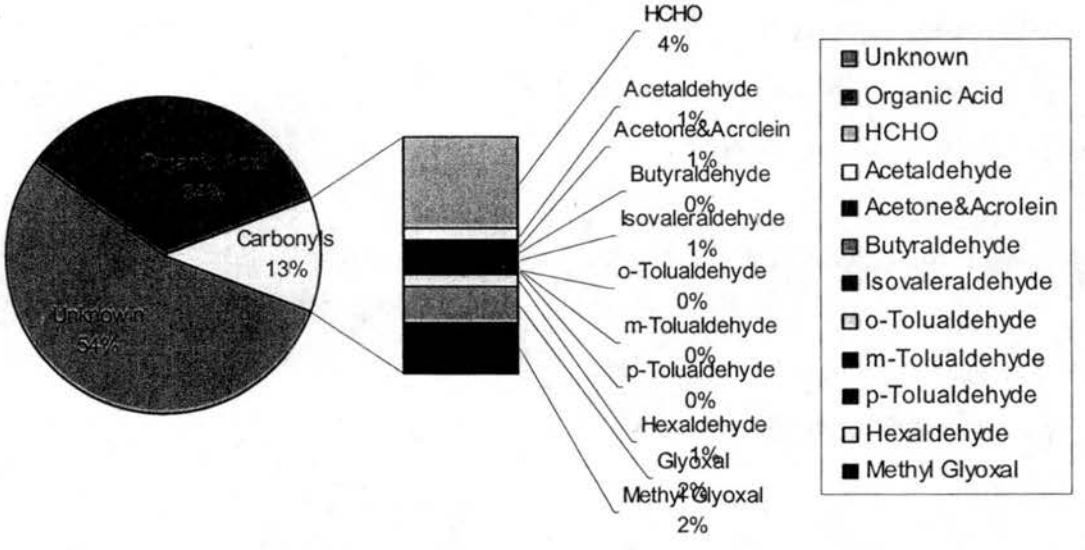

Figure G-2. Composition of carbonaceous material comprising the total dissolved organic carbon (DOC) content observed for FSC01002

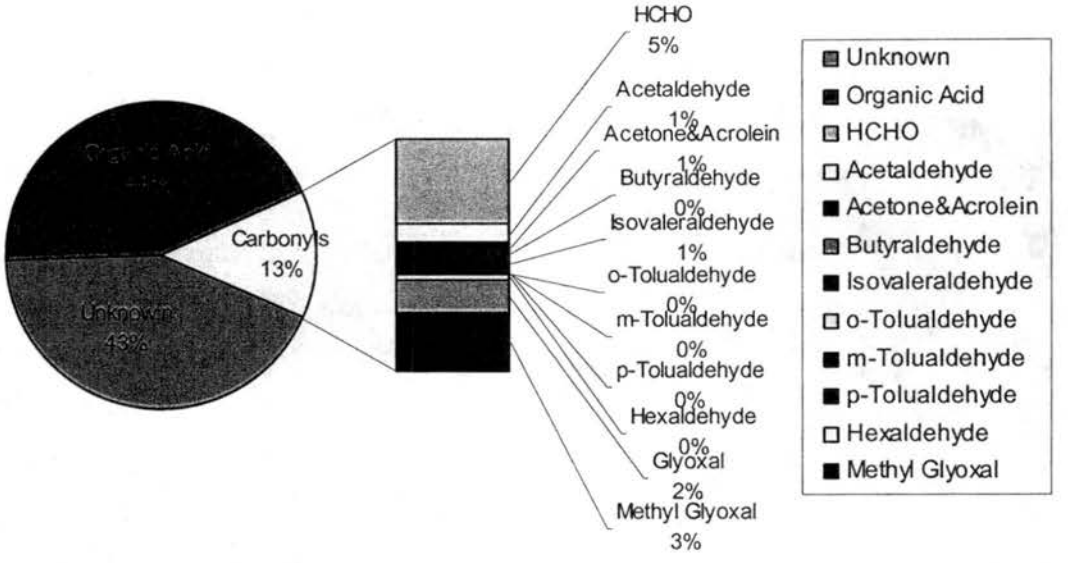

Figure G-3. Composition of carbonaceous material comprising the total dissolved organic carbon (DOC) content observed for FSC01003

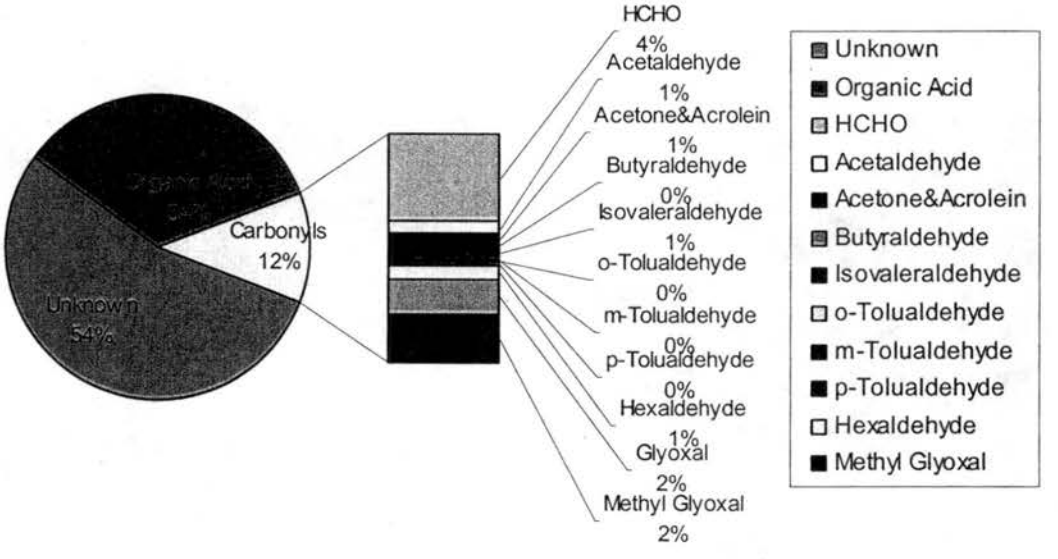

Figure G-4. Composition of carbonaceous material comprising the total dissolved organic carbon (DOC) content observed for FSC01004

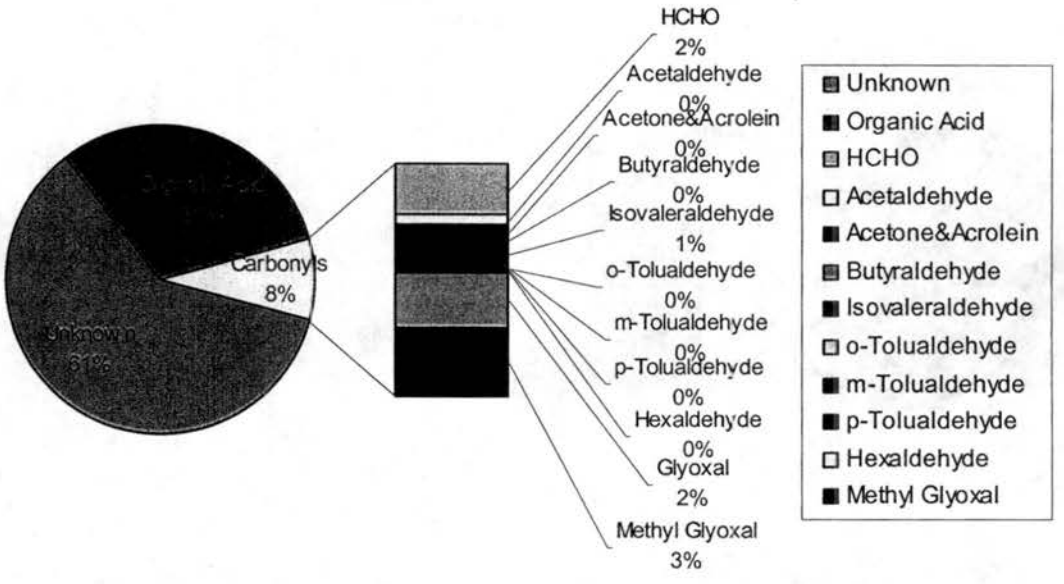

Figure G-5. Composition of carbonaceous material comprising the total dissolved organic carbon (DOC) content observed for FSC01101

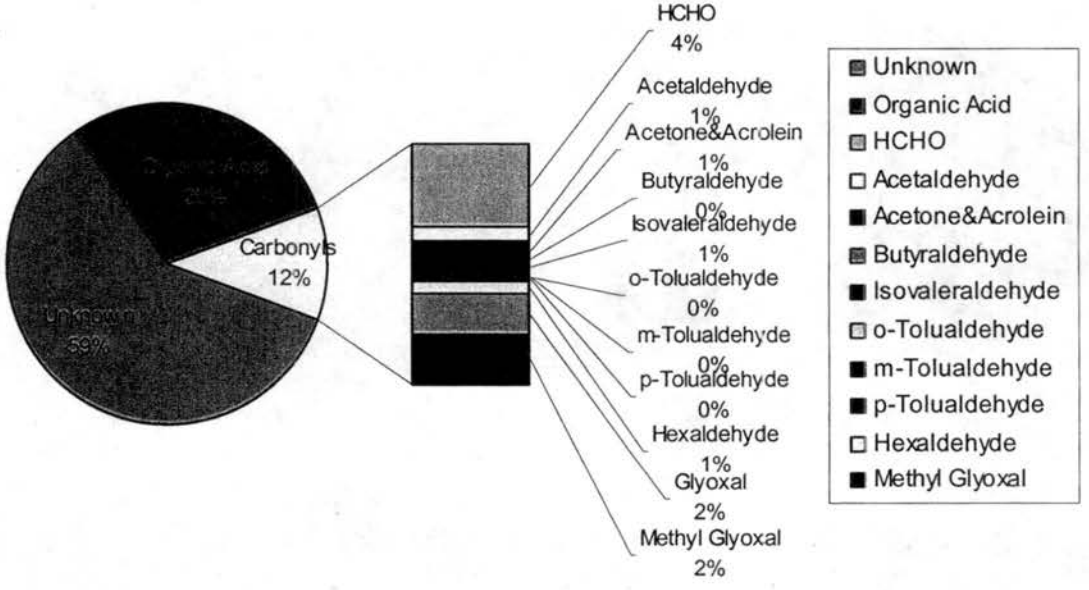

Figure G-6. Composition of carbonaceous material comprising the total dissolved organic carbon (DOC) content observed for FSC01102

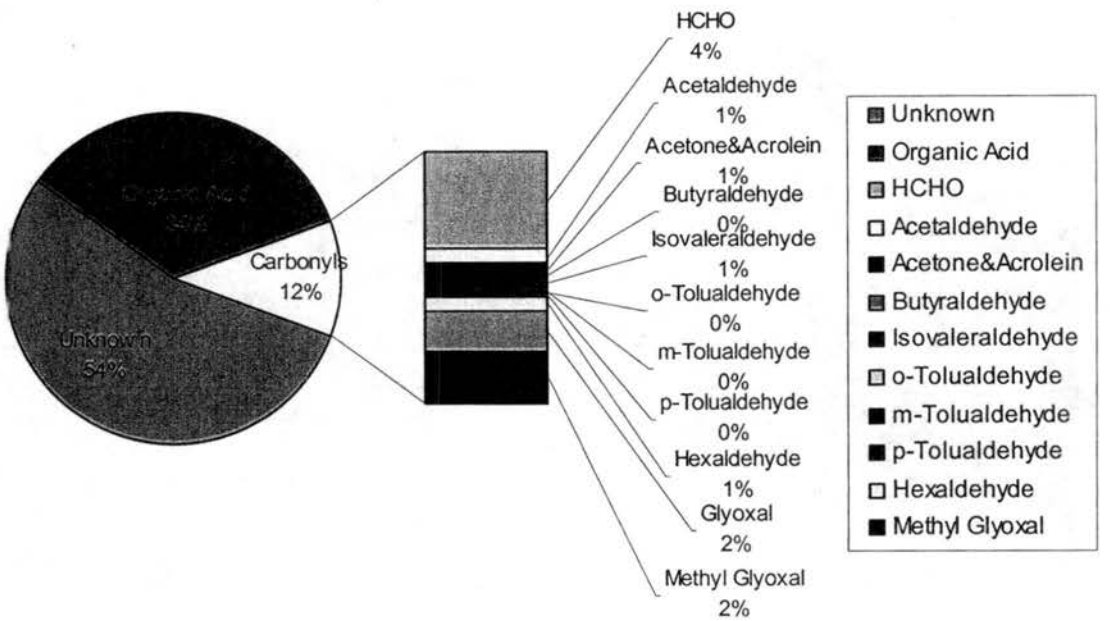

Figure G-7. Composition of carbonaceous material comprising the total dissolved organic carbon (DOC) content observed for FSC01103

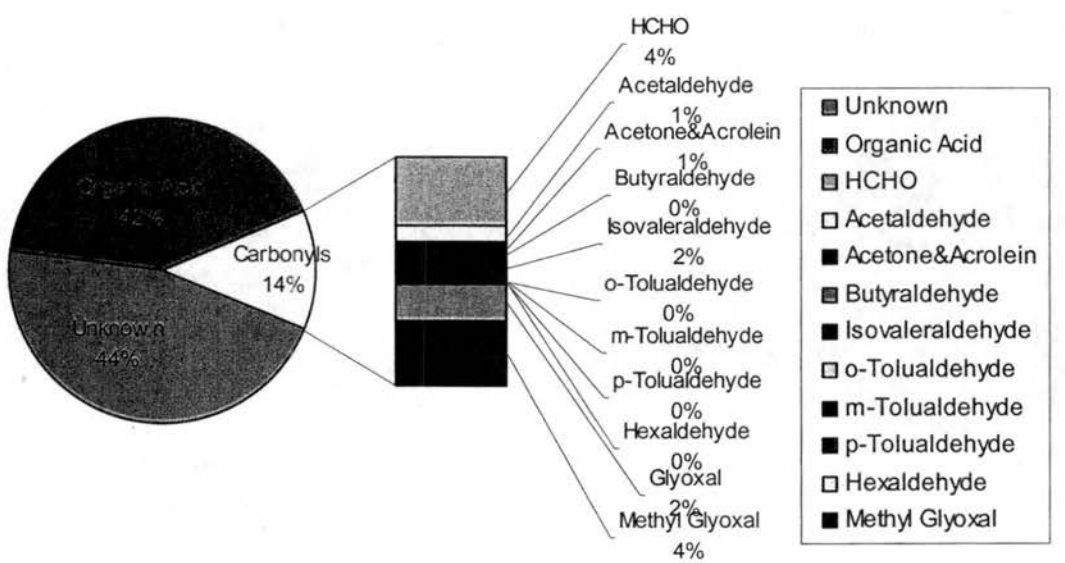

Figure G-8. Composition of carbonaceous material comprising the total dissolved organic carbon (DOC) content observed for FSC36401

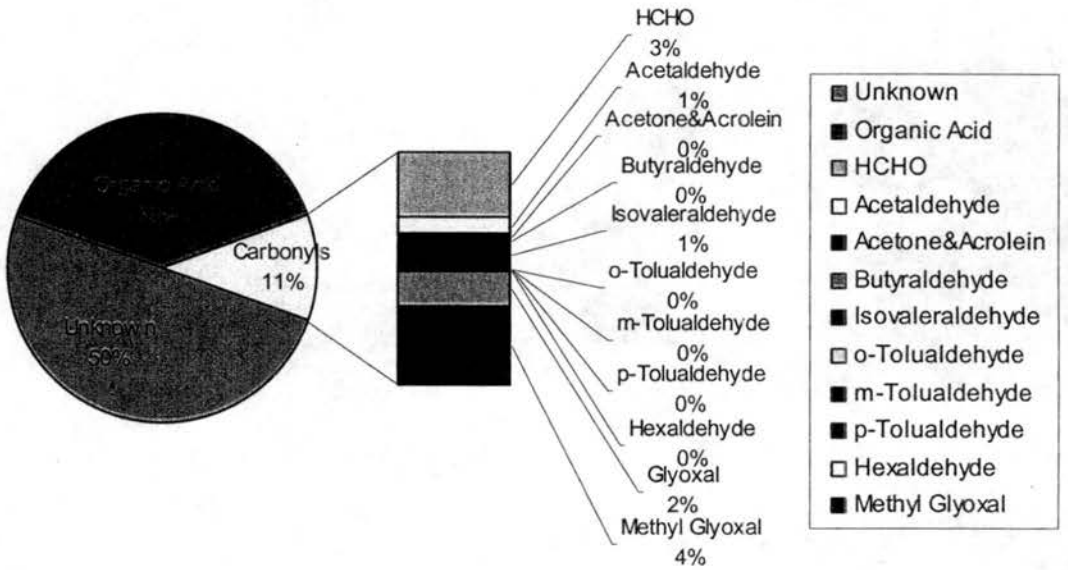

Figure G-9. Composition of carbonaceous material comprising the total dissolved organic carbon (DOC) content observed for FSCL01001

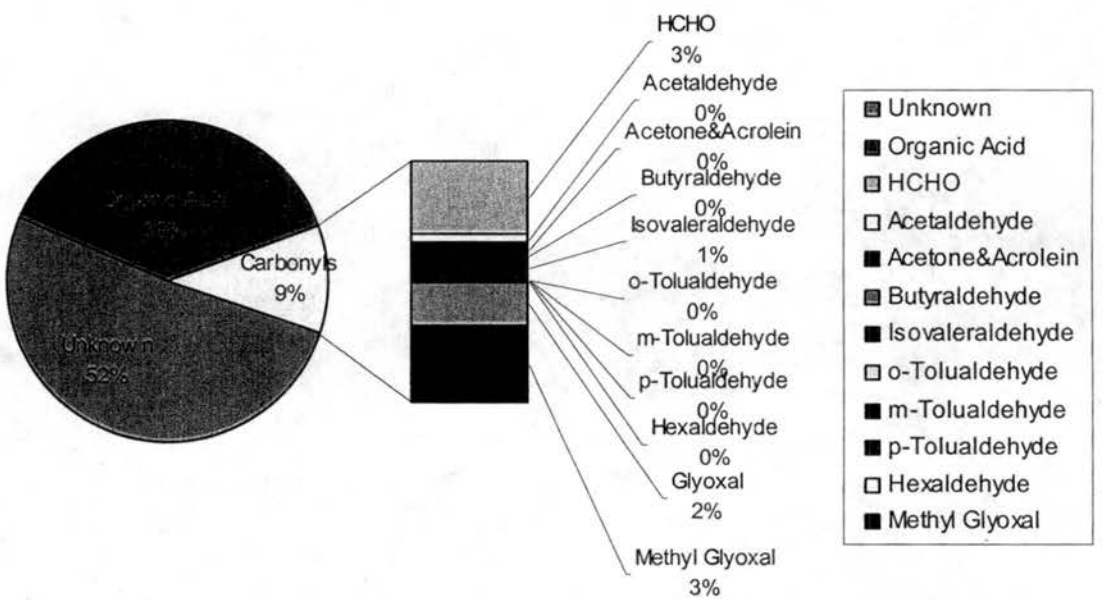

Figure G-10. Composition of carbonaceous material comprising the total dissolved organic carbon (DOC) content observed for FSCL01002

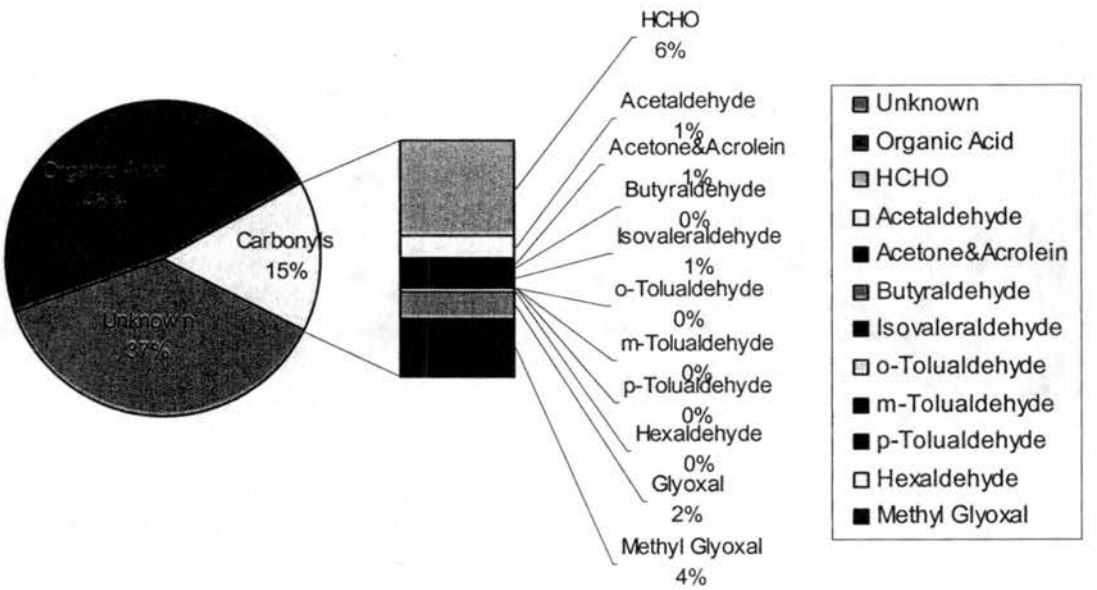

Figure G-11. Composition of carbonaceous material comprising the total dissolved organic carbon (DOC) content observed for FSCL01003

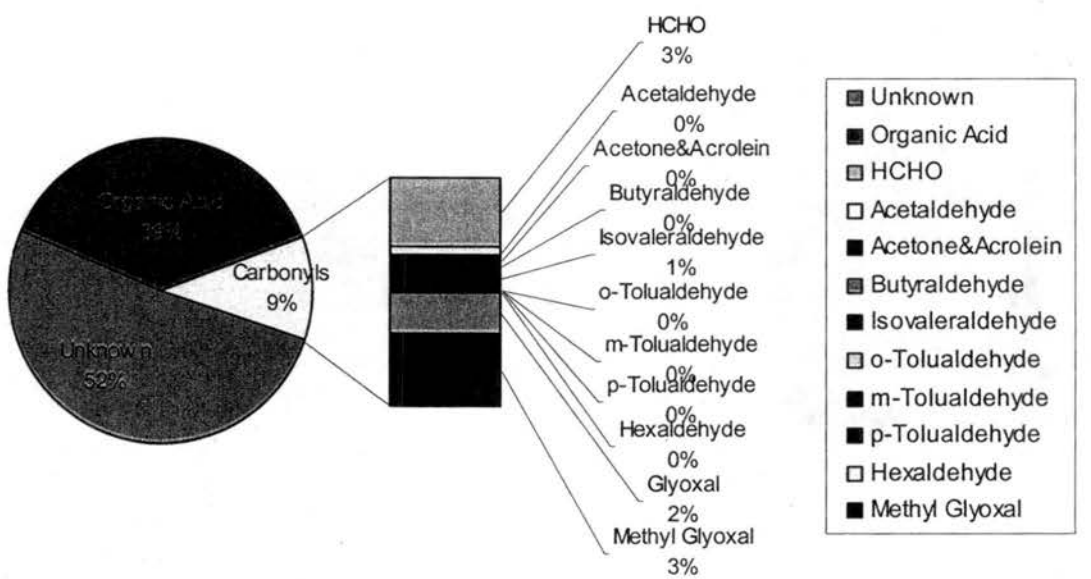

Figure G-12. Composition of carbonaceous material comprising the total dissolved organic carbon (DOC) content observed for FSCL01004

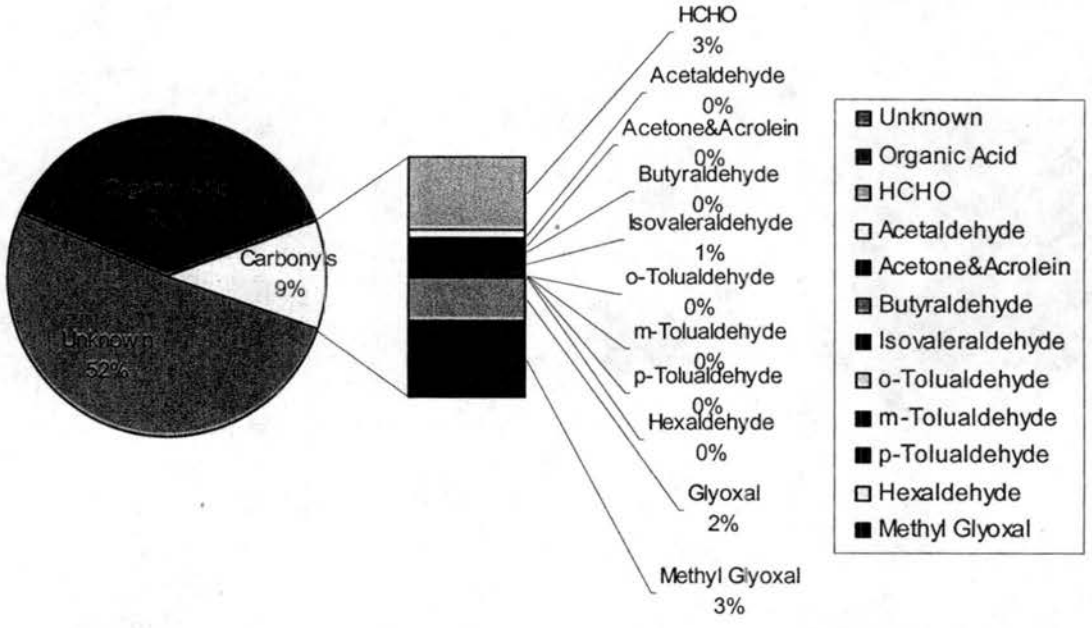

Figure G-13. Composition of carbonaceous material comprising the total dissolved organic carbon (DOC) content observed for FSCL01101

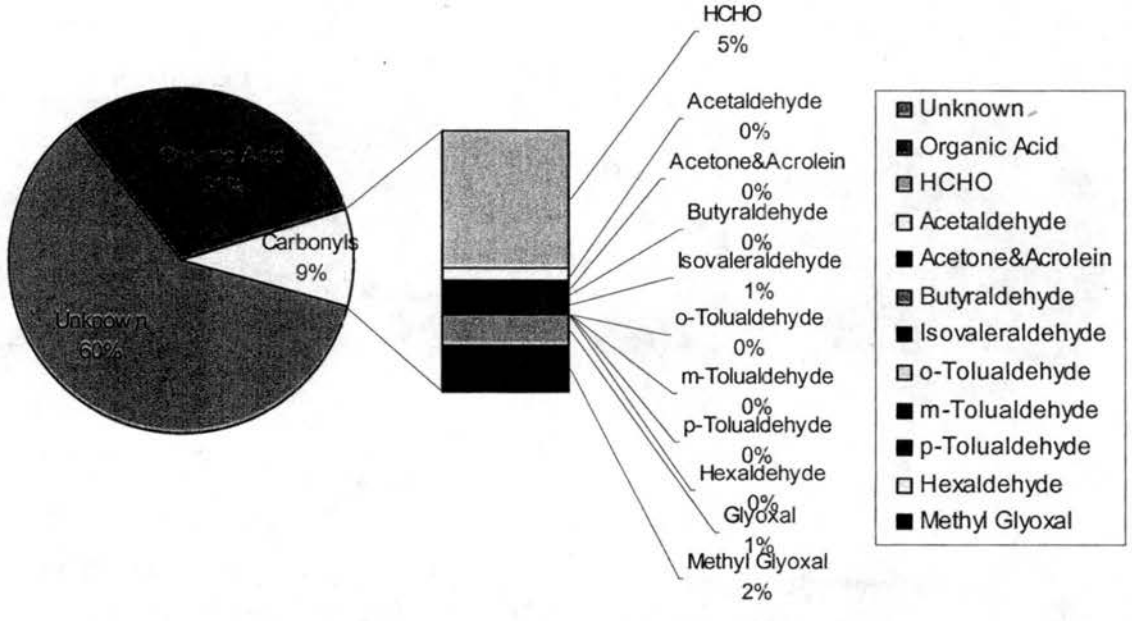

Figure G-14. Composition of carbonaceous material comprising the total dissolved organic carbon (DOC) content observed for FSCL01102

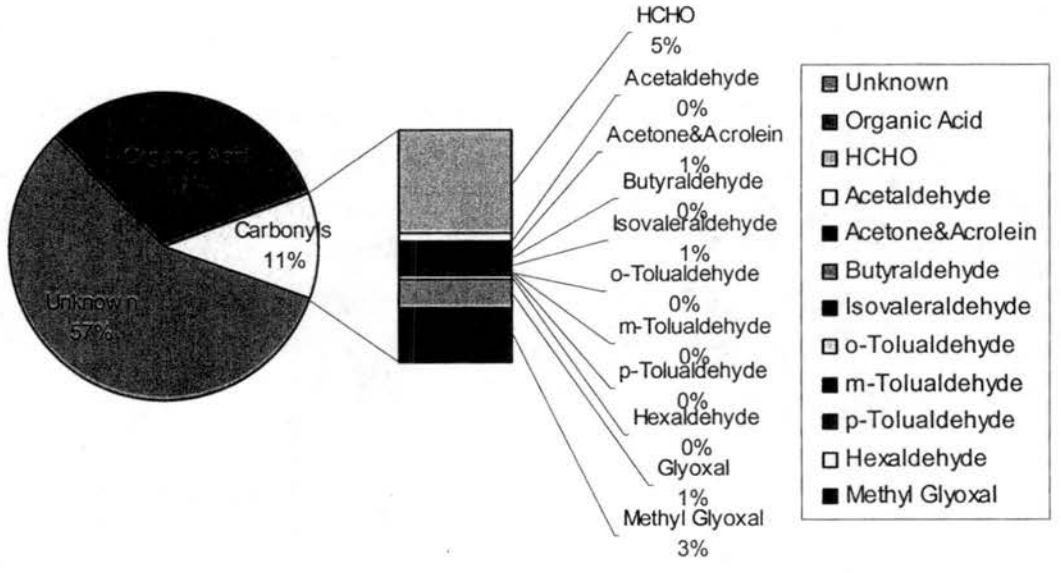

Figure G-15. Composition of carbonaceous material comprising the total dissolved organic carbon (DOC) content observed for FSCL01103

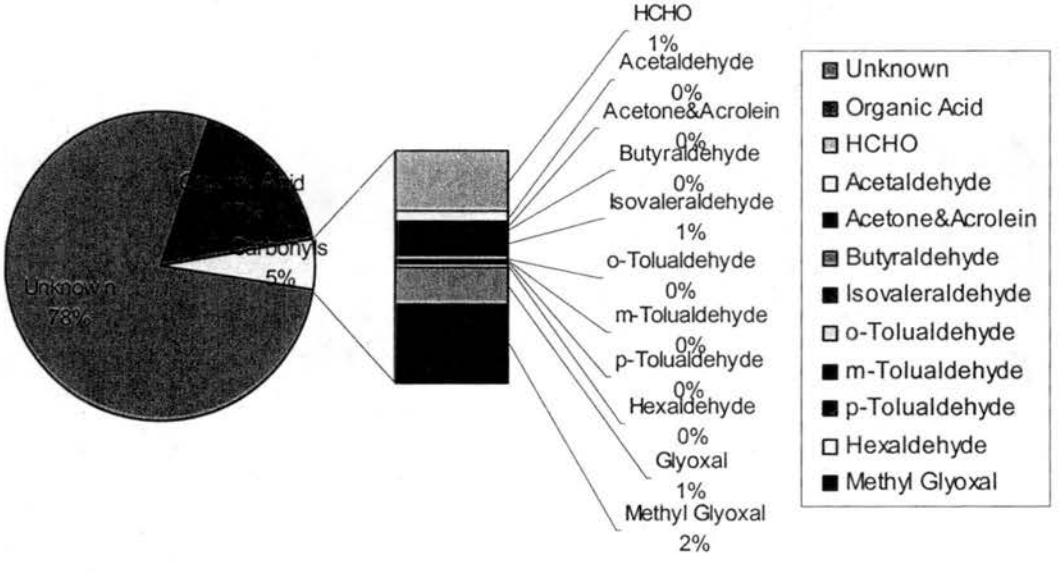

Figure G-16. Composition of carbonaceous material comprising the total dissolved organic carbon (DOC) content observed for FSCS01001

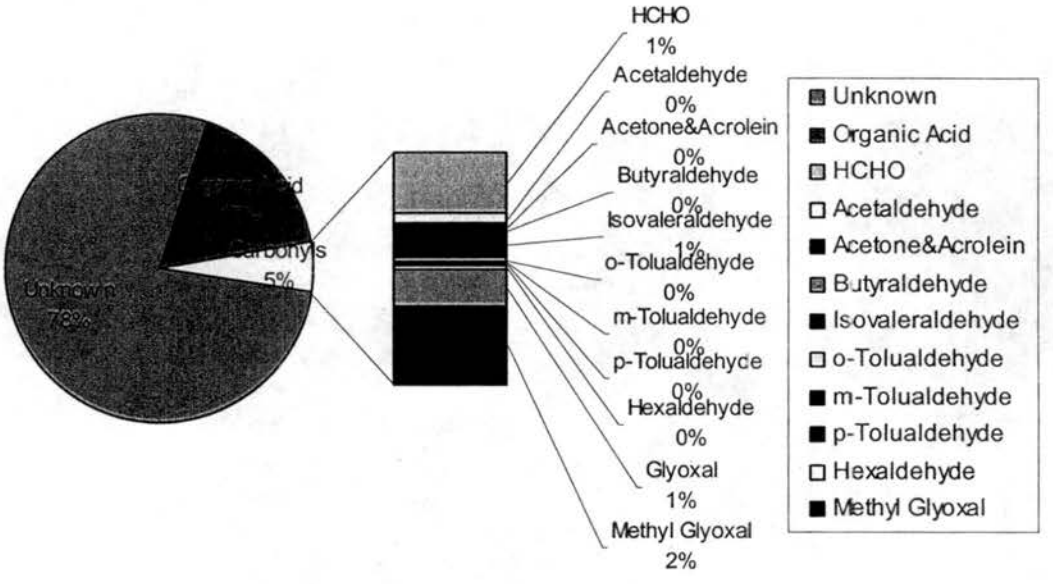

Figure G-17. Composition of carbonaceous material comprising the total dissolved organic carbon (DOC) content observed for FSCS01002

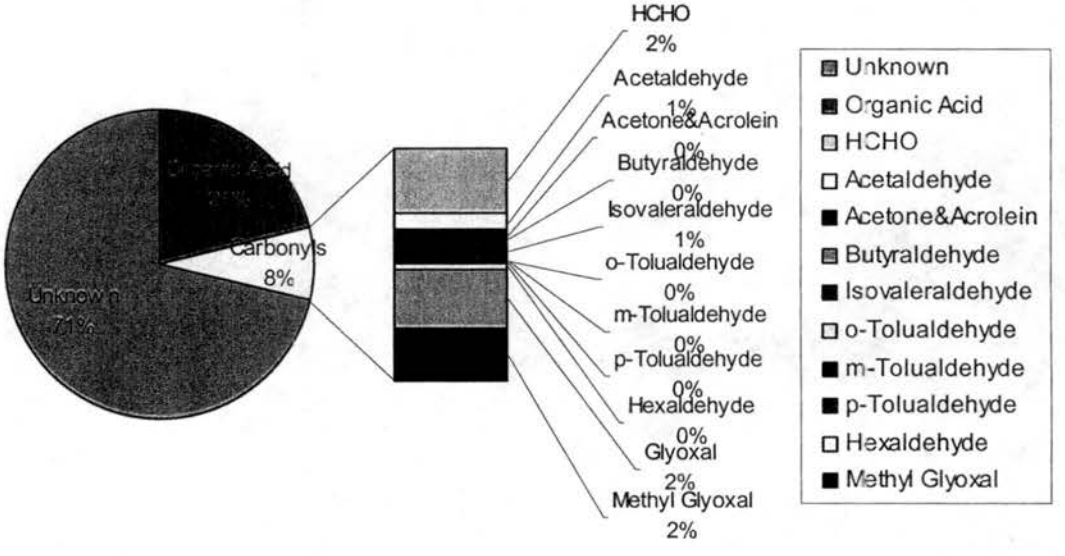

Figure G-18. Composition of carbonaceous material comprising the total dissolved organic carbon (DOC) content observed for FSCS01003

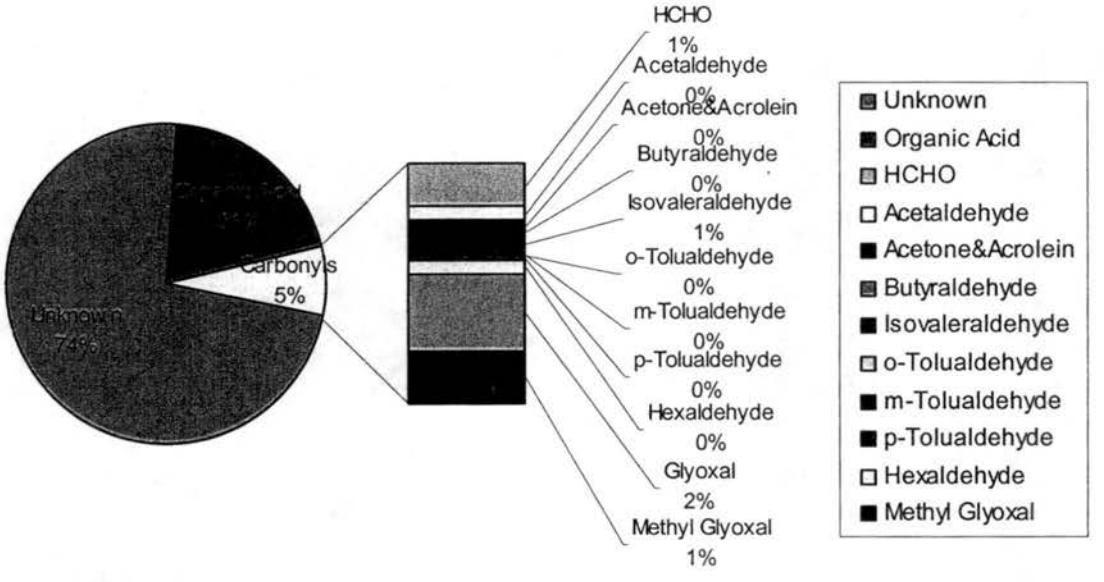

Figure G-19. Composition of carbonaceous material comprising the total dissolved organic carbon (DOC) content observed for FSCS01102